Study *o*f reactio*n* mechanisms f*o*r the synthesis *o*f super-heavy elements

Hope Donglo

Normandie Université

UNIVERSITÉ CAEN NORMANDIE

THÈSE

Pour obtenir le diplôme de doctorat

Spécialité **PHYSIQUE**

Préparée au sein de l'**Université de Caen Normandie**

Study of reaction mechanisms for the synthesis of super-heavy elements

Présentée et soutenue par

DONGLO HOPE

Thèse soutenue le 04/12/2024

devant le jury composé de :

M. ACKERMANN DIETER	Directeur de recherche - 14 GANIL de CAEN	Directeur de thèse
MME GULMINELLI FRANCESCA	Professeur des universités - Université de Caen Normandie (UCN)	Président du jury
M. BOILLEY DAVID	Maître de conférences - Université de Caen Normandie (UCN)	Co-encadrant
MME EVEN JULIA	Maître de conférences - GRONINGEN - UNIVERSITY OF GRONINGEN	Membre du jury
M. ANTALIC STANISLAV	Maître de conférences HDR - Comenius University Bratislava	Rapporteur du jury
M. SHEN CAIWAN	Professeur - Huzhou University	Rapporteur du jury

Thèse dirigée par **ACKERMANN DIETER** (Grand Accélérateur National d'Ions Lourds)

ED 591 PSIME

GANIL laboratoire commun CEA/DRF Spiral2 CNRS/IN2P3

Abstract

This thesis investigates the mechanism of synthesising super-heavy elements (SHE) via fusion evaporation reactions. These are nuclei with atomic numbers $Z \geq 104$ and do not exist in nature due to their vanishing macroscopic fission barriers. They are stabilised by quantum shell correction. The search for new SHE pushes the boundaries of nuclear physics, furthering our understanding of their formation, stability, and structure. However, synthesising SHE is challenging due to decreasing production cross sections as the atomic charge increases, necessitating theoretical simulations to guide experiments and identify optimal reaction conditions.

This work focuses on improving the predictive power of the Kewpie2 model, designed for fusion evaporation simulation. Fusion evaporation is modelled as a three-stage process: capture, formation, and survival. While Kewpie2 independently simulates the capture cross section and survival probability, it has relied on external calculations for formation probability. This thesis implements the formation step in the Kewpie2 code for the first time using both the overdamped and full Langevin formalisms.

The injection point distance (describing projectile-target nuclei starting configuration) is optimised for cold and hot fusion reaction datasets in both cases. An improved injection point distance parametrisation, consistent with the Langevin formalism, reproduces measured evaporation residue cross sections for hot fusion reactions, typically with accuracy better than an order of magnitude. For cold fusion reactions, multiple neutron emission channels are explained by introducing an additional structural term, achieving good agreement with experimental data. In this case, the 1n channel data are described as having a factor deviation from the experimental data, while the 2n and 3n channels are within an order of magnitude. The thesis also investigates survival probability modelling using the latest data for SHE. Both the formation and survival steps are extensively tested and compared with the Fusion-by-Diffusion (FbD) model for sets of 27 cold and 24 hot fusion reactions.

Analysis of the reduced friction coefficients within the overdamped Langevin approach suggests that the dynamic is not fully damped. Therefore, a full one-dimensional Langevin formalism is investigated and implemented in Kewpie2. The formalism is applied to hot fusion reaction data. The fitting coefficients of the model are optimised using a so-called systematic fitting technique, and the results confirm that the dynamic is not fully damped. In this approach, the model predictions are within an order of magnitude deviations from the experimental data. Predictions for the synthesis of elements with atomic numbers $Z_{\mathrm{CN}} = 119$ and 120 align with results from other codes. Additionally, a method for studying ratios of formation probabilities is proposed and discussed for the synthesis of ^{258}No and ^{259}Db.

In conclusion, this work significantly enhances Kewpie2, making it a self-contained tool for studying SHE synthesis and guiding future experimental efforts.

Résumé

Cette thèse étudie le mécanisme de synthèse des éléments super-lourds (SHE) par des réactions de fusion-évaporation. Il s'agit de noyaux de numéro atomique $Z \geq 104$ qui n'existent pas dans la nature en raison de leurs barrières de fission macroscopiques qui disparaissent. Ils sont stabilisés par une correction quantique du modèle en couches. La recherche de nouveaux SHE repousse les limites de la physique nucléaire et nous permet de mieux comprendre leur formation, leur stabilité et leur structure. Cependant, la synthèse des SHE est un défi en raison de la diminution des sections efficaces de production à mesure que la charge atomique augmente, ce qui nécessite des simulations théoriques pour guider les expériences et identifier les conditions de réaction optimales.

Ce travail se concentre sur l'amélioration du pouvoir prédictif du modèle Kewpie2, conçu pour la simulation de la réaction de fusion-évaporation. Cette réaction est modélisée comme un processus en trois étapes : capture, formation et survie. Alors que Kewpie2 simule de manière indépendante la section efficace de capture et la probabilité de survie, il nécessitait des calculs externes pour la probabilité de formation. Cette thèse inclut, pour la première fois, l'étape de formation dans le code Kewpie2 en utilisant les formalismes de Langevin sur-amorti et complet.

La distance du point d'injection (décrivant la configuration initiale de la phase de formation pour le système projectile-cible) est optimisée pour les réactions de fusion froide et chaudes séparément. Une paramétrisation améliorée de la distance du point d'injection, compatible avec le formalisme de Langevin, reproduit les sections efficaces de résidus d'évaporation mesurées pour les réactions de fusion chaude, généralement avec un ratio inférieur à un ordre de grandeur. Pour les réactions de fusion froide, les canaux d'émission de plusieurs neutrons sont expliqués par l'introduction d'un terme structurel supplémentaire, ce qui permet d'obtenir un bon accord avec les données expérimentales. Dans ce cas, les données du canal 1n sont décrites comme ayant une déviation d'un facteur par rapport aux données expérimentales, alors que pour les canaux 2n et 3n, les ratios sont à l'intérieur d'un ordre de grandeur. La thèse étudie également la modélisation de la probabilité de survie en utilisant les données les plus récentes pour SHE. Les étapes de formation et de survie sont testées de manière approfondie et comparées au modèle de fusion par diffusion (FbD) pour 27 réactions de fusion froide et 24 réactions de fusion chaude.

L'analyse des coefficients de frottement réduits dans le cadre de l'approche de Langevin suggère que la dynamique n'est pas sur-amortie. Par conséquent, un formalisme de Langevin unidimensionnel complet est implémenté dans Kewpie2 et appliqué aux données de réaction de fusion chaude. Les paramètres du modèle sont optimisés à l'aide d'une technique d'ajustement systématique. Dans cette approche, les prédictions du modèle se situent dans un ordre de grandeur d'écart par rapport aux données expérimentales. Les prédictions pour la synthèse d'éléments de numéros atomiques Z_{CN} = 119 et 120 s'accordent avec les résultats d'autres codes. En outre, une méthode d'étude des rapports de probabilités de formation est proposée et discutée pour la synthèse des isotopes ^{258}No et ^{259}Db.

En conclusion, ce travail améliore considérablement Kewpie2, ce qui en fait un outil autonome pour l'étude de la synthèse SHE et l'orientation des futurs efforts expérimentaux.

Acknowledgment

This thesis would not have been possible without the contributions of many individuals. I deeply appreciate the guidance of my supervisors D. Boilley and D. Ackermann, whose support and expertise were invaluable throughout this study.

I express my deepest gratitude to T. Cap, who acted as a mentor and guide throughout this journey. His insightful advice, unwavering support, and critical feedback were essential to completing this work. This thesis would not exist without his input. Furthermore, I would like to acknowledge the significant contributions of K. Siwek-Wilczyńska and Michał Kowal, whose insightful discussions and perspectives greatly enriched my research. Their willingness to engage in timeless discussions and share their knowledge broadened my understanding and pushed me to think critically about my work. I also want to thank A. Marchix for making time out of his busy schedules to provide essential assistance with Kewpie2's technical aspects.

I am grateful for the supportive research environment fostered by C. Stodel and J. Piot through regular student update meetings. These meetings provided a valuable platform for exchanging ideas, receiving feedback, and staying connected with the broader research community. I give thanks to the entire administration at the GANIL Research Institute for creating an enabling environment conducive to learn and research. Their commitment to providing the necessary resources and support was instrumental in my progress.

I recognize the vital assistance of Dominique Touchard and Guillaume Lalaire from the IT department, who ensured the smooth operation of the necessary technical infrastructure. I also want to thank my family for their support and encouragement.

Finally, I would like to extend deep gratitude to the NUMERICS fellowship program for funding this study. I also acknowledge the financial support from the COPIGAL project in facilitating collaboration with the National Centre for Nuclear Research, Warsaw, Poland.

Contents

Chapter 1

Introduction

The atomic nucleus has been a subject of interest since the Rutherford's gold foil-alpha scattering experiment in 1911 [1]. In this experiment, Rutherford discovered that the atom has a dense, positively charged central part, which he named the nucleus, where most of its mass is concentrated. This finding came after an earlier discovery of radioactivity by Becquerel and the Curies in 1896 and 1898, respectively [2, 3]. The present picture of the atomic nucleus as containing positively charged protons and neutral neutrons, collectively referred to as nucleons, was solidified after the discovery of neutrons by Chadwick in 1932 [4].

The above foundational discoveries serve as the premise for contemporary research in nuclear physics, encompassing a wide range of topics, both at low and high energies. Today, many nuclear phenomena can be explained, including structural details of the atomic nucleus. One such observation is the stability of atomic nuclei with specific numbers of protons and neutrons (known as magic numbers), which Goeppert-Mayer and Jensen later explained to be a result of quantum mechanical effects stemming from the complete filling of nuclear shells by the nucleons [5, 6]. The phenomenon is now well described by the nuclear shell model (microscopic model) of the atomic nucleus, in analogy to the electronic configuration in atomic shells [7].

A subtle yet significant advancement in the nuclear sciences was the classification of nuclei based on the proton and neutron numbers into the Segrè chart, also known as the nuclide chart. The chart not only categorises all known nuclei but also helps to identify various regions of distinct nuclear properties. It also serves as a tool for nuclear physicists to view the properties of the nuclei in a systematic order [8, 9].

The successes in understanding the atomic nucleus are not limited to research laboratories. Many discoveries have been applied in other areas of science, including engineering applications that meet societal needs. Some of these include advancements in nuclear medicine, diagnosis and treatment, and innovations in nuclear power generation, to name a few [10, 11].

Despite significant advances in our understanding of the atomic nucleus, several theoretical predictions and experimental observations suggest areas for further research. A particularly intriguing question is why there is a finite number of elements found on Earth,

with uranium being the heaviest naturally occurring element in abundant quantity. While some uranium isotopes have long half-lives, they are still unstable against radioactive decay. This underscores the critical role of nuclear stability in determining which nuclei exist naturally.

For instance, nuclei with excess protons or neutrons are prone to beta decay. This instability stems from the fact that having too many protons or neutrons reduces their respective separation energies, which eventually vanish at the proton or neutron drip lines. Beyond these drip lines, nuclei become unbound. These factors impose limits on the existence of proton-rich or neutron-rich nuclei. Additionally, the probability of spontaneous fission increases with nuclear charge, contributing to the finite number of stable nuclides that could occur naturally.

A window of opportunity for the synthesis of artificial nuclei opened when an experiment originally designed to investigate nuclear fission in May 1940 led to a discovery of a previously unknown element with atomic charge greater than uranium, later named neptunium [12]. This breakthrough began the successful path of synthesis experiments of nuclei with proton numbers ranging from 93 to 100, commonly referred to as transuranium elements. Historically, neptunium was synthesized by bombarding a uranium-238 (^{238}U) target with neutron flux:

$$^{238}\mathrm{U} + ^{1}\mathrm{n} \rightarrow \ ^{239}\mathrm{U} \rightarrow ^{239}\mathrm{Np} + e^{-} + \bar{\nu}_e. \tag{1.1}$$

In this reaction, the uranium target captures the impinging neutron and forms a compound nucleus, uranium-239 (^{239}U), which undergoes beta decay to neptunium (^{239}Np) accompanied by an electron (e^{-}) and an electron antineutrino ($\bar{\nu}_e$). Trace amounts of neptunium and plutonium, that can be found in nature [9, 13] originate from the beta decay process as described above [14, 15]. The multi-step process of consecutive neutron captures, followed by the beta decays, was used to synthesize heavier elements up to fermium (Z=100), at which this method reaches its limit due to the change of a decay mode from beta decay to fission [16]. Heavier elements with atomic numbers from 101 to 106 were synthesized using alpha particles or light projectiles such as carbon, nitrogen or argon ions.

As the atomic number of a nucleus increases, it becomes unstable and prone to fission [17]. Nuclear fission has been extensively studied experimentally and theoretically. The first success in describing fission was achieved within the liquid drop model (LDM) framework, also known as the macroscopic model of the atomic nucleus. Here, the nucleus is treated as a droplet of incompressible charged fluid [18, 19]. The macroscopic models have played a pivotal role in explaining the relationship between an increasing proton number and the decreasing stability of the nucleus against fission. The nuclear fission barrier is approximated to vanish around proton numbers between 100 and 104 within the Liquid drop model. The instability is attributed to the intensified Coulomb repulsion among the densely packed protons within the nucleus's limited volume [20].

The liquid drop model offers insights into some nuclear properties and fission mechanisms; however, its limitations must be acknowledged. The liquid drop model overlooks the impact of the nuclear shell effects, which is now understood to critically influence nuclear stability. In contrast, the nuclear shell model integrates the structural details and explains the magic numbers but does not properly describe macroscopic nuclear properties such as masses and binding energies. A combination of both models, known as a macroscopic-microscopic method, solved these issues and predicted the existence of elements beyond the

actinide series, which ends at lawrencium (Z = 103). Transactinide elements are generally called super-heavy elements (SHE). Macroscopic-microscopic calculations predict the next closed shells at Z = 114 or 120 and N = 182. The region around these magic numbers in the nuclide chart is called the island of enhanced stability. Reaching this region is one of the biggest challenges in nuclear physics [9, 21].

Over the years, new elements have been successfully synthesized, culminating in the production of element 118, oganesson [22]. These achievements expand the horizons of low-energy nuclear physics, challenge nuclear models, and allow us to explore the properties of previously unknown elements. These advancements raise fundamental questions, such as, "What is the heaviest possible element that could exist?" Unfortunately, synthesizing heavier elements becomes increasingly difficult due to their minuscule production cross sections. New experiments require accurate theoretical guidance, particularly regarding optimal bombarding energies and projectile-target combinations for higher chances of success. Since the wrong projectile-target combination or probing the experiment at the wrong energies may yield no result. Addressing these challenges is central to this thesis.

1.1 Beyond Transactinide Series

Nuclei that do not exist in Nature or are not available in sufficient quantities can be obtained using various experimental methods, including successive neutron captures and subsequent β^- decays, fragmentation reactions, fission of heavy elements, multinucleon transfer reactions or fusion [23, 24]. These techniques have their capabilities and limitations in exploring various regions in the nuclide chart. For example, nuclear fragmentation is well adapted for obtaining exotic neutron- or proton-rich nuclei. The medium heavy neutron-rich nuclei can be identified in fission fragments of heavy elements. The multinucleon transfer reactions may be used to study nuclei involved in astrophysical r-process [25]. They are also presently considered as a potential technique to synthesise SHE [23, 26–29]. So far, complete fusion reactions followed by evaporation of light particles have proved to be the most successful in synthesizing SHE [24, 30].

Using fusion evaporation reactions to synthesize SHE requires accelerating progressively heavier projectiles and usage of targets made of heavy elements. This was made possible by the advances in constructing powerful heavy-ion accelerators and improvements in separation and identification techniques of reaction products [31]. These developments gave birth to the super-heavy nuclei era, during which 15 transactinide elements have been synthesised. The fusion evaporation reactions leading to SHEs are categorised into cold and hot fusion reactions, depending on the projectile-target combination and the excitation energies reached by the compound nucleus [9, 32].

Cold fusion reactions use targets such as lead or bismuth with projectiles ranging from ^{48}Ca to ^{70}Zn. Due to the Q-value and the Coulomb barrier of these reactions, compound nuclei are formed at low excitation energies around 10 to 20 MeV. This is followed by the emission of one or two neutrons in the cooling-down process. Cold fusion reactions have been employed to synthesise SHE with atomic numbers ranging from 107 to 113 [9].

On the contrary, reactions with a neutron-rich Ca-48 projectile on actinide targets lead to

the so-called hot fusion reactions [32]. Here, the compound nucleus is formed at relatively high excitation energies, ranging from 30 to 55 MeV. This allows for the emission of usually three to five neutrons before the remaining excitation energy goes below the thresholds for the next neutron emission and fission [33, 34]. For hot fusion reactions, the fusion cross section is larger than for cold fusion reactions, but the survival probability is lower. This is because, at each step, the neutron emission competes with fission, which is a dominant decay mode. Hot fusion reactions have been employed to synthesise SHE with atomic numbers 110, and 112-118. Despite their achievements in synthesizing new elements, cold and hot fusion reactions have challenges and limitations.

1.2 Fusion Evaporation Reaction

1.2.1 Experimental Successes and Challenges

The progress in synthesising super heavy elements can be summarised in Fig.1.1. Starting from the left in panel (a) are the elements synthesised using the cold fusion reactions. On the abscissa is the proton number of the compound nucleus (CN). The respective production cross sections are presented on the ordinate for the reactions using projectiles ranging from ^{48}Ca to ^{70}Zn and the ^{208}Pb target (closed symbols) or ^{209}Bi target (open symbols), respectively.

The general trend, as shown in panel (a) of Fig. 1.1, is that the production cross section decreases with the increasing proton number of the compound nucleus formed, i.e., the production cross section in 1n channel decreases by a factor 10^7 from the proton number 102 to 113. As the projectile-target combinations become more symmetric, the Coulomb repulsive forces increase, making fusion less probable. The heaviest nucleus accessible through cold fusion is nihonium, having a proton number equal to 113. The reported production cross section is 22^{+20}_{-13} fb. Only 3 events were observed in 553 days of beam time [9, 35]. With the decreasing trend in the production cross section, this method cannot synthesize heavier elements.

To overcome these limitations, highly neutron-rich ^{48}Ca was used as the projectile in reactions with actinide targets (from ^{232}Th to ^{249}Cf) in hot fusion reactions [22]. In ^{48}Ca-induced reactions, the Coulomb barriers are lower by about 40% [33] in comparison with cold fusion reactions leading to the same atomic numbers. This technique allows nuclei with atomic numbers from Z_{CN} = 112 to 118 to be synthesised, as shown in panel (b) of Fig. 1.1.

As illustrated in panel (b) of Fig. 1.1, synthesising nuclei with proton numbers greater than 118 requires heavier projectile or actinide targets than currently used. However, materials heavier than californium are highly radioactive and are not suitable for targets in synthesis experiments, which presents a hurdle that must be overcome. In addition, the production cross section peaks at a proton number equal to 114 and starts to decrease. The decreasing production cross section is a limiting factor that can only be overcome by investigating alternate projectile-target combinations that can be used in future SHE synthesis experiments.

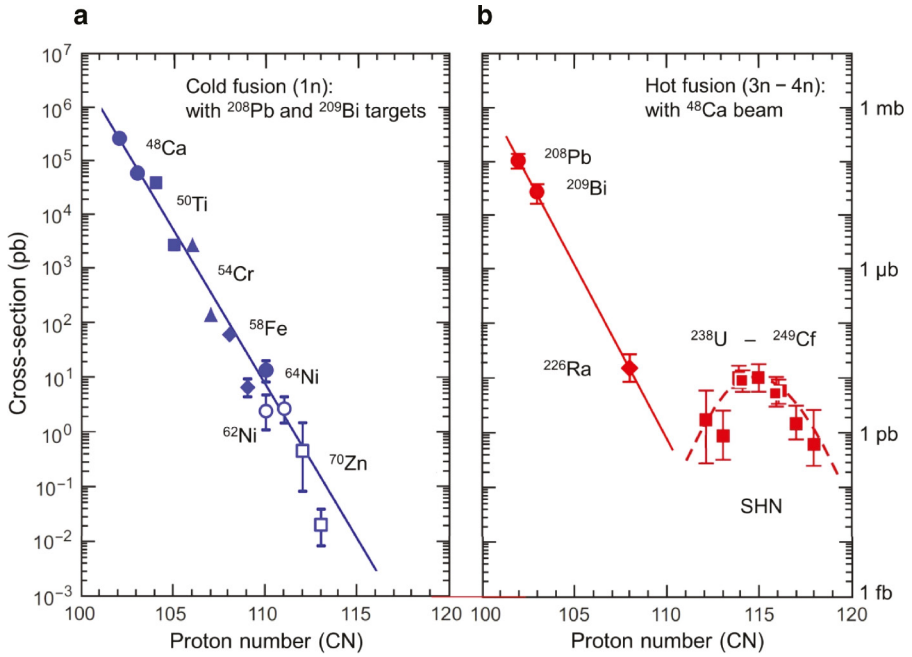

Figure 1.1: The figures summarise measured fusion evaporation reaction cross sections for super heavy element synthesis, plotted against the proton number of the resulting compound nucleus (CN). Panels (a) and (b) show cross sections for cold and hot fusion, respectively. Different symbols represent various projectiles used in cold fusion 1n reactions (panel (a)). Closed and open symbols indicate ^{208}Pb and ^{209}Bi targets, respectively. Panel (b) shows only data for the 3n and 4n evaporation channels. Lines are provided to guide the eye. The figure is reproduced from Ref. [31].

The following are examples of experimental attempts to synthesize new elements with $Z_{CN} = 119, 120,$ and 122 using projectiles heavier than ^{48}Ca [36]: ^{64}Ni +^{238} U [37], ^{58}Fe +^{244} Pu [38], ^{50}Ti +^{249} Bk [39], ^{50}Ti +^{249} Cf [39], and ^{70}Zn +^{238} U [40]. The lack of results in these experiments underscores the need to choose an appropriate projectile, even if the targets are readily available. A recent experimental investigation has utilised ^{50}Ti on ^{244}Pu in an attempt to synthesise the nucleus with $Z = 116$ with a beam other than ^{48}Ca [36]. The production cross section in this experiment is 0.44^{+58}_{-28} pb and is based on two observed events. The element 110 was also achieved using this method to react to ^{48}Ca with ^{232}Th in a Super Heavy Element Factory in JINR, Russia. The reported cross section is $0.7^{+1.1}_{-0.5}$ pb [41–43].

Separate from the progress made and challenges associated with the production cross sections of SHE, other areas such as spectroscopic studies have advanced, thanks partly to developments in nuclear instrumentation and experimental techniques [44]. These advancements are in the structural details, such as the spectrum states and the role of K-isomeric states in their stability [45]. The knowledge and data garnered from these studies are instrumental in refining our existing nuclear models, like the mean field models. These models are crucial in the region of the nuclear chart where shell effects play a key role in explaining the stability of the atomic nuclei [46]. Despite the challenges, breakthroughs are expected as more scientific resources are committed to this frontier, such as the Super Separator Spectrometer (S3) at GANIL. The S3 has been designed to experiment with extremely low cross sections [47]. There are other research facilities dedicated to the

effort to synthesise super-heavy elements, which include RIKEN (Japan), IMP (China), SHE factory in Dubna (Russia), and LBNL (USA). The search for SHE is not limited to experimental investigations alone. There are ongoing theoretical efforts to refine the modelling of the production cross sections and study the structural properties of these nuclei.

1.2.2 Theoretical Successes and Challenges

On the theoretical fronts, there are efforts aimed at modelling the reaction mechanisms[48–54] while some are oriented towards investigating super heavy nuclides structural properties. To begin with, modelling the complete reaction mechanism is a challenge, partly due to a lack of clarity on the heavy ion fusion mechanism. The fusion processes in the SHE regime is known to be several orders of magnitude hindered [55] (see also Fig. 1.1). That is, the fusion cross section (**fusion**) is defined as:

$$\textbf{fusion} = \textbf{capture} \times \textbf{formation}, \tag{1.2}$$

Here, **capture** refers to the cross section for overcoming the entrance channel barrier. At the same time, **formation** is the probability that the fusing system will reach the state of thermal equilibrium and form a compound nucleus. The product of the capture cross section and the formation probability gives a fusion cross section [24, 48, 52]. The fusion dynamic in heavy ion reactions differs from light nuclei where, at energies just above the Coulomb barrier, the total capture cross section is equal to that of fusion [56]. In the context of very heavy nuclei, the scenario is more complex due to the emergence of competitive processes such as quasi-fission, which significantly affect the fusion process [56, 57]. Quasi-fission is the process where the colliding nuclei at capture re-separate into projectile- and target-like fragments without reaching compound nucleus configurations.

The compound nucleus formation probability remains a quantitative ambiguous step in modelling the SHE production cross sections and is difficult to measure experimentally. Furthermore, there is no theoretical consensus on its modelling. This is demonstrated in Fig. 1.2, in which calculations obtained from different modelling approaches differ from 2 to 3 orders of magnitudes. Although the underlying assumptions in modelling may vary, the objective is to estimate the probability of the projectile and target evolving into a compound nucleus from the capture stage.

Many approaches have been developed to describe the fusion probability as shown in Fig. 1.2. An example is the di-nuclear system model (DNS) [58–60] in which a complete fusion is envisioned in a mechanism involving gradual transfer of nucleons between the fusing nuclei at contact (capture phase). On the other hand, there are models [48, 52, 61–65] that describe the fusion dynamics using few collective variables within Langevin formalism. This approach is a direct continuation of the thermal fission studies for which this Langevin approach was introduced [66]. An example of the Langevin based model is the Fusion-by-Diffusion (FbD) model, which assumes that after the contact of two nuclei, the thermal fluctuations in the shape degrees of freedom may bring the system to the compound nucleus configuration [48, 67, 68]. The challenge in the modelling lies in the lack of full understanding of the intricate dynamics of di-nuclei evolution into a

compound nucleus. This is made worse by the scarcity of experimental data to train the models. All these factors contribute to the discrepancies in the theoretical predictions as seen in Fig. 1.2.

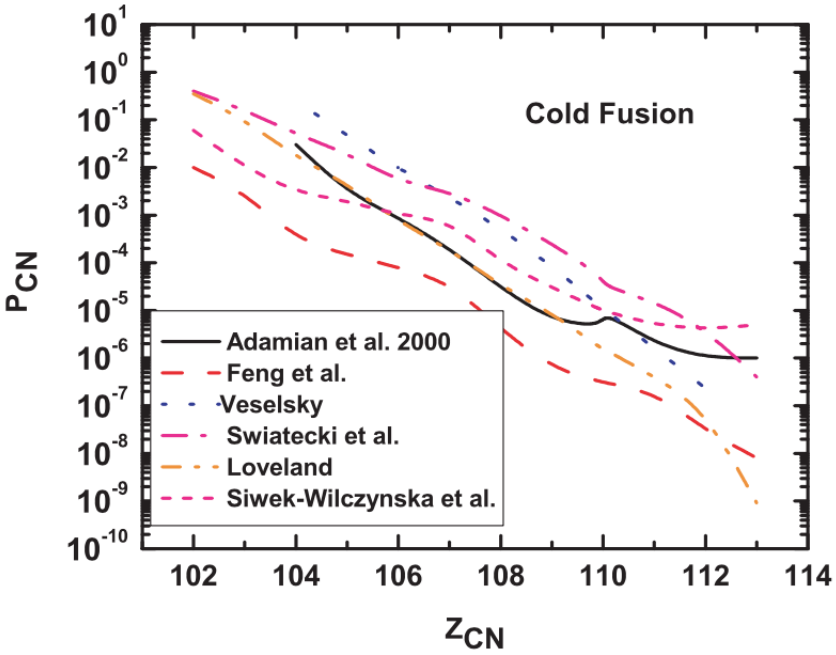

Figure 1.2: Formation probability of the compound nucleus vs atomic charge of the compound nucleus for elements formed in cold fusion reaction. Each line represents the calculations by the different models. The figure is reproduced from [55].

In Fig. 1.2, each solid or dash line shows the compound nucleus formation probability obtained from a different model. Despite the quantitative discrepancies in the calculations, qualitative convergence shows a decreasing tendency with increasing proton number Z_{CN}. The quantitative ambiguities pose a challenge to proper theoretical guides to the experiment. An incorrect theoretical input, such as the optimal energy or projectile-target combination, will lower the chances of a successful experiment. Understanding the compound nucleus formation is important for correctly guiding the experiment, explaining the dynamics of the heavy ion fusion mechanism, and providing reliable predictions for new reactions.

Beyond the challenges in modelling the formation step, theoretical inputs such as nuclear ground state masses, fission barriers, and deformations are crucial for the overall simulation process of the production cross section. The ground state masses and deformations are relevant in evaluating the capture and the formation phases, but their impact becomes even more pronounced in determining the survival probability. The survival probability (**survival**) is the probability that the formed compound nucleus will outlast fission and de-excite by emitting light particles such as neutrons, protons, alpha particles, or gamma rays. The production of charged particles is less likely. The SHE production cross section (EvR) is expressed as:

$$\textbf{EvR} = \textbf{capture} \times \textbf{formation} \times \textbf{survival}. \tag{1.3}$$

Some major factors contributing to the uncertainties in the predicted cross sections are

uncertainties in the **formation** and **survival** steps. In light of this, the calculation of nuclear ground states and saddle point properties, such as fission barriers, remain an area of active research.

Over the years, significant strides have been made towards achieving good agreement between theoretical nuclear properties and experimental data through the development of macroscopic-microscopic models [69, 70] and microscopic models such as the Skyrme-Hartree-Fock-Bogoliubov mass formulas [71, 72]. Despite these advancements, discrepancies persist in the data derived from different formalisms, significantly impacting the calculated production cross sections for super-heavy elements. Consequently, a super heavy element production cross sections calculated using nuclear properties based on different formalisms will likely differ. Studies by B. Cauchois have demonstrated that a 1 to 2 MeV change in the fission barrier could introduce a variation of approximately two orders of magnitude in the survival probability [73]. To address these challenges and ensure consistency in this investigation, the nuclear properties calculated by P. Jachimowicz were adopted in this thesis [69]. This nuclear mass and fission barrier table is particularly optimised for the super-heavy elements.

This thesis aims to enhance the modelling of the production cross section of SHE within the simulation package Kewpie2 [53]. Kewpie is a specialized numerical cascade code designed to simulate the dynamical decay of excited atomic nuclei. It is particularly effective in studying rare events associated with synthesising super-heavy nuclei formed via fusion evaporation reactions [53]. Kewpie [74] has a long history of being iteratively improved, and the recent version is called Kewpie2 [53, 75]. The code is written in C++ and takes advantage of object-oriented programming. The code incorporates several nuclear models to simulate light-particle emission, fission processes, and the statistical behaviour of excited nuclei, as demonstrated in the thesis in Ref. [76]. Despite the numerous advantages, such as different sub-model options and short computational time, Kewpie2 relies on external calculation for formation probability to augment its simulation for super-heavy elements.

The steps taken to enhance the predictive power of Kewpie2 are updating some of the parameters and comparing the results from the code on the capture cross section and the survival probability to the experimental data and calculations from a well-established code. These investigations allowed us to proceed with the further development of the code by tackling the most ambiguous step in modelling the reaction dynamics, the compound nucleus formation probability. Here, we investigated the compound nucleus formation at the overdamped limit of the Langevin formalism. This formalism is consistent with the widely used Fusion-by-Diffusion approach (FbD). Based on the result from the overdamped limit, the formalism is extended to the undamped one-dimensional Langevin formalism to further improve the description of the dynamics. Ultimately, the objective is to make Kewpie2 a standalone numerical code for investigating all three stages leading to the production cross section of super-heavy elements. The thesis concludes by investigating how to possibly constrain the formation probability by assessing and quantifying uncertainties in the modelling process. This thesis follows Ref. [73, 76] in assessing uncertainties in the capture cross section and the survival probability.

The content of the thesis is organised as follows: Chapter (2) present an approach to modelling the production cross section for synthesising elements formed in fusion evap-

oration reactions. The Sections 2.1 and 2.2 outlined the theoretical frameworks of the capture cross section and the survival probability modelling. The formalisms behind these stages are known and already implemented in Kewpie2. This is followed by presenting the formalism of the compound nucleus formation probability. As mentioned, this is the ambiguous step in modelling the production cross section and is investigated in detail. Chapter 3 revisits the formalism of the compound nucleus formation probability within the overdamped limit but from a different perspective, which allows us to obtain an improved parameterization of the free parameter of the FbD model called the injection point distance.

The fitting parameters of the injection point distance are adjusted to the experiment, and the outcomes show that the fusion dynamics within the Langevin formalism may not be overdamped. Therefore, the overdamped approximation is considered too restrictive. Chapter 4 presents the undamped one-dimensional Langevin formalism of the compound nucleus formation probability to investigate this further. This is investigated within the Kewpie2, and the free coefficients are adjusted to the experimental data techniques using a loss function different from the typical χ^2. Finally, Chapter 5 presents a summary of the predictive power of each parameterization. This is reinforced by bench-marking the calculations on new data in the cold fusion regimes ^{207}Pb(^{64}Ni,1n)^{210}Ds. To conclude, we made predictions for planned and ongoing experiments to synthesise elements with atomic numbers $Z = 119$ and 120.

Chapter 2

Approach to Fusion Evaporation Reaction Modelling

This chapter focuses on the theoretical framework for modelling the evaporation residue (EvR) cross sections for super-heavy elements synthesis in fusion evaporation reactions. As mentioned, the EvR cross section is theoretically conceptualized as a three-step sequential process, described by capture cross section (σ_{cap}), formation probability (P_{CN}), and survival probability (P_{surv}) [53, 62, 64, 68, 77].

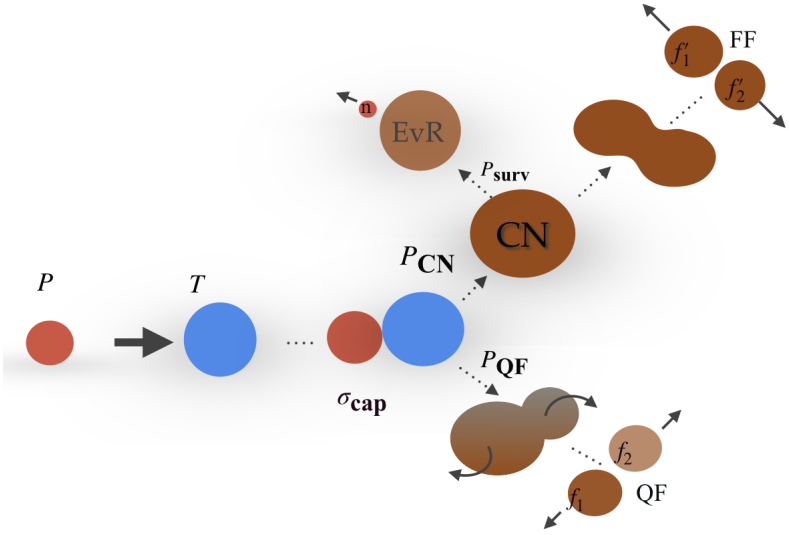

Figure 2.1: Schematic diagram showing the reaction mechanism for synthesising super-heavy elements. The process begins when the projectile (P) is captured (σ_{cap}) by the target (T), bringing both into a di-nuclei configuration. In this configuration, it is possible to proceed either by forming a compound nucleus (CN), with probability denoted as P_{CN} or undergoing quasi-fission (QF) with probability P_{QF}. Here, f_1 and f_2 are the quasi-fission fragments. The probability that the newly formed compound nucleus will survive fission by emitting light particle(s) and reach evaporation residue state (EvR) is called survival probability (P_{surv}). Here, $f_1^{'}$ and $f_2^{'}$ represent the fission fragments originating from fusion-fission (FF). See text for more details.

The capture process is the first stage where the projectile (P) and target (T) nuclei overcome the entrance channel potential barrier, namely the Coulomb-plus-nuclear interaction and the centrifugal barrier. The height of the Coulomb potential barrier and its position are denoted by B and R_{B}, respectively, on the schematic of Fig. 2.2. At capture, the projectile and target nuclei form a di-nuclei in the proximity of the strong nuclear attractive force. However, they can re-separate without forming a compound nucleus in a process known as quasi-fission. During quasi-fission, the colliding nuclei exchange nucleons before separating into projectile-like and target-like fragments labelled f_1 and f_2 at the exit channel (shown in Fig. 2.1) [33, 49, 78].

Quasi-fission, which is inherently associated with heavy-ion collisions [79], has been attributed to the presence of a conditional saddle inside the point of hard contact on the dynamical trajectory of the colliding nuclei [80–82]. The presence of the conditional saddle, which is referred to as the fusion saddle in this study, gives rise to a secondary inner barrier. The inner barrier as depicted B_{sad} in the schematic representation in Fig. 2.2, is an extra barrier that the colliding nuclei must overcome to fuse successfully.

The dynamics around the conditional saddle imply that the colliding nuclei require additional energy to fuse, leading to a two-step fusion in heavy ion collision. Given the strong competition between fusion and quasi-fission, the transition of di-nuclei into a compound nucleus is distinguished by complementary probabilities namely formation (P_{CN}) and quasi-fission probability (P_{QF}) i.e., $P_{\mathrm{CN}} + P_{\mathrm{QF}} = 1$ [57].

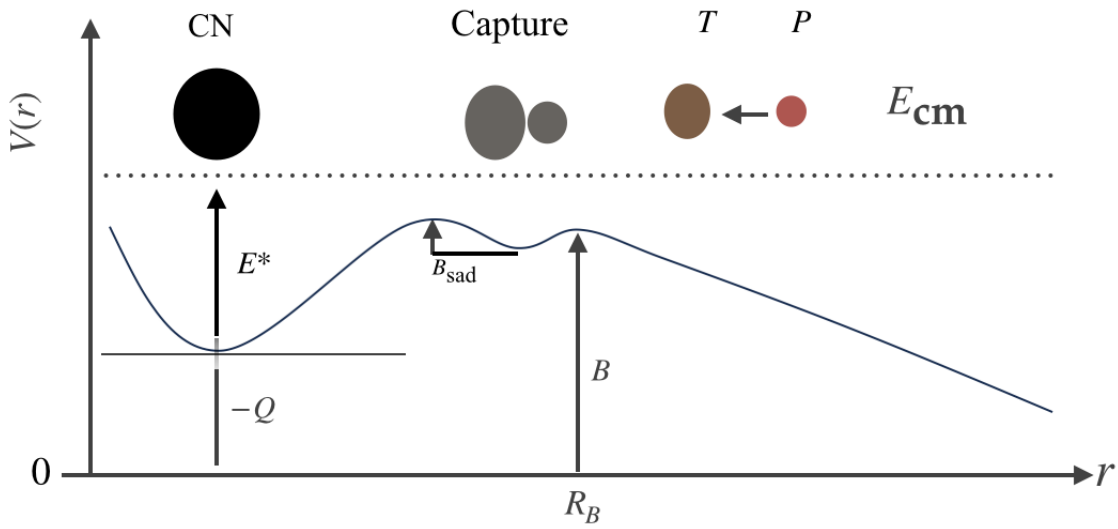

Figure 2.2: Schematic illustration of angular-momentum independent two-step fusion in the formation of super-heavy nuclei showing how potential energy $V(r)$ changes with the distance r between centres of colliding nuclei (not in scale). B and R_{B} are the Coulomb barrier height and its position, respectively. The B_{sad} is an inner energy barrier beyond the Coulomb barrier that colliding nuclei at capture must overcome to form a compound nucleus eventually. Here, Q and E^* stand for the Q-value of the reaction and the excitation energy of the compound nucleus. E_{cm} denotes the energy available in the centre-of-mass system.

P_{CN} usually increases with increasing energy in the centre of mass frame, E_{cm}, but this

may leave the formed compound nucleus at a higher excited state [77], which can quickly fission. Furthermore, the fission barriers of super-heavy elements are rather low [69], contributing to the high fission rate at the survival stage. In the event of instability against fission, the excited compound nucleus proceeds via fission into fragments labelled as $f_1^{'}$ and $f_2^{'}$ in the exit channel, as shown in Fig. 2.1. The probability that the compound nucleus outlives fission and forms a residue nucleus by emitting light particles (neutron, proton, alphas, and gammas) is called the survival probability. The type and number of light particles emitted at this stage depend on the excitation energy E^* of the compound nucleus, which is related to the E_{cm}, and the $Q-$value of the reaction for $\ell = 0$ [49, 53]:

$$E^* = E_{\mathrm{cm}} + Q, \tag{2.1}$$

where, $Q = B(A_{\mathrm{CN}}, Z_{\mathrm{CN}}) - B(A_1, Z_1) - B(A_2, Z_2)$. Here, $B(A_1, Z_1)$ and $B(A_2, Z_2)$ correspond to the binding energies of the projectile P and target T nuclei with mass and charge numbers A_1, Z_1, and A_2, Z_2, respectively. $B(A_{\mathrm{CN}}, Z_{\mathrm{CN}})$ is the binding energy of the compound nucleus with $A_{\mathrm{CN}} = A_1 + A_2$ and $Z_{\mathrm{CN}} = Z_1 + Z_2$.

The EvR cross section $\sigma_{\mathrm{EvR}}^{\mathrm{Theo}}(E_{\mathrm{cm}})$ for the synthesis of a super-heavy nucleus in its ground state can be decomposed into partial waves ℓ and presented as the product of the three sequential steps: capture cross section, the formation, and the survival probability,

$$\sigma_{\mathrm{EvR}}^{\mathrm{Theo}}(E_{\mathrm{cm}}) = \frac{\pi}{k^2}\sum_{l=0}^{\infty}(2\ell+1)\underbrace{T_\ell(E_{\mathrm{cm}},\ell)}_{\textbf{capture}} \times \underbrace{P_{\mathrm{CN}}(E_{\mathrm{cm}},\ell)}_{\textbf{formation}} \times \underbrace{P_{\mathrm{surv}}(E_{\mathrm{cm}},\ell)}_{\textbf{survive}}. \tag{2.2}$$

Here $k = \sqrt{\frac{2\mu E_{\mathrm{cm}}}{\hbar^2}}$ is the wave number and $\mu = \frac{M_1 \times M_2}{M_1 + M_2}$ is the reduced mass of the colliding nuclei: M_1 and M_2 are the masses of the projectile and targets respectively. $T_\ell(E_{\mathrm{cm}}, \ell)$ is the transmission coefficients through the entrance channel barrier. Eq. (2.2) describes two independent processes, namely the formation of a statistically equilibrated compound nucleus ($P_{\mathrm{CN}}(E_{\mathrm{cm}}, \ell)$) and subsequent decay in the exit ($P_{\mathrm{surv}}(E_{\mathrm{cm}}, \ell)$), as envisioned by Bohr [83]. There is some consistency among the models in how to describe the capture cross section and the survival probability, however, for the middle step there are many different approaches [24, 53, 68, 84, 85]. This chapter will discuss the modelling adopted for each stage in the theoretical simulation in the present study.

This thesis aims to enhance the modelling of super-heavy element production cross sections within the Kewpie2 statistical code [53] by incorporating the compound nucleus formation probability into the model. To achieve this, the method of calculating formation probability used in the Fusion-by-Diffusion (FbD) model [68] will be adopted in the Kewpie2 model. Kewpie2 and FbD models are well-established numerical codes for simulating fusion-evaporation reactions. However, they differ in compound nucleus formation probability stage evaluation. While FbD codes can simulate all three independent stages of the modelling, Kewpie2 relies on the external calculations of the formation probability to augment its calculation.

The description of the theoretical framework will start with the capture cross section (in Section 2.1), followed by the survival probability (in Section 2.2). The capture and the survival probability modelling are available in both Kewpie2 and FbD codes and can be readily applied to reactions with or without hindrance. A reaction is said to be hindered

when the fusion process is decreased due to quasi-fission. Even though the underlying framework may be the same in both codes, the input parameters and fine details may differ, resulting in discrepancies between the outcomes of the considered models [53, 68]. It is, therefore, important to compare the fine details and investigate their impact on the final results. This is especially needed in the regions of the nuclear chart where experimental data are scarce or absent. This study will lay the foundation for further developing the Kewpie2 code by incorporating the formation probability.

2.1 The Capture cross section

The capture cross section measures the probability of the projectile and the target nuclei overcoming the entrance channel barrier V_{eff} and coming into contact (forming the di-nuclear configuration) as illustrated in Fig. 2.2,

$$V_{\text{eff}} = B + \frac{\hbar^2 \ell(\ell+1)}{2\mu R_{\text{B}}^2}. \tag{2.3}$$

As described before, B stands for the Coulomb potential barrier at a distance R_{B} between centres of colliding nuclei, whereas the second term is the centrifugal term evaluated for a given angular momentum value, ℓ. The capture radius R_{B} is given as:

$$R_{\text{B}} = r_0(A_1^{\frac{1}{3}} + A_2^{\frac{1}{3}}), \tag{2.4}$$

where r_0 is the nuclear radius constant. For a colliding nuclei with a given energy in the centre of mass frame (E_{cm}), the capture cross section corresponds to the summation of all partial waves [77]:

$$\sigma_{\text{cap}}(E_{\text{cm}}) = \frac{\pi}{k^2} \sum_{\ell=0}^{\infty} (2\ell+1) T_\ell(E_{\text{cm}}, \ell). \tag{2.5}$$

Here, $T_\ell(E_{\text{cm}}, \ell)$ is the transmission coefficient of going through the Coulomb barrier for an angular momentum ℓ. In the present study, the limit of the ℓ summation at a given energy is approximated as the value at which the $T_\ell(E_{\text{cm}}, \ell)$ is numerically equal to 0. In this case, the maximum value of ℓ is called the critical angular momentum and is denoted as ℓ_{c}.

Assuming that $T_\ell(E_{\text{cm}}, \ell) = 1$ for $E_{\text{cm}} > V_{\text{eff}}$ and $T_\ell(E_{\text{cm}}, \ell) = 0$ for $E_{\text{cm}} > V_{\text{eff}}$, the summation in Eq. (2.5) over ℓ is then given as:

$$\sigma_{\text{cap}}(E_{\text{cm}}) = \begin{cases} \frac{\pi}{k^2} \sum_{\ell=0}^{\ell_{\text{c}}} (2\ell+1) = \frac{\pi}{k^2}(\ell_{\text{c}}+1)^2, & \text{if } E_{\text{cm}} > B, \\ 0, & \text{otherwise.} \end{cases} \tag{2.6}$$

Here, ℓ_c is defined by the relation $E_{\text{cm}} = B + \frac{\hbar^2 \ell_c(\ell_c+1)}{2\mu R_B^2}$. Summation over partial waves then leads to the classical capture cross section, given by:

$$\sigma_{\text{class}} = \begin{cases} \pi R_B^2 \left(1 - \frac{B}{E_{\text{cm}}}\right), & \text{if } E_{\text{cm}} \geq B, \\ 0, & \text{if } E_{\text{cm}} < B. \end{cases} \tag{2.7}$$

While this represents the classical capture cross section of two colliding nuclei, it's important to consider sub-barrier capture. To achieve this, we need to derive the barrier transmission coefficients, $T_\ell(E_{\rm cm}, \ell)$. In this study, we will obtain the transmission coefficients by approximating empirical entrance channel barrier distributions using a Gaussian barrier distribution approach [86], similar to the one used in FbD approach [68].

2.1.1 Entrance Channel Barrier Distribution (EBD)

The deformation and vibrations of the colliding nuclei affect the Coulomb barrier. To account for these effects, the single barrier model is replaced by a barrier distribution. Changing the barrier also compensates for the Coulomb barrier tunnelling. In the empirical Gaussian barrier distribution (EBD) approach, the Coulomb barrier is approximated by a Gaussian, where the probability $P(B)$ of encountering the barrier (B) by colliding nuclei is modelled as:

$$P(B) = \frac{1}{\sqrt{2\pi\sigma_B^2}} \exp\left(-\frac{(B-B_0)^2}{2\sigma_B^2}\right). \tag{2.8}$$

Here, σ_B and B_0 are the standard deviation and mean value of the barrier distribution, respectively [86].

In the semi-classical formalism, the empirical entrance channel barrier is approximated by a

The transmission coefficient is then given as,

$$T_\ell(E_{\rm cm}, \ell) = \int_0^\infty \theta\left(E_{\rm cm} - B - \frac{\hbar^2\ell(\ell+1)}{2\mu R_{\rm B}^2}\right) P(B)\, dB, \tag{2.9}$$

where, $\theta\left(E_{\rm cm} - B - \frac{\hbar^2\ell(\ell+1)}{2\mu R_{\rm B}^2}\right)$ is the Heaviside step function. Then, for a given $\ell-$value:

$$\begin{aligned} T_\ell(E_{\rm cm}, \ell) &= \int_0^{E_{\rm cm}-\frac{\hbar^2\ell(\ell+1)}{2\mu R_B^2}} \frac{1}{\sqrt{2\pi\sigma_B^2}} \exp\left(-\frac{(B-B_0)^2}{2\sigma_B^2}\right) dB, \\ &= \frac{1}{\sqrt{2\pi}} \int_{\frac{-B_0}{\sqrt{2}\sigma_B}}^{\frac{E_{\rm cm}-\frac{\hbar^2\ell(\ell+1)}{2\mu R_B^2}-B_0}{\sqrt{2}\sigma_B}} \exp\left(-u^2\right) du. \end{aligned} \tag{2.10}$$

Since $B_0 \gg \sigma_B$, Eq. (2.10) becomes,

$$\begin{aligned} T_\ell(E_{\rm cm}, \ell) &= \int_{-\infty}^{\mathcal{X}(E_{\rm cm},\ell)} \exp\left(-u^2\right) du, \\ &= \frac{1}{2}\left(1 + \mathrm{erf}\left(\mathcal{X}(E_{\rm cm}, \ell)\right)\right), \end{aligned} \tag{2.11}$$

where,

$$\mathcal{X}(E_{\rm cm}, \ell) = \frac{E_{\rm cm} - \frac{\hbar^2\ell(\ell+1)}{2\mu R_B^2} - B_0}{\sqrt{2}\sigma_B}. \tag{2.12}$$

Here, we made use of the following properties of the error function ($\mathrm{erf}(x)$):

$$\mathrm{erf}(x) = \frac{2}{\sqrt{\pi}} \int_0^x \exp(-t^2)\, dt, \tag{2.13}$$

and (2.14)

$$\int_{-\infty}^{0} \exp\left(-t^2\right)\, dt = \frac{\sqrt{2\pi}}{2}. \tag{2.15}$$

The total capture cross section summed over all angular momenta can be directly obtained by folding the classical capture cross section given by Eq. (2.7) with the Gaussian distribution [54, 68, 86]:

$$\begin{aligned} \sigma_{\mathrm{cap}}^{\mathrm{EBD}} &= \int_0^{E_{\mathrm{cm}}} \sigma_{\mathrm{class}} P(B)\, dB, \\ &= \frac{\pi R_B^2 \sigma_B}{\sqrt{2\pi E_{\mathrm{cm}}}} \left[\mathcal{X}\sqrt{\pi}(1 + \mathrm{erf}(\mathcal{X})) + e^{-\mathcal{X}^2} \right]. \end{aligned} \tag{2.16}$$

Here, $\mathcal{X}$ is given as:

$$\mathcal{X}(E_{\mathrm{cm}}) = \frac{(E_{\mathrm{cm}} - B_0)}{\sqrt{2}\sigma_B}. \tag{2.17}$$

This section presents the capture model framework adopted in this work, which is the same as in the FbD model. The capture model parameters such as the capture radius (R_{B}), mean value of the barrier distribution (B_0) and the standard deviation of the barrier distribution (σ_{B}) parametrisations are presented below. The original Kewpie2 code has also Wentzel–Kramers–Brillouin (WKB) approximation of the coupled-channels approach [53] as an alternative to the EBD capture cross section method. However, it is not considered in this study.

2.1.1.1 The Mean Entrance Channel Barrier (B_0)

The mean value of the entrance channel potential barrier in the EBD model is parametrised by a cubic function:

$$B_0 \approx a \times z + \underbrace{b \times z^2 + c \times z^3}_{\text{corrections}}. \tag{2.18}$$

This parameterisation is rooted in the fundamental point-charge Coulomb interaction between colliding nuclei:

$$B = \frac{1}{4\pi\epsilon_0} \frac{e^2 Z_1 \times Z_2}{R_{\mathrm{B}}} = \frac{e^2}{4\pi\epsilon_0 r_0} z, \tag{2.19}$$

where the constant ϵ_0 is the vacuum electric permittivity, Z_1 and Z_2 are the atomic charges of the colliding nuclei, and z is the Coulomb parameter:

$$z = \frac{Z_1 \times Z_2}{A_1^{\frac{1}{3}} + A_2^{\frac{1}{3}}}. \tag{2.20}$$

In Eq. (2.18), the constant a is treated as an adjustable parameter of the model. The higher-order terms bz^2 and cz^3 are corrections due to short-range nuclear forces and are necessary to reproduce experimental data accurately. The parameters a, b and, c were determined by fitting the formula given by Eq. (2.18) to a large set of the experimental data [48]. The semi-empirical formula for the mean value of the entrance channel barrier is given by:

$$B_0 = 0.853315z + 0.0011695z^2 - 0.000001544z^3. \tag{2.21}$$

2.1.1.2 The Coulomb Barrier Width (σ_B)

The standard deviation (σ_{B}) of the entrance channel barrier distribution within the EBD model is the parameter that accounts for variations in the barrier height due to projectile and target deformations. It also incorporates the effects of the quantum tunnelling.

To begin, we examine the impact of projectile and target nuclei deformation on the radii R_1 and R_2 and their overall effect on the point-Coulomb interaction (Eq. (2.19)) which can be expressed as:

$$B = \mathrm{const} \times \frac{Z_1 \times Z_2}{R_1 + R_2}, \tag{2.22}$$

then

$$dB = -B\frac{dR_1}{R_1 + R_2} - B\frac{dR_2}{R_1 + R_2}. \tag{2.23}$$

The changes in the radii of the colliding nuclei, i.e., dR_1 and dR_2 due to the nuclear deformations, lead to variations in the Coulomb barrier height. These variations can be estimated by quantifying the colliding nuclei size deviations, dR_1 and dR_2 around the spherical shapes of radii R_{01} and R_{02}:

$$dR_{i=1,2}(\theta, \phi) = R_i(\theta, \phi) - R_{0i}. \tag{2.24}$$

Here $R_i(\theta, \phi)$ is evaluated by expanding the spherical nuclei radii into a series of the spherical harmonics $Y_{\lambda\nu}$ with the nuclear shape parameters $\beta_{\lambda\mu}$ included [87]:

$$R(\theta, \phi) = R_0\{1 + \sum_{\lambda=1}^{\infty} \sum_{\mu=-\lambda}^{+\lambda} \beta_{\lambda\mu} Y_{\lambda\mu}(\theta, \phi)\}, \tag{2.25}$$

where the indices $i = 1$ and 2 corresponding to the projectile and target nuclei, respectively. By considering only axially symmetric quadrupole deformations, in which the parameters λ and μ are restricted to 2 and 0, respectively [69, 87], Eq. (2.25) reduces to the form,

$$R(\theta, \phi) = R_0\{1 + \beta_{20} Y_{20}(\theta, \phi)\}. \tag{2.26}$$

Only prolate deformation is considered.

Now that we have established the formalism of estimating the deviations in sizes, one can quantify the deviation around the point-Coulomb barrier by calculating the root mean

squared deviation (RMSD) as follows:

$$\begin{aligned} RMSD_i &= \left[\int dR_i(\theta,\phi)^2 d\Omega\right]^{\frac{1}{2}}, \\ &= R_{0i}\beta_{20i}\left[\int Y_{20i}(\theta,\phi)^2 d\Omega\right]^{\frac{1}{2}}, \\ &= \sqrt{\frac{R_{0i}^2\beta_{20i}^2}{4\pi}}. \end{aligned} \tag{2.27}$$

The total $RMSD$ is then given by:

$$RMSD = \sqrt{RMSD_1^2 + RMSD_2^2} \tag{2.28}$$

$RMSD$ can be substituted into Eq. (2.23) to replace $(dR_1 + dR_2)$ term. By replacing with a mean value B_0 we might estimate the deviation in the barrier height due to the projectile and target nuclear deformations as,

$$\sigma_{\mathrm{B}} = \frac{1}{(R_1 + R_2)} \times B_0 \times \sqrt{\frac{R_{01}^2\beta_{201}^2}{4\pi} + \frac{R_{02}^2\beta_{202}^2}{4\pi}}. \tag{2.29}$$

The deformation effect is accounted for through the quadrupole shape parameters β_{20i}, where i denotes projectile or target nuclei. Eq. (2.29) gives an overview of the default parameterization of the empirical Gaussian barrier capture model [34, 86]:

$$\sigma_B = CB_0\sqrt{\sigma_1^2 + \sigma_2^2 + \sigma_0^2}, \tag{2.30}$$

where $\sigma_i = \frac{R_{0i}^2\beta_{20i}^2}{4\pi}$. The optimised values of C and σ_0 are 0.0421 fm^{-1} and 0.531 fm, respectively. Here σ_0 is the parameter accounting for the quantum tunnelling [86].

As shown in Ref. [86], the parameters r_0, (a, b and c) and (C and σ_0) of Eqs. (2.4), (2.18) and (2.30) are adjusted to experimental deduced R_{B}, B_0 and σ_{B} from a set of 42 well-measured experimental fusion excitation functions. The optimised parameters from this analysis are adopted in this study. A similar regression analysis using Eqs. (2.4), (2.21) and (2.29) can be found in Ref. [73], which are summarized in the next Section 2.1.2 to demonstrate uncertainty in the capture model predictions.

The quality of the fitted parameters of Eqs. (2.21) and (2.30) is illustrated in Fig. 2.3. The panel (a) of Fig. 2.3 illustrates the predictive power of mean Coulomb barrier parameterization in Eq. (2.21), which is depicted in the solid line against the experimental values shown by points. Here, B_0 parameterization reproduces the experimental deduced data well. On the contrary, panel (b), which shows the plot of the theoretical standard deviation of the Coulomb barrier distribution (Eq. (2.29)) against the phenomenologically deduced values, is not quite well reproduced. The plot highlights uncertainties in using theoretical modelled σ_{B}.

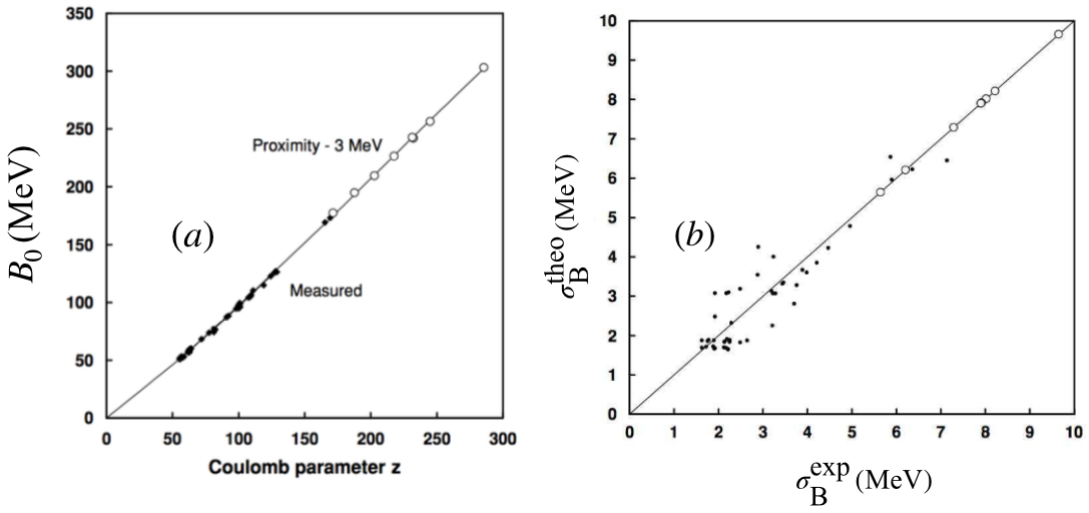

Figure 2.3: (a) The black points correspond to the mean Coulomb barriers (B_0) deduced from accurately measured fusion excitation functions as a function of the Coulomb parameter z. The open symbols are theoretical "Proximity" barriers. The solid line represents the theoretical evaluation from Eq. (2.21). (b) The calculated barrier widths (Eq. (2.29)) are plotted against phenomenologically deduced values. The figure is reproduced from Ref. [48].

2.1.2 Accessing the Uncertainty in Empirical Barrier Capture Model

The capture model presented above relies on several unknown parameters: (r_0, a, b, c, C, and σ_0), which are obtained through regression analysis on 42 experimentally measured fusion excitation functions, as demonstrated in Ref. [73]. It is important to recognize that these optimized values come with inherent uncertainties. These uncertainties must be propagated onto the total capture cross section to ensure accurate results. For clarity, all final formulas needed to calculate the capture cross section will be presented again, this time with numerical values of free parameters and their uncertainties.

The r_0 constant in the capture radius:

$$R_B = r_0 \left(A_1^{1/3} + A_2^{1/3} \right), \tag{2.31}$$

is equal to (1.147 ± 0.027) fm. The parameters a , b and c in the formula for the mean Coulomb barrier:

$$B_0 = az + bz^2 + cz^3, \tag{2.32}$$

were estimated as: $a = (9.184 \pm 0.137) \times 10^{-1}$ MeV, $b = (-9.630 \pm 25.670) \times 10^{-5}$ MeV and $c = (3.898 \pm 1.136) \times 10^{-6}$ MeV. The covariance between these parameters is given in Table 2.1:

	a	b	c
a	1.868×10^{-4}	-3.433×10^{-6}	1.452×10^{-8}
b	-3.433×10^{-6}	6.591×10^{-8}	-2.877×10^{-10}
c	1.452×10^{-8}	-2.877×10^{-10}	1.292×10^{-12}

Table 2.1: The covariance matrix (in MeV^2) of the parameters a, b and c obtained in the formula 2.32 (Table 8.1 of Ref. [73])

The parameters C and σ_0 in the barrier width formula

$$\sigma_B = CB_0\sqrt{\sigma_1^2 + \sigma_2^2 + \sigma_0^2}, \tag{2.33}$$

are (0.0432 ± 0.0048) fm^{-1} and (0.531 ± 0.079) fm, respectively. The covariance $u(C, \sigma_0) = -3.719 \times 10^{-4}$ [73].

With these fitted parameters and their uncertainties, we can readily evaluate the model parameters ($R_\mathrm{B}, B_0,$ and σ_B), and eventually the capture cross section:

$$\sigma_\mathrm{cap} = \frac{\pi R_B^2 \sigma_B}{\sqrt{2\pi E_\mathrm{cm}}}\left[\mathcal{X}\sqrt{\pi}(1 + \mathrm{erf}(\mathcal{X})) + e^{-\mathcal{X}^2}\right], \tag{2.34}$$

where $\mathcal{X}$ is given by,

$$\mathcal{X}(E_\mathrm{cm}) = \frac{(E_\mathrm{cm} - B_0)}{\sqrt{2}\sigma_B}. \tag{2.35}$$

The uncertainty in the capture cross section is given as follows:

$$u^2(\sigma_\mathrm{cap}) = \begin{bmatrix} \frac{\partial\sigma_\mathrm{cap}}{\partial R_\mathrm{B}} & \frac{\partial\sigma_\mathrm{cap}}{\partial B_0} & \frac{\partial\sigma_\mathrm{cap}}{\partial\sigma_B} \end{bmatrix} \begin{bmatrix} u^2(R) & 0 & 0 \\ 0 & u^2(B_0) & u(B_0,\sigma_B) \\ 0 & u(B_0,\sigma_B) & u^2(\sigma_B) \end{bmatrix} \begin{bmatrix} \frac{\partial\sigma_\mathrm{cap}}{\partial R} \\ \frac{\partial\sigma_\mathrm{cap}}{\partial B_0} \\ \frac{\partial\sigma_\mathrm{cap}}{\partial\sigma_B} \end{bmatrix}^T. \tag{2.36}$$

The terms $u^2(R_\mathrm{B})$, $u^2(B_0)$ and $u^2(\sigma_\mathrm{B})$ are the uncertainties due to the capture radius, mean Coulomb barrier and the width of the Coulomb barrier distribution, respectively. $u(B_0, \sigma_\mathrm{B})$ is the covariance between the mean Coulomb barrier and its width [73].

2.1.3 Sample of the Calculations

Fig. 2.4 presents capture cross section calculations compared with experimental data for ^{16}O+^{238}U, ^{16}O+^{208}Pb, and ^{48}Ca+^{208}Pb reactions. For ^{16}O + ^{208}Pb and ^{16}O + ^{238}U reactions the projectile and target charge products, $Z_1 \times Z_2$, are 736 and 656, respectively, which in both cases is below the threshold above which a significant quasi-fission component might be expected [53]. It is usually assumed that for $Z_1 \times Z_2 < 1600$, the formation probability $P_{CN} \approx 1$ and capture cross section is equal to the fusion cross section, $\sigma_\mathrm{cap} = \sigma_\mathrm{fus}$. However, it should be noted that the 1600 threshold is not sharp. For ^{48}Ca + ^{208}Pb is $Z_1 \times Z_2 = 1640$, and the formation probability can still be approximated by one.

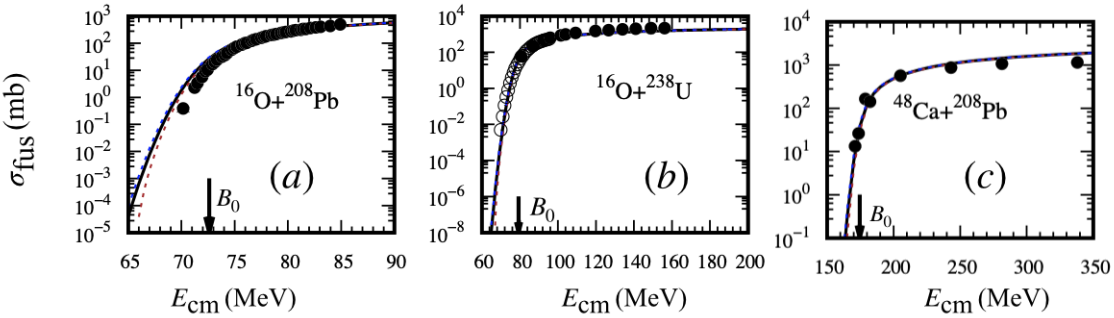

Figure 2.4: Comparison of the capture cross section calculations with experimental data for ^{16}O+^{238}U, ^{16}O+^{208}Pb, and ^{48}Ca+^{208}Pb systems. Solid lines represent the theoretical calculations, and the dashed lines show uncertainty bounds (Eq. (2.36)). Arrows mark the positions of the mean entrance channel barriers B_0 (Eq. (2.21)). The open and solid symbols for ^{16}O+^{238}U represent experimental data taken from Ref. [88] and [89], respectively. The experimental data for ^{16}O+^{208}Pb, and ^{48}Ca+^{208}Pb are taken from Refs. [90] and [91], respectively. Presented reactions represent the limit where the formation probability is equal to one. Therefore, the capture cross section is approximately equal to the fusion cross section.

The solid black lines in panels (a), (b) and (c) of Fig. 2.4 represent the calculations of Eq. (2.34). The blue and brown dashed lines correspond to the uncertainties evaluated using Eq. (2.36). In panel (a), the experimental data points are taken from Ref. [90], whereas those of panel (b) are retrieved from Refs. [88] (open circles) and [89] (solid dots), and that of panel (c) are taken from Ref. [91]. The arrow on each panel indicates the position of the mean entrance channel barrier B_0 (Eq. (2.21)). In these sample calculations, theoretical calculations reproduce the experiment well. For more calculations, please refer to Refs. [73, 86].

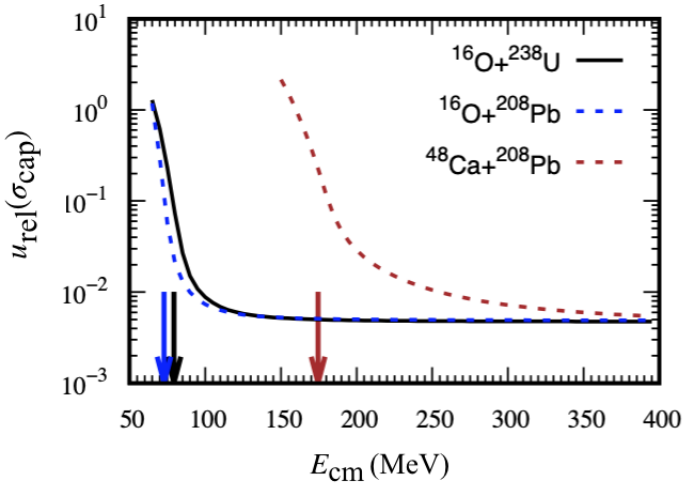

Figure 2.5: The relative uncertainties $u_{\rm rel}(\sigma_{\rm cap}) = \frac{u(\sigma_{\rm cap})}{\sigma_{\rm cap}}$ of the calculated capture cross sections for the reactions ^{16}O+^{238}U, ^{16}O+^{208}Pb, and ^{48}Ca+^{208}Pb. The arrows show the mean entrance channel barrier position for each reaction.

Besides reproducing the experimental cross sections, one can also investigate the uncer-

tainty in the model evaluation as a function of energy. Fig. 2.5 illustrates the relative uncertainty in the model predictions as a function of energy in the centre of the mass frame. The figure shows that the uncertainty of the model calculations several MeV below the barrier is almost 100% of the predictions. This highlights that the model predictions below the barrier are not very reliable. However, the uncertainty in the capture cross section predictions quickly decreases with increasing energy. This trend, as shown in Fig. 2.6 highlights the sensitivity of the model predictions to the uncertainty in the adjustable parameter capture radius R_{B}, mean barrier B_0 and its width σ_{B}.

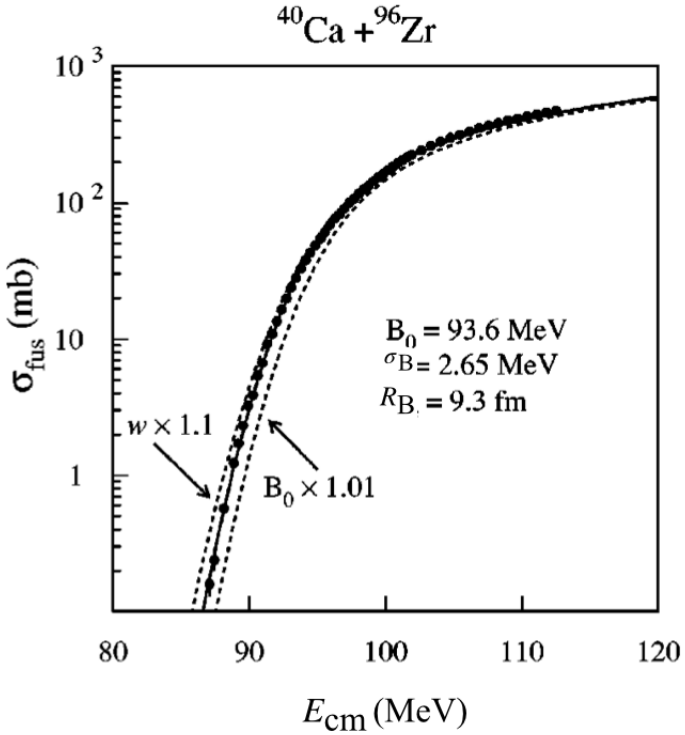

Figure 2.6: A comparison of the experimental fusion excitation function for ^{40}Ca+^{96}Zr with a theoretical fit using Eq. (2.34). The experimental data are taken from Ref. [92]. The sensitivity of the model to variations in the mean Coulomb barrier and its width is illustrated. The figure is reproduced from Ref. [86]. Here, the w and R_σ stand for the Coulomb barrier width (σ_{B}) and the capture radius (R_{B}), respectively.

Fig. 2.6 displays the sensitivity test of the capture formula (Eq. (2.34)) predictions for small variations in the model parameters B_0 and σ_{B}. As shown in the figure, changes in the mean barrier height and the width have opposing effects on the fusion cross section. Increasing the mean barrier by 1% tends to suppress the fusion excitation function, while a 10% increase in the width will enhance it [86]. However, the impact of these changes diminishes with increasing energy above B_0, leading to a convergence with the experiment.

Fig. 2.7 shows examples of capture cross sections in the regime of the super-heavy elements evaluated using Eq. (2.34). The panels (a), (b), and (c) correspond to the reactions ^{50}Ti+^{208}Pb, ^{51}V+^{208}Pb and ^{48}Ca+^{243}Am, respectively. The arrows, as previously, represent the corresponding B_0 values. Different symbols in panel (a) correspond to different experimental measurements of the capture-fission cross section for the ^{50}Ti+^{208}Pb system [93], [94], [55], and [95]. Similarly to the previous figure, the upper and lower

limits of the capture cross section calculations are depicted by the blue and brown dashed lines, respectively. As observed previously, the uncertainties in the theoretical predictions decrease with increasing energy.

The larger uncertainties for the reactions presented in Fig. 2.7 in comparison to Fig. 2.4 are caused by the extrapolations of formulas for B_0 (Eq. (2.21)) and σ_B (Eq. (2.30)) beyond the region in which they were fitted. The free parameters in B_0 and σ_B were optimised based on a set of 42 carefully selected fusion excitation functions of heavy ions; see Refs. [73, 86]. This data did not include reactions leading to super-heavy elements because there are no available high-quality experimental data on capture and fusion cross sections for such reactions. Therefore, extrapolation into the super-heavy regime, where experimental fusion excitation data is lacking, introduces significant uncertainty, as illustrated in Fig. 2.7. However, (2.34) proved good predictive power in evaluating the fusion excitation functions in heavy ion reactions, especially for hot fusion reactions at energies above the Coulomb barrier. It is also simple to use and provides an alternative approach to the more elegant evaluations such as the couple channel calculations [86].

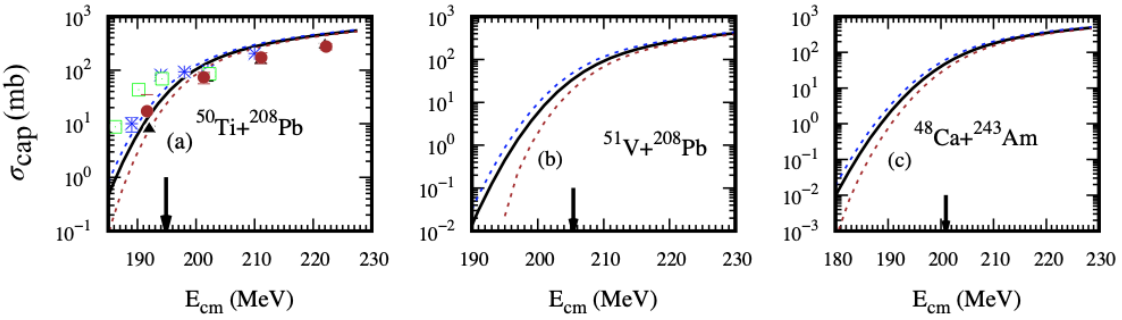

Figure 2.7: Examples of capture cross sections for super-heavy element synthesis reactions evaluated using Eq. (2.34) for (a) ^{50}Ti+^{208}Pb, (b) ^{51}V+^{208}Pb, and (c) ^{48}Ca+^{243}Am reactions, respectively. Arrows show the corresponding entrance channel barriers B_0. The different symbols in the panel (a), triangle (black) [93], star (blue) [94], open triangle (green)[55] and dots (brown) [95] correspond to different experimental measurements of fusion-fission cross section.

In conclusion, this section has presented the capture cross section formula and its effectiveness in reproducing experimental data for heavy-ion reactions, especially in the limit where the formation probability approaches unity. The capture model's sensitivity to the mean value of the entrance channel barrier and its width, which contribute to the uncertainty in the predictions, especially at sub-barrier energies and in the super-heavy regime, was discussed. Despite these limitations, the model's simplicity and demonstrated predictive power in the heavy-ion domain make it a model of choice in FbD calculations and the present study. The following section discusses the compound nucleus survival probability, which can be readily applied in heavy and super-heavy nuclei synthesis reactions.

2.2 The Deexcitation Process and the Survival Probability (P_{surv})

The survival probability describes the final stage of the reaction dynamics leading to the synthesis of the super-heavy elements. At this phase, the compound nucleus (CN) formed with the excited energy E^* decays by emitting light particle(s), namely protons, neutrons, alpha particles and gamma rays, to cool down. In the super-heavy elements synthesis, this stage competes strongly with the fission process, which is usually the dominant decay mode.

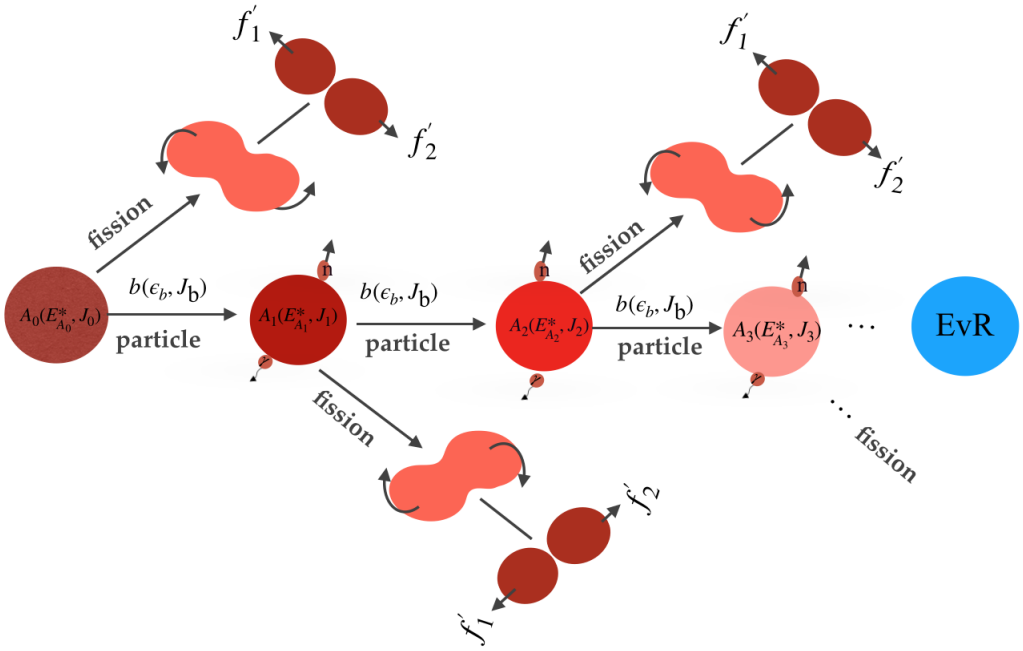

Figure 2.8: The diagram depicts possible processes during deexcitation of an excited compound nucleus, including the sequential emission of light particles. The sequence begins with the compound nucleus $A_0(E^*_{A_0}, J_0)$ emitting light particle $b(\epsilon_{\mathrm{b}}, J_{\mathrm{b}})$ (neutron, proton, or alpha) what leads to a residue $A_1(E^*_{A_1}, J_1)$, which then serves as a seed nucleus for further emission. The process continues until the excitation energy of a residue is below both the particle emission threshold and fission threshold, and the final evaporation residue (EvR) is formed. At each step, the particle emission competes with fission.

Let us start with an example typical for the cold fusion 1n reactions in which the compound nucleus $A_0(E^*_{A_0}, J_0)$ outlives fission and emits a light particle $b(\epsilon_{\mathrm{b}}, J_{\mathrm{b}})$ (neutron in this case) in a process:

$$A_0(E^*_{A_0}, J_0) \rightarrow A_1(E^*_{A_1}, J_1) + b(\epsilon_{\mathrm{b}}, J_b), \tag{2.37}$$

which leads to the formation of a residue nucleus $A_1(E^*_{A_1}, J_1)$. The $E^*_{A_0}$ and $E^*_{A_1}$ are the excitation energies of the compound and the residue nuclei, respectively, while J_0 and J_1 are the corresponding spins. The spin of the emitted particle is denoted by J_{b}, and ϵ_{b} is the kinetic energy taken by a particle. In the case of the cold fusion synthesis $E^*_{A_0}$ is usually of the order of 15 MeV and the remaining energy $E^*_{A_1}$ is not sufficient for the next chance fission or emission of another particle. In a scenario where the compound nucleus,

resulting from a successful complete fusion reaction, has higher excitation energy, as in hot fusion reactions, multiple particles may be emitted, leading to a cascade of particles as illustrated in Fig. 2.8. Here, the residue nucleus formed after the first particle emission serves as the seed for subsequent particle emission or potential fission events.

The emission process continues until the excitation energy of the residue nucleus falls below the thresholds for further particle emission and fission. After that, only gamma rays are emitted, carrying away excess excitation energy and angular momentum. However, gamma emission generally has little impact on the final results, except in cases of zero neutron emission [62]. Additionally, charged particles have low emission probabilities due to high Coulomb barriers that they have to overcome [49]. Although the original version of the Kewpie2 model includes the possibility of gamma and charged particle emission, these processes are not considered in the current study because our primary focus is on the formation dynamics of super-heavy nuclides.

If only neutron and fission competition is considered, the probability of emitting exactly x neutrons from a compound nucleus A_0 initially excited to the energy $E^*_{A_0}$ is given by [53, 96]:

$$P^{x\mathrm{n}}_{\mathrm{surv}}(E^*_{A_0}) = \prod_{i=1}^{x} \frac{\Gamma_{\mathrm{n},i-1}(E^*_{A_{i-1}})}{\Gamma_{\mathrm{n},i-1}(E^*_{A_{i-1}}) + \Gamma_{\mathrm{f},i-1}(E^*_{A_{i-1}})}, \tag{2.38}$$

where $\Gamma_{\mathrm{n},i-1}(E^*_{A_{i-1}})$ and $\Gamma_{\mathrm{f},i-1}(E^*_{A_{i-1}})$ are the neutron emission and fission decay widths evaluated at i-th step of the cascade ($i = 1, 2, ...$). Here, for simplicity, spin dependencies of presented quantities were omitted (they are included in the next section). After each successful neutron emission, the excitation energy is reduced by neutron binding energy B_{n} and its kinetic energy ϵ_{n}. The excitation energy of a nucleus A_i after the emission of i neutrons is then:

$$E^*_{A_i} = E^*_{A_{i-1}} - B_{\mathrm{n},i-1} - \epsilon_{\mathrm{n},i-1}. \tag{2.39}$$

To stop the cascade after x successful neutron emissions the excitation energy E^*_x of nucleus A_x has to fall below the threshold for next chance neutron emission, ($E^*_x < B_{n,x}$) and below fission threshold ($E^*_x < B_{\mathrm{f},x}$, where $B_{\mathrm{f},x}$ is the height of the fission barrier in nucleus A_x).

Because emitted neutrons do not carry out a single value of the kinetic energy, the cascade is usually treated as a statistical process. The simplest method to solve Eq. (2.38) is usually based on a Monte Carlo simulation. Unfortunately, such methods are time-consuming, especially for super-heavy element synthesis reactions where cross sections are in the order of pb. The probability of emitting multiple neutrons in a cascade is extremely small. In some versions of the Fusion-by-Diffusion model, it was assumed that the neutron kinetic energy taken at each step is equal to the average kinetic energy resulting from Maxwell-type distribution equal to $2T$, where T is the nuclear temperature [97]. Kewpie2, however, has adopted another approach to solving Eq. (2.38) that is well-suited to handling such low probabilities. Numerical details and the algorithms are described in Refs. [53, 75]. This part of the Kewpie2 code was not changed in this thesis.

In this study, we calculate the fission decay widths as used in Eq. (2.38) based on the standard Bohr-Wheeler (BW) transition state theory [18, 34, 53]. The Hauer-Feshbach [98] and Weisskopf-Ewing [99, 100] formalisms are implemented in Kewpie2 for the neutron emission width. However, we adopt the latter for its computational efficiency. Further

details on the neutron emission and fission decay widths are outlined in Subsections 2.2.1 and 2.2.2 below.

2.2.1 Neutron Emission Width (Γ_n)

For an excited nucleus, a neutron (n) can be emitted if the excitation energy exceeds its binding energy (B_n). According to the statistical model [99], the probability per unit time that a neutron with kinetic energy ϵ_n is emitted is expressed as:

$$P_n(\epsilon_n)_{A_0^* \to A_1+n}\, d\epsilon_n = \sigma_n^{inv}(\epsilon_n) \frac{g m_n}{\pi^2 \hbar^3} \frac{\rho_{A_1}(E^*_{A_1}, J_1)}{\rho^{gs}_{A_0}(E^*_{A_0}, J_0)} \epsilon_n\, d\epsilon_n. \tag{2.40}$$

In this context, $\rho_{A_1}(E^*_{A_1})$ and $\rho^{gs}_{A_0}(E^*_{A_0})$ represent the densities of nuclear levels between energy intervals E and $E + dE$, measured from the ground states of the residue and compound nuclei, respectively. The variables g and m_n denote the spin degeneracy and the mass of the emitted neutron, respectively. The $\sigma_n^{inv}(\epsilon_n)$ indicates the neutron capture cross section in the reverse reaction, i.e., $A_1(E^*_{A_1}, J_1) + n(\epsilon_n, J_n) \to A_0(E^*_{A_0}, J_0)$. Here, ϵ_n is the kinetic energy of the impinging neutron, and J_n is its total angular momentum. The neutron emission width can be obtained by integrating Eq. (2.40) which leads to the Weisskopf–Ewing formula [99, 100]:

$$\Gamma_n(E^*_{A_0}, J_0) = \frac{(2s_b + 1) m_n}{\pi^2 \hbar^2 \rho^{gs}_{A_0}(E^*_{A_0}, J_0)} \int_0^{E^*_{A_1}} \sigma_n^{inv}(\epsilon_n) \rho_{A_1}(E^*_{A_1} - \epsilon_n, J_1) \epsilon_n\, d\epsilon_n. \tag{2.41}$$

The term $g = (2s_b + 1)$ refers to the spin degeneracy factor of the emitted neutron. In these expressions, $E^*_{A_1}$ stands for the maximum energy available for the neutron to take:

$$E^*_{A_1} = E^* - E^{rot}_{A_1} - B_n, \tag{2.42}$$

and that of the compound nucleus $E^*_{A_0}$ is given as,

$$E^*_{A_0} = E^* - E^{rot}_{A_0}. \tag{2.43}$$

Here, $E^{rot}_{A_1}$ and $E^{rot}_{A_0}$ represent the rotational energies of the residue and compound nuclei, respectively, are evaluated consistently with the Subsection 2.3.1.7.

In the original Kewpie2 [53], Weisskopf–Ewing and Hauser-Feshbach's treatment of particle (e.g. neutron) emission can be found. The Hauser-Feshbach model accounts for angular momentum treatment of the parent, daughter and emitted, making it more accurate but computationally demanding. In contrast, the Weisskopf–Ewing model simplifies angular momentum treatments, focusing on overall emission probabilities. This makes it computationally efficient, but less accurate [53, 101]. This study adopts the Weisskopf–Ewing approach due to its computational advantages and established use in the FbD model. These choices facilitate the seamless incorporation of FbD's compound nucleus formation probability into Kewpie2, allowing for cross-validation of calculations.

2.2.1.1 The Neutron Inverse Capture Cross Section ($\sigma_{\mathrm{n}}^{inv}$)

The neutron inverse capture cross section in Eq. (2.41) is evaluated using the empirical relation [102]:

$$\sigma_{\mathrm{n}}^{\mathrm{inv}}(\epsilon_{\mathrm{n}}) = \alpha\left(1+\frac{\beta}{\epsilon_{\mathrm{n}}}\right)\pi\overline{R}^2, \tag{2.44}$$

where $\alpha = 0.76 + 2.2A_1^{-\frac{1}{3}}$ and $\beta = \frac{2.12A_1^{-\frac{2}{3}}-0.050}{0.76+2.2A_1^{-\frac{1}{3}}}$. Here, $\pi\overline{R}^2$ represents the geometric neutron capture cross section, which is corrected by the energy of the emitted neutron ϵ_{n} to account for the decrease in the neutron capture cross section with increasing energy. On the contrary, in the current version of the FbD model, there is no account for the energy dependence, and the cross section is taken as:

$$\sigma_{\mathrm{n}}^{\mathrm{inv}} = \pi r_0^2 A_1{}^{\frac{2}{3}}, \tag{2.45}$$

where $r_0 = 1.45$ fm. The impact of the energy-dependent neutron capture cross section on the survival probability is later discussed in Subsection 2.3.1.1 and demonstrated in Fig. 2.11.

2.2.2 Fission Decay Width (Γ_f)

The fission decay width in both Kewpie2 and FbD codes is evaluated following transition state theory by Bohr and Wheeler [18]. According to this theory, the excited compound nucleus is viewed as an equilibrated system in various configurations, some considered transient, as depicted in Fig. 2.9.

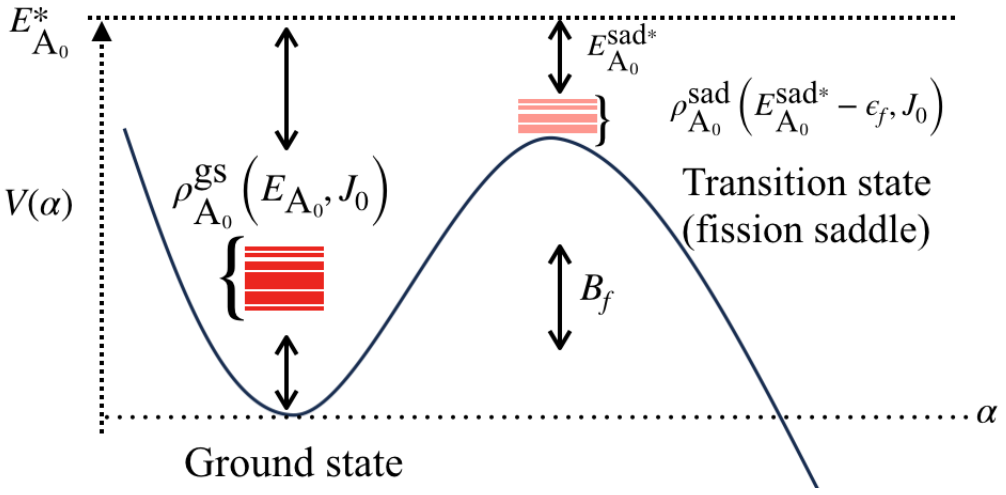

Figure 2.9: The schematic illustration of the transition-state model by Bohr and Wheeler. The one-dimensional potential energy landscape $V(\alpha)$ is depicted along the fission pathway as a function of the elongation α. The figure highlights the changes in the state densities in two configurations: at the ground state, $\rho^{\mathrm{gs}}_{A_0}\left(E^{\mathrm{gs}*}_{A_0}, J_0\right)$, and at the fission saddle, $\rho^{\mathrm{sad}}_{A_0}(E^{\mathrm{sad}*}_{A_0}-\epsilon_f, J_0)$. Here, B_{f} represents the height of the fission barrier and ϵ_f is the kinetic energy associated with the transition state.

As the figure illustrates, these transient states can evolve over a potential energy barrier that constrains fission. The fission decay width is thus defined as the ratio of the number of transition states at the saddle in the energy interval from 0 to $E_{A_0}^{\mathrm{sad}*}$ to the number of possible states of the equilibrated compound nucleus at an excitation energy $E_{A_0}^{*}$:

$$\Gamma_{\mathrm{f}}(E_{A_0}^{*}, J_0) = \frac{1}{2\pi\rho_{A_0}^{\mathrm{gs}}(E_{A_0}^{*}, J_0)} \int_0^{E_{A_0}^{\mathrm{sad}*}} \rho_{A_0}^{\mathrm{sad}}(E_{A_0}^{\mathrm{sad}*} - \epsilon_f, J_0)\, d\epsilon_f. \tag{2.46}$$

Here, ϵ_f represents the kinetic energy of the fissioning system, and $\rho_{A_0}^{\mathrm{sad}}$ is the density of transition levels per energy at the saddle configuration. The integration upper limit is evaluated as:

$$E_{A_0}^{\mathrm{sad}*} = E^* - B_{\mathrm{f}} - E_{A_0}^{\mathrm{Erot(sad)}}. \tag{2.47}$$

The density $\rho_{A_0}^{\mathrm{gs}}$ is the same as in the formula for neutron decay width, and the definition of the $E_{A_0}^{\mathrm{Erot(sad)}}$ is presented in Subsection 2.3.1.7. Even though Eq. (2.46) offers a good description of the thermal fission, further investigations have noted that corrections, such as those proposed by Kramers and Strutinsky [66, 103], are necessary to enhance its modelling of fission dynamics. These corrections are discussed in subsection 2.3.1.4 below.

2.2.3 The Nuclear Level Density Function(ρ)

The neutron and fission decay widths can be evaluated when nuclear level densities are known at given configurations. The nuclear level density refers to the number of possible nuclear states per unit of energy [77]. This concept is crucial in the statistical treatment of nuclear decay processes, as seen in equations for neutron emission and Bohr-Wheeler fission decay rates (Eqs. (2.41) and (2.46)), respectively.

For an atomic nucleus with N neutrons and Z protons, and mass number $A = N + Z$, the two fermion particle level density can be expressed as:

$$\rho(E^*) = \frac{\sqrt{\pi}}{12} \times \frac{\exp(\beta_0 E^* + \frac{a}{\beta_0})}{\left[\beta_0 E^{*3}\right]^{\frac{1}{2}}} \times \left[\frac{g_0^2}{4 g_n g_p}\right]^{\frac{1}{2}} \times \frac{1 - \exp\left(-\frac{a}{\beta_0}\right)}{\left[1 - \frac{1}{2} E^* \beta_0 \exp\left(-\frac{a}{\beta_0}\right)\right]^{\frac{1}{2}}} \tag{2.48}$$

where g_n and g_p represent the single-particle level densities for neutrons and protons at the Fermi energy, respectively [53, 104]. The combined single-particle level density $g_0 = g_n + g_p$. The β_0 parameter is related to the excitation energy E^* implicitly as,

$$\left(\frac{a}{\beta_0}\right) = (aE^*)\left[1 - \exp\left(\frac{a}{\beta_0}\right)\right], \tag{2.49}$$

where a is the level density parameter. This relation allows (2.48) to be defined for two energy regimes. At the limit when $E^* \to 0$, the level density

$$\rho(E^*) = \frac{1}{12}\sqrt{2\pi} e a \exp(aE^*), \tag{2.50}$$

whereas, at high E^* energies, one has [53, 104]:

$$\rho(E^*) = \frac{\sqrt{\pi}}{12} \frac{\exp\left(2\sqrt{aE^*}\right)}{a^{\frac{1}{4}} E^{*\frac{5}{4}}} \tag{2.51}$$

which is the same as well-known formula in an equidistant energy level model [105]. Here, the excitation energy (E^*) should be corrected by the pairing energies of the compound or the decay product, respectively.

The improvement in Eq. (2.48) (in solid red line) over the standard equidistant formalism (in black line) as depicted in Fig. 2.10 is related to eliminating the divergence at low excitation energies when $E^* \rightarrow 0$. The divergence stems from the term $\frac{1}{E^{*\frac{5}{4}}}$ in the prefactor of Eq. (2.51). This is resolved in Eq. (2.48) by employing an implicit relation between E^* and β_0, as defined in Eq. (2.49).

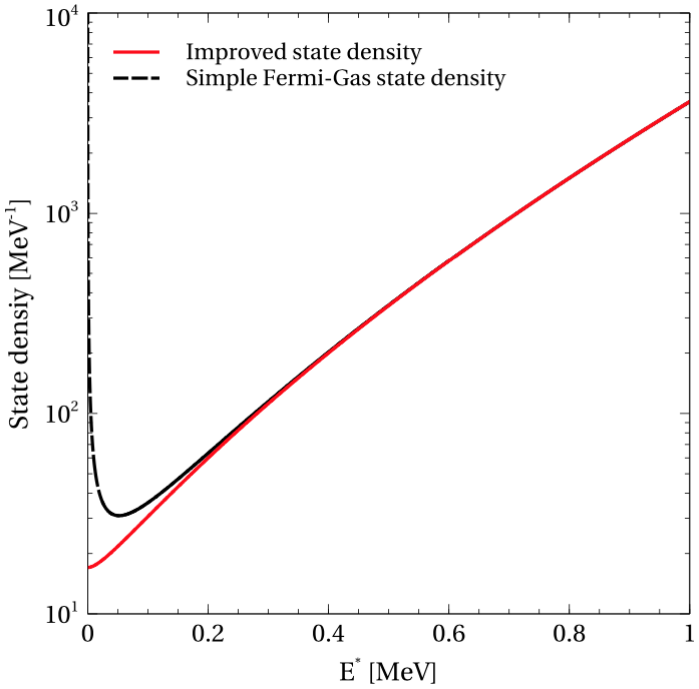

Figure 2.10: Comparison of level density models: the simple Fermi-gas model described by Eq. (2.51) is depicted with a black line, and the improved parametrisation from Eq. (2.48) is shown with a solid red line. The figure is reproduced from Ref. [53].

In contrast to the approach taken by Kewpie2, the FbD model [34, 48], adopts the following parametrisation:

$$\rho(E^*) = C \times \exp\left(2\sqrt{aE^*}\right), \tag{2.52}$$

where the prefactor C is set to unity. This approach also effectively eliminates the singularity at $E^* \rightarrow 0$. The entropy term $2\sqrt{aE^*}$ in the exponential argument is evaluated similarly in both models. This effectively highlights the differences in how both codes handle the level density formalisms.

In both models, the excitation energy, E^* is corrected by the pairing energy of the nucleus according to the back-shift formula to account for a gap in level densities between ground

state and the first excited state. In this work, the following pairing energies are adopted:

$$E_{\text{pair}} = \begin{cases} \frac{21}{\sqrt{A}} \text{ MeV} & \text{for even-even nuclei,} \\ \frac{10.5}{\sqrt{A}} \text{ MeV} & \text{for even-odd nuclei,} \\ 0 \text{ MeV} & \text{for odd-odd nuclei,} \end{cases} \tag{2.53}$$

where A is the mass number of the considered nucleus [34]. In this sense $E^* - E_{\text{pair}} = E_0^*$, where E_0^* is the actual excitation energy with respect to the ground state (or saddle point).

2.2.3.1 Level Density Parameter (a)

An important parameter in the level density function is the level density parameter a. The level density parameter determines how the nuclear level density changes with excitation energy, influencing the number of available nuclear states at a given energy. There are several propositions for the nuclear level density parameter in the literature, and several options can be found in the original Kewpie2 model. The parameterisation proposed in Ref. [106] is adopted in the present study because it also accounts for the deformation of the nucleus. The level density parameter is given as:

$$a = a_v A + a_s A^{\frac{2}{3}} B_s + a_c A^{\frac{1}{3}} B_k, \tag{2.54}$$

where $a_v = 0.0696\ \text{MeV}^{-1}$, $a_s = 0.1801\ \text{MeV}^{-1}$, and $a_c = 0.1644\ \text{MeV}^{-1}$. Here B_s and B_k are the surface and curvature corrections, respectively. These are defined in terms of the effective deformation variable α as,

$$B_s = 1 + (0.6416\alpha - 0.1421\alpha^2)^2, \tag{2.55}$$

$$B_k = 1 + (0.6542\alpha - 0.0483\alpha^2)^2, \tag{2.56}$$

where α is given as [48]:

$$\alpha = \frac{R_{\text{max}} - \text{R}_0}{\text{R}_0}. \tag{2.57}$$

In this context, R_{max} is the length of a semi-major axis of an axially symmetric deformed nucleus (Eq. (2.26)),

$$R_{\text{max}} = R_0 \left(1 + \sqrt{\frac{5}{4\pi}}\beta_2 + \sqrt{\frac{9}{4\pi}}\beta_4 + \sqrt{\frac{13}{4\pi}}\beta_6\right), \tag{2.58}$$

where R_0 represents the radius of a spherical nucleus, given as $R_0 = r_0 A^{\frac{1}{3}}$. By substituting the definition of R_{max} and R_0, Eq. (2.57) reduces to

$$\alpha = \sqrt{\frac{5}{4\pi}}\beta_2 + \sqrt{\frac{9}{4\pi}}\beta_4 + \sqrt{\frac{13}{4\pi}}\beta_6. \tag{2.59}$$

The parameters β_2, β_4, and β_6 characterize the ground-state or saddle-point deformations and are taken from Ref. [69].

2.2.3.2 Nuclear Shell Damping Effect in Level Density

The nuclear shell correction energy (ΔE_{sh}), which plays a crucial role in stabilizing the nucleus, particularly in super-heavy nuclei, is incorporated into the level density function following Ignatyuk's prescription [53, 68, 107]. The level density parameter a given by Eq. (2.54) is modified by a damping function:

$$a_{\mathrm{gs}} = a\left[1 + \left(1 - e^{-\frac{E^*}{E_{\mathrm{d}}}}\right)\frac{\Delta E_{\mathrm{sh}}}{E^*}\right]. \tag{2.60}$$

In this context, a_{gs} represents the ground state level density parameter, whereas E_{d} denotes the shell damping parameter.

Damping energy $E_{\mathrm{d}} = 18.5$ MeV has been proposed as the standard value for nuclei with masses greater than 200, but it has also been pointed out that this value is not unique [62, 84]. This is because it is more often scaled to reproduce the experimental data, which highlights the sensitivity of the modelling to this parameter. In this work, the relation obtained for super-heavy nuclei proposed in [108] was adopted:

$$E_{\mathrm{d}} = \frac{A^{\frac{1}{3}}}{0.423}\ \mathrm{MeV}. \tag{2.61}$$

In the original Kewpie2 model, E_{d} takes values between 13 - 25 MeV. Note that this study does not consider the shell correction energy at the fission saddle point, which is also the case in FbD model calculations.

2.3 Comparison of the Fine Details of Kewpie2 and FbD

This section compares the fine details of the survival probability in Kewpie2 and FbD models. The input parameters necessary for the survival probability calculations, nuclear ground state, and saddle-point properties, such as fission barriers, rest masses, and deformation parameters (shape variables), were taken from Ref. [69]. These are theoretical nuclear properties specifically for heavy and super-heavy nuclei. Implementation of these nuclear tables is a change regarding the original default version of the Kewpie2 model, in which Möller-Nix mass tables from Ref. [109] were used.

2.3.1 Comparison of Level Density Formalism in Kewpie2 and FbD

For consistency, we will refer to the level densities from Eq. (2.48) and (2.52) as the Kewpie2 and FbD formalisms, respectively. That being said, we begin by comparing the two different level density formalisms by evaluating the ratios of the level densities in one-neutron emission configuration (A_1+n) to that of the compound nucleus (A_0) denoted as $\left(\frac{\rho^{\mathrm{gs}}_{A_1}}{\rho^{\mathrm{gs}}_{A_0}}\right)$. Similarly, this is repeated for the first-chance fission decay by evaluating the ratios of the level density at the fission saddle to that of the compound nucleus $\left(\frac{\rho^{\mathrm{sad}}_{A_0}}{\rho^{\mathrm{gs}}_{A_0}}\right)$. The

ratios $\left(\frac{\rho^{gs}_{A_1}}{\rho^{gs}_{A_0}}\right)$ and $\left(\frac{\rho^{sad}_{A_0}}{\rho^{gs}_{A_0}}\right)$ are illustrated in the panel (a) and (b) of Fig. 2.11, respectively, for the ^{208}Pb(^{58}Fe, 1n)^{265}Hs reaction as a test case. These calculations aim to evaluate the quantitative differences between the two-level density formulas as a function of energy.

Fig. 2.11 illustrates the ratios of the level densities calculated using the Kewpie2 (red solid line) and FbD (blue dashed-dotted lines) approaches, shown as a function of the excitation energy E^*. Ratios are evaluated for each configuration without accounting for angular momentum using the definitions of the excitation energies in Eqs. (2.43), (2.42) and (2.47), respectively. Note that the kinetic energy (ϵ_n) of the neutron and that associated with the fission coordinates (ϵ_f) are not summed over.

As shown in panels (a) and (b) of Fig. 2.11, the Kewpie2 formalism predicts higher $\left(\frac{\rho^{gs}_{A_1}}{\rho^{gs}_{A_0}}\right)$ and $\left(\frac{\rho^{sad}_{A_0}}{\rho^{gs}_{A_0}}\right)$ ratios compared to the FbD formalism. These observations imply that the choice of level density formalism can impact the calculated neutron evaporation and fission decay widths (shown in Fig. 2.12), which are essential for understanding the de-excitation process of excited nuclei. The question is how these subtle differences will affect the neutron emission and fission decay widths and, eventually, the survival probability.

Note that Ignatyuk shell damping corrections to the level density (Eq. (2.60)) are applied only to the ground state level densities, where the shell damping E_d is taken as 18.5 MeV for the sake of comparing the results with the FbD calculations. In the subsequent analysis in Section 2.5, the semi-empirical approximation given by Eq. (2.61) will be adopted.

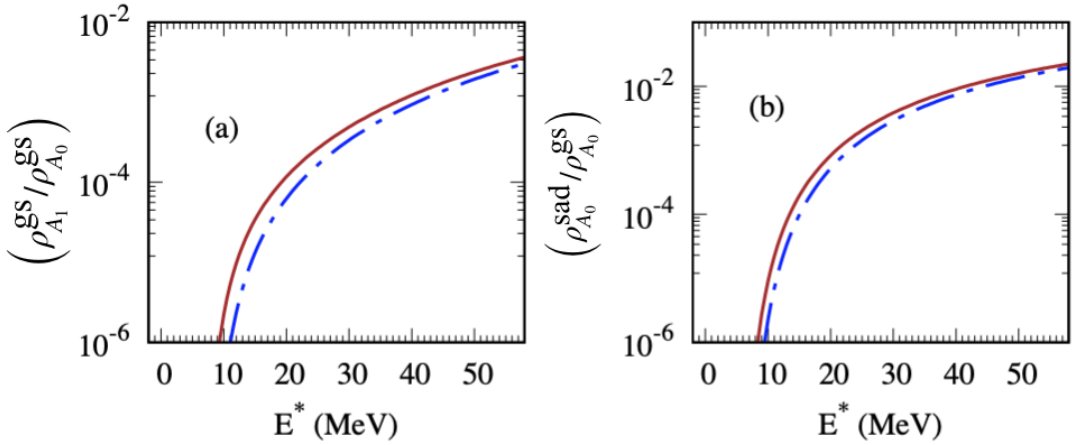

Figure 2.11: Comparison of a default level density formalisms in Kewpie2 (red solid line) and FbD (blue dashed-dotted line) models. Panels (a) and (b) show the ratios of level densities for the one-neutron emission configuration $\left(\frac{\rho^{gs}_{A_1}}{\rho^{gs}_{A_0}}\right)$ and fission saddle point configuration $\left(\frac{\rho^{sad}_{A_0}}{\rho^{gs}_{A_0}}\right)$, respectively, to the level density of the compound nucleus. Ground state and saddle point properties are taken from Ref. [69].

2.3.1.1 Impact of Level Density Formalism on Neutron Emission and Fission Decay Width

As demonstrated in Fig. 2.11, the choice of level density formalism can potentially influence the neutron emission and fission decay widths evaluated from a statistical model. To further quantify these differences, we will now evaluate these widths using Eq. (2.41) and Eq. (2.46). This investigation is done within the Kewpie2 framework, where the default level density will be replaced with the one used in the FbD approach. This allows us to directly compare the influence of each formalism on the calculated neutron emission Γ_n and fission Γ_f widths.

Fig. 2.12 illustrates how changing the level density formalism will affect the Γ_n and Γ_f shown in the panels (a) and (b), respectively, for excited $^{266}Hs^*$. The Kewpie2 approach (in solid red lines) gives higher neutron emission and fission widths than the FbD approach (in dotted dashed blue line). The question is, how are the observed differences in level densities propagated along the cascades, considering the relevance of the neutron emission width (Γ_n) and the fission decay width (Γ_f) in estimating the overall survival probability. To answer this, the ratio of the neutron emission width to the total decay width $\left(\frac{\Gamma_n}{\Gamma_{tot}}\right)$ is shown in Fig. 2.13, where $\Gamma_{tot} = \Gamma_f + \Gamma_n$. This ratio indicates the probability of neutron emission (Γ_n) as a function of the excitation energy, evaluated using both level density formalisms.

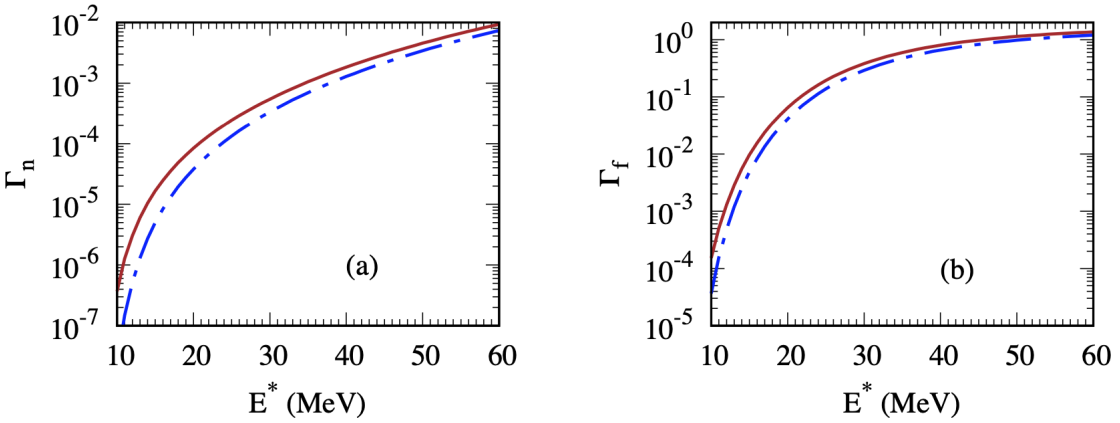

Figure 2.12: Neutron emission and fission decay widths calculated using different level density formalisms for excited $^{266}Hs^*$. Panel (a) shows the neutron emission width, where the red line and blue dashed-dotted lines represent Kewpie2 and FbD level densities, respectively. Panel (b) depicts the fission decay width using the same colour and line conventions.

Fig. 2.13 illustrates the $\frac{\Gamma_n}{\Gamma_{tot}}$ as a function of the excitation energy. Similar to Fig. 2.12, the red solid and blue dashed-dotted lines represent calculations using the Kewpie2 and FbD level densities, respectively. Although both models predict a similar qualitative trend, quantitative differences are observed, particularly at lower excitation energies, with the Kewpie2 approach predicting a higher probability of neutron emission than the FbD model. As we will see later, the observed differences are expected to propagate along the cascade.

Besides, comparing the curves in terms of their magnitude, they depict competition between neutron emission and fission as possible decay channels of the compound nucleus. The tendency of the curve is driven by the balance between neutron emission and fission decay widths as a function of excitation energy. Around 10-20 MeV the probability of emitting neutron is of the order of 10^{-3} , but as the energy increases, neutron emission becomes more favourable, leading to the increase in $\frac{\Gamma_n}{\Gamma_{\text{tot}}}$. The differences between the curves are given by a factor denoted f. The difference indicates the sensitivity of the ratio to the underlying assumptions in the respective level density formalisms. The differences between the impacts of the level density formalisms become evident when considering the survival probability along the neutron emission cascades, as illustrated by Fig. 2.14. Fig. 2.14 shows the results obtained using Kewpie2 (solid red lines), which consistently predicts higher survival probabilities compared to the level density formalism used in FbD (dashed-dotted blue lines).

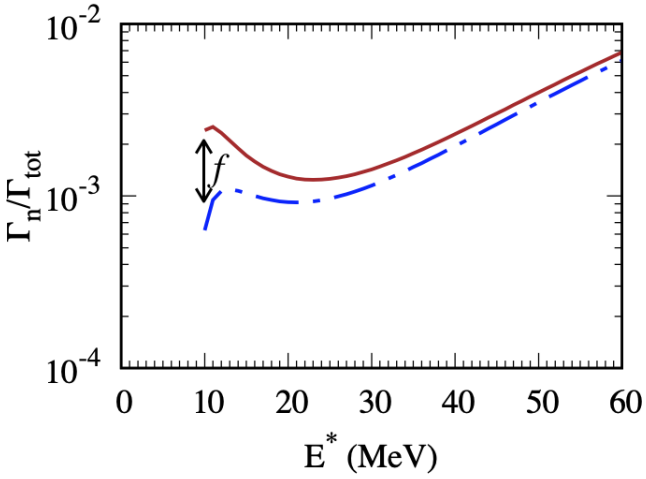

Figure 2.13: The $\frac{\Gamma_n}{\Gamma_{\text{tot}}}$ calculated using the level density formalisms given by Eq. (2.48) and Eq. (2.52) shown in red solid line and dashed-dotted lines respectively. Here, $\Gamma_{\text{tot}} = \Gamma_f + \Gamma_n$ and f corresponds to the differences between the two calculations (see text for details).

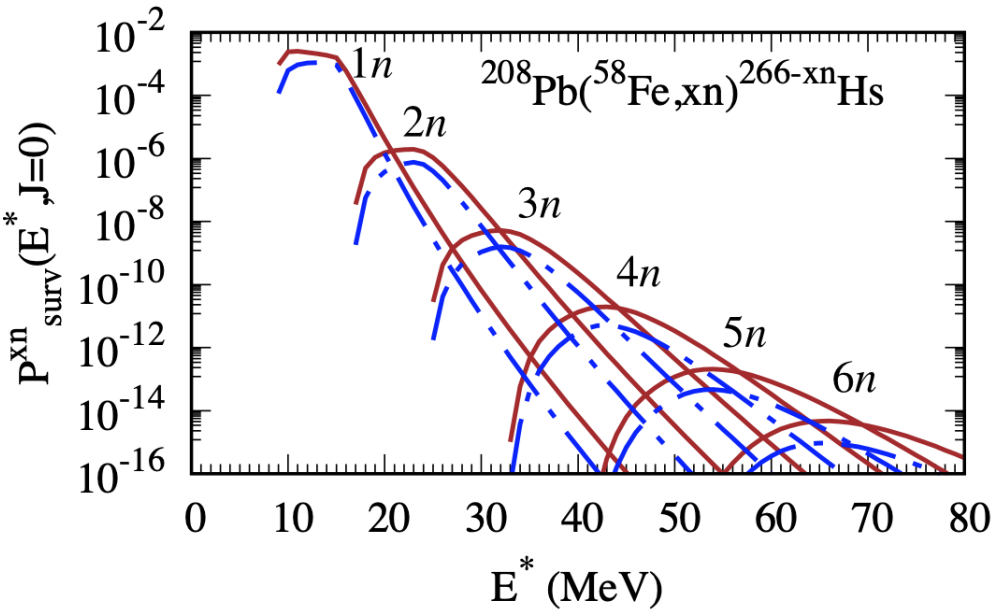

Figure 2.14: Calculated neutron emission cascade (1n-6n) for the ^{208}Pb(^{58}Fe, xn)$^{266-x\text{n}}$Hs reaction. The solid red lines represent calculations obtained using the Kewpie2 level density formalism, while the blue dashed-dotted lines correspond to the FbD formalism. Nuclear ground states and saddle points properties are taken from Ref. [69]. Here, rotational energies are not accounted ($J = 0$).

2.3.1.2 The Impact of Neutron Capture Formalism

This section compares two approaches to calculating the neutron inverse capture cross section, as given by Eq. (2.44) and Eq. (2.45), and their respective effects on the survival probability as shown in Fig. 2.15. The former approach is the default in Kewpie2 modelling, while the latter is used in FbD calculations. The two approaches are geometric neutron capture cross sections, except that the Kewpie2 approach varies with energy. The energy-dependent is necessary to account for the decrease in the neutron capture cross section with the increasing energy.

In Fig. 2.15, the solid red lines denote the calculations using the Kewpie2 approach to evaluating the neutron capture cross section. The FbD formalism calculations are shown in the blue dashed-dotted lines. To only investigate the impact due to the change in the neutron inverse capture cross section, the level density function is evaluated using only the Kewpie2 formalism (Eq. (2.48)). The results, as illustrated in Fig. 2.15, show that the impact due to the energy dependency on the neutron capture cross section is small at the lower energies, where there is no noticeable difference for the 1n to 4n neutron emission channels. The difference can only be seen at the high energies. This finding highlights the influence of the chosen neutron inverse capture cross section on the calculated survival probability, particularly at higher excitation energies. However, its impact is insignificant compared to the impact of using different level density formalisms, as shown in the previous chapter.

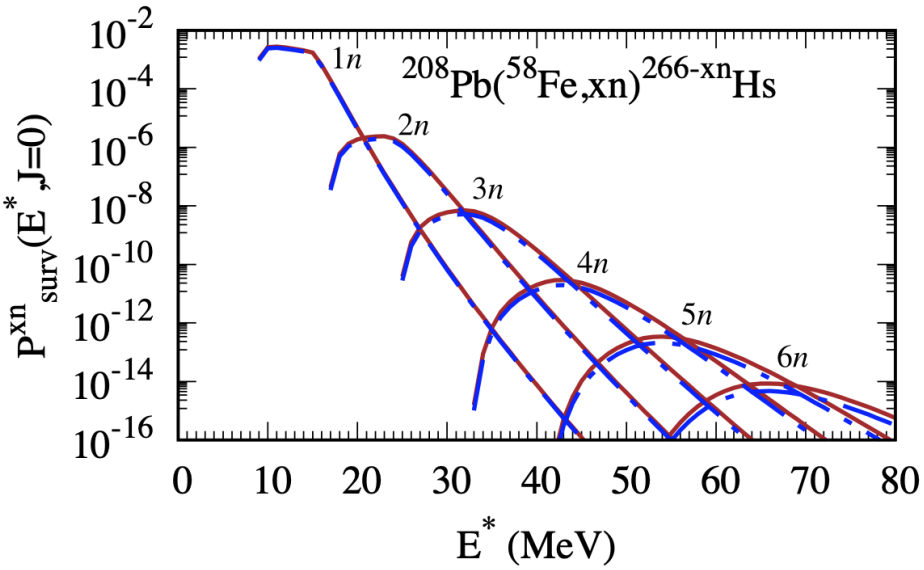

Figure 2.15: Comparison of the impact of neutron inverse capture cross section formalism on compound nucleus survival probabilities using the ^{208}Pb(^{58}Fe, xn)$^{266-xn}$Hs reaction. The calculations with the Kewpie2 and FbD approaches are indicated by the red solid and the dashed-dotted blue lines, respectively.

2.3.1.3 Comparison of Sample Calculation: Kewpie2 Compared to FbD

The next step involves comparing the results of each code obtained for the reaction ^{295}Am(^{48}Ca, xn)$^{291-x\text{n}}$Mc. In this case, results were obtained using original FbD code [68] (T. Cap, personal communication) and are compared with the Kewpie2 calculations. The comparison is shown in Fig. 2.16 with the FbD calculations in blue dashed-dotted lines [68] and Kewpie2 with the default configurations in solid red lines. The results show that Kewpie2 consistently predicts higher survival probabilities compared to FbD calculations throughout the neutron emission cascade.

The discrepancies highlight the fine details in the modelling, stemming from the choice of level density function formalisms and neutron inverse capture formalisms. These are illustrated in Fig. 2.14 in the previous section, where it was demonstrated that switching between level density formalisms results in about an order of magnitude difference in the survival probability at higher energies. A noticeable enhancement in the survival probability at higher energy is observed when the energy-dependent geometric neutron capture (Eq. (2.44)) is replaced with an energy-independent version (Eq. (2.45)), as shown in Fig. 2.15. Therefore, differences between the current versions of Kewpie2 and FbD modelling of the survival probability are primarily due to these subtle differences.

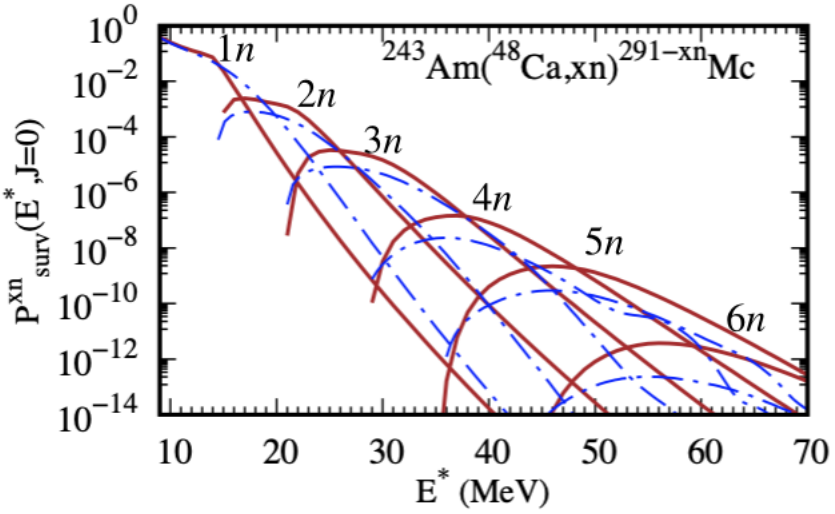

Figure 2.16: Comparison of numerical calculations for the reaction ^{295}Am(^{48}Ca, xn)$^{291-x\text{n}}$Mc, using the Kewpie2 and FbD [68] codes. The red solid lines represent Kewpie2, and the blue dotted lines show FbD calculations. The difference between the fine details in the two models lies in the choice of the level density and neutron capture cross section formalisms.

In conclusion, this study highlights the impact of the nuclear level density function and the neutron inverse capture cross section formalisms on the survival probability. Notably, switching between the level density formalism from Eq. (2.48) to that given by Eq. (2.52) results in approximately an order of magnitude change in the survival probability at higher energies. However, the choice of neutron capture formalism exhibits a relatively minor impact.

2.3.1.4 The Kramers and Strutinsky Correction Factor

After comparing the fine details of Kewpie2 and FbD modelling of compound nucleus survival probability, this section investigates how incorporating dynamical factors into the statistical description affects the overall survival probability. This is done within the Kewpie2 framework since the FbD calculation does not account for these factors.

To begin with, the Kramers corrections adapt the purely statistical formalism presented in Eq. (2.46) to match the dynamical limit by introducing the corrective term:

$$K_{\mathrm{f}} = \sqrt{1 + \left(\frac{\beta}{2\omega_{\mathrm{sad}}}\right)^2} - \frac{\beta}{2\omega_{\mathrm{sad}}}, \tag{2.62}$$

known as the Kramers factor [53, 66, 103, 110]. In this expression, β represents the reduced friction coefficient, while ω_{sad} is the angular frequency of the fission saddle potential barrier. The Kramers factor highlights the influence of nuclear matter viscosity on the fission rate, indicating that higher viscosity results in a lower fission rate and vice versa. Typically, the values for β range from $(1-9)\times 10^{21}\ \mathrm{s}^{-1}$, and $\hbar\omega_{\mathrm{sad}}$ is set to 1MeV [53].

Additionally, Strutinsky pointed out the necessity to consider the variation in the number of stationary collective states between the ground state and the fission saddle. This is quantified by the factor:

$$S_{\mathrm{f}} = \frac{\hbar\omega_{\mathrm{gs}}}{T_{\mathrm{gs}}}, \tag{2.63}$$

where ω_{gs} represents the characteristic width of the ground state potential well and is set such that $\hbar\omega_{\mathrm{gs}} = 1$ MeV. The nuclear temperature T_{gs} is defined as:

$$T_{\mathrm{gs}} = \sqrt{\frac{E^*}{a}}, \tag{2.64}$$

with a being the nuclear level density parameter. Combining these factors, the refined statistical model that matches it to the dynamical limits is expressed as:

$$\Gamma_f^{'} = K_{\mathrm{f}} \cdot S_{\mathrm{f}} \cdot \Gamma_{\mathrm{f}}, \tag{2.65}$$

where Γ_{f} represents the value obtained with Eq. (2.46). The impact of these corrective terms on the calculations of the survival probability is demonstrated in Fig. 2.18 below.

2.3.1.5 Collective Enhancement of the Intrinsic Level Density

Furthermore, to account for the collectivity of the intrinsic nuclear states, the level density function (Eq. (2.48)) is corrected by the so-called collective enhancement factor:

$$\kappa_{\mathrm{coll}}(E^*) = \kappa_{\mathrm{rot}}(E^*)\phi(\beta_2) + \kappa_{\mathrm{vib}}(E^*)\left[1 - \phi(\beta_2)\right], \tag{2.66}$$

where,

$$\phi(\beta_2) = \left[1 + \exp\left(\frac{\beta_2^0 - |\beta_2|}{\Delta\beta_2}\right)\right]^{-1}. \tag{2.67}$$

Here, β_2^0 and $\Delta\beta_2$ are the parameters of the model that are determined to be 0.15 and 0.04, respectively [53, 62, 111]. The terms $\kappa_{\rm rot}(E^*_{\rm C_0})$ and $\kappa_{\rm vib}(E^*_{\rm C_0})$ in the equation are responsible for collectivity due to rotational and vibrational collective states, respectively.

The collectivity factor for each of these states is related to the spin-cut-off parameter $\sigma_\perp$:

$$\kappa_{\rm coll}(E^*) = \begin{cases} (\sigma_\perp^2 - 1) f(E^*) + 1 & \text{if} \quad \sigma_\perp^2 > 1, \\ 1 & \text{if} \quad \sigma_\perp^2 \leq 1, \end{cases} \tag{2.68}$$

and the $\sigma_\perp$ in this framework is defined for the two collective states as,

$$\sigma_\perp^2 = \begin{cases} \frac{\mathcal{I}_\perp T}{\hbar^2} & \text{if} \quad |\beta_2| > 0.15, \quad \text{rotational}, \\ S\theta^2 \frac{\mathcal{I}_\perp T}{\hbar^2} & \text{if} \quad |\beta_2| \leq 0.15, \quad \text{vibrational}. \end{cases} \tag{2.69}$$

constrained by the degree of quadrupole deformation parameter β_2. The free parameter, represented by S, has an optimal value of 25 [53, 111]. Here, $\theta = 0.22{+}0.003\Delta N{+}0.005\Delta Z$ and ΔN and ΔZ are the valence nucleons.

The cut-off factor, $f(E^*)$, is defined as

$$f(E^*) = \frac{1}{1 + \exp\left[\frac{E^* - E_{\rm cr}}{d_{\rm cr}}\right]}, \tag{2.70}$$

where $E_{\rm cr}$ and $d_{\rm cr}$ are set to 40 MeV and 10 MeV, respectively.

The rigid body moments of inertia $\mathcal{I}_\perp$ are used in Eq. (2.69) and are defined as [34],

$$\mathcal{I}_\perp \approx \frac{1}{5} M R^2 \left[(1+\alpha)^2 + (1+\alpha)^{-1}\right] + 2 M b_f^2, \tag{2.71}$$

where α is the nuclear effective deformation parameter as outlined in Eq. (2.57). Here, M is the mass of the compound nucleus and b_f stands for nuclear surface diffuseness, $b_f \approx 1$ fm.

This parameterisation of the moment of inertia is adopted to ensure consistency in evaluating the rotational energy at the nuclear ground state, fission saddle, and conditional saddle when describing the hindrance factor, as seen in the next Section 2.4.2.2.

Finally, to account for nuclear collectivity, the refined level density is given by:

$$\rho'(E^*) = \kappa_{\rm coll}(E^*) \times \rho(E^*). \tag{2.72}$$

where $\rho'(E^*)$ is the enhanced level density and $\rho(E^*)$ is the intrinsic level density calculated using the formulas in Subsection 2.2.3.

2.3.1.6 Impact of KS and CE Corrections on the Survival Probability

Fig. 2.17 illustrates how the fission decay width changes with the reduced friction coefficient, β. The β is a free parameter (in Eq. (2.62)) that must be tuned within the present version of the Kewpie2 model. The results in Fig. 2.17 show a decrease in fission decay width with increasing β, and this difference is more pronounced at higher energies due to the temperature variation with excitation energy dependence in the Strutinsky term (see Eq. (2.63)). Panel (a) of Fig. 2.18 shows how this influences the overall survival probability.

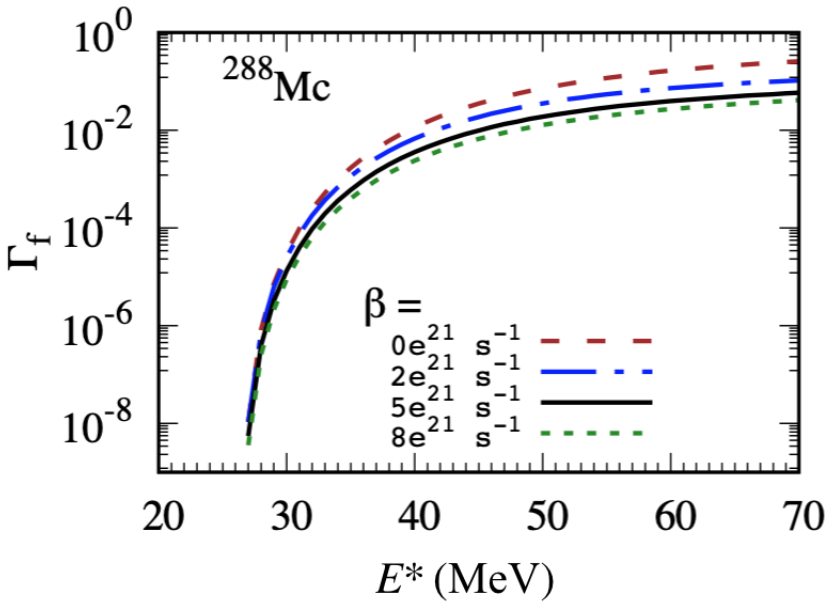

Figure 2.17: Calculated fission width for ^{288}Mc as a function of excitation energy for different values of the friction parameter β. This plot highlights the impact of frictional forces within the nucleus on the fission width, illustrating the critical role of β in modulating nuclear fission dynamics. The fission barrier, $B_f = 6.21$ MeV [69].

Fig. 2.18 shows the impact of the KS and CE corrective terms on the compound nucleus survival probability. Panel (a) specifically compares the influence of the KS factor, which considers the nuclear viscosity, depicted by the short blue dashed line. The solid lines are the reference calculations that do not consider any corrective factors (shown in the solid red line). Here, β is set to the Kewpie2 default value, 5×10^{21} s^{-1} [53]. The survival probability is enlarged compared to the solid lines due to decreasing fission decay width comparable to the neutron emission width. This subsequently enhances the nucleus survival probability along the cascade. In contrast, enabling the collective enhancement of the intrinsic level density (CE) (described in Section 2.3.1.5 decreases nucleus survival probability, as shown in panel (b) of Fig. 2.18.

The CE factor, which accounts for nuclear deformation at the ground state and saddle point, also depends on excitation energy via the empirical relation in Eq. (2.70). These factors influence the behaviour of survival probability along the cascade, where fission dominates the neutron emission. The combined effects shown in panel (c) almost produce a balanced outcome. However, the impacts of CE dominate at lower energies (i.e., 1n, 2n,

3n neutron channels), whereas KS has a more pronounced effect at higher energies (i.e., 5n and 6n channels). It is important to note that this behaviour may vary depending on the values β. This is illustrated by panel (d), which shows a lower survival probability when the reduced friction parameter of the model is decreased by 40%. This is reflected in panel (e), which illustrates a lower trend along the cascade compared to the calculations without any corrective factors.

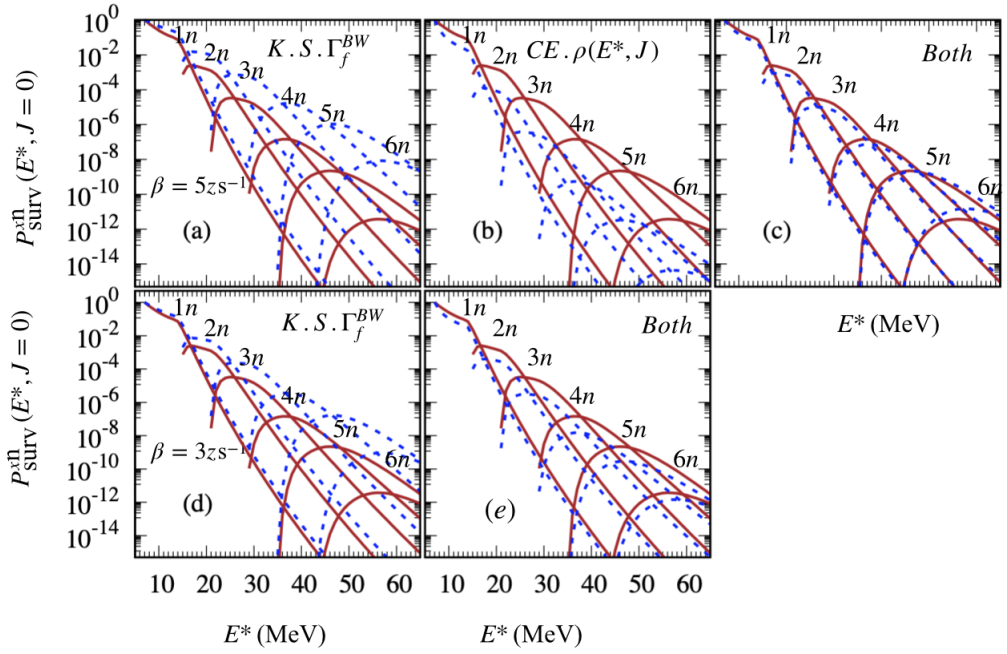

Figure 2.18: Impact of Kramers-Strutinsky correction factors on the fission decay width and collective enhancement of intrinsic level densities on the survival probability along the cascade for the reaction $^{295}\mathrm{Am}\left(^{48}\mathrm{Ca}, x\mathrm{n}\right)^{291-x\mathrm{n}}\mathrm{Mc}$ at $J = 0$ using Kewpie2. Solid lines represent calculations without correction or enhancement factors. Panel (a): Blue dotted lines show Kramers and Strutinsky's effects on the fission width. Panel (b): Effect of collective enhancement on survival probability. Panel (c): Combined impact of both correcting factors.

2.3.1.7 The Impact of Angular Momentum on The Survival Probability

Previously, survival probabilities were evaluated only for total angular momentum $J = 0$, corresponding to zero orbital angular momentum (ℓ) and intrinsic spin (s). This analysis is now extended to include cases with non-zero ℓ in the simulations. The rotational energy is one of the most important factors that influences the survivability of an excited compound nucleus. The atomic nucleus, with non-vanishing rotational energy, implies deviation from the sphericity. Furthermore, the fission barrier of the nucleus has an inverse relation with the angular momentum, such that the survival probability vanishes beyond a certain critical value [77].

In the Kewpie2 model, the rotational energies:

$$E_{\text{rot}} = \frac{\hbar^2 \ell(\ell+1)}{2\mathcal{I}}, \tag{2.73}$$

are accounted for in the fission saddle, residue and compound nuclei ground states according to Eqs. (2.47), (2.42) and (2.43). Here, $\mathcal{I}$ stands for the moment of inertia given by Eq. (2.71). This is evaluated for each configuration state: parent nucleus ground state (A_0), the ground state of the daughter nucleus (A_1), and the saddle point of the parent nucleus (A_0^{sad}).

Fig. 2.19 shows the 2D spectrum for the 3n channel, with excitation energy on the x-axis and angular momentum on the y-axis. The colour gradient, ranging from blue (low) to red (high), represents the varying intensity of the survival probability. The highest P_{surv} values (red) are concentrated at low angular momentum and excitation energies around 25-30 MeV. As either excitation energy or angular momentum increases, the survival probability decreases, transitioning from yellow and green to blue (lowest values). The survival probability decreases rapidly with increasing angular momentum and excitation energy. This highlights the significant role of angular momentum in determining the survival of the compound nucleus.

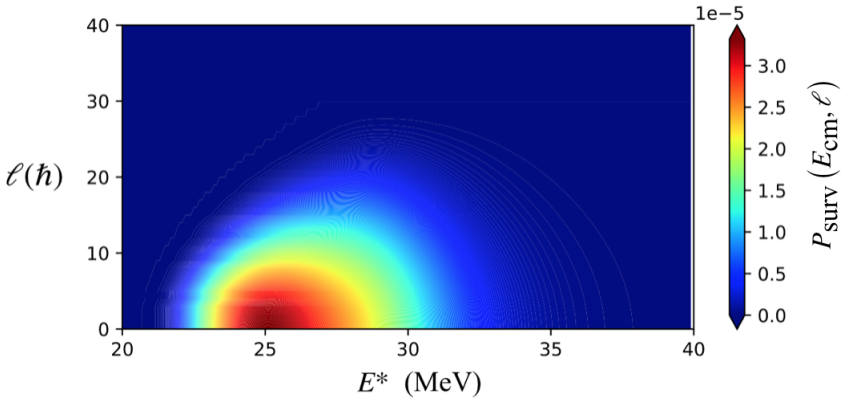

Figure 2.19: Calculated two-dimensional spectrum of the survival probability (P_{surv}) for the 3n neutron emission channel in the reaction ^{295}Am(^{48}Ca, xn)$^{291-xn}$Mc as a function of excitation energy (E^*) and angular momentum (ℓ).

2.3.2 Sample Calculations without Fusion Hindrance

The analysis of the survival probability concludes by evaluating the evaporation residue excitation functions for selected reactions leading to the synthesis of heavy and super-heavy elements. In this section, we only consider reactions with large asymmetry, where the product of projectile and target charges are below the threshold for the reaction to be hindered: $Z_{\text{pro}} \times Z_{\text{pro}} \leq 1600$. The objective here is to apply the updated Kewpie2 in reproducing the production cross sections of the reactions without hindrance, as illustrated in Figs. 2.20 and 2.21.

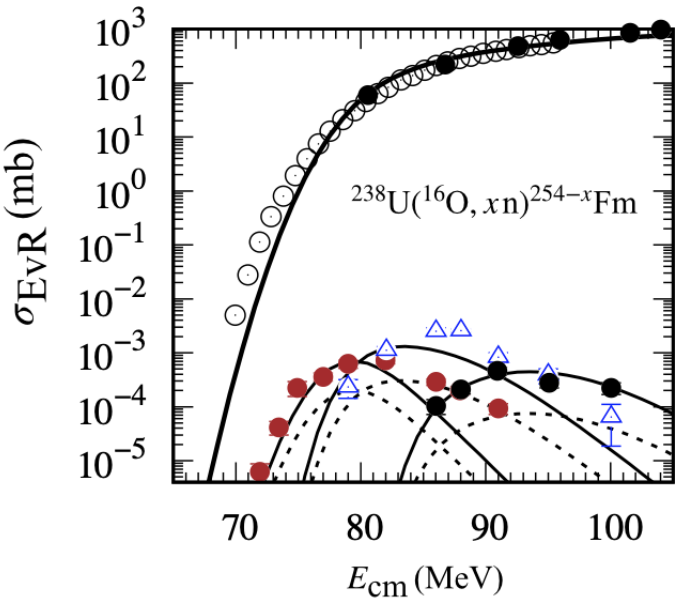

Figure 2.20: The excitation functions for 4n, 5n and 6n channels in ^{238}U(^{16}O, xn)$^{254-xn}$Fm reaction. The calculations are made using Kramers-Strutinsky factors and collective enhancement of the intrinsic level density. Here, E_{d} is taken as 18.5 MeV in combination with $\beta = 5{\times}10^{21}$ s^{-1} (in dashed line) and $\beta = 8{\times}10^{21}$ s^{-1} (in solid lines). The experimental data are taken from Ref. [112], and the theoretical curves are evaluated using ground state and saddle properties from Ref. [69].

Fig. 2.20 illustrates a fusion cross section in the solid black line (label σ_{fus}) as already presented in the panel (a) of Fig. 2.4. Our interest is in the evaporation residue cross section, which is shown for the 4n, 5n and 6n channels. The experimental data are taken from Ref. [112]. The experimental data are well reproduced when Kramers-Strutinsky factors and the collective enhancement of the level densities are considered. The shell damping energy $E_{\text{d}} = 18.5$ MeV, while β is set for the default value 5×10^{21} s^{-1} (in dashed line) and later adjusted to 8×10^{21} s^{-1} (in solid black) to reproduce the experiment data.

Similarly, Fig. 2.21 illustrates calculations for the reactions with light projectiles and heavy actinide targets leading to the formation of nuclei in the region of super-heavy elements. Panel (a) shows the EvR excitation function for the 4n channel in ^{248}Cm(^{15}N, 4n)^{259}Lr reaction. The red points are the experimental data from Refs. [84, 113]. The dashed line is the theoretical curve without KS-CE corrections and E_{d} set to 25 MeV in an attempt to

fit the experiment. The solid line denotes calculations with KS-CE corrections with the parameters β and E_d taken as 8×10^{21} s^{-1} and 18.5 MeV, respectively.

Panel (b) and (c) illustrate similar reactions, ^{249}Bk(^{15}N, 4n)^{260}Rf and ^{249}Cf(^{18}O, 4n)^{263} Sg, for which formation probability is also close to one. Similarly, the dashed lines represent the theoretical curves without KS-CE and E_d = 25 MeV. The solid lines correspond to the theoretical calculations with β and E_d set to 9×10^{21} s^{-1} and 23 MeV (in panel (b)) and 9×10^{21} s^{-1} and 21 MeV (in panel (c)), respectively. The experimental data is initially fitted by adjusting the reduced friction coefficient (β). If any discrepancy remains after adjusting β to the maximum, the shell damping energy (E_d) is increased gradually from its initial value of 18.5 MeV to 25 MeV to improve the agreement with the experimental data. The experimental data on ^{249}Bk(^{15}N, 4n)^{260}Rf and ^{249}Cf(^{18}O, 4n)^{263}Sg are taken from Refs. [84, 114] and [84, 115], respectively.

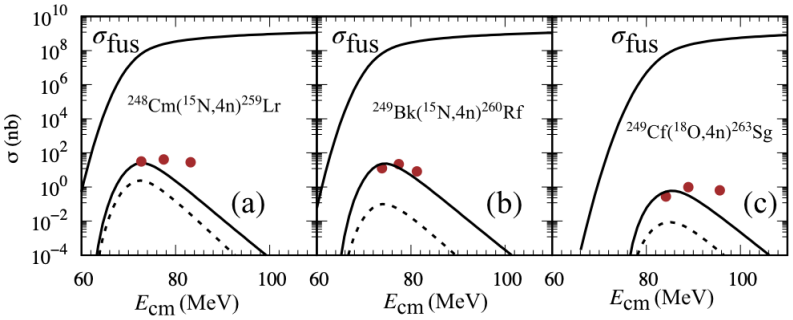

Figure 2.21: Evaporation residue cross sections (a) ^{249}Cf(^{18}O, 4n)^{263}Sg, (b) ^{248}Cm(^{15}N, 4n)^{259}Lr, and (c) ^{249}Cf(^{15}N, 4n)^{260}Db. Theoretical calculations without Kramers-Strutinsky corrections and collective enhancement (KS-CE) are evaluated with E_d = 25 MeV and are represented by dashed lines. The solid lines represent calculations with KS-CE corrections. The parameters for KS-CE corrections are $\beta = 8 \times 10^{21}$ s^{-1} and E_d = 18.5 MeV in panel (a), $\beta = 9 \times 10^{21}$ s^{-1} with E_d = 23 MeV in panel (b), and $\beta = 9 \times 10^{21}$ s^{-1} with E_d = 21 MeV in panel (c). Red points denote experimental data from Refs. [84, 113] (in panel (a)), Refs. [84, 114] (panel (b)) and Refs. [84, 115] (panel (c)).

This section concludes by presenting test calculations performed with Kewpie2 for reactions without hindrance, as illustrated in Figs. 2.20 and 2.21. In some studies, the shell damping energy, E_d, is adjusted to fit the theoretical curve to the experimental data [84]. In case of the need for predictions, a global fit of E_d can be made. The quality of the theoretical calculations also depends on the accuracy of the theoretical fission barrier heights and mass tables used in the simulation. The statistical limit of the fission decay widths is extended by incorporating KS-CE corrections. However, this introduces an additional free parameter β, which also influences the survival probability, as demonstrated in Fig. 2.18. As shown in Fig. 2.17, increasing β decreases fission decay width, favouring neutron emission and enhancing the production cross sections. The E_d and β parameters serve as free parameters that can be adjusted to fit the experiment. For further examples of heavy nuclei simulations where the formation probability is assumed to be 1, please refer to Ref. [53].

Now that we have concluded the presentation of the capture and survival part of the

modelling, we will proceed to investigate the formalism of the compound nucleus formation probability. This is a crucial step for accurately predicting the production cross sections of super-heavy elements.

2.4 Compound Nucleus Formation probability (P_{CN})

This section describes the formalism of the hindrance associated with the shape evolution of the di-nuclei formed at capture into a compound nucleus (CN) over the conditional saddle (fusion saddle). As mentioned earlier, several approaches exist for calculating the formation probability; however, this study focuses on diffusion over a potential barrier as a mechanism enabling two colliding nuclei to form a compound nucleus within the Langevin formalism [61, 67, 68]. This approach is distinct from the problem of leaking thermally equilibrated particles in a potential well, as discussed in Kramers' work on the fission decay rate [66] within the Langevin formalism. Here, we investigate the probability of a nucleus facing uphill potential at the fusion saddle to diffuse to the other side as a mechanism of compound nucleus formation within the Langevin formalism [52, 116].

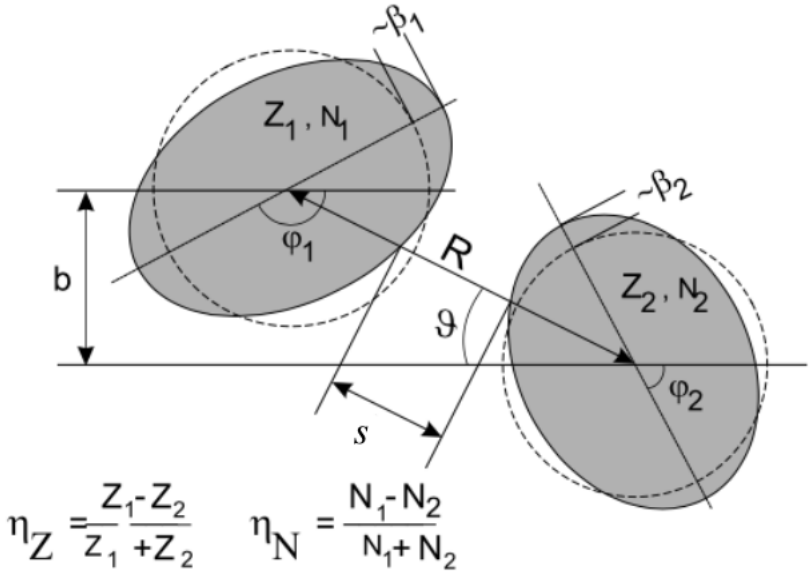

Figure 2.22: The schematic illustration of di-nuclei at contact. Here, the indexed 1 and 2 variables correspond to the projectile and target nuclei, respectively. The figure is reproduced from [49].

The evolution of the di-nuclei into a compound nucleus within the Langevin formalism may be described by several collective variables (Q_i), as depicted in Fig. 2.22, and their conjugate momenta, (P_i). For example, as shown in Fig. 2.22, the collective variables are charge and neutron asymmetries η_Z and η_N, respectively. The relative distance between the centres of the colliding nuclei is denoted as R. $\beta_{1,2}$ stand for the colliding nuclei deformation parameters from spherical shape, and the surface separation between them is denoted by s. The variables $\varphi_{1,2}$ represent the orientation of the projectile and target

nuclei's principal axes relative to the line connecting their centres. ϑ describes the orientation of the projectile and target to each other. These degrees of freedom are chosen to allow the description of the dynamics, including deep inelastic scattering and quasi-fission (in Eq. (2.74) in low-energy heavy ion collisions [49, 117].

The coupled Langevin-type equations (Eq.(2.74)) to describe the dynamics are given as [61, 116]:

$$\begin{aligned} \frac{dP_i}{dt} &= -\frac{\partial U}{\partial Q_i} - \sum_{j,k} \frac{1}{2} \frac{\partial}{\partial Q_i} (m^{-1})_{ij} P_j P_k - \sum_{j,k} \gamma_{ij} (m^{-1})_{jk} P_k + \sum_j g_{ij} \Gamma_j(t), \\ \frac{dQ_i}{dt} &= \sum_j (m^{-1})_{ij} P_j. \end{aligned} \tag{2.74}$$

The strength of the random force g_{ij} is connected to the friction coefficient γ_{ij} via the Einstein relation:

$$\sum_k g_{ik} g_{jk} = T \gamma_{ij}, \tag{2.75}$$

which ensures that the system adheres to the fluctuation-dissipation theorem [61, 116]. U is the potential that governs the dynamics while $\gamma_{ij}(m^{-1})_{jk}P_k$ is the frictional force or torque responsible for the dissipation in the dynamics, with γ_{ij} being the friction coefficient matrix. $g_{ij}\Gamma_j(t)$ is the Gaussian random force or torque, which is statistically characterized by its moments:

$$\langle \Gamma_j(t) \rangle = 0 \quad \text{and} \quad \langle \Gamma_j(t) \Gamma_j(t') \rangle = 2\delta_{ij}(t - t'). \tag{2.76}$$

This implies that the force or torque has a zero-average value, ensuring no net force or torque over time. The Kronecker delta δ_{ij} indicates that different components of the force are uncorrelated, and the Dirac delta $\delta(t - t')$ ensures that the force values are uncorrelated at different times. Although this is a comprehensive attempt to explain the reaction dynamics, the approach is computationally resource-intensive. Alternative approaches using a single effective collective variable solved analytically for a quadratic potential have also been considered [48, 52, 64] and provide key insights into describing the dynamic.

In this work, we will use the one-dimensional Langevin-type equation [52, 61]:

$$\frac{d^2 s}{dt^2} + \beta \frac{ds}{dt} - \omega^2 s = r(t), \tag{2.77}$$

with the surface separation s serving as the effective collective variable and solved for a parabolic barrier: $V(s) = -\frac{\mu\omega^2 s^2}{2}$ as illustrated by Fig. 2.23. μ and ω are the reduced mass of the colliding nuclei and angular frequency of the parabolic barrier, respectively. β is the reduced friction, and $r(t)$ is the Gaussian random force characterised by its first and second moments:

$$\langle r(t) \rangle = 0 \quad \text{and} \quad \langle r(t) r(t') \rangle = \frac{2\beta\mathcal{T}}{\mu} \delta(t - t'), \tag{2.78}$$

respectively. Here $\mathcal{T}$ is the temperature of the di-nuclei. However, in a large dissipative environment, the friction term dominates and the impact of the inertia term ($\frac{d^2 s}{dt^2}$) is

neglected. This is called the strong friction limit or the Smoluchowsky equation [116]. This assumption forms the basis of the Fusion-by-Diffusion modelling of the formation probability [48, 64, 68].

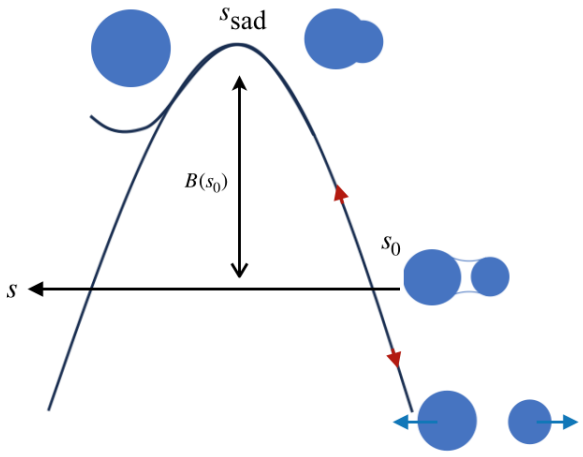

Figure 2.23: Illustration of the shape evolution along the one-dimensional parabolic potential energy landscape around the fusion saddle. Here, s represents the collective variable (surface separation) and its initial condition, denoted as s_0. The system evolves towards the top of the inner barrier height (into a spherical shape), causing the value of s to decrease from its initial condition s_0. $B(s_0) = \frac{\mu\omega^2(s_0-s_{sad})^2}{2}$ is the inner barrier height with respect to the fusion saddle s_{sad} and the s_0. Conversely, the system is evolving such that s increases relative to the initial condition s_0 may signify re-separation (quasi-fission). The angular frequency of the potential barrier is $\omega = \sqrt{\frac{\partial^2 V(s)}{\mu \partial s^2}}|_{s=s_{sad}}$, and μ stands for the reduced mass of the composite nuclei.

2.4.1 Formation probability in 1D Overdamped Langevin Systems

In the context of highly dissipative nuclear dynamics, where the friction coefficient is much larger than the inertia term, i.e., $\left|\frac{d^2s}{dt^2}\right| \ll \left|\beta\frac{ds}{dt}\right|$, the Langevin equation describing the system's evolution into a spherical shape is written as,

$$\beta\frac{ds}{dt} - \omega^2\,(s - s_{sad}) = r(t). \tag{2.79}$$

The first and second moments of the random force (r) are given as:

$$\langle r(t)\rangle = 0 \quad \text{and} \quad \langle r(t)r(t')\rangle = \frac{2\beta\mathcal{T}}{\mu}\delta(t-t'). \tag{2.80}$$

At the overdamped limit, the remaining kinetic energy at the capture event is converted into internal degrees of freedom. Fluctuations in the shape degrees of freedom of the nucleus due to temperature are solely responsible for the transition from di-nuclei into a spherical shape [34, 48].

Eq. (2.79) provides analytical insight into the fusion hindrance dynamics around the fusion saddle. The solution can be obtained by applying the Laplace transform to both sides of

the equation:

$$\begin{aligned} \mathcal{L}\left\{\beta\frac{ds}{dt} - \omega^2\left(s - s_{\text{sad}}\right)\right\} &= \mathcal{L}\{r(t)\}, \\ S(\sigma) &= \frac{\beta s_0 - \omega^2 s_{\text{sad}}}{\beta\sigma - \omega^2} + \frac{\mathcal{L}\{r(t)\}}{\beta\sigma - \omega^2}, \end{aligned} \tag{2.81}$$

where $s(0) = s_0$, and σ denotes the Laplace domain variable. The Laplace technique transforms the original differential equation into an equivalent algebraic expression Eq. (2.81), which makes it easier to solve. The solution in the time domain is then obtained by taking the inverse Laplace transform:

$$\begin{aligned} s(t) &= \mathcal{L}^{-1}\{S(\sigma)\}, \\ &= (s_0 - s_{\text{sad}})e^{-\frac{\omega^2}{\beta}t} + s_{\text{sad}} + \frac{1}{\beta}\int_0^t r(\tau)e^{-\frac{\omega^2}{\beta}(t-\tau)}d\tau. \end{aligned} \tag{2.82}$$

If one assumes a symmetric barrier around the fusion saddle, and $s_{\text{sad}} < s_0$, the probability at a given time for a nucleus with an initial surface s_0 to diffuse over the fusion saddle with s_{sad} into a spherical shape is approximated as:

$$\begin{aligned} P_{\text{CN}}(t, s_0) &= \int_{-\infty}^{s_{\text{sad}}} \frac{1}{\sqrt{2\pi}\sigma_s}\exp\left(-\frac{(s - \langle s(t)\rangle)^2}{2\sigma_s^2}\right) ds, \\ &= \int_{-\infty}^{\frac{s_{\text{sad}} - \langle s(t)\rangle}{\sqrt{2}\sigma_s}} \frac{1}{\sqrt{\pi}}\exp\left(-w^2\right) dw. \end{aligned} \tag{2.83}$$

Here, the substitution $w = \frac{s - \langle s(t)\rangle}{\sqrt{2}\sigma_s}$ has been made to transform the integral into a standard Gaussian form. The Gaussian integral, with the limit from $-\infty$ to $\frac{s_{\text{sad}} - \langle s(t)\rangle}{\sqrt{2}\sigma_s}$, simplifies to a complementary error function:

$$P_{\text{CN}}(t, s_0) = \frac{1}{2}\text{erfc}\left(\frac{-\left(s_{\text{sad}} - \langle s(t)\rangle\right)}{\sqrt{2}\sigma_s}\right). \tag{2.84}$$

What remains is to evaluate the average trajectory $\langle s(t)\rangle$ and the standard deviation $\sigma_s(t)$ along the trajectory. The average trajectory is determined as,

$$\langle s(t)\rangle = (s_0 - s_{\text{sad}})e^{\frac{\omega^2}{\beta}t}, \tag{2.85}$$

since the mean value of the random force is 0. The standard deviation of the fluctuations around the mean trajectory, denoted by $\sigma_s(t)$, is obtained as follows:

$$\begin{aligned} \sigma_s^2(t) &= \langle(s(t) - \langle s(t)\rangle)^2\rangle, \\ &= \int_0^t\int_0^t \langle r(\tau)r(\tau')\rangle e^{\frac{\omega^2(2t-\tau-\tau')}{\beta}} d\tau d\tau', \\ &= \frac{\mathcal{T}}{\mu\omega^2}\left(e^{\frac{2\omega^2 t}{\beta}} - 1\right). \end{aligned} \tag{2.86}$$

The double integral takes into account the autocorrelation of the random force $r(t)$, which is a function of two time variables τ and τ'.

In the scenario over an extended period, the probability of di-nuclei diffusing into a compound nucleus becomes:

$$P_{\mathrm{CN}}(t \to \infty, s_0) = \begin{cases} \frac{1}{2}\mathrm{erfc}\left(\sqrt{\frac{\mathcal{B}(s_0)}{\mathcal{T}}}\right) & \text{if } s_0 \geq s_{\mathrm{sad}}, \\ \frac{1}{2}\mathrm{erfc}\left(-\sqrt{\frac{\mathcal{B}(s_0)}{\mathcal{T}}}\right) & \text{if } s_0 \leq s_{\mathrm{sad}}. \end{cases} \tag{2.87}$$

The compound nucleus formation probability is evaluated within the Fusion-by-Diffusion (FbD) model, using Eq. (2.87) [48, 118]. The inner barrier $\mathcal{B}(s_0)$ and the initial conditions s_0 are determined based on a realistic approximation of the potential energy surface, achieved through nuclear shape parameterization on a liquid-drop type potential energy surface [48, 118], which are presented in the Section 2.4.2 below.

2.4.2 The Potential Deformation Energy Surface

The parameterisation of the deformation potential energy landscape, initially presented in Ref. [48] and later refined in Ref. [34], is restated here for completeness. The deformation energy surface is a liquid drop type potential energy surface of two colliding nuclei with radii R_1, and R_2 joined smoothly by a portion of a spheroid or hyperboloid (as illustrated in Fig. 2.24). The deformation energy surface, expressed in the unit of surface energy (E_{surf}) is denoted as ξ:

$$\xi = \frac{E_{\mathrm{def}}}{E_{\mathrm{surf}}}. \tag{2.88}$$

The ξ is evaluated following the quadratic expressions:

$$\xi = \begin{cases} a + b\left(\frac{s}{R}\right) + c\left(\frac{s}{R}\right)^2 & s \geq 0, \\ p\left(\frac{s}{R}\right) - \sigma_0)^2 - q\left(\left(\frac{s}{R}\right) - \sigma_0\right)^3 & s < 0, \end{cases} \tag{2.89}$$

depending on whether the colliding nuclei are separated ($s \geq 0$) or overlapping ($s < 0$) at the point of capture. R is the radius of the compound nucleus. The deformation energy (E_{def}) at any given surface separation (s) is evaluated as

$$E_{\mathrm{def}} = \xi \times E_{\mathrm{surf}}. \tag{2.90}$$

The surface energy E_{surf} is taken as [48]:

$$E_{\mathrm{surf}} = 17.9439\left(1 - 1.7826\left(\frac{N_{\mathrm{CN}} - Z_{\mathrm{CN}}}{A_{\mathrm{CN}}}\right)^2\right) A_{\mathrm{CN}}^{\frac{2}{3}}, \tag{2.91}$$

where, A_{CN}, N_{CN} and Z_{CN} are the mass, neutron and proton numbers of the combined system. The surface separation (s) is the distance between the surfaces of the colliding nuclei at capture. This is illustrated by Fig. 2.24, where s is related to the total length (L) of the di-nuclei system and the radii R_1 and R_2 of the individual colliding nuclei:

$$s = L - 2(R_1 + R_2). \tag{2.92}$$

The parameter σ_0 in Eq. (2.89) represents the ratio of spherical limit surface separation distance to the radius of the compound nucleus:

$$\sigma_0 = 2 - \frac{4}{(2+6\mathcal{D})^{\frac{1}{3}}}, \tag{2.93}$$

where, $\mathcal{D} = \Delta^2$. Δ is the mass asymmetry parameter of the colliding nuclei:

$$\Delta = \frac{|A_1 - A_2|}{A_1 + A_2}. \tag{2.94}$$

A_1 and A_2 are the masses of the colliding nuclei. The coefficients a, b, c, p and q of Eq. (2.89) are defined by Eqs. (2.95) to (2.97), which are optimised in the interval $0.85 < x < 1.05$ and $-0.25 < \Delta < 0.25$, of nuclear fissility (x) and mass asymmetry (Δ), respectively. The coefficients are given as follows:

$$a = \alpha_1 + \alpha_2(1-x) + \alpha_3(1-x)^2, \tag{2.95}$$
$$b = \beta_1 + \beta_2(1-x) + \beta_3(1-x)^2, \tag{2.96}$$
$$c = \gamma_1 + \gamma_2(1-x) + \gamma_3(1-x)^2, \tag{2.97}$$
$$p = \frac{b}{\sigma_0} + \frac{3a}{\sigma_0^2}, \tag{2.98}$$
$$q = \frac{-b}{\sigma_0^2} - \frac{2a}{\sigma_0^3}. \tag{2.99}$$

The nuclear fissility parameter (x), which is a measure of the ratio of the nuclear electrostatic energy to twice the liquid drop surface potential energy, is taken as [48]:

$$x = \frac{Z_{\mathrm{CN}}^2}{50.883 A_{\mathrm{CN}} \left(1 - 1.7826 \left(\frac{N_{\mathrm{CN}} - Z_{\mathrm{CN}}}{A_{\mathrm{CN}}}\right)^2\right)}. \tag{2.100}$$

The parameters $\alpha_{i=1-3}$, $\beta_{i=1-3}$, and $\gamma_{i=1-3}$ as used in Eqs. (2.95) to (2.97) are given as:

$$\alpha_1 = -0.00564 - 0.01936\exp(-\mathcal{D}/0.02240), \tag{2.101}$$
$$\alpha_2 = 0.05122 + 0.11931\exp(-\mathcal{D}/0.03800), \tag{2.102}$$
$$\alpha_3 = -0.07424 + 0.95959\mathcal{D}, \tag{2.103}$$
$$\beta_1 = -0.06080 + 1.37825D - 10.7077\mathcal{D}^2, \tag{2.104}$$
$$\beta_2 = 0.27691 - 2.93119\mathcal{D} + 12.60944\mathcal{D}^2, \tag{2.105}$$
$$\beta_3 = -0.02398 - 1.14854\mathcal{D}, \tag{2.106}$$
$$\gamma_1 = -0.02722 + 0.2231\mathcal{D}, \tag{2.107}$$
$$\gamma_2 = 0.02050 + 0.32122\mathcal{D}, \tag{2.108}$$
$$\gamma_3 = 0.03843 + 1.03731\mathcal{D}. \tag{2.109}$$

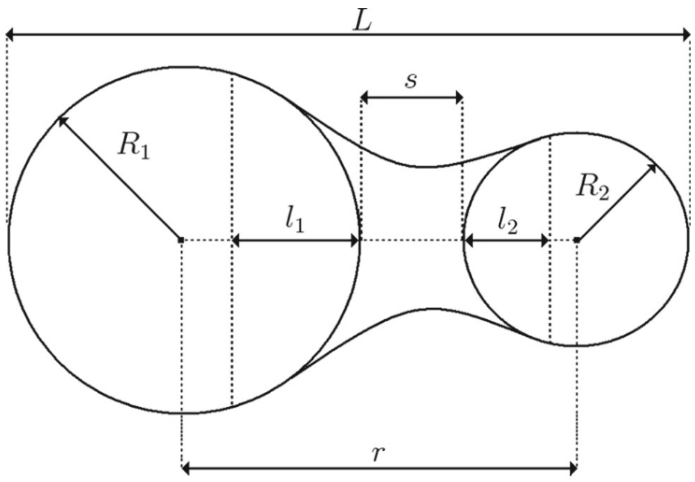

Figure 2.24: Shape parameterisation of di-nuclear system with the radii R_1 and R_2 respectively at capture. s is the surface separation between the colliding nuclei and L is the total length, whereas, l_1 and l_2 are the degree of opening of the neck. The figure is reproduced from [68, 119].

2.4.2.1 Example of Deformation Potential Energy Surface

Fig. 2.25 illustrates examples of the deformation potential energy surfaces (E_{def}) in 1D for reactions leading to the synthesis of super-heavy elements using cold fusion reactions. The E_{def} is calculated using Eq. (2.89) for the projectile-target combinations of ^{50}Ti, ^{58}Fe, and ^{70}Zn on ^{208}Pb leading to the synthesis of nuclei with atomic numbers equal to Z_{CN}=104, Z_{CN}=108, and Z_{CN}=112, without the inclusion of the rotational energies ($\ell = 0$). This is evaluated for a fixed asymmetry parameter (Δ) given by Eq. (2.94).

E_{def} in Eq. (2.89) as illustrated by Fig. 2.25 is calculated using arbitrary values of surface separation (s) within the interval -10 fm $\leq s \leq 6$ fm. This range of s is chosen just for the purpose of visualizing the E_{def} landscape. The red dots indicate each reaction's asymmetric fusion saddle point, while the corresponding s_{sad} values denote surface separation at the fusion saddle (negative value means a compact mononuclear configuration). In this context, a fusion saddle refers to the maximum deformation energy along the asymmetric valley that the merging nuclei must overcome to attain a compound nucleus configuration.

Beyond the fusion saddle is the spherical limit (labelled 'sphere' in the figure), where the spherical configuration is reached, and E_{def} values converge for all projectile and target nuclei combinations. The vertical red dashed line at $s = 0$ fm indicates the points of hard contact between the colliding nuclei. The further the saddle point is from the point of hard contact, the more hindered the fusion process becomes, which correlates with progressively increasing compound nucleus charges (Z_{CN}). As the atomic number Z_{CN} of the projectile-target combination increases: Z_{CN} = 104, 108, and 112, the Coulomb repulsion between the positively charged protons also increases, and so is the fissility parameter, x =0.88, 0.92 and 0.95, respectively. It has been well established that a compound nucleus formation probability decreases with a fissility parameter greater than 0.7 [48].

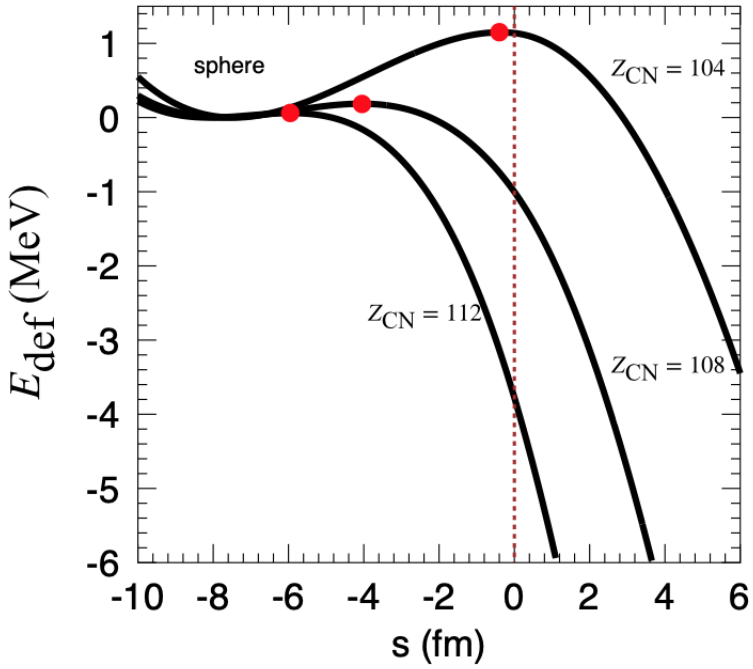

Figure 2.25: The deformation 1D potential energy surfaces for ^{50}Ti + ^{208}Pb, ^{58}Fe + ^{208}Pb and ^{70}Fe + ^{208}Pb which corresponds to Z_{CN} = 104, 108 and 112, respectively. The red dots show the positions of the fusion saddles, whereas the dashed vertical line represent the point of hard contact, s = 0 fm.

Similarly, Fig. 2.26 illustrates E_{def} for $\ell = 0$ calculated for hot fusion reactions. In this case, Δ is not frozen. It takes values as calculated for the asymmetric path and 0 in case of full symmetrical path. This is because di-nucler shape attains a more compact shape at the fusion saddle in hot fusion reactions than in cold fusion. Consequently, a symmetric saddle configuration dominates over the asymmetric one as the system elongation decreases. Therefore, the deformation energy of the symmetric saddle is evaluated as follows:

$$E_{def}^{sym} = E_{def}\left(s_{sad}^{sym}\right), \tag{2.110}$$

where E_{def} is given by Eq. (2.90) with $\Delta = 0$. s_{sad}^{sym} is the spherical limit of the surface separation parameter, given as

$$s_{sad}^{sym.} = \sigma_0 + 2\alpha_{sad}. \tag{2.111}$$

Here, α_{sad} is the effective deformation of the compound nucleus given by Eq. (2.59). These are evaluated using the shape variables β_2, β_4 and β_6 of the fission saddle. σ_0 is as defined by Eq. (2.93) above.

The Fig. 2.26 illustrates an example of E_{def} for hot a fusion reaction, ^{48}Ca + ^{243}Am, as an example. The solid line depicts the asymmetric deformation energy path, whereas the corresponding symmetric path is denoted by the black dotted line. The asymmetric saddle is denoted by the red dot beyond the spherical limit. Consequently, the E_{def} of the fusion saddle is determined using the prescription in Eqs. (2.111) and (2.110) denoted by the

green dot on the symmetric deformation energy path. The point of hard contact $s = 0$ fm is shown by a black point. Now that we have expressed the formalism for obtaining the E_{def} and its saddle values, we will proceed with the discussion of inner barrier evaluation.

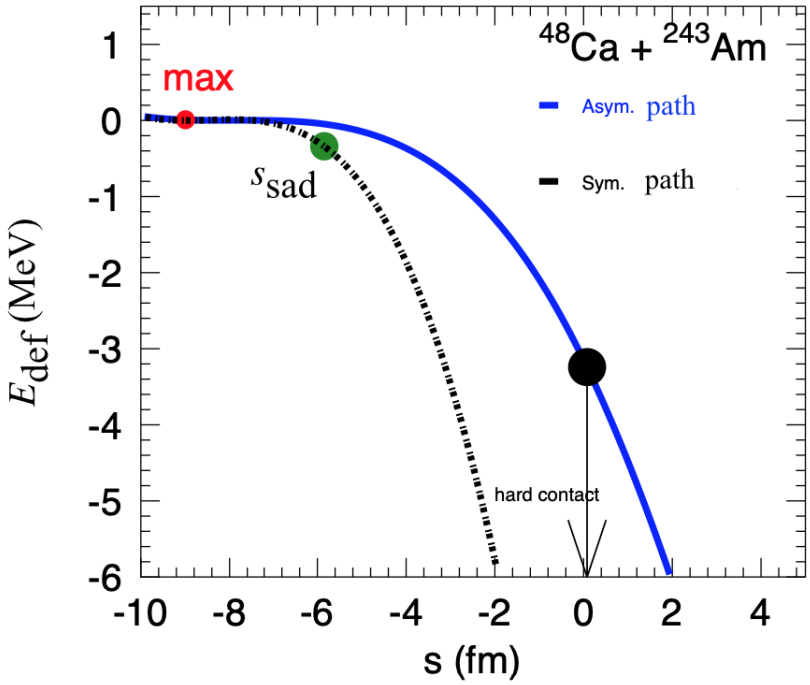

Figure 2.26: Deformation potential energy surface for ^{291}Mc along the symmetric fission path (black dotted line) and the asymmetric fission path (blue solid line). The green point denotes the fusion saddle. The red dot depicts the maximum of the asymmetric path. The black point is the point of hard contact.

2.4.2.2 The Inner Barrier ($\mathcal{B}$)

The height of the inner barrier $\mathcal{B}$ opposing fusion is evaluated as the difference between the deformation potential energy at the fusion saddle, $E^{\text{sad}}_{\text{def}}$, and that of the injection point, $E^{\text{inj}}_{\text{def}}$. The injection point corresponds to the initial configuration of the colliding nuclei. The inner barrier is given as

$$\mathcal{B} = (E^{\text{sad}}_{\text{def}} + E^{\text{sad}}_{\text{rot}}) - (E^{\text{inj}}_{\text{def}} + E^{\text{inj}}_{\text{rot}}) = E^{\text{sad}}_{\text{def}} - E^{\text{inj}}_{\text{def}} + \frac{\hbar^2 \ell\,(\ell+1)}{2}\left(\frac{1}{\mathcal{I}_{\text{sad}}} - \frac{1}{\mathcal{I}_{\text{inj}}}\right), \quad (2.112)$$

where $E^{\text{sad}}_{\text{rot}}$ and $E^{\text{inj}}_{\text{rot}}$ are the rotational energies at the fusion saddle and the injection points, respectively. The $\mathcal{I}_{\text{sad}}$ and $\mathcal{I}_{\text{inj}}$ are the moments of inertial at the saddle and the injection point, respectively. The inner barrier is formed entirely due to the differences in the macroscopic and rotational energies. To calculate the rotational energy at the injection point ($E^{\text{inj}}_{\text{def}}$), we adopt the rigid body moments of inertia [34]:

$$\mathcal{I}_{\text{inj}} = \mu r^2_{\text{inj}} + \frac{2}{5}M_1R_1^2 + \frac{2}{5}M_2R_2^2. \quad (2.113)$$

Here, $r_{\text{inj}} = s_{\text{inj}} + R_1 + R_2$, and R_1 and R_2 are the individual radii of the projectile and the target nuclei. M_1 and M_2 correspond to the masses of the projectile and the target

nuclei, respectively. s_{inj} represents the surface separation between the colliding nuclei at the injection point. Within the model, the rotational energy of the fusion saddle ($E_{\text{rot}}^{\text{sad}}$) for the cold fusion reaction is determined using Eq. (2.113). Conversely, for hot fusion reactions, the moment of inertia at the fusion saddle is calculated assuming an ellipsoidal mono-nuclear configuration, as defined in Eq. (2.71) [34], using deformation parameters from [69]. This completes the formalism necessary to compute the inner barrier within the Fusion-by-Diffusion model.

2.4.2.3 Evaluation of the Temperature

The temperature $\mathcal{T}$ in Eq. (2.87) is the geometric mean of the temperatures at the injection point ($\mathcal{T}_{\text{inj}}$) and the saddle point ($\mathcal{T}_{\text{sad}}$):

$$\mathcal{T} = \sqrt{\mathcal{T}_{\text{sad}} \times \mathcal{T}_{\text{inj}}}, \tag{2.114}$$

where the temperatures at the injection and the saddle points are calculated as follows:

$$\mathcal{T}_{\text{sad}} = \sqrt{\frac{E^* - E_{\text{def}}^{\text{sad}} - E_{\text{rot}}^{\text{sad}}}{a}}, \tag{2.115}$$

and

$$\mathcal{T}_{\text{inj}} = \sqrt{\frac{E^* - E_{\text{def}}^{\text{inj}} - E_{\text{rot}}^{\text{inj}}}{a}}, \tag{2.116}$$

respectively. Here, $E_{\text{rot}}^{\text{sad}}$ and $E_{\text{rot}}^{\text{inj}}$ are the rotational energies at the saddle and injection points, respectively. The level density parameter is approximated as $a = \frac{A}{8.5}$ MeV^{-1}, where A is the mass number of the compound nucleus. E^* corresponds to the excitation energy of the compound nucleus.

2.4.2.4 Test Case

This section details the formation probability calculations as described in the previous sections. The first step is to evaluate the deformation potential energy surface (E_{def}), from which the inner barrier and the temperature are determined. For the test case, these parameters are plotted as a function of separation distance. The curve labelled Z_{CN} = 108 in Fig. 2.25 illustrates the driving potential energy surface (E_{def}) for the ^{58}Fe + ^{208}Pb reaction without the rotational energies. From the deformation potential energy surface of Fig. 2.25, the corresponding inner barrier $\mathcal{B}$ is evaluated with respect to the fusion saddle (s_{sad}) as shown in the panel (a) of Fig. 2.27. As expected, the larger the initial surface separation, the higher the inner barrier. This increase in inner barrier height with initial surface separation translates into a decreasing formation probability, as shown in panel (b) of Fig. 2.27. A special case is the injection exactly at the fusion barrier position, then $\mathcal{B}$=0, and the probability equals to 0.5 and it does not depend on temperature.

The black, blue, and red lines in panel (b) of Fig. 2.27 represent calculations for geometric average temperatures of 0.8 MeV, 1.3 MeV, and 1.8 MeV, respectively. The impact of

temperature on formation probability depends on where the system is initially injected on the E_{def} relative to the fusion saddle. For injections to the right of the fusion saddle the system has to climb uphill over the fusion saddle, and then higher temperatures increase the formation probability. However, for systems that are already "injected" or positioned behind the barrier, lower temperatures are more favourable. This is because higher temperatures increase thermal fluctuations, making it more likely for the system to escape over the barrier which decreases the probability of fusion.

According to Eqs. (2.112) and (2.114), the inner barrier and the temperature are readily evaluated provided the injection point distance is known. Hence, for a given system, we need to evaluate the injection point distance to predict the compound nucleus formation probability. Therefore, it remains an adjustable parameter in the model and has to be evaluated using the existing experimental data. Attempts [81, 82, 82] have been made to explain the physics behind it, and subsequently, phenomenological models are made to predict it. See Section 2.5 for further details.

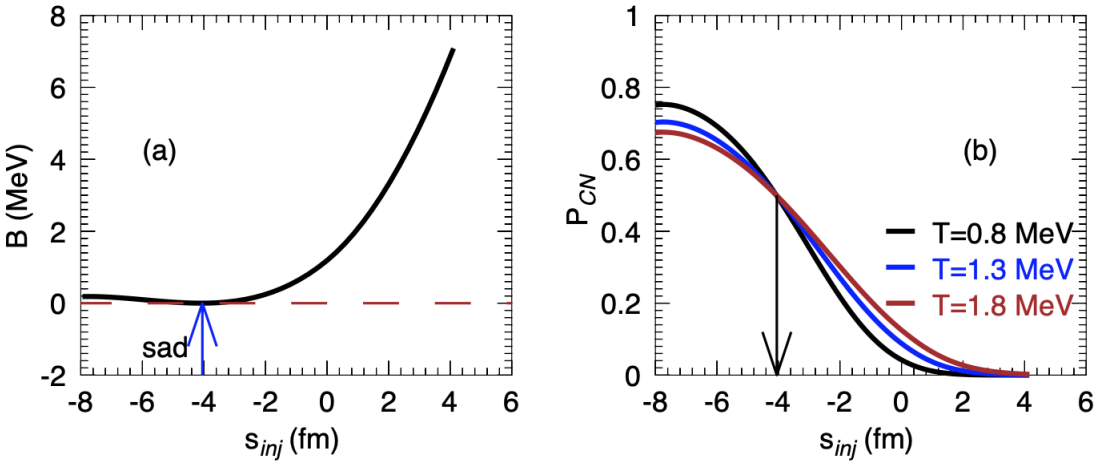

Figure 2.27: Inner barrier height for the ^{58}Fe + ^{208}Pb reaction as a function of initial surface separation calculated without rotational energies. (b) Formation probability for the same reaction as a function of initial surface separation is shown for three different temperatures.

2.4.2.5 Phenomenologically Deduced Injection Point Distances ($s^{\mathbf{d}}_{\mathbf{inj}}$)

Modelling and subsequent optimisation of fitting parameters inherently require comparison with experimental data. In this particular case, the model's injection point distance parameter s_{inj} is determined by fitting the theoretical production cross sections (Eq. (2.2)) to the experimental excitation functions. This approach is necessary because the formation probability is not directly measured quantity, making the production cross section a suitable choice.

As previously mentioned, the theoretical production cross section is the product of capture cross section, formation, and survival probabilities. If the ground state and fission saddle properties are well-defined, then the capture cross section and survival probability could be determined, leaving the formation probability as the sole remaining unknown. Therefore, by tuning the s_{inj} to reproduce the experimental data, one can obtain an insight into the

formation step. This highlights the relevance of the s_{inj} parameter as the key parameter that can also compensate for any deficiencies in the overall modelling of the residue production cross section.

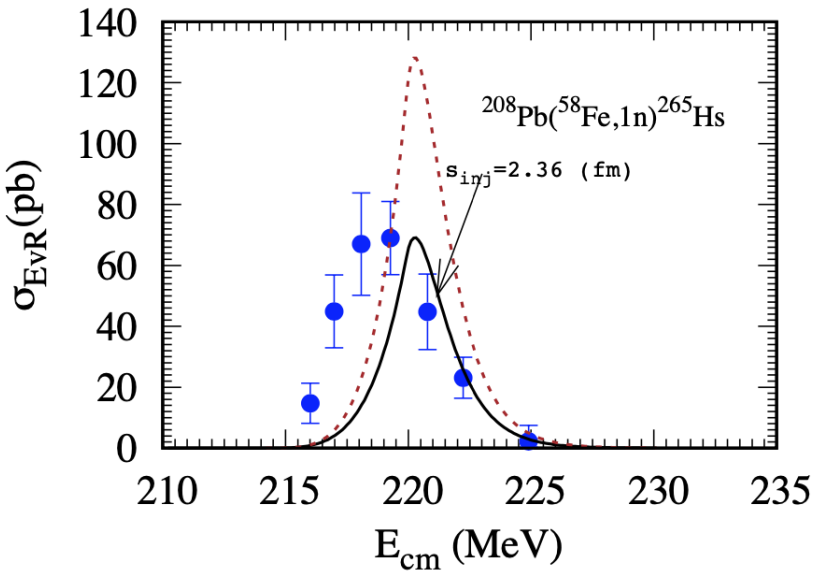

Figure 2.28: Production cross section of ^{265}Hs. Blue dots represent experimental data [120], and the solid black line depicts the theoretical fit (with $s_{\text{inj}} = 2.36$ fm) without Kramers-Strutinsky and the collective enhancement of the level density (Eq. (2.2)). The red dashed line shows the calculated cross section incorporating Kramers-Strutinsky corrections and collective enhancement of the intrinsic level density evaluated with $s_{\text{inj}} = 2.36$ fm. The reduced friction of the Kramers correction is taken 3×10^{21} s^{-1} and the shell damping energy E_{d} taken consistent with Eq. (2.61).

Fig. 2.28 illustrates the comparison between the theoretical model given in Eq. (2.2) (black solid line) and experimental data (blue dotted lines) for the excitation function. This is evaluated without Kramers-Strutinsky corrections and collective enhancement of the level density. The goal is to adjust the theoretical simulation (black solid line) via the s_{inj} to reproduce the maximum of the experimental excitation function (blue points). In this case, the optimum s_{inj} value is 2.36 fm, representing the relative distance between colliding nuclei after capture. Henceforth, we will refer to this phenomenologically deduced injection point distance as $s^{\text{d}}_{\text{inj}}$. In this analysis, the uncertainties associated with the maximum production cross section are not considered. While the overall shape of the cross section is reproduced, the theoretical optimum production energy is shifted to 1.2 MeV higher than the experiment.

If one matches the statistical survival probability to the dynamical limit by incorporating the Kramers-Strutinsky factor and the collective enhancement of the intrinsic level density (as shown by the red dashes in Fig. 2.28), the production cross section increases by a factor of 1.85. To recover the original fit, the $s^{\text{d}}_{\text{inj}}$ parameter must be increased by approximately 8.5%. The viscosity parameter β is taken as 3×10^{21} s^{-1}. Since the fission decay width decreases with increasing β (see Fig. 2.17), one would expect the theoretical cross section to increase with β implying that s_{inj} increases with β. However, as s_{inj} serves as an umbrella parameter that accounts for any deficiencies in the model, we will henceforth omit the

impact of the Kramers-Strutinsky factor and collective enhancement of the intrinsic level density in the fit procedure.

Similarly, for hot fusion reactions, where multiple neutrons are emitted, the theoretical simulations are adjusted by tuning the s_{inj} parameter to reproduce the maximum of each channel's excitation functions. Fig. 2.29 exemplifies how $s^{\mathrm{d}}_{\mathrm{inj}}$ is adjusted to match the experimental production cross sections of the 2n, 3n, and 4n channels reaction in ^{48}Ca+^{243} Am (shown as blue dots), respectively. The obtained $s^{\mathrm{d}}_{\mathrm{inj}}$ values are 3.7 fm, 1.2 fm, and 0.05 fm, respectively. In the 2n channel, there is only one experimental point, and the 3.7 fm serves as a lower limit. It is also important to note that the typical energy accuracy of experimental data is ±2 MeV or more due to the usage of thick targets. The energy uncertainties are not shown in the figure.

The decreasing tendency of the injection point distance with energy can be studied by deducing the $s^{\mathrm{d}}_{\mathrm{inj}}$ for each xn peak. The decreasing $s^{\mathrm{d}}_{\mathrm{inj}}$ tendency indicates increasing formation probability with increasing beam energy. This effectively leads to an increase in the fusion cross section, compensating for the typical decreasing tendencies in the survival probability along the cascade, as shown in Fig. 2.16.

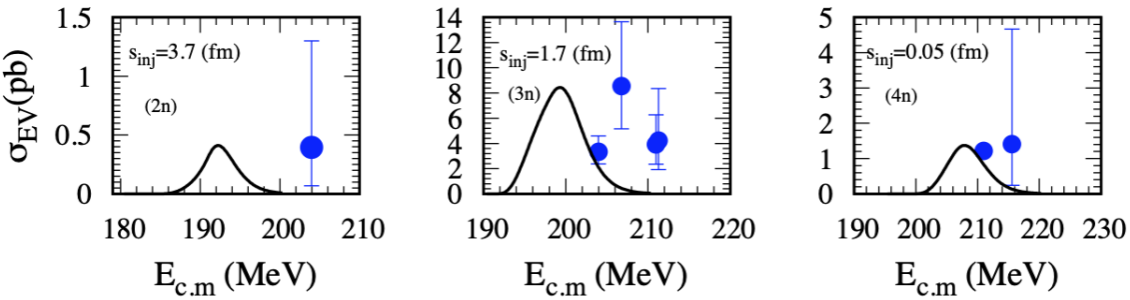

Figure 2.29: Production cross sections for ^{289}Mc, ^{288}Mc, and ^{287}Mc in the ^{48}Ca +^{243} Am reaction. Experimental data are shown as blue dots, while the solid lines represent theoretical calculations. The panels (2n), (3n), and (4n) correspond to each channel's excitation function. The $s^{\mathrm{d}}_{\mathrm{inj}}$ values used for each fit are indicated on the graph. The experimental data are taken from Ref. [33]. The figure does not show the energy uncertainties in the experimental data (±2 MeV).

In conclusion, one should expect some variations in the deduced $s^{\mathrm{d}}_{\mathrm{inj}}$ values due to the input parameters used in the theoretical simulation, such as the nuclear ground states and the fission saddle point properties. Since most of these parameters are unknown experimentally, uncertainties in the simulated theoretical excitation functions are inevitable. For instance, a 1 MeV change in the fission barrier induces a change of one to two orders of magnitude in the production cross section [73]. Therefore, if the change in the fission barrier leads to an increased cross section, the $s^{\mathrm{d}}_{\mathrm{inj}}$ value will be increased in the fit procedure, and vice versa. Additionally, averaging the theoretical calculations over the target thickness can affect the production cross section. This is due to the projectile's energy loss within the target, which tends to decrease the cross section.

2.5 Parameterisation of Injection Point Distance (s_{inj})

It is apparent from the previous sections that one needs to parameterise the injection point distance to make predictions related to the synthesis of super-heavy elements in the FbD model. We will begin this section by presenting the default method used in the FbD model, which is referred to as the linear approach ($s^{\mathcal{L}}_{inj}$).

2.5.1 Linear Approach ($s^{\mathcal{L}}_{inj}$)

In the linear approach, the injection distance ($s^{\mathcal{L}}_{inj}$) is modelled as a linear function of the excess energy in the centre of the mass frame above the Coulomb barrier ($E_{cm} - B_0$). B_0 is the mean entrance channel barrier for the colliding nuclei, as given in Eq. (2.21). The injection point distance function is given as:

$$s^{\mathcal{L}}_{inj} = \alpha \times (E_{cm} - B_0) + \beta_0, \tag{2.117}$$

where α and β_0 are the coefficients which are determined by fitting to a set of phenomenologically deduced injection point distances (s^{d}_{inj}) obtained using methods described in the previous chapter.

The panel (a) of Fig. 2.30 illustrates the s^{d}_{inj} values obtained for a set of 1n cold fusion reactions. The different colours of the points denote the laboratories where the excitation functions were measured: red for LBNL, black for GSI, and blue for RIKEN. The regression line of the fit on the cold fusion is given as:

$$s^{cold}_{inj} = 0.878\,\text{fm} - 0.294 \times (E_{cm} - B_0)\ \text{fm/MeV}. \tag{2.118}$$

A similar trend was observed for hot fusion reactions using ^{48}Ca on actinide targets ranging from ^{242}Pu to ^{249}Cf [68] as shown in Fig. 2.30. Here, the line of best of fit is given by:

$$s^{hot}_{inj} = 3.291\,\text{fm} - 0.196 \times (E_{cm} - B_0)\ \text{fm/MeV}. \tag{2.119}$$

Given the subtle differences between the FbD and Kewpie2 survival probabilities, the parameterised injection distances cannot simply be applied in Kewpie2. Therefore, our initial attempt is to obtain parameterisations for the same reaction data sets using Kewpie2 formalism.

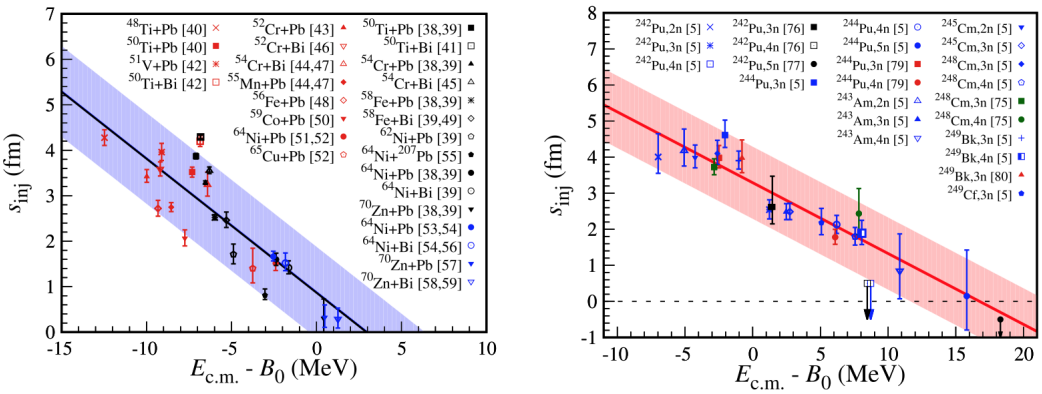

Figure 2.30: Systematics of injection point distance s_{inj}. The points show the deduced values of s_{inj}, while the solid lines represent the linear fits to these data points. The shaded region highlights ±1 fm corridor of the s_{inj}, which is determined from careful examination of the experimental data [68]. Panel (a) shows the data for 1n excitation functions measured for the cold fusion reactions using projectile-target combinations as shown on the graph. Panel (b) shows calcium-48 induced hot fusion reactions with multiple neutron emission channels. The figure from Ref. [68] contains references for the specified reactions listed therein.

2.5.2 Optimising Injection Distance Model Coefficients with Kewpie2

To optimise the coefficients of the injection distance model parameterisation in Eq. (2.117), we would adopt the same set of reactions used in the references provided in Fig. 2.30 for both cold and hot fusion reactions. The reactions used in the fit are listed in Tables 2.2 and 2.3, respectively. Here, we only focus on the one neutron emission channel for the cold fusion reactions. As we would see later, the model does not quite describe the multiple neutron emissions channels. Similarly, the set of Calcium-48 induced reactions is consistent with what is presented in panel (b) of Fig. 2.30. Since this is the first time the compound nucleus formation probability is evaluated within the Kewpie2, adopting a similar approach to the FbD [68] allows us to establish the accuracy of the fits.

To fit the coefficients α and β_0 of the injection distance function $s_{\text{inj}}^{\mathcal{L}}$, the variable $s_{\text{inj}}^{\text{d}}$ and $E_{\text{cm}} - B_0$ are taken as observation and the explanatory variables, respectively. These variables are evaluated using the Kewpie2 code for each reaction channel individually as described in the Subsection 2.4.2.5 with the following assumptions:

- The capture cross section is given by Eq. (2.5) and B_0 is given by Eq. (2.21).
- The survival probability is evaluated as described in Subsections 2.3 without the Kramers-Strutinsky and collective enhancement (KS-CE) factors and with $E_{\text{d}} = \frac{A^{\frac{1}{3}}}{0.423}$ [108] for the shell damping of the level density function. As already mentioned, the $s_{\text{inj}}^{\text{d}}$ depends on the value chosen for the reduced friction coefficient (β) in the Kramers corrective factor, which is arbitrarily chosen. Therefore, the KS-CE corrective factors are not considered in the fit.
- The formation probability is given by Eq. (2.87) where $s_{\text{inj}}^{\text{d}}$ is treated as an adjustable parameter.
- The E_{cm} energy taken is the energy at which the calculated excitation function has its

maximum. These settings of the Kewpie2 align closely with the FbD approach,

Table 2.2 presents data from cold fusion experiments conducted at GSI, LBNL, and RIKEN laboratories. It includes essential information on fusion reactions, such as the atomic numbers and masses of the projectile and target nuclei, the deduced injection distance, and the excess energy in the centre of the mass frame. The columns labelled Z_2 and A_2 represent the atomic number and mass number of the target nucleus, respectively, and that of the projectiles are denoted (Z_1 and A_1). The resulting compound nucleus from the fusion of the projectile and the targets are given denoted Z_{CN} and mass number A_{CN} by their charge and target, respectively.

The $E_{\mathrm{cm}} - B_0$ column provides the excess energy in the centre of the mass frame, calculated as the difference between the collision energy and the Coulomb barrier B_0. The $s^{\mathrm{d}}_{\mathrm{inj}}$ column presents the deduced injection distance, which refers to the effective surface separation between the projectile and target nuclei at the injection point. The table also shows the multiple neutron emission channels during the reaction.

Similarly, Table 2.3 presents hot fusion reaction data from experiments carried out at Dubna, TASCA, and LBNL laboratories, which were used in the fitting process. The **Ch** column indicates the neutron emission channels, where reactions such as 2n, 3n, 4n, or 5n signify the emission of multiple neutrons.

Table 2.2: Table of the cold fusion reaction data sets from GSI, LBNL, and RIKEN. s^{d}_{inj} fm and $E_{cm} - B_0$ MeV represent the deduced injection point distance and excess energy in the centre of mass frame, respectively. Column Refs. shows the references to the experimental data.

Z_1	A_1	Z_2	A_2	Z_{CN}	A_{CN}	Refs.	$E_{cm} - B_0$ (MeV)	s^{d}_{inj} (fm)
GSI								
1n channel								
22	50	82	208	104	258	[120]	-6.195	4.07
22	50	82	208	104	258	[120]	1.805	2.71
22	50	83	209	105	259	[121]	-6.731	4.05
22	50	83	209	105	259	[121]	1.269	3.93
24	54	82	208	106	262	[120]	-5.789	3.07
24	54	83	209	107	263	[122]	-6.024	3.23
24	54	82	208	106	262	[120]	2.211	2.56
24	54	83	209	107	263	[122]	2.976	2.64
26	58	82	208	108	266	[120]	-4.987	2.36
26	58	83	209	109	267	[120]	-4.917	2.08
28	62	82	208	110	270	[120]	-4.342	1.44
28	64	82	207	110	271	[123]	-1.956	0.93
28	64	82	208	110	272	[120]	-0.971	1.35
28	64	83	209	111	273	[124]	-1.198	0.89
2n channel								
22	50	83	209	105	259	[121]	1.269	3.93
22	50	82	208	104	258	[120]	1.805	2.71
24	54	83	209	107	263	[122]	2.976	2.64
24	54	82	208	106	262	[120]	2.211	2.56
26	58	82	208	108	266	[120]	4.013	1.78
3n channel								
22	50	83	209	105	259	[121]	6.269	3.51
22	50	82	208	104	258	[120]	7.805	1.50
24	54	82	208	106	262	[120]	10.211	2.10
LBNL								
1n channel								
22	50	82	208	104	258	[125]	-6.195	3.40
22	48	82	208	104	256	[125]	-11.34	4.35
24	52	82	208	106	260	[126]	-9.068	3.46
24	54	83	209	107	263	[122]	-6.024	2.87
25	55	82	208	107	263	[127]	-8.204	2.41
24	52	83	209	107	261	[128]	-8.796	3.28
26	56	82	208	108	266	[129]	-7.776	2.52
27	59	82	208	109	267	[130]	-7.536	1.67
28	64	82	208	110	272	[131]	-0.971	1.53
29	65	82	208	111	273	[132]	-3.460	0.89
23	51	82	208	105	259	[133]	-8.174	3.76
22	50	83	209	105	259	[133]	-6.731	3.95
2n channel								
22	50	83	209	105	259	[133]	1.269	4.47
22	50	82	208	104	258	[125]	1.805	2.51
22	48	82	208	104	256	[125]	-2.340	4.03
24	52	82	208	106	260	[128]	-1.068	3.43
24	54	83	209	107	263	[122]	2.976	2.27
25	55	82	208	107	263	[127]	0.796	2.27
23	51	82	208	105	259	[133]	-1.174	3.72
RIKEN								
1n channel								
28	64	82	208	110	272	[134]	-0.971	1.32
28	64	83	209	111	273	[135]	-1.198	0.91
30	70	82	208	112	278	[136]	1.004	0.57
30	70	83	209	113	279	[35, 137]	1.167	0.11

Table 2.3: Table of the hot fusion reaction data set with ^{48}Ca projectile from Dubna, Tasca, and LBNL. s^{d}_{inj} fm and $E_{cm} - B_0$ MeV represent the deduced injection point distance and excess energy in the centre of mass frame, respectively. Column Ch shows the reaction channel. Column Refs. list the references to experimental data.

Z_2	A_2	Z_{CN}	A_{CN}	Ch	Refs.	$E_{cm} - B_0$ (MeV)	s^{d}_{inj} (fm)
DUBNA							
94	242	114	290	3n	[138]	1.996	1.9
94	242	114	290	4n	[138]	9.996	-1.75
94	242	114	290	2n	[138]	-6.004	3.85
94	244	114	292	3n	[139]	-0.491	3.9
94	244	114	292	4n	[139]	7.509	1.3
94	244	114	292	5n	[139]	16.509	-1.05
95	243	115	291	2n	[140]	-4.078	3.7
95	243	115	291	3n	[140]	2.922	1.7
95	243	115	291	4n	[140]	10.922	0.05
96	245	116	293	2n	[141]	-3.511	3.6
96	245	116	293	3n	[141]	4.489	2.0
96	245	116	293	4n	[141]	12.489	0.75
96	248	116	296	3n	[142]	-0.507	3.3
96	248	116	296	4n	[142]	8.493	0.95
97	249	117	297	3n	[143]	0.096	3.05
97	249	117	297	4n	[143]	9.096	0.9
98	249	118	297	3n	[144]	6.832	1.8
TASCA							
94	244	114	292	3n	[145]	1.996	1.9
94	244	114	292	4n	[145]	9.996	-1.75
96	248	116	296	3n	[146]	7.509	1.3
96	248	116	296	4n	[146]	16.509	-1.05
97	249	117	297	3n	[147]	-0.491	3.9
LBNL							
94	242	114	290	3n	[148]	1.996	1.9
94	242	114	290	4n	[148]	9.996	-1.75

2.5.3 Fit Results

This section presents the results of the fit of the linear approach for the injection point distance (Eq. (2.117)) to the data obtained for cold and hot fusion reactions listed in the Tables 2.2. As indicated by Eq. (2.117), the goal is to determine the coefficients α and β_0 using the deduced injection point distance $s^{\mathrm{d}}_{\mathrm{inj}}$ as the response variable and the excess energy above the Coulomb barrier $(E_{\mathrm{cm}} - B_0)$ as the explanatory variable to optimise β_0 and α.

2.5.3.1 Results for Cold Fusion Data Set

Applying the linear regression techniques to the cold fusion reactions data set (Table 2.2) gives optimized parameters values $\alpha = (-0.318 \pm 0.041)$ fm/MeV and $\beta_0 = (0.767 \pm 0.242)$ fm:

$$s^{\mathcal{L}}_{\mathrm{inj}} = -0.318 \times (E_{\mathrm{cm}} - B_0) + 0.767. \tag{2.120}$$

The current fit result is similar to what is obtained in the literature and stated in Eq. (2.118) and is presented in panel (a) of Fig. 2.31.

Importantly, the R-squared and the root mean squared error (RMSE) of the fit are 0.71 and 0.66 fm, respectively. The R-squared value indicates that the model can explain 71% of the variance in the data, suggesting a reasonably good fit. However, the remaining 29% of the variance is unexplained, implying the model doesn't capture all factors influencing the injection point distance. The RMSE quantifies the average deviation between predicted and observed values, measuring the model's accuracy. A lower RMSE indicates better model performance.

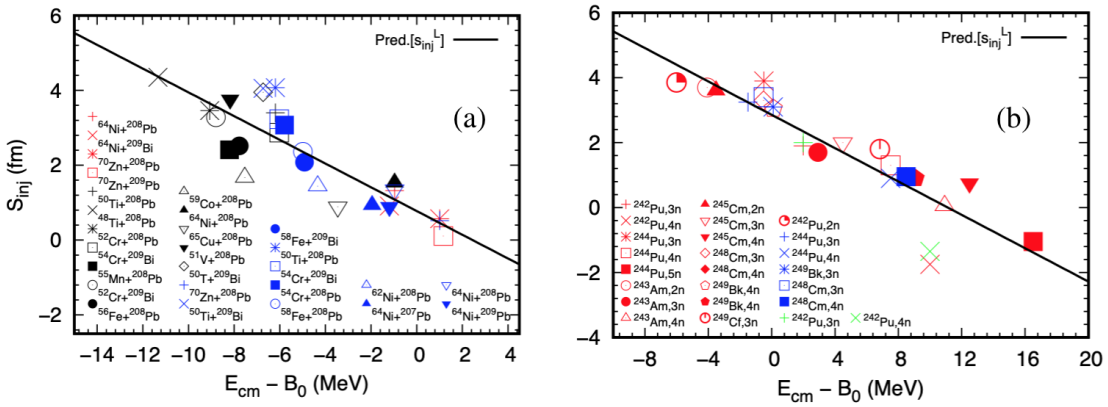

Figure 2.31: The deduced injection point distances, $s^{\mathrm{d}}_{\mathrm{inj}}$, shown as a function of $(E_{\mathrm{cm}} - B_0)$. (a) Cold fusion reaction data where the markers colours depict the laboratories: black for LBNL, blue for GSI, and red for RIKEN at which the corresponding excitation functions were obtained. The solid line depicts the optimised linear parameterization given by Eq. (2.120). (b) Hot fusion reaction data, where, the red, blue and green markers correspond to experimental data from Dubna, Tasca and LBNL, respectively. The solid line depicts the calculations using (2.121).

2.5.3.2 Results for Hot Fusion Data Set

For the hot fusion reactions data set (shown in Table 2.3), the optimized parameters α and β_0 are (-0.258 ± 0.025) fm/MeV and (2.883 ± 0.184) fm, respectively. The line of best fit is stated as

$$s_{\text{inj}}^{\mathcal{L}} = -0.258 \times (E_{\text{cm}} - B_0) + 2.883, \tag{2.121}$$

which is similar to what is obtained in Eq. (2.119) and is presented in panel (b) of Fig. 2.31. The R-squared of the fit is 0.83, an improvement over the cold fusion fit. The RMSE is 0.70 fm, a slight increase compared to the cold fusion data.

In conclusion, the linear model approach $s_{\text{inj}}^{\mathcal{L}}$ for estimating injection point distance obtained within Kewpie2 is consistent with previous studies, particularly in reproducing the results of Ref. [68].

2.5.4 Evaluation of the Compound Nucleus Formation Probability

Now that we have established the compound nucleus formation probability consistent with the FbD approach, we can evaluate the formation probability. In this case, we will use a definition of the average formation probability given as [68]:

$$\langle P_{\text{CN}}(E_{\text{cm}}) \rangle = \frac{1}{(\ell_{\max} + 1)^2} \sum_{\ell=0}^{\ell_{\max}} (2\ell + 1) \times P_{\text{fus}}(E_{\text{cm}}, \ell). \tag{2.122}$$

where $\ell_{\max}$ is the maximum angular momentum contributing to the capture process (in the sharp cut-off approximation) obtained by inverting the formula

$$\sigma_{\text{cap}} = \frac{\pi}{k^2} (\ell_{\max} + 1)^2, \tag{2.123}$$

where the σ_{cap} is the capture cross section given by Eq. (2.16), and the k is the wave number as defined previously.

The panels (a) and (b) of Fig. 2.32 illustrate the average formation probabilities (brown lines) for the reactions ^{58}Fe +^{208} Pb and ^{48}Ca +^{243} Am, respectively. These are evaluated using the injection point distance parametrisations given by Eqs. (2.120) and (2.121) for cold and hot fusions, respectively. The calculations are compared with independent calculations from Ref. [68] using the parameterisations given by Eqs. (2.118) and (2.119). The comparisons are made to check the accuracy of implementing the formation probability in the Kewpie2 code and the FbD limits and the quality of the s_{inj} fit.

The calculations in panel (a) compare well with the FbD calculations for the cold fusion reaction; however, there is a deviation for the hot fusion reaction, as shown in panel (b). As described in Section 2.3, the discrepancies between the models are expected due to the differences in the choice of neutron inverse capture cross sections, level density functions, and level density parameters. The impact of these parameters is less noticeable at the one-neutron emission but becomes pronounced along the cascade.

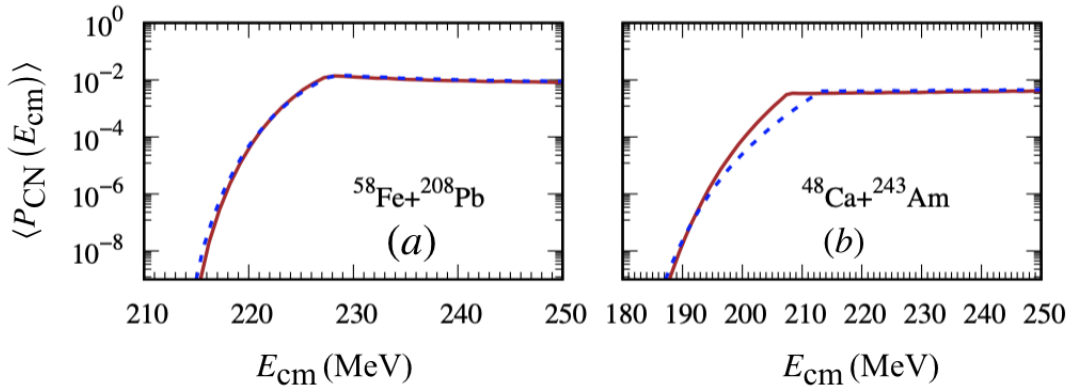

Figure 2.32: Average compound nucleus formation probabilities as a function of (E_{cm}) for (a) the cold fusion reaction of ^{58}Fe +^{208} Pb and (b) the hot fusion reaction of ^{48}Ca +^{243} Am. The blue dashed lines show independent calculations from the FbD code [68]. The brown solid line represents the calculations from the present fit of the s_{inj} within the Kewpie2 code.

Furthermore, in these calculations, the injection point distances are restricted to the positive values, i.e., $s_{inj} \geq 0$. This gives rise to the plateau, or the saturation of the formation probability with increasing energy. The restriction of s_{inj} to non-negative values may not be universally valid, as some phenomenologically deduced s_{inj} values (given in Table 2.3) for hot fusion reactions are negative. However, extrapolation into energies beyond the energies considered in the fits (shown in the Tables 2.2 and 2.3) has to be taken with caution. This case will be later discussed in Chapter 4.

Finally, the panels (a) and (b) of Fig. 2.33 illustrate the capture, fusion, and evaporation residue cross sections of the reactions ^{58}Fe +^{208} Pb and ^{48}Ca +^{243} Am, respectively. The solid black lines labelled σ_{cap} correspond to the capture cross sections. This overlaps with the blue dashed lines obtained with the FbD model because the same coefficients of the capture cross sections are adopted in both codes. The curves labelled σ_{fus} correspond to the fusion cross sections evaluated as the product of the capture cross section and the average formation probability given by Eqs. (2.16) and (2.122), respectively. The solid brown lines show the EvR cross section calculations with the current version of the Kewpie2 code.

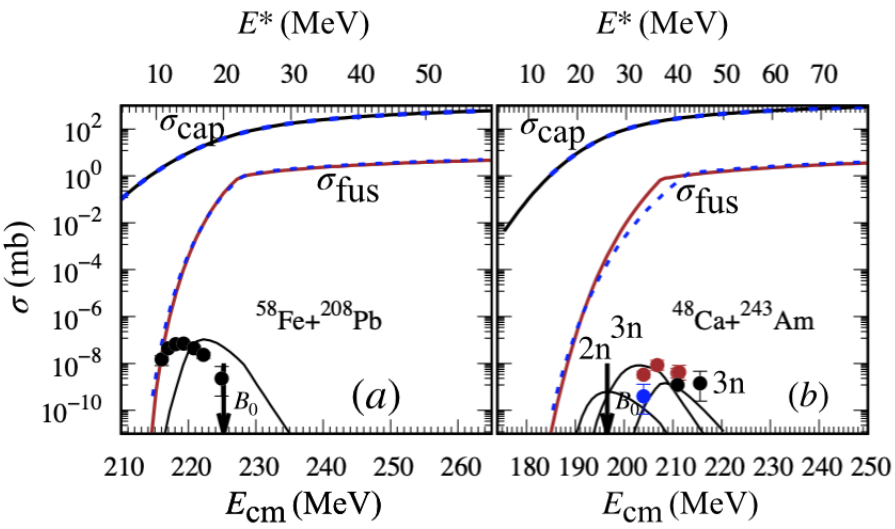

Figure 2.33: Comparison of theoretical and experimental cross sections for the reactions ^{58}Fe + ^{208}Pb and ^{48}Ca + ^{243}Am. The panels (a) and (b) illustrate the capture (σ_{cap}), fusion (σ_{fus}), and residue production cross sections. The solid black lines represent the capture cross sections σ_{cap}, which coincide with the blue dashed lines from the independent FBD calculations. The solid brown lines and blue dashed lines labelled σ_{fus} depict fusion cross section calculations using the current version of the Kewpie2 code and independent FBD calculations, respectively. The black dots in panel (a) are the excitation function of ^{208}Pb(^{58}Fe,1n)^{265}Hs [120] while the blue, red, and black dots correspond to 2n, 3n, and 4n channels for ^{243}Am(^{48}Ca,xn)$^{291-x}$Mc [33]. The solid lines correspond to the theoretical excitation functions. The theoretical ground state and saddle properties are taken from Ref. [69]. The arrows correspond to the mean Coulomb barrier.

Finally, the theoretical residue production cross sections are evaluated only within the Kewpie2 model, and the results are compared with the experimental data. The experimental data on the ^{208}Pb(^{58}Fe,1n)^{265}Hs and ^{243}Am(^{48}Ca,xn)$^{291-x}$Mc (x = 2, 3, 4) are taken from Refs. [120] and [33], respectively. In both cases, the experimental cross sections are reproduced except for the optimum bombarding energies, which are 1.2 MeV shifted in the ^{208}Pb(^{58}Fe,1n)^{265}Hs case. These discrepancies are attributed to the theoretical input data, such as the ground state and saddle properties, masses, and fission barriers used in the calculations. Since these nuclear properties are not precisely known in these regions, these shifts in the optimum energies can be expected. Moreover, the experimental uncertainty in the energy determination of the data is usually of the order of ±2 MeV due to the usage of thick targets.

2.5.5 Some Challenges with the s_{inj} Parameterisation

The cold fusion systematic in Fig. 3.3 does not account for two and three neutron emission channels. This is because the inclusion of these channels leads to a very low correlation between the phenomenologically deduced injection point distances (s^{d}_{inj}) and the excess energy ($E_{cm} - B_0$) as illustrated in Fig. 2.34.

The figure shows the deduced values s^{d}_{inj} for 1n (dot), 2n (star) and 3n (triangle) neutron emission channels in reactions with lead and bismuth targets. As shown in the figure, the combined data exhibit poor correlations between the s^{d}_{inj} and ($E_{cm} - B_0$) and therefore, the linear parameterisation cannot be applied. These challenges will be later addressed in Chapter 3.

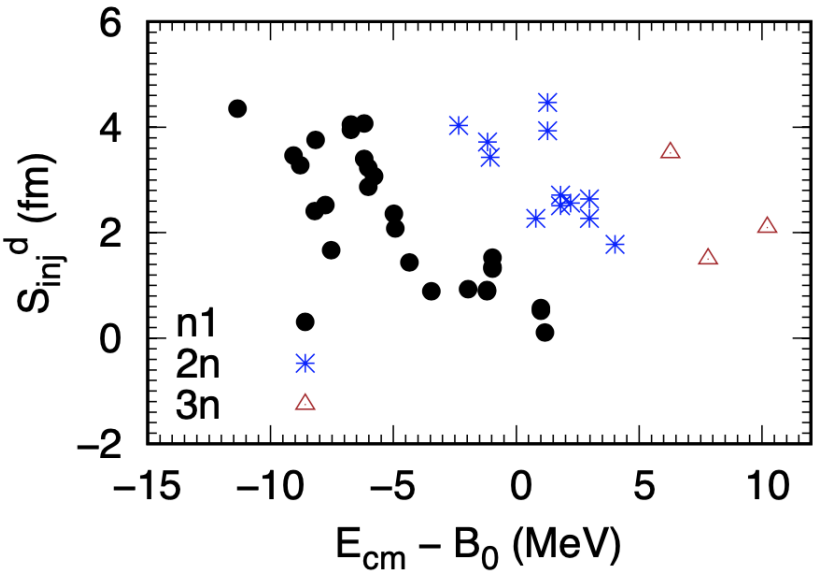

Figure 2.34: Deduced injection point distance as a function of the excess energy above the Coulomb barrier for one (black dots), two (blue stars) and three (brown triangle) neutron emission channels. The data is obtained from the reactions presented in Table 4.2.

2.6 Conclusion

The main focus of this thesis is to enhance the modelling capabilities of the Kewpie2 numerical code and to describe the production cross sections of super-heavy elements formed through fusion evaporation reactions. The reaction mechanism is modelled in three sequential steps: captured cross section, formation probability, and survival probability. The capture and survival probability models readily apply to super-heavy elements, providing the nuclear ground state and saddle point properties.

The capture cross section, discussed in Section 2.1, represents the initial stage where the colliding nuclei surpass the Coulomb barrier. In this study, we utilized the Empirical Barrier Distribution (EBD) consistent with the Fusion-by-Diffusion (FbD) approach. The EBD model is a semi-empirical model that is simple to evaluate yet has a good predictive power (see Fig. 2.4). The discussion on the capture cross section is followed by presenting the formalism of the survival probability in Section 2.2. Here, we utilized the standard statistical model of the atomic nucleus. The fine details were compared with the FbD simulations. The results reveal that switching between level density formalisms can significantly alter the survival probability, especially at high energies. Selection of the damping parameters is also important. Additionally, an energy-dependent geometric neutron capture cross section (default in Kewpie2) is shown to slightly enhances the survival probability at high energies compared to the energy-independent version (default in FbD). These are the two main subtle differences between the current Kewpie2 and FbD modelling of the survival probability.

Additionally, we also investigated the impact of Kramers-Strutinsky (KS) refinement of the Bohr-Wheeler fission decay rate and the collective enhancement (CE) of the intrinsic level density on survival probability within Kewpie2. It was observed that KS enhances the survival probability by decreasing the fission decay width (see Fig. 2.18), while CE reduces it. The model is tested on heavy nuclei synthesis reactions for which the formation probability is close to one (reactions without hindrance). The model accurately describes the maximum amplitudes of the residue cross sections by adjusting the shell damping parameter. Incorporating KS-CE introduces the reduced friction (β) as another free parameter of the model.

Finally, we present the framework for the compound nucleus formation probability at the overdamped limit of the Langevin-type equation. The formation step is implemented in a manner consistent with the Fusion-by-Diffusion model by adopting the same parameterization of the inner barrier around the fusion saddle and by fitting the free parameter of the model: the injection point distance. The results from current calculations are compared with sample calculations from the FbD model and experimental data. The results agree with the FbD and the experiments, highlighting the seamless formation probability implementation.

Chapter 3

Revisiting the Dynamics of the Formation Probability

In the previous chapter, we implemented in the Kewpie2 model the compound nucleus formation probability within the overdamped limit of the Langevin formalism, consistent with the Fusion-by-Diffusion (FbD) evaluation in Ref. [68]. We have also adopted the FbD model's linear parameterisation of the injection point distance (s_{inj}), which is the adjustable parameter in the model, and optimised it for the Kewpie2 code. Here, the s_{inj} is parameterised as a linear function of $E_{\mathrm{cm}} - B_0$, the excess energy in the centre of the mass frame above the mean entrance channel barrier. The $s^{\mathrm{d}}_{\mathrm{inj}}$ distances were deduced by analysing excitation functions. The general trend is that s_{inj} has an inverse relation with increasing energy in the centre of mass frame (see Fig. 2.30), and the heavier projectiles and targets combinations require shorter injection point distances, to form a compound nucleus.

The linear fit provided a good description of the data, yielding R^2 scores of approximately 0.71 and 0.83 for the cold and hot fusion data, respectively. Although these are statistically satisfactory descriptions, we must consider whether improvements are possible, given that the injection distance is a critical parameter in the FbD modelling, especially for accurately reproducing and predicting production cross sections. Beyond reproducing the production cross sections, is there more to the dynamics that could be learned? To address these questions, we will revisit the dynamics of compound nucleus formation within the Langevin formalism. This study led to a new approach to the injection distance parameterization [81, 82] from a different perspective consistent with the Langevin formalism from the default linear approach.

This chapter is organised as follows: Section 3.1 is dedicated to presenting the modelling of the new injection distance parametrization. Here, the parameters of the new approach are fitted on both cold and hot fusion reaction data. The predictive power of the new injection point distance is compared with the linear approach (FbD approach). To improve the modelling, Subsections 3.1.5 and 3.1.6 explore the mass asymmetry and Coulomb parameter as possible explanatory features that could potentially improve the overall fit. Subsection 3.1.7 attempted to explain cold and hot fusion data with one parameterization of the injection point distance.

Furthermore, we introduced angular momentum treatment in the injection point distance (s_{inj}) as illustrated in Section 3.2. The fitting parameters of the injection point distance are re-optimised using a new technique described in Section 3.3. In all of these fits, the theoretically predicted production cross sections are compared with the experiment data to check the quality of the fit as shown in Sections 3.4 and 3.5.

3.1 New Approach to Injection Point Distance Parametrisation ($s_{\mathrm{inj}}^{\mathcal{N}}$)

As discussed earlier, the nuclear shape transition from capture (di-nuclear shape) to a spherical compound nucleus involves several dynamical variables. These variables can be classified as slow (S) or fast (F) collective variables, depending on their rate of evolution in the dynamics. The fast and slow variables are coupled via the friction tensor, hence the rapid evolution of the fast collective variables is expected to alter the initial conditions of the slower ones. Due to this phenomenon, one can investigate the impact on the initial condition of the slow variables when the fast variables are eliminated. This allows us to gain insight into the impact on the dynamics of the selection of a single effective variable as used in the overdamped limit (Eq. (2.4.1)).

To begin, the multidimensional Langevin equation describing the dynamics of the collective variables is given as [81, 82]:

$$\frac{d}{dt}\begin{bmatrix} F \\ S \end{bmatrix} = \begin{bmatrix} D_f & C_{fs} \\ C_{sf} & D_s \end{bmatrix}\begin{bmatrix} F \\ S \end{bmatrix} + \begin{bmatrix} R_f(t) \\ S_s(t) \end{bmatrix}, \tag{3.1}$$

where, F and S are the set of n_{f} and n_{s} dimensional fast and slow collective variables, respectively. The collective variables are coupled via the coupling matrices C_{fs} and C_{sf}. D_f and D_s represent their corresponding drift matrices. The auto-correlation functions of the random forces are defined consistent with the dissipation-fluctuation theorem:

$$\begin{bmatrix} R_f(t) \\ R_s(t) \end{bmatrix} \cdot \langle \begin{bmatrix} R_f(t'), & R_s(t') \end{bmatrix} \rangle = \begin{bmatrix} \rho_f & \rho_{fs} \\ \rho_{sf} & \rho_s \end{bmatrix} \delta(t - t'). \tag{3.2}$$

For simplicity, we consider a symmetric reaction where the transition to a spherical compound nucleus is described by two collective variables: the neck (ϵ) and the surface separation (s) [81, 82]. The neck (ϵ), neck velocity $\dot{\epsilon}$, and the initial surface velocity ($\dot{s}$) are considered fast variables due to their rapid evolution and convergence in the dynamics. The surface separation (s) is considered a slow variable since it ultimately determines the final fate of the system. With these assumptions, the dynamics of the system can be described by a set of coupled Langevin equations along a parabolic potential:

$$\ddot{\epsilon} + \beta_{\epsilon\epsilon}\dot{\epsilon} + \beta_{\epsilon s}\dot{s} + \omega_{\epsilon}^2\epsilon = r_{\epsilon}(t), \tag{3.3}$$

$$\ddot{s} + \beta_{ss}\dot{s} + \beta_{s\epsilon}\dot{\epsilon} - \omega_{s}^2 s = r_{s}(t). \tag{3.4}$$

The variables are considered coupled via the friction tensors $\beta_{s\epsilon}$ and $\beta_{\epsilon s}$. The ω_{ϵ} and ω_s are the angular frequency that defines the parabolic well and barrier of the neck and surface separation, respectively.

The aim is to solve the coupled Langevin Eqs. (3.3) and (3.4) which enters into Eq. (3.1) as:

$$\frac{d}{dt}\begin{bmatrix}\dot{\epsilon}\\ \epsilon\\ \dot{s}\\ s\end{bmatrix} = \begin{bmatrix}-\beta_{\epsilon\epsilon} & -\omega_\epsilon^2 & -\beta_{\epsilon s} & 0\\ 1 & 0 & 0 & 0\\ -\beta_{s\epsilon} & 0 & -\beta_{ss} & +\omega_s^2\\ 0 & 0 & 1 & 0\end{bmatrix}\begin{bmatrix}\dot{\epsilon}\\ \epsilon\\ \dot{s}\\ s\end{bmatrix} + \begin{bmatrix}r_\epsilon(t)\\ 0\\ r_s(t)\\ 0\end{bmatrix}, \tag{3.5}$$

at the overdamped limit. Considering all the above assumptions, the Eqs. (3.3) and (3.4) converges into one-dimensional Smoluchowsky equation:

$$\dot{s} - \frac{\omega_s^2}{\beta_{\text{ss}}}s = \frac{1}{\beta_{\text{ss}}}r_s(t), \tag{3.6}$$

but with a shift of the initial condition s_0 of s due to coupling between it and the fast collective variables. The new initial condition in s after eliminating the fast ones is given as:

$$\mathcal{S}_0 = s_0 + \frac{\beta_{s\epsilon}}{\beta_{\text{ss}}}\epsilon_0 + \frac{\dot{s}_0}{\beta_{\text{ss}}}. \tag{3.7}$$

In this context, the term $\frac{\beta_{s\epsilon}}{\beta_{\text{ss}}}\epsilon_0$ represents the impact of eliminating the neck. This positive term indicates that eliminating the neck tends to increase the s_0 or induce slip of the initial condition in the opposite direction relative to the fusion saddle. The term $\frac{\dot{s}_0}{\beta_{\text{ss}}}$ is the slip in initial surface separation s_0 due to eliminating the initial velocity. This negative term favours a reduction in s_0 when all remaining kinetic energy is not thermalised [81, 82]. Therefore, Eq. (3.7) highlights the bridge between the undamped Langevin equation in Eq. (3.4) and the strong friction limit in Eq. (3.6).

The initial velocity $\dot{s}_0$ is determined by evaluating the remaining kinetic energy $K_{\text{rem}}(B, b)$ at capture [81, 82]:

$$K_{\text{rem}}(B, b) = E_{\text{cm}} - B - \frac{b^2}{R_B^2}E_{\text{cm}}, \tag{3.8}$$

where B and b are the Coulomb barrier height and the impact parameter. From Eq. (3.8), the remaining kinetic sum over all impact parameters and Coulomb barriers within the framework of the empirical Gaussian barrier distribution is obtained as [81, 82],

$$\langle K\rangle_{\text{rem}} = \sqrt{\frac{2}{\pi}}\sigma_B \frac{\frac{\sqrt{\pi}}{4}\left(2\mathcal{X}^2+1\right)\left(1+\text{erf}(\mathcal{X})\right) + \frac{\mathcal{X}}{2}\exp(-\mathcal{X}^2)}{\mathcal{X}\left(1+\text{erf}(\mathcal{X})\right) + \frac{1}{\sqrt{\pi}}\exp(-\mathcal{X}^2)}, \tag{3.9}$$

where $\mathcal{X}(E_{\text{cm}}) = \frac{E_{\text{cm}}-B_0}{\sqrt{2}\sigma_{\text{B}}}$. As defined previously in Eq. (2.17), all parameters remain the same. The remaining kinetic energy, $\langle K\rangle_{\text{rem}}$ as a function of energy parameter, $\mathcal{X}(E_{\text{cm}})$ is shown in Fig. 3.1. The figure shows that the average remaining kinetic increases rapidly for energies above the Coulomb barrier, contrary to the behaviour below the barrier.

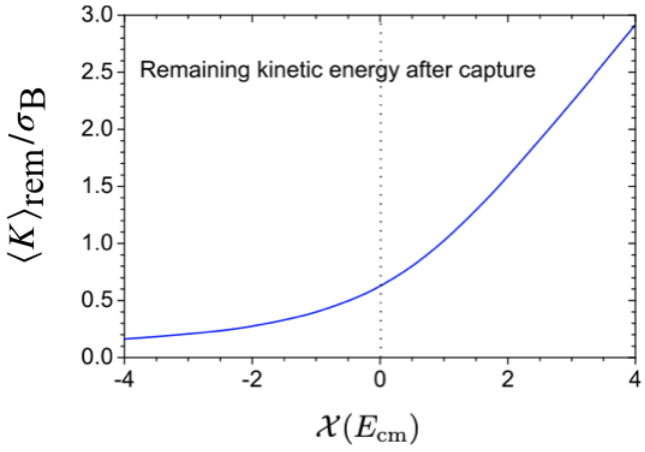

Figure 3.1: The average remaining kinetic in a unit of σ_{B} as function of $\mathcal{X}(E_{\text{cm}})$. The figure is reproduced from the Ref. [81, 82].

Now that we have established the formalism of calculating the remaining kinetic energy, the shifted initial condition in Eq. (3.7) can be restated as,

$$s_{\text{inj}}^{\mathcal{N}} = s_0 - \frac{c}{\beta_{\text{ss}}}\sqrt{\frac{2\langle K \rangle_{\text{rem}}}{\mu c^2}}, \tag{3.10}$$

where the term $\frac{\beta_{s\epsilon}}{\beta_{\text{ss}}}\epsilon_0$ from eliminating the neck is absorbed into s_0. Here, μ represents the reduced mass of the colliding nuclei, c is the speed of light, and $\langle K \rangle_{\text{rem}}$ is the remaining kinetic energy. Given that we have absorbed the slip $\frac{\beta_{s\epsilon}}{\beta_{\text{ss}}}\epsilon_0$ into s_0, the parameters remaining to evaluate $s_{\text{inj}}^{\mathcal{N}}$ are s_0 and β_{ss}.

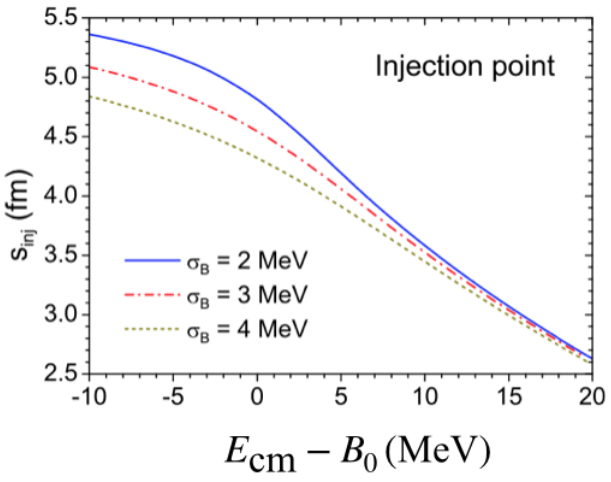

Figure 3.2: The s_{inj} point distance as a function of excess energy over the Coulomb barrier in the centre of the mass frame. Here, the parameters s_0, β_{ss} and μ are arbitrarily set to 6 fm, 2×10^{21} s^{-1} and 40 u, respectively. The brown and red dashed lines correspond to σ_B equals 4 MeV and 3 MeV, respectively, whereas the solid line denotes $\sigma_B = 2$ MeV. The figure is reproduced from the Ref. [81, 82].

For arbitrary values of s_0 = 6 fm and $\beta_{ss} = 2 \times 10^{21}$ s^{-1} one can visualise the tendency of Eq. (3.10) as a function of excess energy in the centre of the mass frame, as shown in Fig. 3.2. Fig. 3.2 exhibits two characteristics at the energies below and above the mean Coulomb barrier B_0. Below the barrier, s_{inj} takes different values for the barrier widths and converges at higher energies. This implies that s_{inj} is sensitive to the barrier widths and the straight line fit adopted in the Ref. [68], which is repeated in the Section 2.5 is insufficient to evaluate the injection point distance for cold systems. This is because s_{inj} will take different values for different systems at the same energy due to different barrier widths. However, the linear fit and the current model are expected to converge at higher energies, as evident in Fig. 3.2. This will be investigated when the parameters of both linear and new models are adjusted to the experiment.

Having discussed the new formalism of the injection point distance modelling ($s_{inj}^{\mathcal{N}}$), we now turn to adjust the coefficients to match experimental data. The strategy is the same as in Chapter 2, where deduced injection point distances were used in the linear fit procedure.

3.1.1 Optimising Injection Distance Model Coefficients

Similar to what was done in Section 2.5, we will adopt the same set of reactions as used in the linear fit. For completeness, the reactions are restated as shown in the Tables 3.1 and 3.2 for cold and hot fusion, respectively with their respective deduced injection point distances (s_{inj}^{d}) and $E_{cm} - B_0$ values. The energy excess $E_{cm} - B_0$ is used to evaluate the average remaining kinetic energy ($\langle K \rangle_{rem}$) and the surface separation velocity ($\dot{s}_0$):

$$\dot{s}_0 = -c\sqrt{\frac{2\langle K \rangle_{rem}}{\mu c^2}}. \tag{3.11}$$

All variables are defined in Eq. (3.10). The variables s_{inj}^{d} and $E_{cm} - B_0$ are the same as in the linear fit (Eq. (2.117)).

In order to apply the regression technique to fitting s_0 and β_{ss}, Eq. (3.10) can be rewritten as,

$$s_{inj}^{\mathcal{N}} = \beta_0 + \beta_1 x_1. \tag{3.12}$$

In this context, β_1 is equal to $\frac{1}{\beta_{ss}}$, the intercept β_0 corresponds to the s_0. x_1 stands for the surface separation velocity defined by Eq. (3.11). The uncertainties in $s_{inj}^{\mathcal{N}}$ predictions are derived by propagating the uncertainties of optimised s_0 and β_{ss} onto it:

$$\begin{aligned} u^2(s_{inj}^{\mathcal{N}}) = u^2(s_0) + \left(\frac{c}{\beta_{ss}^2}\sqrt{\frac{2\langle K \rangle_{rem}}{\mu c^2}}\right)^2 u^2(\beta_{ss}), \\ + 2\frac{c}{\beta_{ss}^2}\sqrt{\frac{2\langle K \rangle_{rem}}{\mu c^2}}u(s_0, \beta_{ss}). \end{aligned} \tag{3.13}$$

The first and the second terms are the uncertainty contribution due to s_0 and the β_{ss}, respectively. The last term is the contribution from the correlation between the parameters s_0 and the β_{ss}. Furthermore, we will explore mass asymmetry and the Coulomb parameter

as explanatory features in the fitting parameters of the model. These features are considered to potentially improve the $s_{\text{inj}}^{\mathcal{N}}$. These extra features are shown for the respective reactions in the Tables 3.1 and 3.2.

Table 3.1: Table of the cold fusion reaction data set from GSI, LBNL, and RIKEN. Δ denotes the projectile-target mass asymmetry. s^{d}_{inj} fm, and $E_{cm} - B_0$ MeV represent the deduced injection distance and excess energy in the centre of mass frame, respectively, obtained by adjusting Eq. (2.2) to the experimental data. z is the coulomb parameter, $\dot{s}_0$ fm/s is the surface shift velocity. The references to the experimental data are indicated in Table 2.2.

Z_p	A_p	Z_t	At	Z_{CN}	A_{CN}	Δ	$E_{cm} - B_0$ (MeV)	z	$\dot{s}_0$ (fm/s)	s^{d}_{inj} (fm)
GSI										
1n channel										
22	50	82	208	104	258	0.612	-6.195	187.740	-2.847e+21	4.07
22	50	82	208	104	258	0.612	1.805	187.740	-3.855e+21	2.71
22	50	83	209	105	259	0.614	-6.731	189.842	-2.821e+21	4.05
22	50	83	209	105	259	0.614	1.269	189.842	-3.792e+21	3.93
24	54	82	208	106	262	0.588	-5.789	202.787	-3.134e+21	3.07
24	54	83	209	107	263	0.589	-6.024	205.060	-3.138e+21	3.23
24	54	82	208	106	262	0.588	2.211	202.787	-4.072e+21	2.56
24	54	83	209	107	263	0.589	2.976	205.060	-4.201e+21	2.64
26	58	82	208	108	266	0.564	-4.987	217.643	-3.327e+21	2.36
26	58	83	209	109	267	0.566	-4.917	220.084	-3.359e+21	2.08
28	62	82	208	110	270	0.541	-4.342	232.321	-3.298e+21	1.44
28	64	82	207	110	271	0.528	-1.956	231.557	-3.481e+21	0.93
28	64	82	208	110	272	0.529	-0.971	231.335	-3.582e+21	1.35
28	64	83	209	111	273	0.531	-1.198	233.933	-3.579e+21	0.89
2n channel										
22	50	83	209	105	259	0.614	1.269	189.842	-3.792e+21	3.93
22	50	82	208	104	258	0.612	1.805	187.740	-3.855e+21	2.71
24	54	83	209	107	263	0.589	2.976	205.060	-4.201e+21	2.64
24	54	82	208	106	262	0.588	2.211	202.787	-4.072e+21	2.56
26	58	82	208	108	266	0.564	4.013	217.643	-4.370e+21	1.78
3n channel										
22	50	83	209	105	259	0.614	6.269	189.842	-4.636e+21	3.51
22	50	82	208	104	258	0.612	7.805	187.740	-4.908e+21	1.50
24	54	82	208	106	262	0.588	10.211	202.787	-5.337e+21	2.10
LBNL										
1n channel										
22	50	82	208	104	258	0.612	-6.195	187.740	-2.847e+21	3.40
22	48	82	208	104	256	0.625	-11.34	188.718	-2.483e+21	4.35
24	52	82	208	106	260	0.600	-9.068	203.779	-2.741e+21	3.46
24	54	83	209	107	263	0.589	-6.024	205.060	-3.138e+21	2.87
25	55	82	208	107	263	0.582	-8.204	210.733	-3.026e+21	2.41
24	52	83	209	107	261	0.602	-8.796	206.062	-2.787e+21	3.28
26	56	82	208	108	266	0.576	-7.776	218.648	-2.924e+21	2.52
27	59	82	208	109	267	0.558	-7.536	225.504	-3.071e+21	1.67
28	64	82	208	110	272	0.529	-0.971	231.335	-3.582e+21	1.53
29	65	82	208	111	273	0.524	-3.460	239.098	-3.472e+21	0.89
23	51	82	208	105	259	0.606	-8.174	195.777	-2.742e+21	3.76
22	50	83	209	105	259	0.614	-6.731	189.842	-2.821e+21	3.95
2n channel										
22	50	83	209	105	259	0.614	1.269	189.842	-3.792e+21	4.47
22	50	82	208	104	258	0.612	1.805	187.740	-3.855e+21	2.51
22	48	82	208	104	256	0.625	-2.340	188.718	-3.336e+21	4.03
24	52	82	208	106	260	0.600	-1.068	203.779	-3.551e+21	3.43
24	54	83	209	107	263	0.589	2.976	205.060	-4.201e+21	2.27
25	55	82	208	107	263	0.582	0.796	210.733	-3.957e+21	2.27
23	51	82	208	105	259	0.606	-1.174	195.777	-3.480e+21	3.72
RIKEN										
1n channel										
28	64	82	208	110	272	0.529	-0.971	231.335	-3.582e+21	1.32
28	64	83	209	111	273	0.531	-1.198	233.933	-3.579e+21	0.91
30	70	82	208	112	278	0.496	1.004	244.867	-3.763e+21	0.57
30	70	83	209	113	279	0.498	1.167	247.619	-3.802e+21	0.11

Table 3.2: Table of the ^{48}Ca induced hot fusion reaction data set from Dubna, Tasca, and LBNL. Column Ch shows the reaction channel. Δ denotes the projectile-target mass asymmetry. s^{d}_{inj} fm and $E_{cm} - B_0$ MeV represent the deduced injection distance and excess energy in the centre of mass frame, respectively, obtained by fitting Eq. (2.2) to the experimental data. z is the coulomb paramter, $\dot{s}_0$ fm/s is the surface shift velocity. The references to the experimental data are indicted in the Table 2.3.

Z_t	A_t	Z_{CN}	A_{CN}	Ch	Δ	$E_{cm} - B_0$ (MeV)	z	$\dot{s}_0$ (fm/s)	s_{inj} (fm)
DUBNA									
94	242	114	290	3n	0.669	1.996	190.555	-4.414e+21	1.9
94	242	114	290	4n	0.669	9.996	190.555	-5.621e+21	-1.75
94	244	114	292	3n	0.671	-0.491	190.225	-4.090e+21	3.9
94	244	114	292	4n	0.671	7.509	190.225	-5.220e+21	1.3
94	244	114	292	5n	0.671	16.509	190.225	-6.672e+21	-1.05
95	243	115	291	2n	0.670	-4.078	192.415	-3.716e+21	3.7
95	243	115	291	3n	0.670	2.922	192.415	-4.561e+21	1.7
95	243	115	291	4n	0.670	10.922	192.415	-5.782e+21	0.05
96	245	116	293	2n	0.672	-3.511	194.105	-3.840e+21	3.6
96	245	116	293	3n	0.672	4.489	194.105	-4.832e+21	2.0
96	245	116	293	4n	0.672	12.489	194.105	-6.062e+21	0.75
96	248	116	296	3n	0.676	-0.507	193.607	-4.174e+21	3.3
96	248	116	296	4n	0.676	8.493	193.607	-5.427e+21	0.95
97	249	117	297	3n	0.677	0.096	195.457	-4.269e+21	3.05
97	249	117	297	4n	0.677	9.096	195.457	-5.534e+21	0.9
98	249	118	297	3n	0.677	6.832	197.472	-5.253e+21	1.8
94	242	114	290	2n	0.669	-6.004	190.555	-3.502e+21	3.85
TASCA									
94	244	114	292	3n	0.669	1.996	190.555	-3.971e+21	1.9
94	244	114	292	4n	0.669	9.996	190.555	-5.220e+21	-1.75
97	249	117	297	3n	0.671	-0.491	190.225	-4.269e+21	3.9
96	248	116	296	3n	0.671	7.509	190.225	-4.174e+21	1.3
96	248	116	296	4n	0.671	16.509	190.225	-5.427e+21	-1.05
LBNL									
94	242	114	290	3n	0.669	1.996	190.555	-4.414e+21	1.9
94	242	114	290	4n	0.669	9.996	190.555	-5.621e+21	-1.75

3.1.2 Fit Results

Here, we present the results of fitting the new injection distance formula (Eq. 3.10) to the cold and hot fusion reaction data. As mentioned, the goal is to determine the coefficients s_0 and β_{ss} using the deduced injection point distances s^{d}_{inj}.

3.1.2.1 Results for Cold Fusion Reaction Data

The optimised parameters of s_0 and β_{ss} from the regression model of Eq. (3.12) for the cold fusion reaction data are $s_0 = (12.478 \pm 0.785)$ fm and $\beta_{ss} = (0.314 \pm 0.024) \times 10^{21}$ s^{-1}. The covariance between the fitted parameters $u(s_0, \beta_{ss}) = -1.87 \times 10^{19}$ fm/s.

The relative uncertainty in the obtained s_0 and β_{ss} are 0.06 and 0.80, respectively, which implies s_0 is better determined compared to β_{ss} on the data set. The new injection distance formula with the optimised parameters s_0 and β_{ss} is stated as,

$$s^{\mathcal{N}}_{inj} = 12.478 - \frac{c}{0.314 \times 10^{21}} \sqrt{\frac{2\langle K \rangle_{rem}}{\mu c^2}}, \tag{3.14}$$

and the corresponding linear model as defined in the previous Chapter 2 is restated here for comparison:

$$s^{\mathcal{L}}_{inj} = -0.318 \times (E_{cm} - B_0) + 0.767. \tag{3.15}$$

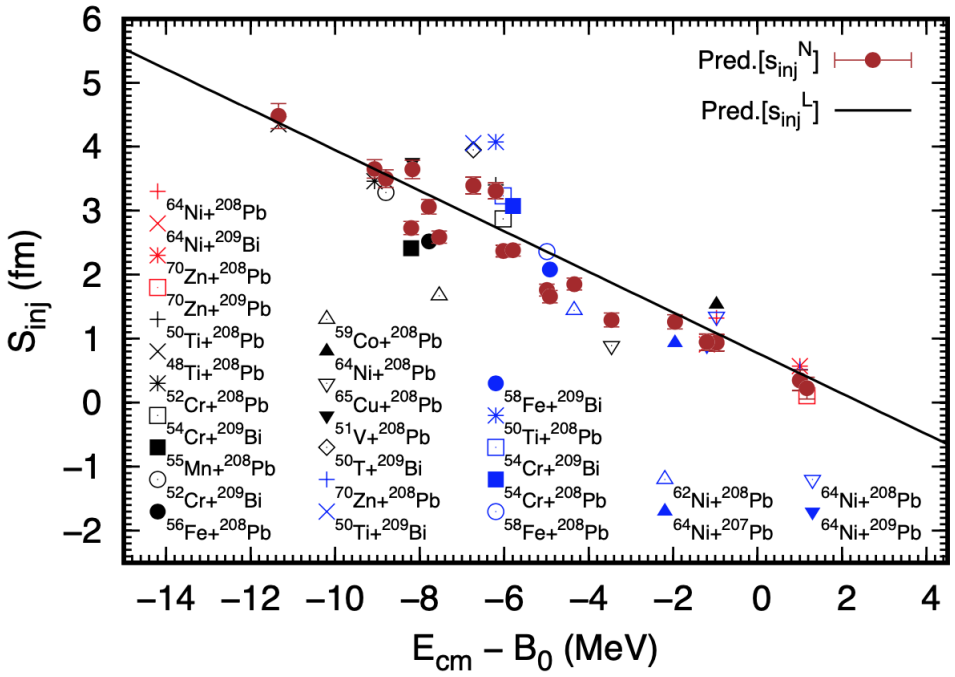

Figure 3.3: The deduced injection point s^{d}_{inj} vs $(E_{cm} - B_0)$. The black, blue, and red markers depict the laboratories: black for LBNL, blue for GSI, and red for RIKEN, at which the corresponding excitation functions were obtained. The brown points with the uncertainty bars are the $s^{\mathcal{N}}_{inj}$ values obtained with Eq. 3.14. The solid line depicts the linear approach in Eq. (3.15).

The injection distance model predictions $\left(\mathbf{s}^{\mathcal{N}}_{\rm inj} \pm u(\mathbf{s}^{\mathcal{N}}_{\rm inj})\right)$ on the various reactions are summarised in the Table B.1 whereas, Fig. 3.3 illustrates how the predicted values compare with the $s^{\rm d}_{\rm inj}$ values. Here, the red dots correspond to the values obtained using Eq. (3.14). Each different symbol represents a specific reaction, with the corresponding reaction indicated on the plot. The fluctuations as seen in the predicted $s_{\rm inj}$ stemmed from the variations in the Coulomb barrier width $\sigma_{\rm B}$ (given by Eq.(3.9)) with the projectile-target combinations. The solid black line depicts the predictions from the linear model (Eq. (3.15)) while the brown dotted line represents the predictions from the new approach, $s^{\mathcal{N}}_{\rm inj}$. The uncertainty bars associated with the predictions are determined using Eq. (3.13).

3.1.2.2 Results for Hot Fusion Reaction Data

Similarly, the optimised parameters s_0 and $\beta_{\rm ss}$ for the hot fusion reaction data presented in the Table 3.2 are (10.572 ± 0.929) fm and $(0.550 \pm 0.057) \times 10^{21}$ s^{-1}, respectively. The covariance between the s_0 and the $\beta_{\rm ss}$ is obtained as -5.244×10^{19} fm/s. The relative uncertainties in the optimised parameters s_0 and $\beta_{\rm ss}$ are 0.09 and 0.1, respectively. In contrast to the cold fusion data, $\beta_{\rm ss}$ is better optimised and the relative uncertainty in s_0 is similar to the one obtained for the cold fusion reaction data set.

The $s^{\mathcal{N}}_{\rm inj}$ with the optimised parameters is stated as,

$$s^{\mathcal{N}}_{\rm inj} = 10.572 - \frac{c}{0.550 \times 10^{21}} \sqrt{\frac{2\langle K \rangle_{\rm rem}}{\mu c^2}}, \tag{3.16}$$

and the linear fit is,

$$s^{\mathcal{L}}_{\rm inj} = -0.258 \times (E_{\rm cm} - B_0) + 2.883. \tag{3.17}$$

Similarly, Table B.2 summarizes the results for the hot fusion reaction data presented in Table 3.2. As with the cold fusion reaction data, the deduced injection point distances are plotted against the excess energy in the centre of mass frame, $(E_{\rm cm} - B_0)$ as illustrated in Fig. 3.4. Here, the hot fusion reaction data exhibits less variance in the deduced injection point distances than the cold fusion reaction data set, except for two reactions that deviate significantly from the fit.

This reduced variance likely stems from the use of a single projectile (^{48}Ca) in the hot fusion reactions, in contrast to the wider range of projectiles used in the cold fusion experiments (see Fig. 3.3). Furthermore, the variations in $s_{\rm inj}$ should get smaller with increasing energy, as illustrated in Fig. 3.2.

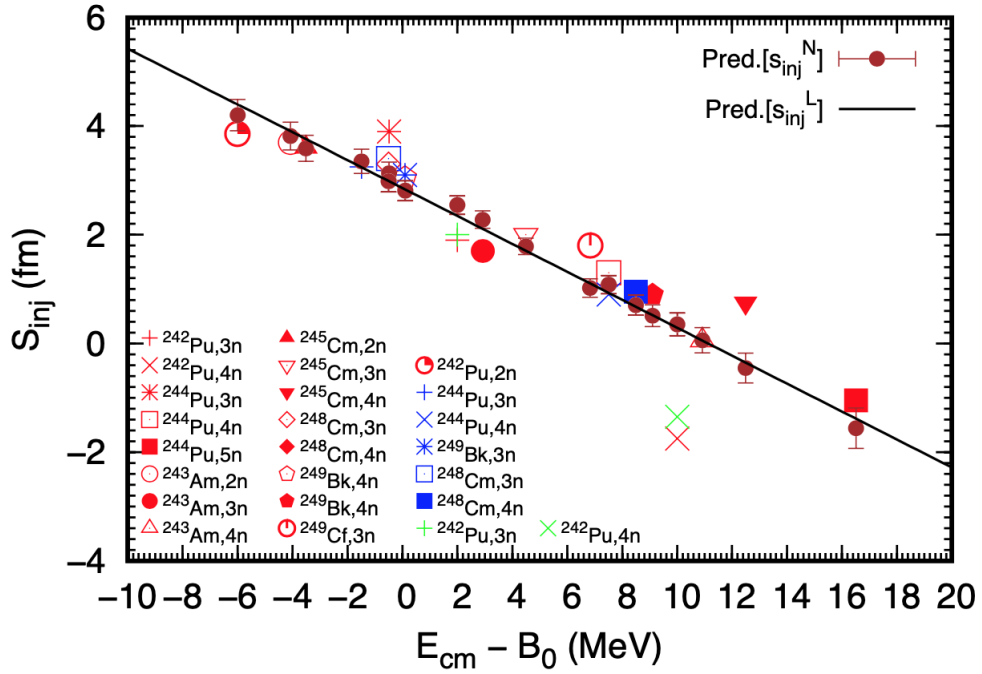

Figure 3.4: The deduced injection point distances $s^{\mathrm{d}}_{\mathrm{inj}}$ for hot fusion reactions plotted as a function of $(E_{\mathrm{cm}} - B_0)$. The red, blue and green markers correspond to excitation function data from Dubna, Tasca and LBNL, respectively. The brown points with the uncertainty bars are the $s^{\mathcal{N}}_{\mathrm{inj}}$ predictions given by Eq. (3.16). The solid line depicts the linear approach in Eq. (3.17).

3.1.2.3 Comparison of the Linear and New Injection Distance Model

Having presented the two approaches for the injection point distance parameterization, we now evaluate their performance in describing the data. The models' performance is assessed using the R^2 and root mean squared error (RMSE) metrics. For the cold fusion data, the new approach ($s^{\mathcal{N}}_{\mathrm{inj}}$) provides a better fit, with a $R^2 = 0.86$, compared to 0.71 for the linear approach ($s^{\mathcal{L}}_{inj}$). This indicates that the new approach explains 86% of the variance in the data, while the linear approach only explains 71%.

	Cold Fusion		Hot Fusion	
Metrics Score	$s^{\mathcal{L}}_{\mathrm{inj}}$	$s^{\mathcal{N}}_{\mathrm{inj}}$	$s^{\mathcal{L}}_{\mathrm{inj}}$	$s^{\mathcal{N}}_{\mathrm{inj}}$
R^2	0.71	0.86	0.83	0.82
RMSE fm	0.66	0.46	0.70	0.71

Table 3.3: Metrics scores for $s^{\mathcal{L}}_{\mathrm{inj}}$ and $s^{\mathcal{N}}_{\mathrm{inj}}$ for Cold Fusion and Hot Fusion.

Both models perform similarly for the hot fusion reaction data, with R^2 values of 0.82 and 0.83 for the new approach and the linear model, respectively. Both approaches to the injection distance have similar descriptions of the hot fusion reaction data because the data exhibit linear tendencies. This may stem from the fact that the same projectile induces the reactions and the effect of the entrance channel characteristics, such as the mean Coulomb barrier, barrier width, and mass asymmetry similar for all reactions.

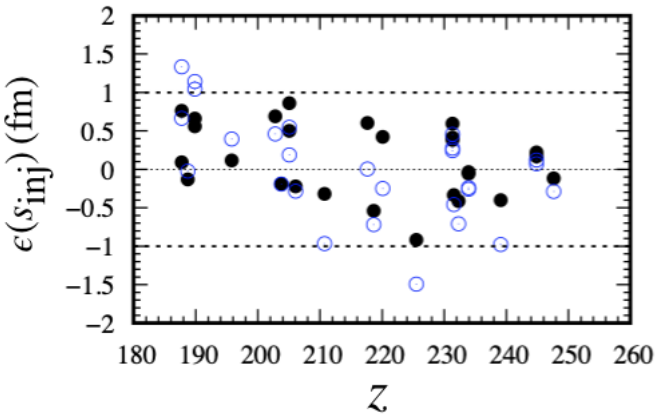

Figure 3.5: Deviations, $\epsilon(s_{\rm inj})$, of the predicted injection point distances from the deduced values vs Coulomb parameter z for cold fusion 1n reactions listed in Table 3.2. The predicted values are evaluated using Eq. (3.16) (in black) and Eq. (3.15) (in open blue).

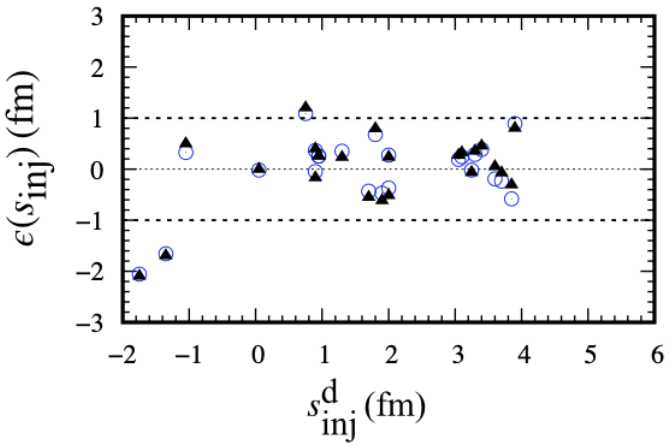

Figure 3.6: Deviations, $\epsilon(s_{\rm inj})$, of the predicted injection point distances from the deduced values as the function of the former for hot fusion reactions listed in Table 2.3. The predicted values are evaluated using Eq. (3.16) (in black) and Eq. (3.15) (in open blue).

The data description is further illustrated by studying the residue values, $\epsilon(s_{\rm inj})$, as a function of the Coulomb parameter (see Eq. 2.20) in Fig. 3.5. Because of the significant changes in the projectile's charge in the cold fusion reactions, the Coulomb parameter seems to be an appropriate choice since it identifies the reaction in an unambiguous way. The residue values are obtained by taking the difference between $s^{\rm d}_{\rm inj}$ deduced from the experimental data and those calculated. Here, the open symbols correspond to the $\epsilon(s_{\rm inj})$ residues obtained for the linear parameterization (Eq. (3.15)). This is compared with residues obtained with the optimised new approach to the injection distance (black points) given by Eq. (3.14).

The figure shows that the predictions from both methods deviate from the deduced values by about ±1 fm. The figure shows that the blue symbols deviate more, with some going beyond the ±1 fm margin, while the black points are confined within the ±1 fm range. These deviations translate into predicting power of the production cross sections. The

cross sections for the reactions for which the residues are beyond the ±1 fm range will be reproduced worse than those for which residues are close to zero.

Figure 3.6 shows the injection point distance deviations as a function of the phenomenological deduced values for hot fusion systems. The Coulomb parameters are not used in this case because they are very similar for the reactions with the same projectile. Here, the linear and new approaches to the injection point distance give similar results. The results are within the ±1 fm range except for two reactions. This observation is re-emphasised by the same R^2 values of both fits to the data.

3.1.3 Evaluation of the Compound Nucleus Formation Probability

Now that we have optimised the free parameters of the model, we can evaluate the compound nucleus formation probability using the new parameterisation of the injection point distance. We will adopt the exact definition of the averaged over ℓ formation probability [34] given in Eq. (2.122). However, open questions remain regarding the limit of s_{inj} value at higher bombarding energies, as inferred in Chapter 2, where s_{inj} was restricted to positive values only. Here we will address that issue.

The panels (a) and (b) of Fig. 3.7 illustrate examples of the average compound nucleus formation probabilities given by Eq. (2.122) for cold (^{58}Fe+^{208}Pb) and hot (^{48}Ca+^{243}Am) fusion reactions. The blue dashed line in each panel represents calculations from the FbD model [68], which are used for comparison. The black dashed-dotted lines show calculations using the new approach to the injection point distance with the maximum angular momentum from Eq. (2.123), similar to the FbD calculation. The results are comparable, with minor differences arising from the choice of injection distance parameterization.

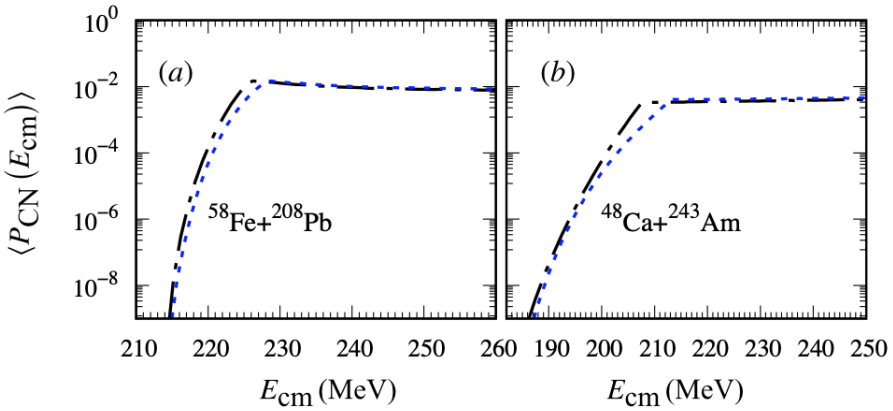

Figure 3.7: Average compound nucleus formation probabilities as a function of (E_{cm}) for (a) the cold fusion reaction of ^{58}Fe+^{208}Pb and (b) the hot fusion reaction of ^{48}Ca+^{243}Am. The blue dashed lines show calculations from the FbD code [68]. The black dashed-dotted line is evaluated with the new approach.

In the calculations presented in Fig. 3.7, the injection point distances are restricted to the positive values ($s_{\text{inj}} \geq 0$ fm) only, which gives rise to the plateau, or the saturation of the formation probability with increasing energy. The restriction of s_{inj} to non-negative

values may not be universally valid, as some deduced s_{inj} values (given in Table 2.3) for hot fusion reactions are negative. Moreover, the extrapolation into energies beyond the energies considered in the fits (shown in the Tables 2.2 and 2.3) has to be taken with caution. In this study, we adopted the limit of s_{inj} comparable to the smallest deduced injection point distance: $s_{\text{inj}} \geq -2$ fm.

The impact of extending the limit of the s_{inj} to -2 fm in the evaluation of the average formation probability is shown in Fig. 3.8. Panels (a) and (b) of Fig. 3.8 correspond to the cold and hot fusion reaction test cases, respectively. The brown and green lines are the reference calculations for $s_{\text{inj}} \geq 0$ fm and $s_{\text{inj}} \geq -2$ fm, respectively. As shown in both figures, decreasing the s_{inj} 0 fm to -2 fm elevates the saturation levels by about a factor of five in the case of ^{58}Fe +^{208} Pb reaction and by two orders of magnitude in the case of ^{48}Ca +^{243} Am reaction.

The energy deformation parametrization used in this study to obtain the heights of the fusion barriers is based on the assumption that both projectile and target nuclei are spherical [149] (see Subsection 2.4.2). However, this is not true in hot fusion reactions where target nuclei exhibit strong quadrupole deformations. Thus, negative values of the injection parameter might, in some sense, account for more compact side-to-side collisions possible in reactions between calcium-48 and actinide targets.

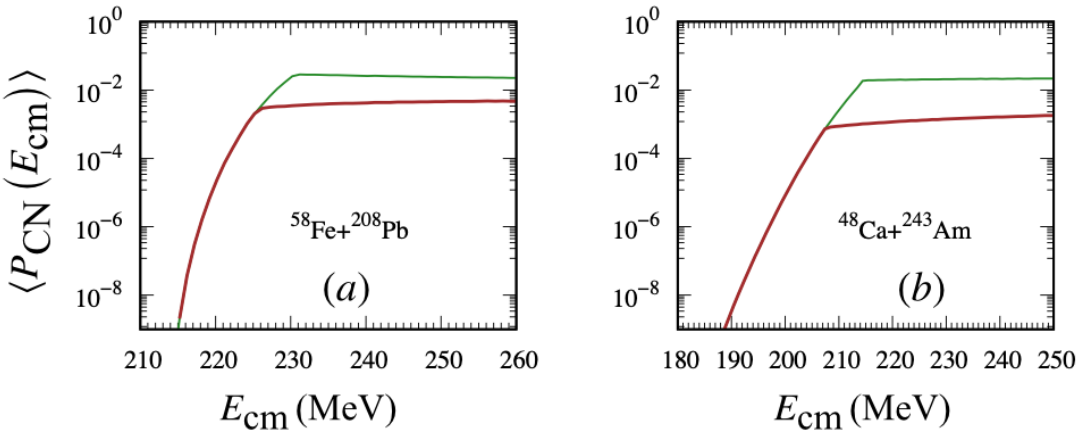

Figure 3.8: Average compound nucleus formation probabilities as a function of the centre of mass energy (E_{cm}) for (a) cold fusion reaction of ^{58}Fe +^{208} Pb and (b) hot fusion reaction of ^{48}Ca +^{243} Am. The calculations are done using the injection point distance parameterizations of Eqs. (3.14) and (3.16) in panel (a) and (b), respectively. Brown lines show the case of the injection point distance restriction to 0 fm, and green lines show the case of -2 fm restriction. See text for more details.

3.1.4 Evaluation of the EvR cross sections

Besides investigating the quality of the injection distance fit in terms of how well it reproduced the values obtained from the experimental data, we can also investigate its predictive power of reproducing the evaporation residue cross sections. This is illustrated in Fig. 3.9 using the ratio of the calculated cross section value in the excitation function peak to the experimental value $\left(\frac{\sigma_{\text{th}}}{\sigma_{\text{exp}}}\right)$ as a function of the Coulomb parameter given by Eq. (2.20). The blue open symbols correspond to the linear parameterization in Eq. (3.17), and the black points are the new parameterization given by Eq. (3.14). The new parameterization has a little edge over the linear approach. In this case, all ratios are within an order of magnitude difference. On the contrary, the linear approach has three points overestimated, and one point underestimated. This is evident from injection point distance residual plots in Fig. 3.5, as this quantity is directly related to calculated values of the EvR cross sections.

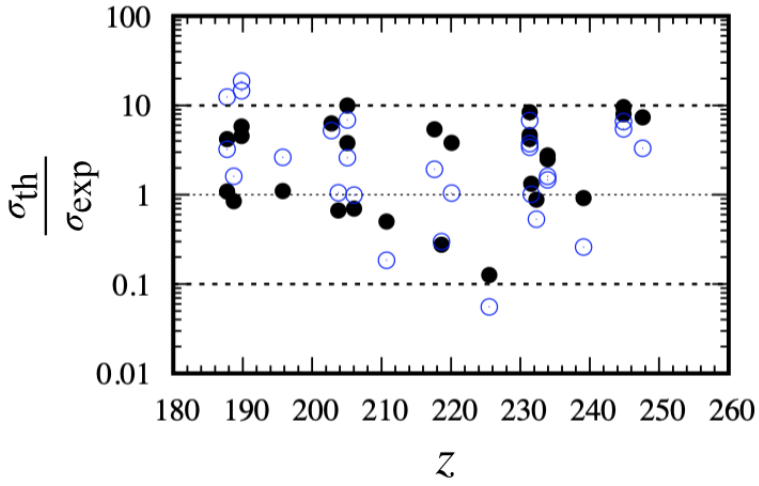

Figure 3.9: Comparison of the linear injection point functions (open blue points) given by Eq. (3.14) and the new approach (solid black points) in Eq. (3.15) in reproducing experimental EvR cross sections for cold fusion reactions. $\left(\frac{\sigma_{\text{th}}}{\sigma_{\text{exp}}}\right)$ is the ratio of theoretical predictions to experimental observations for the reactions used in the fit procedure. z is the Coulomb parameter.

Fig. 3.10 illustrate similar plots for the hot fusion reaction data, where panels (a) and (b) correspond to the linear and new approaches to parameterizing the injection points distances, respectively. The figure illustrates the $\left(\frac{\sigma_{\text{th}}}{\sigma_{\text{exp}}}\right)$ as the function of the target materials used in the reactions with ^{48}Ca projectile. The data for the 2n, 3n, 4n and 5n neutron emission channels are depicted by the symbols of the cross, star, open square and solid squares. Here, the colours of the points: black, blue, and brown correspond to the laboratories in Dubna, GSI (TASCA), and LBNL, where these reactions were measured. The panels show that both parameterizations describe the data similarly, with most of the reactions within an order of magnitude deviation from the experimental production cross sections.

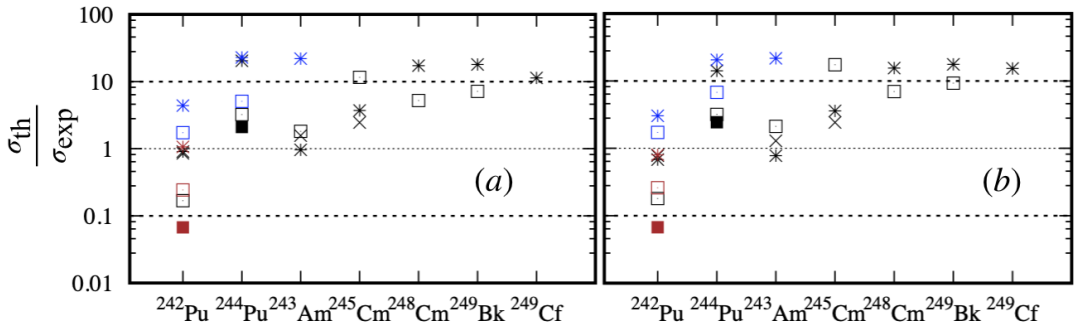

Figure 3.10: Comparison of the linear (panel (a), Eq. (3.15)) and new approach (panel (b), Eq. 3.16) parametrizations in reproducing experimental EvR cross sections for hot fusion reactions of ^{48}Ca with indicated targets. $\left(\frac{\sigma_{\text{th}}}{\sigma_{\text{exp}}}\right)$ is the ratio of the theoretical predictions to the experimental values evaluated in a maximum of a given channel. The 2n, 3n, 4n and 5n reaction channels are depicted by the cross, star, open square and solid squares symbols, respectively. Here, the colours: black, blue, and brown correspond to the laboratories in Dubna, GSI (TASCA), and LBNL, where these cross sections were measured.

Up to this point, we have optimised the new approach's fitting coefficients. The quality of the fit parameters was compared to the deduced injection point distances and the experimental production cross sections. In the next section, we will consider other explanatory features that can improve the predictive power of the new approach to the injection point distance.

3.1.5 Addition of the Mass Asymmetry Feature to $s^{\mathcal{N}}_{\text{inj}}$

Here, we introduced mass asymmetry (Eq. (2.94)) as an explanatory feature considering the injection distance model in Eq. (3.10) is modelled for a symmetric reaction:

$$s^{\mathcal{N}}_{\text{inj}} = s_0 - \frac{c}{\beta_{\text{ss}}}\sqrt{\frac{2\langle K\rangle_{\text{rem}}}{\mu c^2}} + \varsigma\left(\frac{|A_1 - A_2|}{A_1 + A_2}\right), \tag{3.18}$$

where ς is a free parameter associated with mass asymmetry. This is done in attempt to improve explanation of the variations observed in the deduced injection point distance. In order to apply the linear regression technique, the above Eq. (3.18) can be written as

$$s^{\mathcal{N}}_{\text{inj}} = \beta_0 + \beta_1 x_1 + \beta_2 x_2, \tag{3.19}$$

where the coefficient β_0, β_1, β_2 are parameters to be obtained in the fit, and x_2 represents the mass asymmetry. As in Eq. (3.12), all other parameters remain the same.

The fitted value of s_0 (equivalent to the β_0 in the model) is (-14.19 ± 3.11) fm. The β_{ss} which is the nuclear viscosity term is determined as -3.35×10^{21} s^{-1} with the uncertainty of 1.28×10^{25} s^{-1}. The coefficient ς is obtained as (73.58 ± 8.51) fm. Here, s_0 and the nuclear viscosity terms are physically unrealistic, which suggests that the asymmetry variable should be taken into account in a different way.

3.1.6 Addition of the Coulomb Parameter Feature to $s^{\mathcal{N}}_{\mathrm{inj}}$

In the cold synthesis, the projectiles changes from Ti to Zn what leads to a significant changes in the entrance channel asymmetry in comparison with the hot fusion reactions. As a result, the variations in the Coulomb interactions also changes significantly from one reaction to the other, increasing the role of the entrance channel effects. The question is whether introducing a Coulomb parameter related term can improve the fit and also explain the cold fusion data for multiple neutron emission channels, i.e., 1n, 2n and 3n. With this in mind, we can redefine Eq. (3.10) to include a Coulomb parameter term directly proportional to z (Eq. (2.20) and readjust the coefficients to investigate any sign of improvement. The refined equation is given as,

$$s^{\mathcal{M}}_{\mathrm{inj}} = s_0 + \Omega z - \frac{c}{\beta_{\mathrm{ss}}}\sqrt{\frac{2\langle K\rangle_{\mathrm{rem}}}{\mu c^2}}. \tag{3.20}$$

In this context, all the parameters remained the same as in the previous fits. We have only added the Coulomb term dependent on parameter $z = \frac{Z_1 \times Z_2}{A_1^{\frac{1}{3}} + A_2^{\frac{1}{3}}}$, where Ω is a free parameter that must be adjusted to the experimental data.

In a similar fashion, the model parameters s_0, Ω and β_{ss} are obtained from the set of reactions listed in the Table 3.1 as follows: $s_0 = (15.98 \pm 0.82)$ fm, $\Omega = (-0.054 \pm 0.004)$ fm and $\beta_{\mathrm{ss}} = (1.623 \pm 0.219) \times 10^{21}$ s^{-1}. The optimised model is stated as

$$s^{\mathcal{M}}_{\mathrm{inj}} = 15.98 - 0.054z - \frac{c}{1.623 \times 10^{21}}\sqrt{\frac{2\langle K\rangle_{\mathrm{rem}}}{\mu c^2}}. \tag{3.21}$$

The injection point distances obtained with the optimised model are compared to the deduced values in Fig. 3.11. Here, the deduced injection point distances are shown by the solid blue points, and the model predictions are shown by the black points. Note that this is shown for all channels (1n, 2n and 3n) measured in cold fusion reactions. The solid points and times symbols denote the deduced and model injection distances for the 1n channel, respectively. The data for 2n channel are depicted with solid squares and plus symbols, corresponding to the deduced and the model values. The data for the 3n channel are shown by the solid blue triangles and opened black triangles for the deduced and model values, respectively.

The comparison of the model $s^{\mathcal{M}}_{\mathrm{inj}}$ values with the ones obtained from the experimental data shows that this method has strong predictive power for the 1n and 2n emission channels. The 3n channels are reasonably reproduced. This indicates that the cold fusion injection point distances strongly correlate with the Coulomb parameter. To further investigate the nuances of the predictions, we might look at the injection point distances residual plots shown in Fig. 3.12.

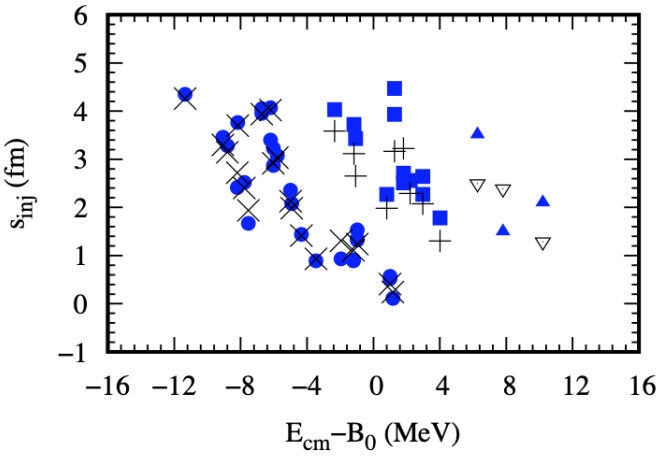

Figure 3.11: Comparison of the calculated and obtained from the experimental data injection point distances vs $(E_{cm} - B_0)$ for the cold fusion data from the Table 3.1. The solid blue symbols correspond to the deduced injection point distances, while the black points correspond to the model values. The solid blue dots, squares and triangles symbols correspond to the values for 1n, 2n and 3n emission channels (from experimental data). The times, plus, and open triangle symbols denote the values for respective channels obtained with Eq. (3.21).

Fig. 3.12 illustrates the residual plots of the calculated injection point distances with Eq. (3.21). Here, the black points correspond to the 1n emission channels used in the previous fits, and the open circles and triangles correspond to the 2n and 3n channels. The figure reinforces the good predictive power of the modified injection distance parameterization as seen in Figs. 3.11 and 3.12. Here, Eq. (3.20)) gives a description of the 1n channel data which agrees within a factor with the data deduced from the experimental cross sections. This is an improvement over what is seen in Fig 3.3 using the original parameterization given by Eq. (3.16).

In addition, the fit also describes the multiple neutron emission channels observed in the cold fusion reactions within ±1 fm deviation range from the deduced injection point values. This provides a reasonable solution to the limitations of the model highlighted in the Subsection 2.5.5, where the default parameterization could not explain the multiple neutron emission channels in the cold fusion reactions.

To investigate this observation further, we compare the calculated production cross sections with the experimental cross sections in Fig. 3.13. Figure 3.13 shows as previously the ratios of the $\left(\frac{\sigma_{th}}{\sigma_{exp}}\right)$ as a function of the Coulomb parameter. Here, the 1n neutron emission channels are well reproduced with a factor deviation as expected from Fig. 3.20. The 2n and 3n channels are also described using the modified parameterization of the injection point distance. Differences with experimental data are within one order of magnitude. Building on the success of describing the 1n, 2n and 3n channels within one parameterization, we will attempt to describe the combined, cold and hot, reaction data using one systematic.

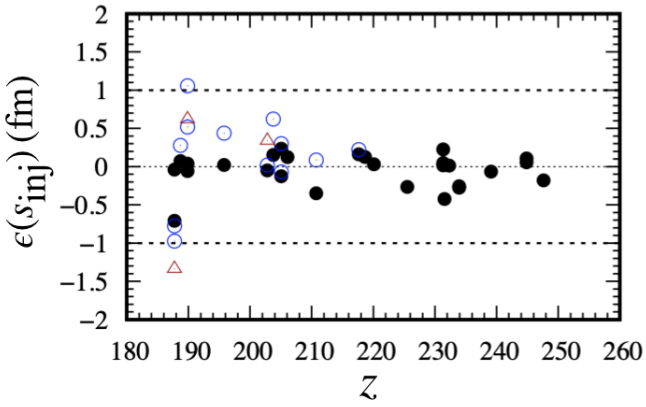

Figure 3.12: Deviations, $\epsilon(s_{inj})$, of the predicted injection point distances from the deduced values as the function of the Coulomb parameter. The black points correspond to the 1n emission channel. The blue open circles and the brown triangles represent the 2n and 3n neutron emission channels, respectively. This is shown for the cold fusion reactions data used in the fit (given in Table 3.1). The predicted values are obtained using the modified injection point distance formula given by Eq. (3.21).

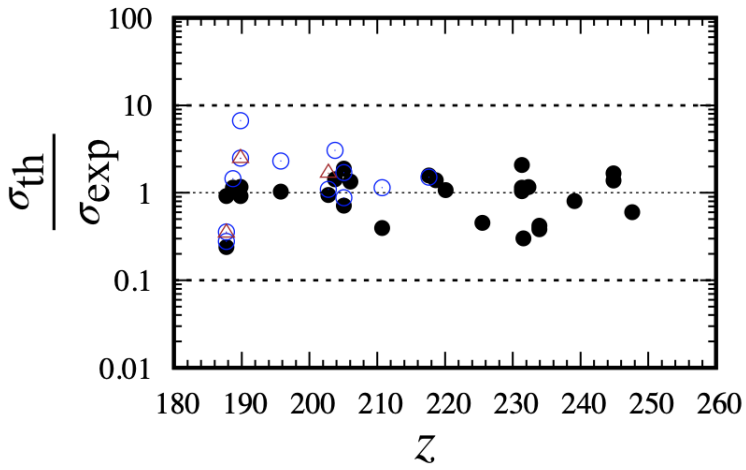

Figure 3.13: Comparison of the calculated cross sections (σ_{th}) with the corresponding experimental (σ_{exp}) production cross sections in the maxima of the excitation functions. The ratio $\left(\frac{\sigma_{th}}{\sigma_{exp}}\right)$ is evaluated for the reactions given in Table 3.1. z is the Coulomb parameter. The black points, blue, and brown open triangles represent 1n, 2n and 3n channels, respectively. The predictions are made using the injection point distance given by Eq. (3.21).

3.1.7 Global Injection Fit for Cold and Hot Reactions

The objective here is to optimise the parameters of the modified injection point distance formula (s_0, Ω and β_{ss}) to describe both cold and hot reaction data. This would allow us to replace the separate cold and hot fusion reaction formulas with one parameterization.

The procedure here is the same as previously, but the fit is made to both cold and hot reaction data sets from Tables 3.1 and 3.2, combined. The fitting function is given by Eq. (3.20). The obtained parameters are: $s_0 = (17.548 \pm 1.281)$ fm, $\Omega = (-0.051 \pm 0.005)$ fm, and $\beta_{ss} = (0.813 \pm 0.066) \times 10^{21}$ s^{-1}, and the new modified injection point distance parameterization is given as

$$s_{\text{inj}}^{\mathcal{M}} = 17.54 - 0.051z - \frac{c}{0.813 \times 10^{21}} \sqrt{\frac{2\langle K \rangle_{\text{rem}}}{\mu c^2}}. \tag{3.22}$$

Let us focus briefly on how the combined cold and hot fusion reaction data set affects the fit coefficients compared to the fit to cold fusion reactions only in the previous Subsection 3.1.7. First, the s_0 has increased by approximately 10% while the Ω parameter decreased by 6%. The β_{ss} decreased by 50%. The decrease in β_{ss} offsets the impact due to the increase in the s_0 value. The small change in the Ω parameter indicates that the hot fusion systematic does not strongly depend on the Coulomb impact parameter z. This case is where the same projectile induces all the hot fusion reactions. The quality of the fitted parameters in predicting the deduced injection point distances is shown in Fig. 3.14

Panel (a) of Fig. 3.14 illustrates a comparison of the injection point distance calculations using Eq. (3.22) with the experimental deduced values. The figure shows that the $s_{\text{inj}}^{\mathcal{M}}$ for the 1n channel depicted with the black times symbol are more enhanced in comparison with experimental deduced values shown by the black points. On the contrary, the $s_{\text{inj}}^{\mathcal{M}}$ for 2n and 3n channels, which are illustrated by the plus and the open triangle, respectively, are underestimated. Panel (b) illustrates a similar plot for the hot fusion data using Eq. (3.22). Here, the $s_{\text{inj}}^{\mathcal{M}}$ are shown in the black points, and the brown circles correspond to the experimental deduced values. In contrast with the cold fusion data, $s_{\text{inj}}^{\mathcal{M}}$ compared well with the experimental deduced values.

These observations are further revealed by the residual plots in Fig. 3.22. Here, the black points are the residual for the 1n neutron emission channel, which, as illustrated by the figure, are below $\epsilon(s_{\text{inj}})$ in comparison to what is seen Fig. 3.12. The $s_{\text{inj}}^{\mathcal{M}}$ for the 2n and 3n channels, as illustrated by the open circles and the brown triangles, are mostly above the line $\epsilon(s_{\text{inj}})$. The green triangles correspond to the $s_{\text{inj}}^{\mathcal{M}}$ residuals on the hot fusion experimental deduced injection values, which are within $\pm$1fm margin.

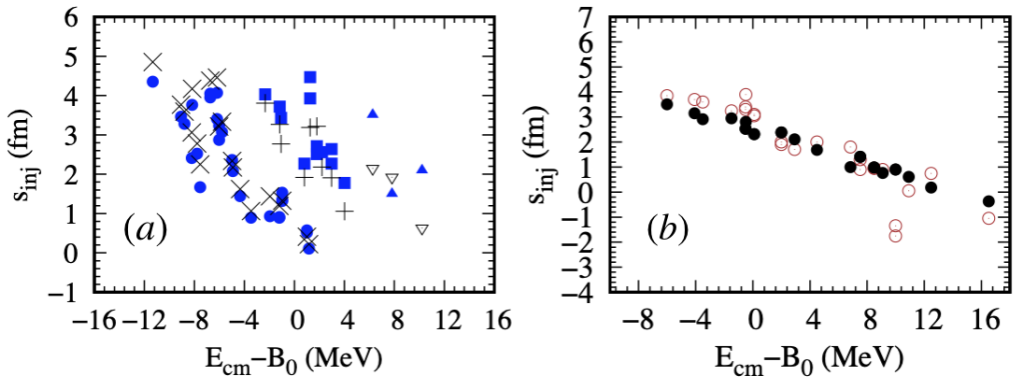

Figure 3.14: Comparison of the calculated and obtained from the experimental data injection point distances vs $(E_{cm}-B_0)$. Panel (a) shows cold fusion data from the Table 3.1. Here, the experimental deduced values are shown in blue, where points, squared and solid triangles correspond to the 1n, 2n and 3n channels, respectively. The corresponding model calculations are shown by the black markers: times, plus, and the open triangles. Panel (b) depicts the data corresponding to the hot fusion reactions. Here, the open brown symbols denote the experimentally obtained values, while the black points are calculated. This is shown for the data in Table 3.2. The calculated values are obtained using Eq. (3.22).

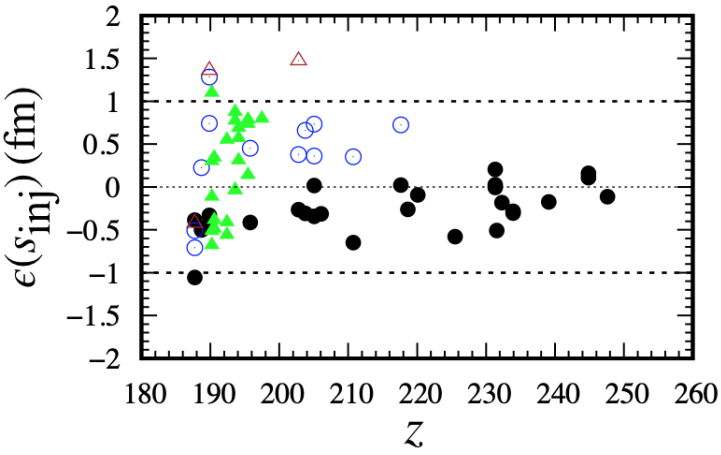

Figure 3.15: Deviations, $\epsilon(s_{inj})$, of the predicted injection point distances from the deduced values as the function of the Coulomb parameter. The black points correspond to the 1n emission channel. The blue open circles and the brown triangles represent the 2n and 3n neutron emission channels, respectively. This is shown for the cold fusion reactions data used in the fit (given in Table 3.1). The green triangles correspond to the hot fusion data in Table 3.2. The predicted values are obtained using the modified injection point distance formula given by Eq. (3.22).

The quality of the new procedure is demonstrated for the cold fusion experimental residue cross section in Fig. 3.16 using $\left(\frac{\sigma_{th}}{\sigma_{exp}}\right)$. The figure shows that the model's predictive power for the cold fusion data is reduced compared to the parametrization in the previous subsection. These are evident from the injection distance and residual plots in Fig. 3.14 and 3.15, respectively. On the contrary, Fig. 3.15 shows that predictions for the hot fusion

reactions are similar to the original version of the injection point distance formula (see Eq. (3.16)). The results show great promise in combining cold and hot fusion descriptions using one systematic fit.

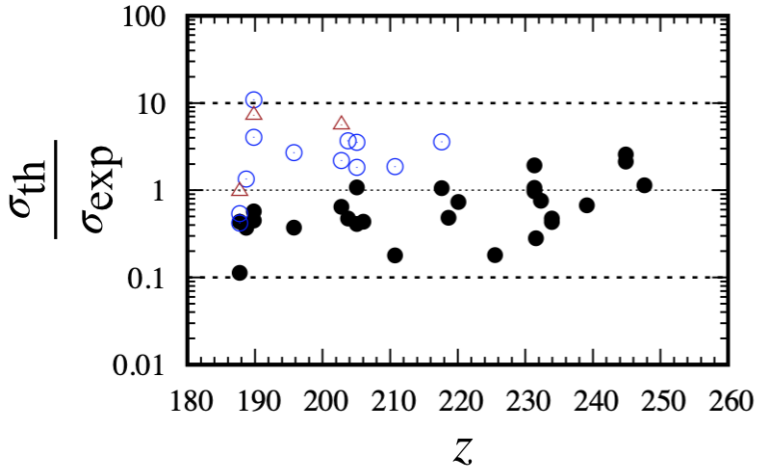

Figure 3.16: Comparison of the calculated cross sections (σ_{th}) with the corresponding experimental (σ_{exp}) production cross sections in the maxima of the excitation functions. The ratio $\left(\frac{\sigma_{\text{th}}}{\sigma_{\text{exp}}}\right)$ is evaluated for the reactions given in Table 3.1. z is the Coulomb parameter. The black points, blue, and brown open triangles represent 1n, 2n and 3n channels, respectively. The predictions are made using the injection point distance given by Eq. (3.22).

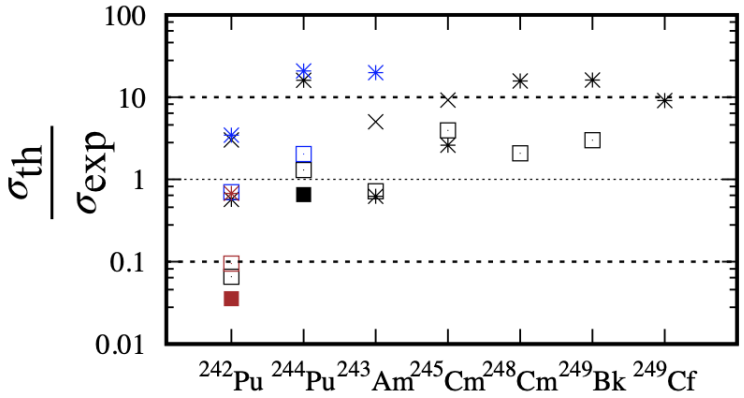

Figure 3.17: Comparison of theoretical and experimental evaporation residue cross sections for hot fusion data given in Table 3.2. $\left(\frac{\sigma_{\text{th}}}{\sigma_{\text{exp}}}\right)$ is the ratio of the theoretical predictions to the experimental values evaluated in a maximum of a given channel. The 2n, 3n, 4n and 5n reaction channels are depicted by the cross, star, open square and solid squares symbols, respectively. Here, the colours: black, blue, and brown correspond to the laboratories in Dubna, GSI (TASCA), and LBNL, where these cross sections were measured. The theoretical calculations use the injection point distance function in Eq. (3.22).

Until now, we have shown fits for different parameterizations of the injection point distances. The goal is to determine and apply the best fit to evaluate the complete excitation functions for studied reactions. In that regard, the optimised parameters for the injection distance given by Eqs. (3.21) and (3.22) are used to evaluate the excitation functions for cold and hot fusion reactions, respectively. There are no particular preferences for choosing Eq. (3.22) for the hot fusion since all the optimised injection distance functions give similar descriptions of the data.

As presented in Fig. 3.18, the excitation functions for the cold fusion reactions are well reproduced. The optimal bombarding energies are also well-reproduced for most of the calculated excitation functions. The exception here is ^{58}Fe+^{208}Pb reaction, for which the predicted maximum is shifted by about 1.2 MeV to higher energies. This could be further investigated.

Similarly, Fig. 3.19 shows the excitation functions calculated for the hot fusion reactions. Unfortunately, the model calculations have not reproduced the optimal bombarding energies for all presented reactions. The differences are usually greater than a typical energy resolution of the experimental data, which is ±2 MeV. The bumps on the curves visible at the highest energies are due to the limitation of the s_{inj} to -2 fm. At this limit, the formation probability tends to plateau with increasing energy, as shown in the curves in Fig. 3.8.

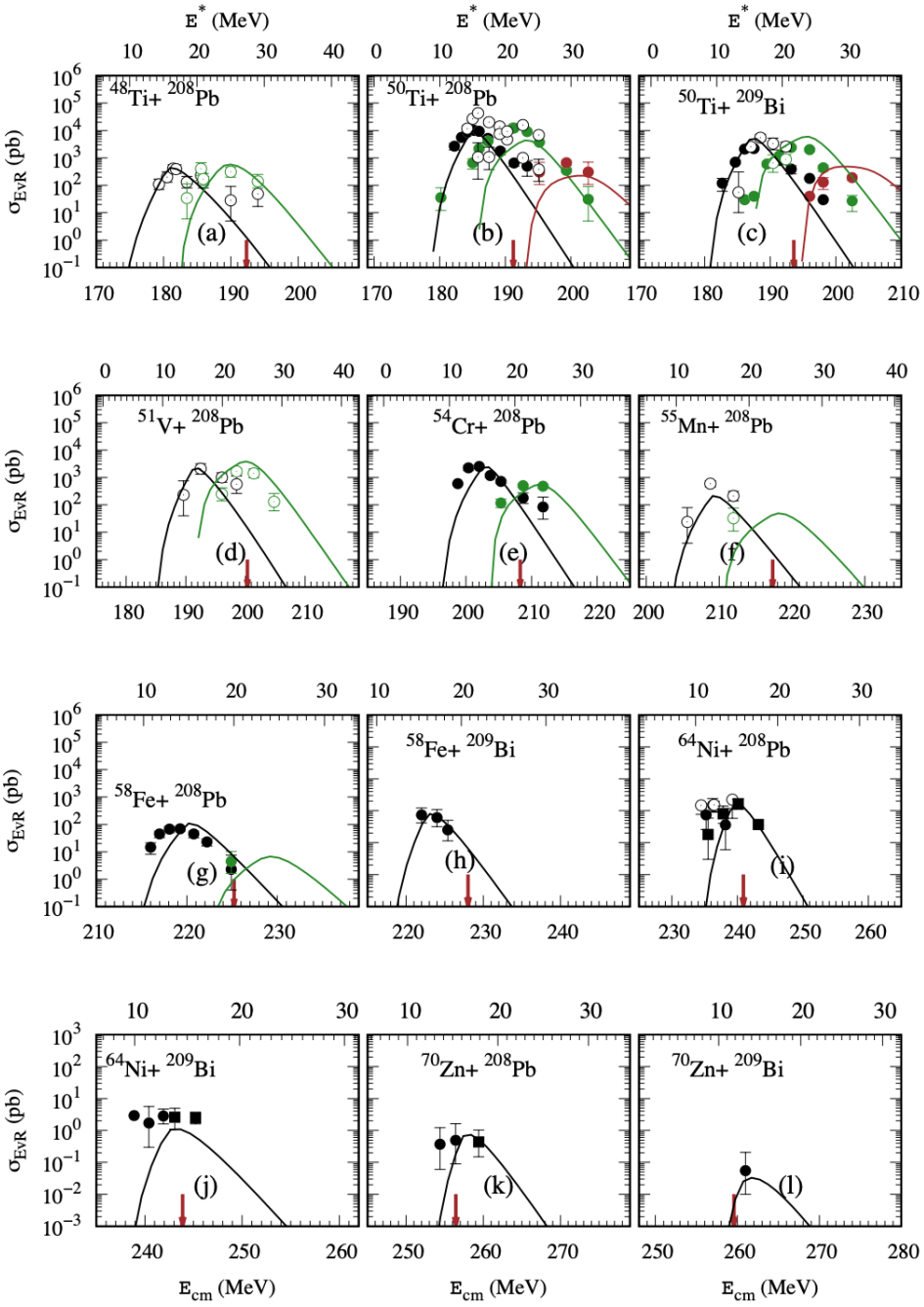

Figure 3.18: The excitation functions for the cold fusion reactions using the optimised injection point distance parametrization given by Eq. (3.21). Here, the black solid points are the GSI data, the open circles are LBNL data, and the solid squares are RIKEN data. The black, green, and brown curves correspond to the 1n, 2n and 3n channels. The position of the arrows is the respective mean Coulomb barrier of the reaction. The references to the data are indicated in Table 2.2.

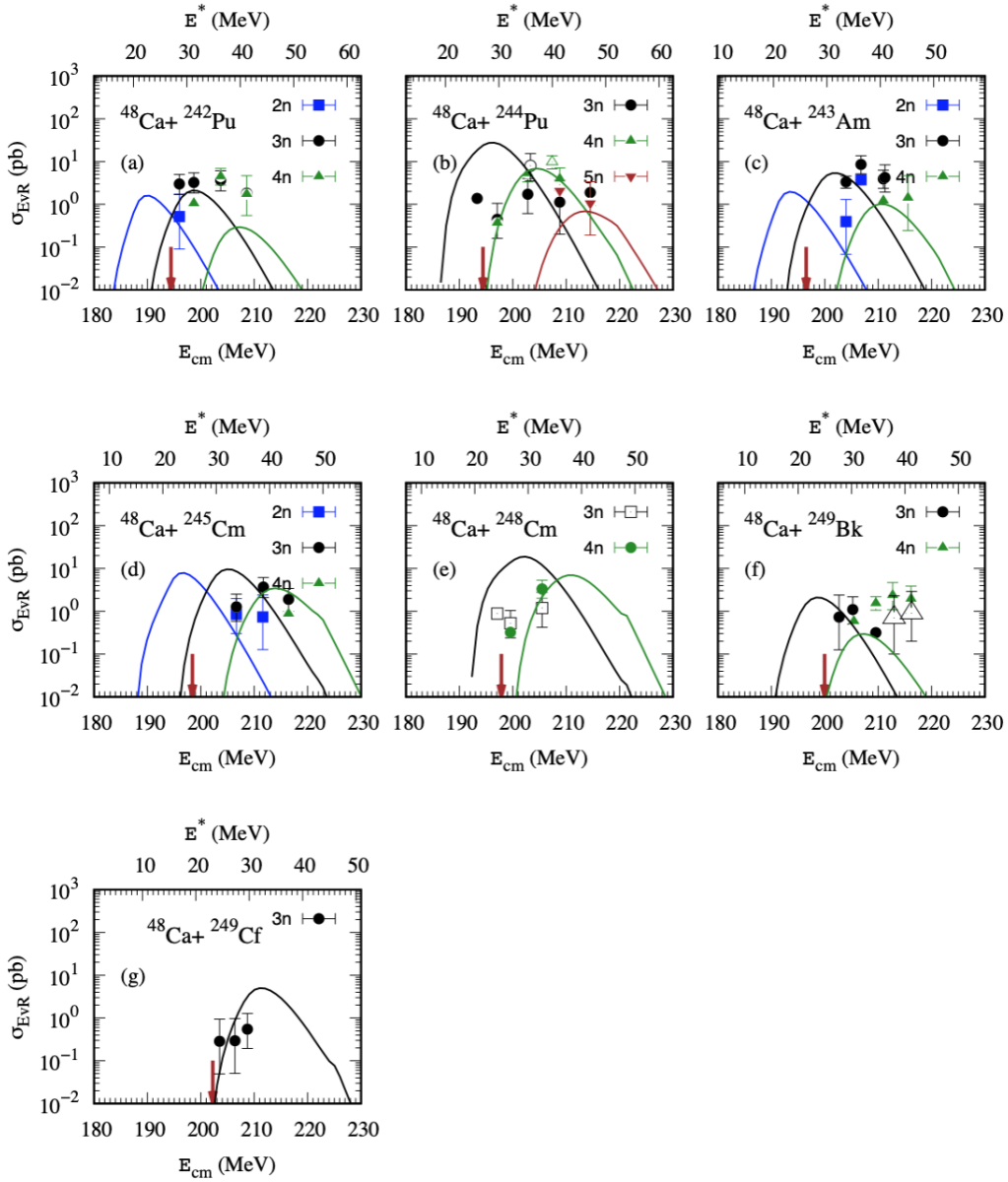

Figure 3.19: The calculated excitation functions for the hot fusion reactions using the optimised injection point distance parametrization given by Eq. (3.21). Here, the solid symbols correspond to the data taken from DUBNA, and the open symbols denote that of the GSI (TASCA). The 2n, 3n, 4n and 5n channels are represented by the blue, black, green, and brown symbols, respectively. The references to the experimental data are indicated in Table 2.3. The brown arrows indicate the positions of the mean Coulomb barriers.

3.2 Angular momentum Dependent s_{inj} Parameterisation

In the previous section, we optimized the parameters (s_0 and β_{ss}) for the injection point distance parameterization for hot and cold fusion reactions. However, we observed an energy-dependent shift in both parameterizations (Eqs. (3.10) and (2.117)), suggesting that the injection point distance s_{inj} should also be a function of angular momentum. In this section, we will detail the implementation and assess the impact of the angular momentum-dependent injection point distance parametrization on the evaporation residue cross section.

3.2.1 Partial Remaining Kinetic Energy

In the previous section, the remaining kinetic energy ($K_{\text{rem}}(B, \ell)$) of the capture events was averaged over all impact parameters and the Coulomb barrier distribution, as given by Eq. (3.9). However, to evaluate the remaining kinetic energy for each partial wave, it will be averaged only over the Coulomb barrier distribution, with the angular momentum held fixed:

$$K_{\text{rem}}(E_{\text{cm}}, \ell) = \frac{\int_0^{+\infty} \theta\left(E_{\text{cm}} - B - E_{\text{rot}}\right)\left(E_{\text{cm}} - B - E_{\text{rot}}\right) P(B)\, dB}{\int_0^{+\infty} \theta\left(E_{\text{cm}} - B - E_{\text{rot}}\right) P(B)\, dB}, \tag{3.23}$$

where, $\theta(E_{\text{cm}} - B - E_{\text{rot}})$ is the Heaviside step function. As we have seen previously in Section (2.1.1), the denominator evaluates to the Coulomb barrier transmission coefficient:

$$\begin{aligned} T_l(E_{\text{cm}}, \ell) &= \int_0^{+\infty} \theta\left(E_{\text{cm}} - B - E_{\text{rot}}\right) P(B)\, dB, \\ &= \frac{1}{2}\left(1 + \text{erf}\left(\mathcal{X}(E_{\text{cm}}, \ell)\right)\right). \end{aligned} \tag{3.24}$$

The final expression for the partial remaining kinetic energy (Eq. (3.23)) is given as:

$$\begin{aligned} K_{\text{rem}}(E_{\text{cm}}, \ell) &= \frac{\int_0^{B_{\max}(\ell)} \left(E_{\text{cm}} - B - E_{\text{rot}}\right) \exp\left(-\frac{(B-B_0)^2}{2\sigma_B^2}\right) dB}{\sqrt{2\pi}\sigma_B T_\ell(E_{\text{cm}}, \ell)}, \\ &= \sqrt{2}\sigma_B \mathcal{X}\left(E_{\text{cm}}, \ell\right) + \frac{\sigma_B \exp\left(-\mathcal{X}\left(E_{\text{cm}}, \ell\right)^2\right)}{\sqrt{2\pi} T_\ell\left(\mathcal{X}(E_{\text{cm}}, \ell)\right)}. \end{aligned} \tag{3.25}$$

Here, $\mathcal{X}(E_{\text{cm}}, \ell) = \frac{E_{\text{cm}} - B_0 - \frac{\hbar^2 \ell(\ell+1)}{2\mu R_B}}{\sqrt{2}\sigma_B}$. σ_B and B_0 are the width and the mean of the Coulomb barrier distribution given by Eq. (2.30) and (2.21), respectively. μ and R_{B} are the reduced mass of the colliding nuclei and the position of the effective Coulomb barrier.

Fig. 3.20 shows remaining kinetic energy denoted as K_{rem} for different values of ℓ as a function of $E_{\text{cm}} - B_0$. The figure demonstrates an inverse relationship between remaining

kinetic energy and angular momentum despite a general increase with the centre of mass energy. Higher angular momentum increases the effective entrance barrier, effectively reducing the remaining kinetic energy. The solid red line in the figure represents the average remaining kinetic energy given by Eq. (3.9). In contrast, the dashed lines correspond to the remaining kinetic energies ($K_{\rm rem}(E_{\rm cm}, \ell)$) of a specific angular momenta. The figure shows more remaining kinetic energies for smaller angular momenta than averaged momentum calculations for the same energy. The trend reverses for the larger values of the angular momentum. The effect of these dynamics on the partial wave injection point distances $s_{\rm inj}^{\mathcal{N}}(E_{\rm cm}, \ell)$ is shown in Fig. 3.21.

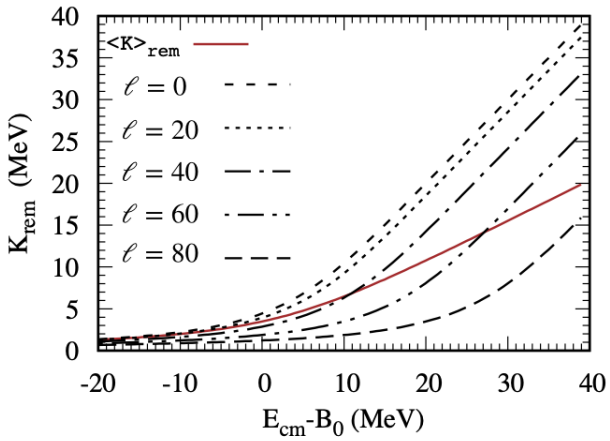

Figure 3.20: The remaining kinetic energy ($K_{\rm rem}$) for different values of ℓ (dashed lines) of as a function of $E_{\rm cm} - B_0$. The solid red and black dashes denote average (Eq. 3.9) and partial (the (Eq. 3.25)) remaining kinetic energies. This is shown for ^{58}Fe+^{208}Pb as an example. Here, σ_B= 5.6 MeV and B_0 = 225 MeV.

With the inclusion of the angular momentum in the remaining kinetic energy, the new parametrization of the injection point distance ($s_{\rm inj}^{N}$) is given as,

$$s_{\rm inj}^{\mathcal{N}}(E_{\rm cm}, \ell) = s_0 - \frac{c}{\beta_{\rm ss}}\sqrt{\frac{2K_{\rm rem}(E_{\rm cm}, \ell)}{\mu c^2}}. \tag{3.26}$$

Here, all the parameters are as defined previously. A key question is how incorporating rotational energies into evaluating the remaining kinetic energy, instead of the sum averaged in Eq. (3.10), influences this shift and, eventually, the formation probability. In order to investigate the tendency of $s_{\rm inj}^{\mathcal{N}}(E_{\rm cm}, \ell)$ as a function of the ℓ, the parameters s_0 and β_{ss} are set for an arbitrary values: s_0 = 6 fm and $\beta_{\rm ss} = 2\times10^{21}$ s^{-1} as shown in Fig. 3.21. The solid red curve represents $s_{\rm inj}$ evaluated using the average remaining kinetic energy given in Eq. (3.9), while each of the dashed lines corresponds to the $\ell-$dependent approach (Eq. (3.26) shown for various values of ℓ.

As previously gleaned from Fig. 3.20, increasing ℓ results in less remaining kinetic energy. Therefore, one expects a minimal shift in the initial condition s_0, which results in a less steep slope of $s_{\rm inj}(E_{\rm cm}, \ell)$ with increasing centre of mass energy for high values of ℓ. Given the impact of the ℓ on the injection point distances, the optimized parameters (s_0

and β_{ss}) from Subsection 3.1.2 of Chapter 4 cannot be simply substituted into Eq. (3.26). This is evident in the Figs. 3.27 and 3.28 as test cases. Hence, we need to re-optimise these parameters, accounting for all partial waves in the formation phase.

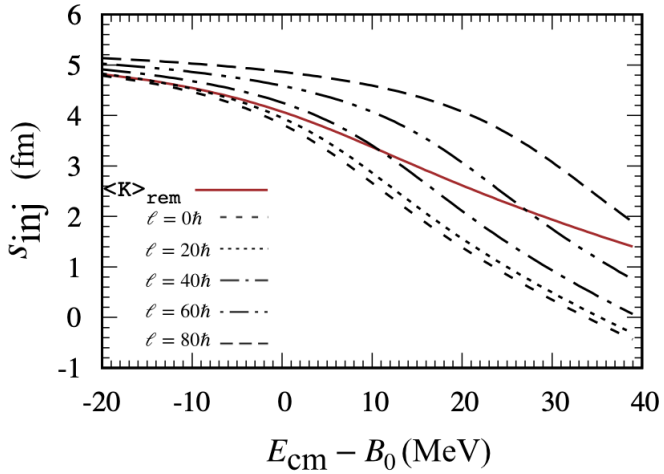

Figure 3.21: The injection point distance, s_{inj} (Eq. (3.26)) shown for various values of angular momentum (dashed lines) as a function of $E_{cm} - B_0$. The solid red line represents calculation using the average remaining kinetic energy given by Eq. (3.10). This is shown for ^{58}Fe+^{208}Pb, where σ_B= 5.6 MeV and B_0=225 MeV. Here, s_0 = 6 fm and $\beta_{ss} = 2 \times 10^{21}$ s^{-1}.

Having defined injection point distances in terms of angular momentum, the critical question becomes, what is the impact on formation probability and the simulated residue cross section? To answer this, we will investigate each dynamics stage: capture, formation, and survival probability as a function of angular momentum. This study will provide insights into how angular momentum influences the dynamics at each simulation stage and the overall reaction process.

3.2.2 Partial Evaporation Residue Cross Section

This section shows a demonstration of the ℓ-dependent formalism. The Figs. 3.22 and 3.23 illustrate selected quantities evaluated for ^{58}Fe + ^{208}Pb and ^{48}Ca + ^{243}Am reactions. Each stage of the reaction (capture, formation, and survival) is discussed as a function of angular momentum. One neutron channel in the reaction ^{58}Fe + ^{208}Pb at the centre of mass energy of 220 MeV and four neutron channel in ^{48}Ca + ^{243}Am reaction at 205 MeV will be discussed in details.

The panel (a) of Fig. 3.22 represents the partial capture cross section for ^{58}Fe + ^{208}Pb system evaluated based on Eq. (2.5). The inset (the panel (b)) is the formation probability of ^{266}Hs as a function of angular momentum. The formation probability was evaluated using Eq. 3.26. For a demonstration purposes the parameters s_0 and β_{ss} were taken as s_0 = 12.478 fm and $\beta_{ss} = 0.314 \times 10^{21}$ s^{-1} for ^{58}Fe + ^{208}Pb reaction and s_0 = 10.572 fm and $\beta_{ss} = 0.550 \times 10^{21}$ s^{-1} for the ^{48}Ca + ^{243}Am reaction. These parameters were obtained using Eq. (3.16).

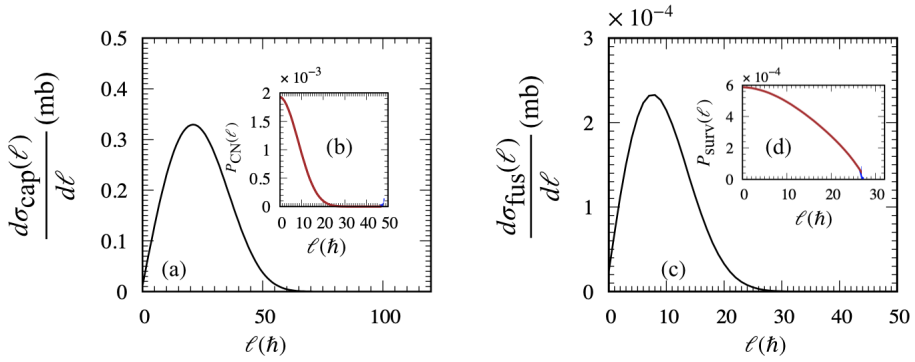

Figure 3.22: Angular momentum dependencies of various quantities for ^{58}Fe+^{208}Pb reaction at E_{cm} = 220 MeV. (a) Partial capture cross section, (b) formation probability and (c) partial fusion cross section. Panel (d) shows the survival probability for the 1n channel. The mean Coulomb barrier (B_0) is 225 MeV, and the Q-value of the reaction is -205 MeV.

The product of the capture cross section (panel (a)) and the formation probability (panel (b)) gives the partial fusion cross section shown in panel (c). The probability that the compound nucleus will survive fission and emit a neutron is denoted by the inset panel (d). Fig. 3.23 describes the same quantities for the ^{48}Ca + ^{243}Am reaction. In this case, the survival probability is evaluated for the four neutron emission channel.

For the respective reactions, the capture cross section increases with ℓ and peaks at approximately 21 and 46, then decreases with increasing ℓ due to decreasing Coulomb barrier transmission coefficients. As shown in panels (b) of both figures, the formation probability is the highest at $\ell = 0$. The formation probability decreases with increasing ℓ, which is caused by increasing the fusion barrier. The projectile-target touching configuration is less compact than the fusion saddle configuration. The moment of inertia of the saddle configuration is lower, and the energy of this point rises quicker with angular momentum than the energy of the injection point. This raises the effective height of the barrier with increasing ℓ (see Eq. (2.112)).

The panel (d) of Fig. 3.22 illustrates the partial survival probability of one-neutron emission channel in ^{58}Fe + ^{208}Pb reaction. Panel (d) in Fig. 3.23 shows 4n channel for ^{48}Ca+^{243}Am. In both cases, the survival probability decreases with increasing angular momentum. The height of the fission barrier is inversely related to the angular momentum, and for higher partial waves, the survival probability is getting lower [77].

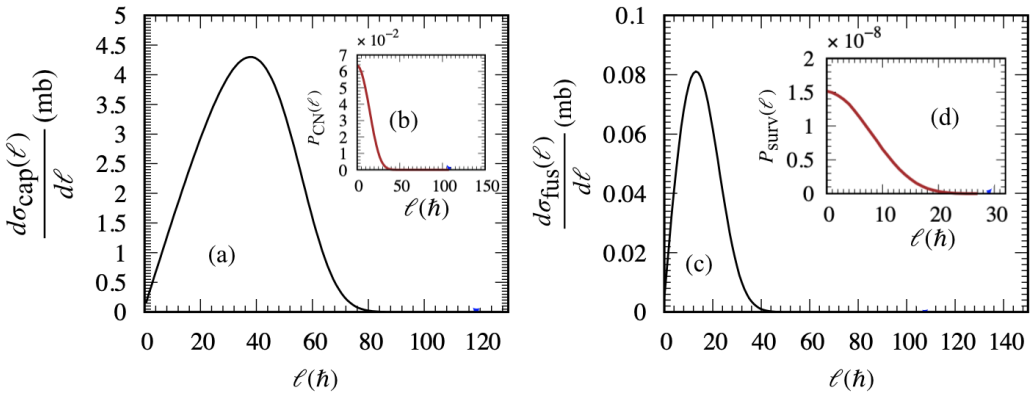

Figure 3.23: Angular momentum dependencies of various quantities for ^{48}Ca+^{243}Am reaction at E_{cm} = 205 MeV. (a) Partial capture cross section, (b) formation probability and (c) partial fusion cross section. Panel (d) shows the survival probability for the 4n channel. The mean Coulomb barrier (B_0) and the Q-value are 196 MeV and - 170 MeV, respectively.

The figures 3.22 and 3.23 demonstrate the role of angular momentum in the calculations. As mentioned before, the reduction in the fusion cross section is due to the increasing fusion hindrance with increasing ℓ. This is quantified by the formation probability, which is the highest at $\ell = 0$ at the order 10^{-3} and 10^{-2} for ^{266}Hs and ^{291}Mc, respectively, and then decreases. Furthermore, the survival probability is of the order of 10^{-4} (for ^{58}Fe + ^{208}Pb) and 10^{-8} (for ^{48}Ca + ^{243}Am) which indicates that fission is the dominate decay mode in the deexcitation process. The fission barriers in this mass region are rather low, as previously mentioned. Finally, the partial EvR cross sections for both reactions are presented in Fig. 3.24.

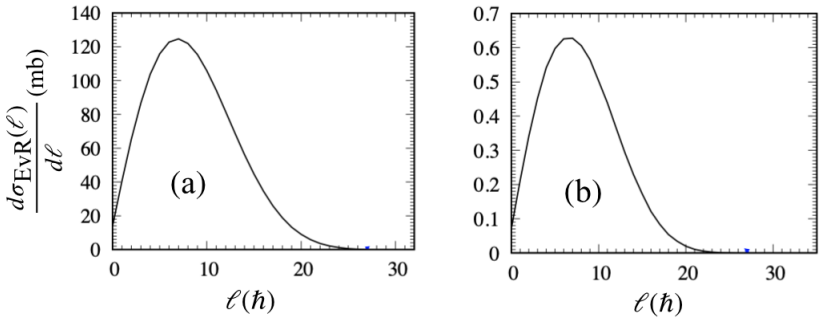

Figure 3.24: Panels (a) and (b) show partial evaporation residue cross sections (σ_{EvR}) as a function of angular momentum (ℓ) for ^{58}Fe + ^{208}Pb at E_{cm} = 220 MeV (1n channel) and ^{48}Ca + ^{243}Am at E_{cm} = 205 MeV (4n channel), respectively.

This can be further investigated by analysing the 2D spectrum distribution of the energy and angular momentum. These are shown in the Figs. 3.25 and 3.23 for the one and four neutron emission channels in the reaction ^{58}Fe + ^{208}Pb and ^{48}Ca + ^{243}Am, respectively. The colour scheme in the figures represents the magnitude of the cross section, with warmer colours (red, yellow) signifying higher values and cooler colours (blue, green) indicating lower values. As we move away from the peak, the cross section values decrease, indicating

a lower probability of emission at other energy and angular momentum combinations. This decrease may be attributed to decreasing survival probability at high energies and angular momenta. The figure allows one to identify the specific energy and angular momentum ranges where significant changes in the cross section occur, illustrating the steep dependence of the reaction dynamics on these parameters. In both cases, the highest contribution to the EvR cross section is for $\ell \approx 8$, which clearly shows that super-heavy nuclides are mostly formed in rather central collisions.

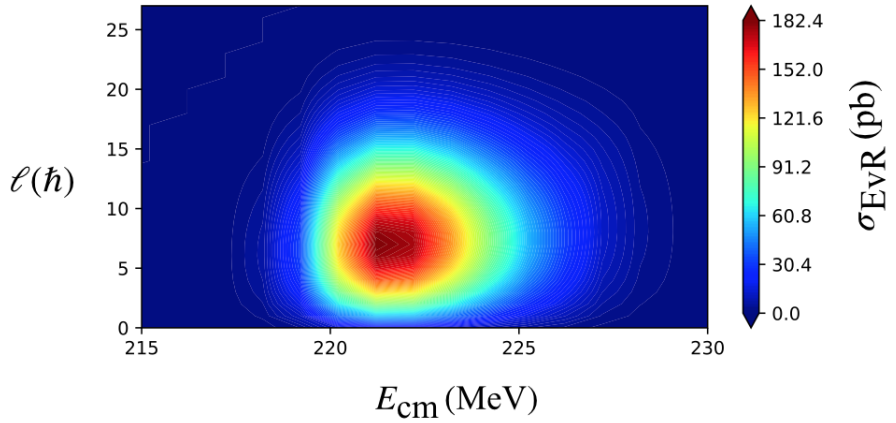

Figure 3.25: 2D contour plot showing the evaporation residue cross section for the reaction ^{58}Fe + ^{208}Pb in 1n channel, as a function of the centre of mass energy (E_{cm}) and angular momentum (ℓ).

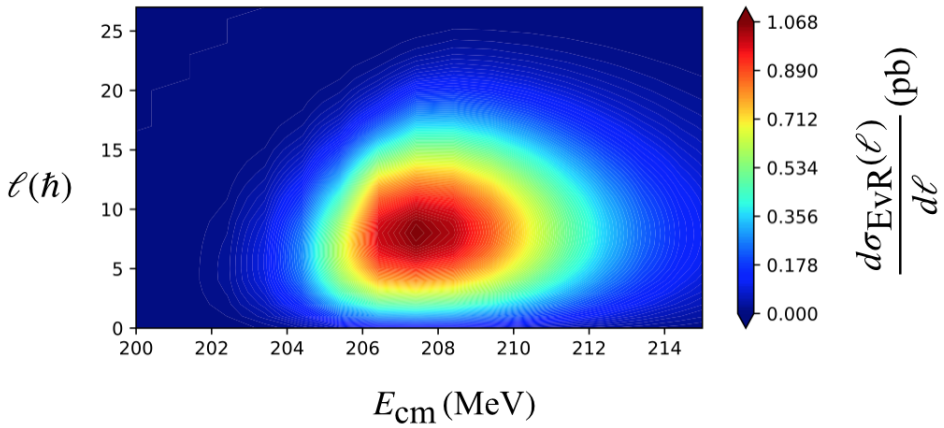

Figure 3.26: 2D contour plot showing the evaporation residue cross section for the reaction ^{48}Ca + ^{243}Am in 4n channel, as a function of the centre of mass energy (E_{cm}) and angular momentum (ℓ).

Before concluding this section, we will attempt to highlight the need to re-optimise the parameters of the angular momentum-dependent injection model (Eq. (3.26)). To begin, the formation probabilities and the residue cross sections are evaluated for the reactions ^{58}Fe+^{208}Pb and ^{48}Ca+^{243}Am as shown in Figs. 3.27 and 3.28, which exemplify test cases of cold and hot fusion reactions, respectively.

Panel (a) of each figure compares the average formation probability (Eq. (2.122)) obtained using the $\ell-$dependent injection point distance (dashed red lines) to that obtained with $\ell-$independent (solid black lines). Although the average formation probability is not directly used to calculate the production cross section (shown in panel (b) of Figs. 3.27 and 3.28), it serves as a valuable indicator of the impact of the ℓ treatment in evaluating s_{inj}. Here, dash curves show smoothing at the limit $s_{\text{inj}} = -2$ fm due to the inclusion of the angular momentum.

As shown in Figs. 3.20 and 3.21, for angular momenta less than 40, there is more remaining kinetic energy, resulting in a shorter injection point distance compared to the situations with higher angular momentum. Shorter s_{inj} corresponds to a lower fusion barrier and, consequently, to a higher formation probability, as detailed in Subsection 2.4.2.4 of the previous chapter. This leads to the higher production cross section when using the partial remaining kinetic energy formalism compared to the angular momentum-averaged remaining kinetic energy formalism.

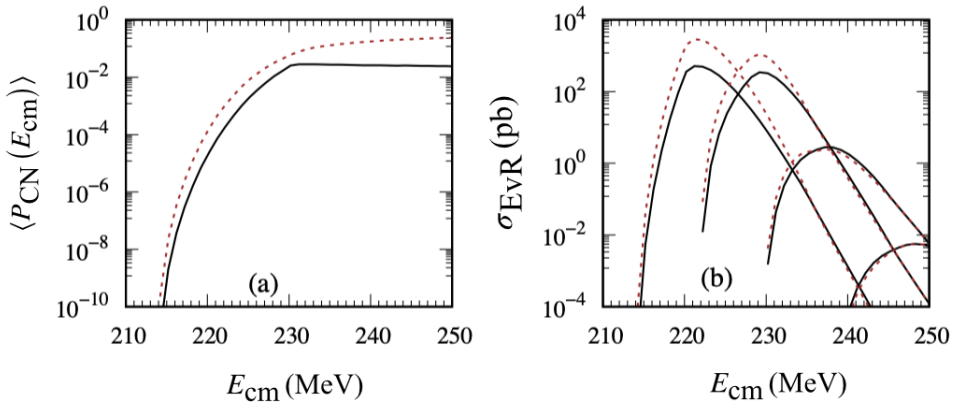

Figure 3.27: The impact of angular momentum dependent s_{inj} on the formation probability and production cross section for the ^{58}Fe + ^{208}Pb reaction. (a) The average formation probability ($\langle P_{\text{CN}}(E_{\text{cm}})\rangle$) as a function of E_{cm}. (b) The production cross section (σ_{EvR}) in 1n, 2n, 3n, and 4n channels. The solid black lines represent calculations using $\ell-$independent s_{inj} (Eq. (3.10)) whereas, the dashed lines are $\ell-$dependent s_{inj} (Eq. (3.26)). The curves are evaluated using the parameters $s_0 = 12.478$ fm and $\beta_{\text{ss}} = 0.314 \times 10^{21}$ s^{-1} of the injection point distance.

Panel (b) of Figs. 3.27 and 3.28 further illustrate this effect by showing the production cross sections evaluated using both $\ell-$independent s_{inj} (red dashed lines) and the $\ell-$dependent s_{inj} (black solid lines). At lower energies, where the total angular momentum contributing to the reaction is not large, the production cross section calculated with the $\ell-$dependent s_{inj} is larger. However, this trend reverses as the energy increases and the total angular momentum contributing to the production cross section increases as well, as explained by Fig. 3.21.

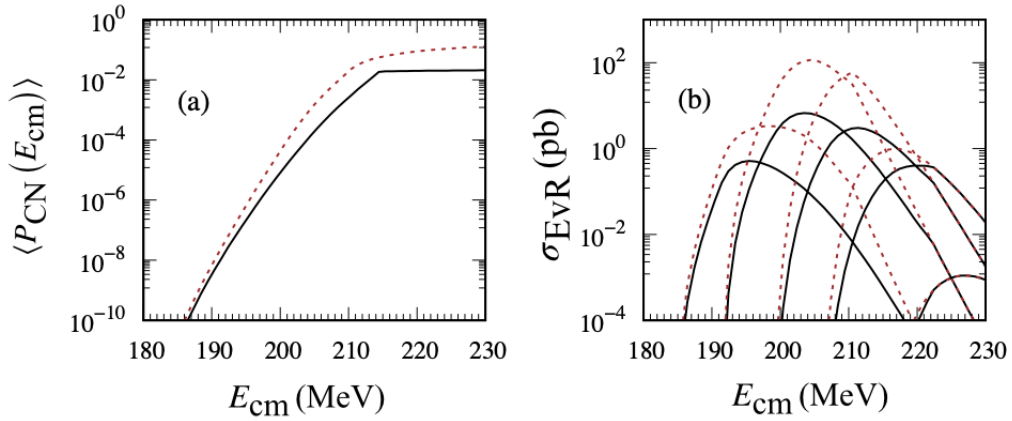

Figure 3.28: The impact of angular momentum dependent s_{inj} on the formation probability and production cross section for the ^{48}Ca + ^{243}Am reaction. (a) The average formation probability ($\langle P_{CN}(E_{cm})\rangle$) as a function of E_{cm}. (b) The production cross section (σ_{EvR}) in 2n, 3n, 4n and 5n channels. The solid black lines represent calculations using $\ell-$independent s_{inj} (Eq. (3.10)) whereas, the dashed lines are that of $\ell-$dependent approach (Eq. (3.26)). The curves are evaluated using the parameters $s_0 = 10.572$ fm and $\beta_{ss} = 0.550 \times 10^{21}$ s^{-1} of the injection point parameterization.

In conclusion, this section evaluates the impact of angular momentum on the three reaction stages. The next step is to re-optimize the parameters s_0 and β_{ss} of the injection distance model (Eq. 3.26) to ensure a proper treatment of angular momentum.

3.3 Systematic Approach to fitting s_0 and β_{ss}

In the previous approach, as outlined in the Subsections 2.5.2 and 3.1.1, the parameters of the injection distance parameterization (s_0 and β_{ss}) were adjusted to the set of deduced injection point distances values (s^{d}_{inj}) from the experiment. Because of the angular momentum treatment, that approach cannot be applied to optimising Eq. (3.26) since it implies adjusting each wave's parameters. This is technically challenging. Therefore, a systematic fitting technique has been employed, as described below.

The systematic fit or the global optimization process aims at identifying a set of parameters (s_0 and β_{ss}) that provide the best overall fit across the given data set. This would be done using a readily available Bayesian optimisation algorithm [150]. Bayesian optimization is a technique that efficiently optimizes objective functions that are computationally expensive to evaluate. It is particularly well-suited for problems with continuous parameter spaces of moderate dimensionality (typically fewer than 20 dimensions) and can handle noisy function evaluations. At its core, Bayesian optimization constructs a probabilistic surrogate model, often using Gaussian process regression, to approximate the unknown objective function. This surrogate model predicts the objective's value at unobserved points and quantifies the uncertainty in its predictions. By leveraging this uncertainty information, Bayesian optimization employs an acquisition function to strategically select the next point to sample, balancing exploration (probing uncertain regions) and exploitation (sampling where the surrogate predicts high values) [151].

3.3.1 A Systematic Approach with Bayesian Optimisation

In this study, we employ Bayesian optimization, leveraging the GP-Minimize Skopt library in Python, to solve optimization problems by identifying the parameter values that minimize our loss functions. The Bayesian optimization approach to solving the optimization problem revolves around finding optimal values of the input parameters that minimise (maximise) objective functions [150–152]:

$$p^* = \arg\min_{p \in \mathcal{P}} f(p) \tag{3.27}$$

Here $f(p)$ is the objective function to be minimised or maximised. $\mathcal{P}$ correspond to the parameter search space, while p^* are the optimal parameters in $\mathcal{P}$ that minimises (maximises) $f(p)$. The objective function is treated as a black box, meaning we do not have direct access to its mathematical form, and it is computationally expensive to evaluate.

The goal of the Bayesian optimisation is to iteratively (given by the Algorithm (1)) build a model of the $f(p)$ and use it to guide the search towards promising regions of the search space where optimal parameters could be found. This uses a probabilistic model, typically a Gaussian Process (GP). The GP provides a flexible and powerful way to model complex functions and guide the search towards promising regions of the parameter space with fewer function evaluations compared to a grid search or random search.

An integral part of the Bayesian optimization is using an acquisition function. The acquisition function is a strategy used to select the next point in the parameter space to evaluate based on the current output from the objective function. An example of an acquisition function aimed at optimizing (minimizing or maximizing) a given objective function is the lower confidence bound (LCB):

$$LCB(p) = \mu_{\mathrm{GP}}(p) \mp \kappa \sigma_{\mathrm{GP}}(p), \tag{3.28}$$

where $\mu_{\mathrm{GP}}(p)$ is the mean prediction of the objective function at a point x as determined by the Gaussian Process (GP) after a certain number of evaluations. The $\sigma_{\mathrm{GP}}(p)$ represents the model's uncertainty about the objective function's value at a point p. The LCB acquisition function subtracts a scaled version of this uncertainty from the mean prediction, encouraging the exploration of regions where the model is less certain about the true objective function value. The scaling factor κ regulates the optimisation process's balance between exploration and exploitation. The use of the LCB acquisition function allows one to ensure control over the trade-off between exploration and exploitation, leading to efficient optimisation.

The principle of Bayesian optimization is employed using the algorithm outlined below (Algorithm 1). The concept is based on an iterative process which systematically searches for the best possible parameters within the search space $\mathcal{P}$. Here, n_0 is the number of the initial data points selected from the parameter space, which is used to construct the Gaussian process model. $\mathcal{D}$ is the dataset of evaluated parameters p_n and the corresponding objective values $f(p)$. This is used to continually update the GP process to guide the optimisation process towards the optimum region of the search space. These steps are, subsequently, generalised to our optimisation problems in obtaining s_0 and β_{ss} using Kewpie2 code.

Algorithm 1 Overview of Pseudo Algorithm for Bayesian Minimisation

Require: Objective function $f(p)$, parameter space $\mathcal{P}$, initial design size n_0, maximum iterations $\mathcal{N}$, acquisition function $u(p)$
Ensure: Optimal parameters $p^* \approx \arg\min_{p \in \mathcal{X}} f(p)$
  Place a Gaussian Process (GP) prior on $f(p)$
  Select n_0 initial points $\{p_1, ..., p_{n_0}\}$ from $\mathcal{P}$
  Evaluate the objective function at initial points: $y_i = f(p_i)$ for $i = 1, ..., n_0$
  Initialize data set $\mathcal{D} = \{(p_1, y_1), ..., (p_{n_0}, y_{n_0})\}$
  for $n = n_0 + 1$ to N **do**
    Update the GP model with data set $\mathcal{D}$
    Optimize the acquisition function $u(p)$ over $\mathcal{P}$ to find $p_n = \arg\max_{p \in P} u(p)$
    Evaluate $y_n = f(p_n)$ and append (p_n, y_n) to $\mathcal{D}$
    if convergence criterion or other stopping condition is met **then**
      break
    end if
  end for
  Determine the point with the best observed value: $p^* = \arg\min_{(p,y) \in \mathcal{D}} y$
  return p^* (and optionally p^*_{GP})

3.3.2 Application of systematic fitting to Kewpie2 Simulations

The aim is to have optimised parameters s_0 and β_{ss} that are robust enough to reproduce each excitation function of the reactions in the Tables 2.2 and 2.3. Consistent with the algorithm (1), we will have to define a parameter search space for both s_0 and β_{ss}: $1 \leq s_0 \leq 13$ fm and $(0.001 \leq \beta_{\mathrm{ss}} \leq 3) \times 10^{21}$ s^{-1}. For each iteration in the parameter space, Kewpie2 simulates the production cross sections for all reactions in the data set. The theoretical predictions are then compared with the respective experimental production cross sections (maximum residue cross section) using a loss function. The loss functions are evaluated as the objective function during the optimisation process.

3.3.2.1 The Loss Functions

The fitting process is initially tested on the chi-squared (χ^2) and the modified chi-squared (χ^2_{mod}) as given by the Eqs. (3.29) and (3.30). However, due to their poor data description, we have adopted a hybrid loss function, which will be refered to in this study as the symmetrized loss function (χ^2_{sym}). The results on the symmetrized loss function are reported.

To begin, the χ^2 used in the optimisation is given as,

$$\chi^2 = \frac{1}{N-2} \times \sum_i^N \left(\frac{O_i - E_i}{u(O_i)} \right)^2, \tag{3.29}$$

where O_i and $u(O_i)$ are the experimental observation and the corresponding uncertainties. E_i stands for the model predictions, while N is the total number of observations or data

points, which normalizes the sum. The modified chi-squared is stated as,

$$\chi^2_{\text{mod}} = \frac{1}{N-2} \times \sum_i^N \left(\frac{O_i - E_i}{O_i} \right)^2, \tag{3.30}$$

where all the parameters are defined by Eq. (3.29). The χ^2 loss function is valued for incorporating the uncertainty associated with each experimental measurement. This is advantageous when the uncertainty of individual measurements varies significantly, as in the case of production cross sections associated with the synthesis of super-heavy elements. The χ^2 gives greater weight to observations with more minor uncertainties and penalizes larger ones. This effectively mitigates the impact of less reliable observations with significant uncertainties, resulting in a reliable model. On the other hand, the modified chi-square, χ^2_{mod}, does not account for measurement uncertainties. The normalisation by the magnitude of the observations (O_i) is expected to ensure each data point contributes to the total loss functions and that the fit is not biased. However, as indicated by Fig. 3.29 it leads to overfitting large experimental residue cross sections and under-estimating smaller ones.

The poor description of the data of the loss functions is partly because the experimental data span several orders of magnitudes (10^7). Hence, deviations from the small value experimental cross sections are poorly explained. To solve this, we used a symmetrised loss function:

$$\chi^2_{\text{sym}} = \frac{1}{N-2} \times \sum_i^N \frac{(O_i - E_i)^2}{O_i \times E_i}, \tag{3.31}$$

which can penalise both small and large deviations from experimental observations symmetrically, as demonstrated in Fig. 3.29. Figure 3.29 illustrates the tendency of the aforementioned loss functions as the function of a ratio of observed to expected values (O/E). This is particularly relevant to understanding how the choice of loss function influences the optimization process.

The black, brown, and blue curves represent the χ^2, χ^2_{mod}, and χ^2_{sym} loss functions, respectively. The χ^2 and χ^2_{mod} loss functions exhibit a steep rise for small O/E ratios, indicating a significant penalty for underestimating small observables. This characteristic encourages the optimization algorithm to prioritize accurately fitting such values with heavy penalties, further leading to their underestimation. The symmetric χ^2_{sym} loss function aims to mitigate the issue of underestimation by penalizing overestimation and underestimation symmetrically. This is shown in the figure, where both underestimation and overestimation of the data are penalised equally.

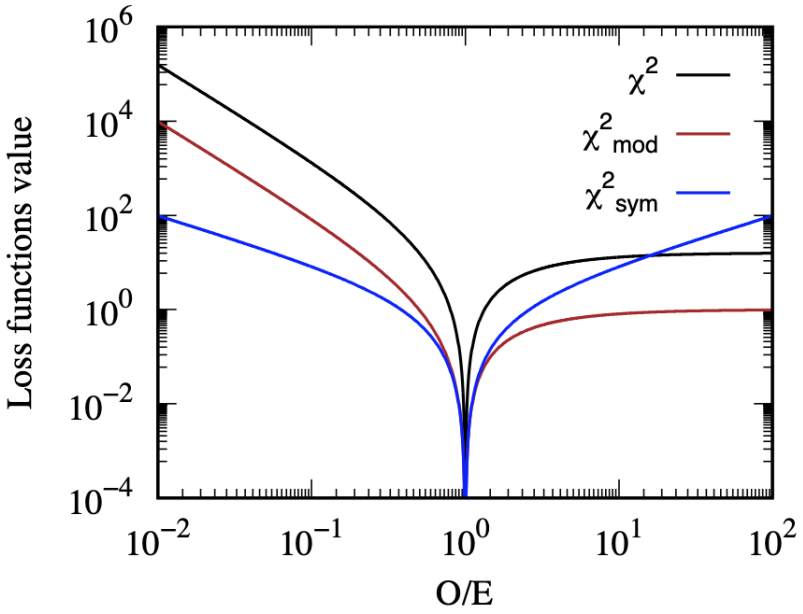

Figure 3.29: Comparison of different loss function values, χ^2 (in black), χ^2_{mod} (in brown), χ^2_{sym} (in blue) as a function of the ratio of observed to expected value (O/E). In χ^2 evaluation it was assumed that $u(O_i)/O_i = 0.25$ for demonstration purposes.

3.4 Testing the new fitting method with a ℓ-independent injection point

The objective of this section is to optimise the parameters (s_0 and β_{ss}) in the partial remaining kinetic energy injection point distance formula, which is referred to as the $\ell-$dependent injection model. However, before proceeding with fitting the $\ell-$dependent injection point distance, we would apply the systematic fitting technique to obtaining the coefficients of the parameters (s_0 and β_{ss}) of the injection distance with average remaining kinetic energy: $\ell-$independent injection point distance, which are obtained in Section 3.1.2. This exercise allows one to investigate the impact of different fitting techniques on optimising the parameters of the injection distance model. Furthermore, comparing the results allows one to benchmark the systematic fitting technique since it is the first time it will be applied to this problem.

The Bayesian optimization loop described in Algorithm 1 is applied to optimising the s_0 and β_{ss} on the experimental data within the respective search spaces mentioned above. For example, the search for the best parameters that minimise the loss function as a function of iteration is shown in Fig. 3.30. The figure shows that the Bayesian optimization algorithm iteratively refines its estimates of the optimal values for parameters s_0 and β_{ss} within the search space.

The main plot demonstrates a rapid initial decrease in the best objective value (lowest loss functions), followed by fluctuations as the algorithm explores the parameter space. The insets (a) and (b) show the exploration of the s_0 and β_{ss} search spaces at each iteration, respectively. The distinct patterns in the parameter sampling (insets a and b)

reveal different sensitivities to optimization. The parameter s_0 exhibits larger fluctuations, suggesting it is more sensitive to changes compared to β_{ss}, which shows less variation. This is likely because the preferred values of β_{ss} in the optimization lie within a smaller region of the search space. This implies that adjusting s_0 has a greater impact on the loss function than adjusting β_{ss}. Additionally, the pairing of s_0 and β_{ss} significantly influences the loss function, as opposite changes in these parameters appear to lead to a decrease, indicating a potential trade-off or correlated behaviour.

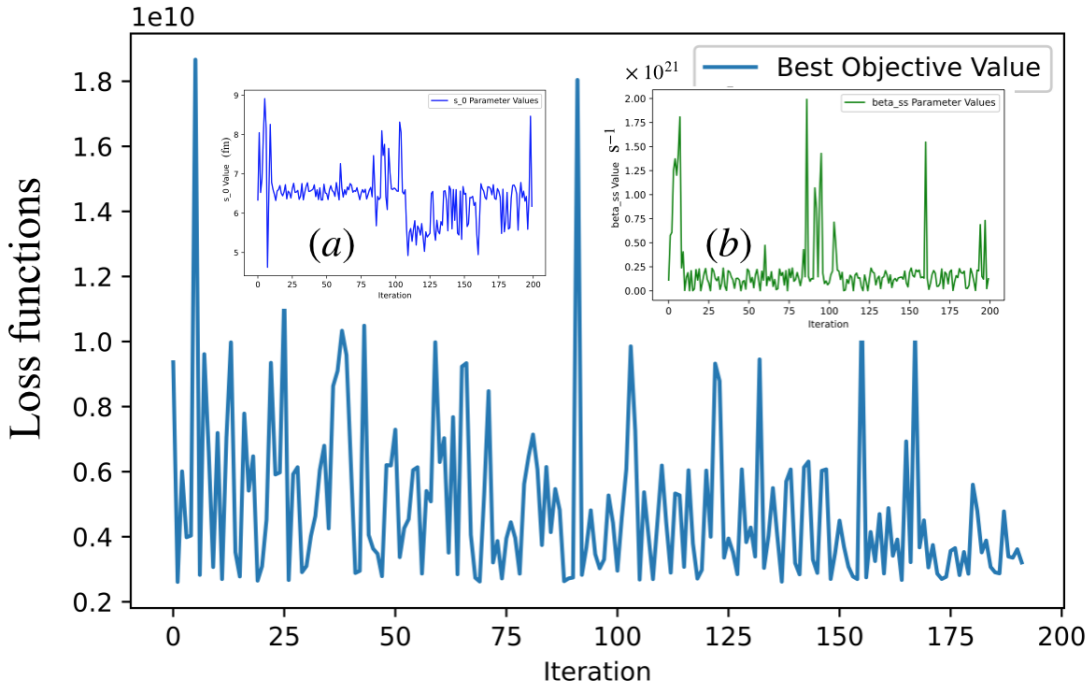

Figure 3.30: Bayesian Optimization for minimising the loss functions. The blue line represents the best MSE value achieved at each iteration, demonstrating the algorithm's iterative improvement in finding optimal parameter configurations.

3.4.1 Results

Here, only the results using χ^2_{sym} are reported. The other loss functions (χ^2 and χ^2_{mod}) are considered, but the observations are that they largely overfit large experimental value cross sections, and the fits are skewed. The optimised parameters from 1n channel of the cold fusion data (Table 3.1) are $s_0 = 12.68$ fm and $\beta_{ss} = 0.321 \times 10^{21}$ s^{-1}:

$$s^{\mathcal{N}}_{inj} = 12.681 - \frac{c}{0.321 \times 10^{21}} \sqrt{\frac{2\langle K \rangle_{rem}}{\mu c^2}}, \tag{3.32}$$

The fitted parameters are similar to those obtained using the linear ordinary regression, $s_0 = 12.478$ fm and $\beta_{ss} = 0.314 \times 10^{21}$ s^{-21}. The s_0 and β_{ss} increased by about 2% and 0.7%, respectively, in comparison with the results of the ordinary linear regression in Subsection 3.1.2.

Similarly, the optimised parameters of the fits on the hot fusion data (Table 3.2) are

$s_0 = 10.095$ fm and $\beta_{\rm ss} = 0.615 \times 10^{21}$ s^{-1}:

$$s_{\rm inj}^{\mathcal{N}} = 10.095 - \frac{c}{0.615 \times 10^{21}} \sqrt{\frac{2\langle K \rangle_{\rm rem}}{\mu c^2}}. \tag{3.33}$$

These parameters are comparable with the results obtained with the ordinary linear regression in Subsection 3.1.2. A decrease by about 4% in s_0 and an increase by about 12% in $\beta_{\rm ss}$ parameters is observed.

In conclusion, the results from the current fits show that the systematic fitting technique is promising and can be applied to more complicated injection parameterization, such as the one given by Eq. (3.26).

3.5 Fits and Results on $\ell-$dependent Injection Distance

In Section 3.4, we showed that we could obtain the parameters of the ℓ-independent injection point distance ($s_{\rm inj}^{\mathcal{N}}$) with the systematic fitting technique. Building on what was done in the previous section, we will now attempt to optimise the parameters of the $\ell-$dependent injection point distance formula. As mentioned, this is an improved version of the injection point distance model given in Eq. (3.10) because of the angular momentum treatment.

3.5.1 Cold Fusion

The optimised parameters for only 1n emission channel are $s_0 = 4.706$ fm and $\beta_{\rm ss} = 1.218 \times 10^{21}$ s^{-1}:

$$s_{\rm inj}^{\mathcal{N}}(\ell) = 4.708 - \frac{c}{1.218 \times 10^{21}} \sqrt{\frac{2K_{\rm rem}\left(E_{\rm cm}, \ell\right)}{\mu c^2}}. \tag{3.34}$$

With the inclusion of the angular momentum, the s_0 value is decreased by 62% and $\beta_{\rm ss}$ increased by 73% in comparison with the results from the $\ell-$independent formula in the previous Subsection 3.4.1.

The accuracy of this method is presented in Fig. 3.31 where ratios $\left(\frac{\sigma_{\rm th}}{\sigma_{\rm exp}}\right)$ are presented as a function of the Coulomb parameter z. The data in the figure is expected to cluster near $\left(\frac{\sigma_{\rm th}}{\sigma_{\rm exp}}\right) = 1$ as we have seen in the previous section. However, the figure demonstrates a tendency with z, which shows that calculations with these parameter values do not converge with the experimental data.

As discussed in Subsection 3.1.6, including the Coulomb parameter dependent term Ωz significantly improves the fit quality. This term was not included here.

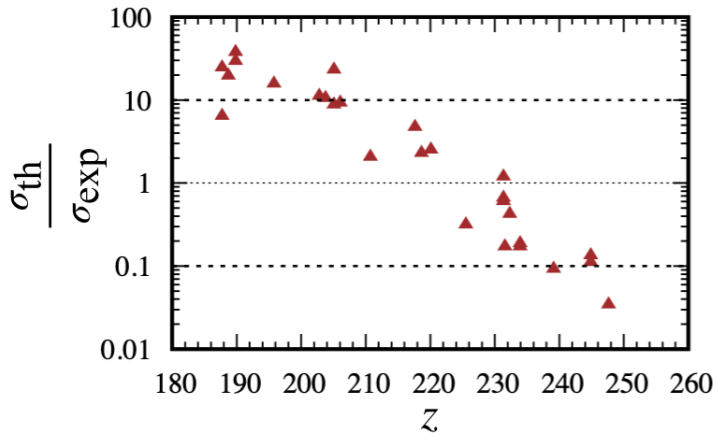

Figure 3.31: Comparison of the calculated cross sections (σ_{th}) with the corresponding experimental (σ_{exp}) production cross sections in the maxima of the excitation functions. The ratio $\left(\frac{\sigma_{\text{th}}}{\sigma_{\text{exp}}}\right)$ is evaluated for 1n channels of the reactions given in Table 3.1. z is the Coulomb parameter. The theoretical predictions are made using the optimised injection model in Eq. (3.34).

In conclusion, the optimised parameters in this case are incorrect and should not be used in further analysis.

3.5.2 Hot Fusion

This section reports the results of fitting the $\ell-$dependent injection point distance to the hot fusion reaction data set. The parameters obtained from the fit are $s_0 = 7.833$ fm and $\beta_{\text{ss}} = 1.104 \times 10^{21}$ s^{-1}:

$$s_{\text{inj}}^{\mathcal{N}}(\ell) = 7.833 - \frac{c}{1.104 \times 10^{21}} \sqrt{\frac{2K_{\text{rem}}\left(E_{\text{cm}}, \ell\right)}{\mu c^2}}. \tag{3.35}$$

By evaluating the remaining kinetic energies in terms of the angular momentum, the optimised parameter s_0 decreased by 22% and β_{ss} increased by 79% in comparison with what was obtained with the $\ell-$independent fit in Subsection 3.4.1.

Fig. 3.32 shows the quality of the $\ell-$dependent injection distance formula for the hot fusion reaction data. Here, the fit results show a good reproduction of the experimental data, where the quantity $\left(\frac{\sigma_{\text{th}}}{\sigma_{\text{exp}}}\right)$ clusters around 1, with the majority of the calculations being within an order of magnitude accuracy from the experimental values. In contrast to the result in Fig. 3.19, the optimised angular momentum-dependent injection point distance tends to be pessimistic. The complete excitation functions are illustrated in Fig. 3.33, where the theoretical calculations underestimate or reproduce the maximum of the experimental data used in the fit.

Finally, the values of the friction coefficient β_{ss} obtained from the fit on the cold and hot fusion data using the ordinary linear regression are $\beta_{\text{ss}} = (0.314 \pm 0.024) \times 10^{21}$ s^{-1} and

$\beta_{ss} = (0.550 \pm 0.06) \times 10^{21}$ s^{-1}. That obtained with the systematic fitting technique of the $\ell-$dependent formula on the hot fusion data is 1.104×10^{21} s^{-1}. The above values of the β_{ss} parameters are small in comparison to a typical value of the angular frequency of the parabolic potential (1.5×10^{21} s^{-1}) i.e., $\beta_{ss} < 2\omega$ [61]. This therefore suggests the dynamics may not be fully damped, as assumed in the derivation of the new injection point formula.

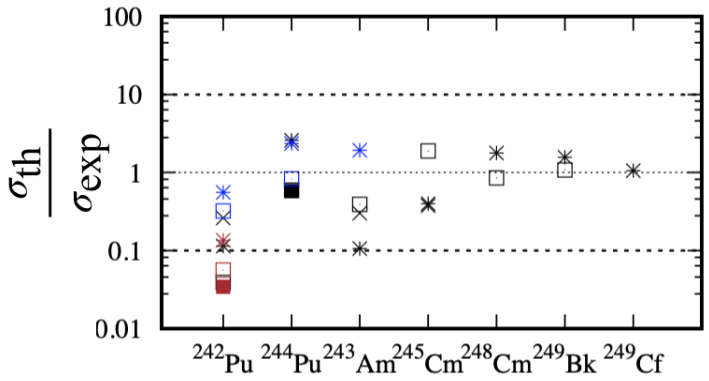

Figure 3.32: Comparison of theoretical and experimental evaporation residue cross sections for hot fusion data given in Table 3.2. $\left(\frac{\sigma_{th}}{\sigma_{exp}}\right)$ is the ratio of the theoretical predictions to the experimental values evaluated in a maximum of a given channel. The 2n, 3n, 4n and 5n reaction channels are depicted by the cross, star, open square and solid squares symbols, respectively. Here, the colours: black, blue, and brown correspond to the laboratories in Dubna, GSI (TASCA), and LBNL, where these cross sections were measured. The theoretical calculations are evaluated using the optimised injection distance parameterization in Eq. (3.35).

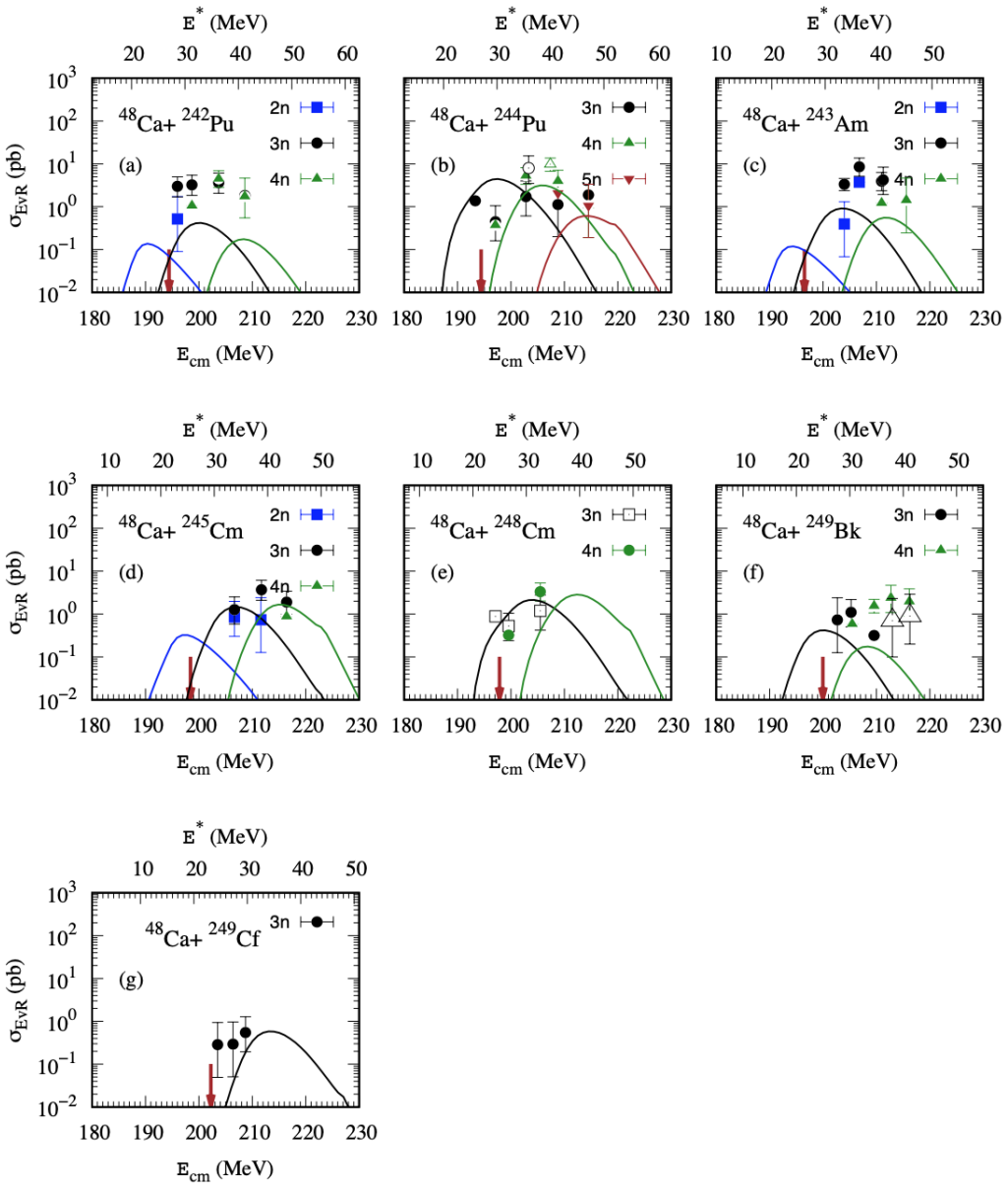

Figure 3.33: The excitation functions for the hot fusion reactions. Here, the solid symbols correspond to the data taken from DUBNA, and the open symbols denote that of the GSI (TASCA). The 2n, 3n, 4n and 5n channels are represented by the blue, black, forest-green, and brown symbols, respectively. The theoretical curves are evaluated using the optimised injection point distance parameters given in Eq. (3.35). The sources of the experimental data are indicated in Table 2.3. The position of the brown arrows indicates the mean Coulomb barrier of the reactions.

3.6 Conclusion

This chapter presents the new parameterization of the injection distance according to the Ref. [81, 82]. The new parameterization is obtained consistent with multidimensional Langevin formalism, where coupling between fast and slow collective variables induces slip in the initial condition of the former. This induced slip in the initial condition is analogous to the phenomenological injection distance (s_{inj}) within the Fusion-by-Diffusion (FbD) model [34, 68]. The new s_{inj} model is considered an improvement over the default linear approach used in the FbD model.

The new model offers the advantage of accounting for entrance channel characteristics, such as the Coulomb barrier distribution and the remaining kinetic energy after capture. The parameters of the new injection point distance models are adjusted to the cold and hot fusion experimental data. Firstly, 1n neutron emission channels are considered in the fitting process to cold fusion data. The Coulomb parameter z is added as an additional explanatory feature to improve the model's prediction. The optimised parameters of the modified model could explain the 1n channels within a factor. The 2n and 3n channels are explained within an order of magnitude. The modified new injection distance parameterisation is optimised on both, cold and hot fusion data sets, to have one global systematic fit for both reaction types. In this case, the experimental data are within one order of magnitude accuracy from the experimental data.

We further refined the new parameterization of the injection point distance without the Coulomb parameter by incorporating the treatment of angular momentum. Subsequently, the refined injection point distance parameters are optimised using a new fitting technique designed for this purpose. The angular momentum dependent injection point distance is considered only for the hot fusion parameterization. Here, the optimised parameters describe the experimental data to within an order of magnitude deviation.

Finally, the optimised friction coefficient (β_{ss}) obtained from the fit, suggests that the overdamped approximation might be too restrictive for accurately modelling of the reaction dynamics. Therefore, in the next chapter 5, we will investigate the dynamics within the undamped Langevin limit given by Eq. (2.77).

Chapter 4

Formation Dynamics with a One-dimensional Undamped Langevin System

The previous chapter shows that the parameterization of the injection point distance ($s_{\text{inj}}^{\mathcal{N}}$) of the overdamped formation probability can be obtained consistently with the Langevin formalism. The parameters of the $s_{\text{inj}}^{\mathcal{N}}$ are subsequently adjusted to the experiment, and the results show that the reduced friction parameter describing the dynamics is not large enough for it to be considered damped. This brings the question of whether the overdamped approximation is too strong. This chapter describes the dynamics at the undamped limit of the full Langevin formalism given by Eq. (2.77), where remaining kinetic energy at capture plays a role in the dynamics. The energy-dependent injection point parameterization of the overdamped formalism is replaced with an initial value problem due to the impact of remaining kinetic energy in the dynamics.

The chapter begins by presenting the solution to the full Langevin equation (Eq. (2.77)) in Section 4.1. Section 4.2 describes the fitting parameters of the model, which are optimised using the systematic fitting method described in Section 4.3. The chapter concludes by comparing the theoretical excitation functions of the reactions studied with the experimental data.

4.1 Formation probability in 1D Langevin Systems

The undamped Langevin equation that describes the shape evolution of the di-nuclear system after the capture step with initial surface separation s_0 into a compound nucleus is given by (see Chapter 2):

$$\ddot{s} + \beta\dot{s} - \omega^2(s - s_{\text{sad}}) = r(t). \tag{4.1}$$

The first and second moments of the random force are given as,

$$\langle r(t)\rangle = 0, \text{ and } \langle r(t)r(t')\rangle = \frac{2\mathcal{T}\beta}{\mu}\delta(t - t'), \tag{4.2}$$

where $s_{\rm sad}$ is the distance variable describing the position of the saddle point. The objective is to solve Eq. (4.1). However, for simplicity, we can shift the position of the fusion saddle to 0 by substituting $q = s - s_{\rm sad}$. This substitution reduces Eq. (4.1) to:

$$\ddot{q} + \beta\dot{q} - \omega^2 q = r(t). \tag{4.3}$$

The solution to Eq. (4.3) is presented in Refs. [52, 54, 61] and is repeated here for completeness.

The solution to Eq. (4.3) is obtained by applying the Laplace transform ($\mathcal{L}$) to both sides:

$$\mathcal{L}\left\{\ddot{q} + \beta\dot{q} - \omega^2 q = r(t)\right\}, \tag{4.4}$$

which yields,

$$\begin{aligned} q(\sigma) &= \frac{\frac{p_0}{\mu} + \beta q_0 + \sigma q_0}{\sigma^2 + \beta\sigma - \omega^2} + \frac{r(\sigma)}{\sigma^2 + \beta\sigma - \omega^2}, \\ &= \frac{\frac{p_0}{\mu} + \beta q_0 + \sigma q_0}{(\sigma - \sigma_1)(\sigma - \sigma_2)} + \frac{r(\sigma)}{(\sigma - \sigma_1)(\sigma - \sigma_2)}. \end{aligned} \tag{4.5}$$

where σ denotes the Laplace domain variable.

Here, $\sigma_1 = \frac{-\beta+\sqrt{\beta^2+4\omega^2}}{2}$ and $\sigma_2 = \frac{-\beta-\sqrt{\beta^2+4\omega^2}}{2}$ are zeros of the denominator, $\sigma^2+\beta\sigma-\omega^2$. With this decomposition, the solution in the time domain is obtained by employing the inverse Laplace transform $\mathcal{L}^{-1}$ of Eq. (4.5):

$$\begin{aligned} q(t) &= \mathcal{L}^{-1}\{q(\sigma)\}, \\ &= q_0\left[\left(e^{\sigma_1 t} + e^{\sigma_2 t}\right) + \frac{\beta}{2\sqrt{\beta^2+4\omega^2}}\left(e^{\sigma_1 t} - e^{\sigma_2 t}\right)\right] + \frac{p_0}{\mu\sqrt{\beta^2+4\omega^2}}\left(e^{\sigma_1 t} - e^{\sigma_2 t}\right) \\ &+ \int_0^t r(\tau)\left(\frac{e^{\sigma_1(t-\tau)} - e^{\sigma_2(t-\tau)}}{\sqrt{\beta^2+4\omega^2}}\right)d\tau, \\ &= e^{-x\omega t}\left[q_0\cosh\left(\sqrt{1+x^2}\omega t\right) + \frac{q_0 x}{\sqrt{1+x^2}}\sinh\left(\sqrt{1+x^2}\omega t\right) + \frac{p_0}{\mu\omega\sqrt{1+x^2}}\sinh\left(\sqrt{1+x^2}\omega t\right)\right] \\ &+ \int_0^t r(\tau)\left(\frac{e^{\sigma_1(t-\tau)} - e^{-\sigma_2(t-\tau)}}{\sigma_1 - \sigma_2}\right)d\tau, \end{aligned} \tag{4.6}$$

where $x = \frac{\beta}{2\omega}$ and the initial conditions are, $q(0) = q_0$ and $\dot{q}(0) = \frac{p_0}{\mu}$. The probability for a di-nuclear with an initial separation q_0 to diffuse over the fusion saddle ($q = 0$) into a compound nucleus is given as:

$$\begin{aligned} P_{\rm CN}(t, q(0)) &= \int_{-\infty}^{0} \frac{1}{\sqrt{2\pi}\sigma_{\rm q}(t)}\exp\left(\frac{-(q - \langle q(t)\rangle)^2}{2\sigma_{\rm q}^2(t)}\right)dq, \\ &= \frac{1}{2}\mathrm{erfc}\left(\frac{< q(t) >}{\sqrt{2}\sigma_{\rm q}(t)}\right). \end{aligned} \tag{4.7}$$

The average trajectory $< q(t) >$ is obtained from Eq. (4.6) as,

$$\begin{aligned} < q(t) > &= e^{-x\omega t} q_0\left[\cosh\left(\sqrt{1+x^2}\omega t\right) + \frac{x}{\sqrt{1+x^2}}\sinh\left(\sqrt{1+x^2}\omega t\right)\right] \\ &+ \frac{p_0 e^{-x\omega t}}{\mu\omega\sqrt{1+x^2}}\left[\sinh\left(\sqrt{1+x^2}\omega t\right)\right], \end{aligned} \tag{4.8}$$

whereas, the variance $\sigma_q^2(t)$ is determined as follows:

$$\begin{aligned}
\sigma_q^2(t) &= \langle (q(t) - \langle q(t) \rangle)^2 \rangle, \\
&= \left[\int_0^t \langle r(\tau^{'}) \rangle \left(\frac{e^{\sigma_1(t-\tau^{'})} - e^{-\sigma_2(t-\tau^{'})}}{\sigma_1 - \sigma_2} \right) d\tau^{'} \right]^2, \\
&= \int_0^t \int_0^t \langle r(\tau) r(\tau^{'}) \rangle \left(\frac{e^{\sigma_1(t-\tau)} - e^{\sigma_2(t-\tau)}}{\sigma_1 - \sigma_2} \right) \times \left(\frac{e^{\sigma_1(t-\tau^{'})} - e^{\sigma_2(t-\tau^{'})}}{\sigma_1 - \sigma_2} \right) d\tau d\tau^{'}, \\
&= \frac{2\mathcal{T}\beta}{\mu(\sigma_1 + \sigma_2)^2} \left[\frac{(e^{2\sigma_1 t} - 1)}{\sigma_1} + \frac{2(1 - e^{(\sigma_1+\sigma_2)t})}{\sigma_1 + \sigma_2} + \frac{(e^{2\sigma_2 t} - 1)}{\sigma_2} \right], \\
&= \frac{2\mathcal{T}\beta}{\mu(\sigma_1 + \sigma_2)^2} \left[\frac{\sigma_2 e^{\sigma_1 t} + \sigma_1 e^{\sigma_2 t}}{\sigma_1 \sigma_2} - \frac{2e^{(\sigma_1+\sigma_2)t}}{\sigma_1 + \sigma_2} - \frac{(\sigma_1 - \sigma_2)^2}{2\sigma_1\sigma_2(\sigma_1 + \sigma_2)} \right].
\end{aligned} \tag{4.9}$$

From here, one can make the substitution for the hyperbolic functions, and the final expression for the variance is written as:

$$\sigma_q^2(t) = \frac{\mathcal{T}}{\mu\omega^2} \left[e^{-2x\omega t} \left(\frac{2x^2}{1+x^2} \sinh^2 \left(\sqrt{1+x^2}\omega t \right) + \frac{x}{\sqrt{1+x^2}} \sinh \left(2\sqrt{1+x^2}\omega t \right) + 1 \right) - 1 \right]. \tag{4.10}$$

With the expression for the mean trajectory and the variance obtained, we can further evaluate the formation probability (Eq. (4.7)). At the asymptotic time limit, Eq. (4.7) converges to:

$$P_{\mathrm{CN}}\,(t \to \infty, q_0, p_0) = \frac{1}{2} \mathrm{erfc} \left(\sqrt{\frac{\mathcal{B}(q_0)}{\mathcal{T}^{'}}} - \frac{1}{(x + \sqrt{1+x^2})} \sqrt{\frac{K}{\mathcal{T}^{'}}} \right). \tag{4.11}$$

Here, $K = \frac{p_0^2}{2\mu}$ represents the excess kinetic energy after capture. Based on this Eq. (4.11), we can further define effective kinetic energy:

$$K_{\mathrm{eff}} = \left(x + \sqrt{1+x^2} \right)^2 \mathcal{B}(q_0), \tag{4.12}$$

from Eq. (4.11) at which the probability is $\frac{1}{2}$ for compound nucleus formation. Likewise, the effective barrier is given as,

$$\mathcal{B}_{\mathrm{eff}}(q_0) = \left(x + \sqrt{1+x^2} \right)^2 \mathcal{B}(q_0). \tag{4.13}$$

Here, $\mathcal{T}^{'}$ is the dynamical temperature defined as:

$$\mathcal{T}' = 2\mathcal{T}x \left(\sqrt{1+x^2} - x \right), \tag{4.14}$$

where $\mathcal{T}$ is the temperature of the random force in the Langevin formalism [52, 54].

As evident in Eq. (4.11), the compound nucleus formation probability depends on the three variables, namely the height of the inner barrier ($\mathcal{B}(q_0)$), temperature ($\mathcal{T}$) and the remaining kinetic energy after the capture step (K). These variables impact the evolution of the di-nuclear systems from contact configuration into a spherical configuration, as

shown in Fig. 4.1. The panels in Fig. 4.1 are dimensionless plots highlighting the impact of the remaining kinetic energy (K) and the temperature ($\mathcal{T}$) on the fusion dynamics using the full Langevin solution (Eq. (4.11 The first row presents the average particle trajectories as a function of dimensionless time (ωt) for $K < \mathcal{B}_{\rm eff}(q_0)$ (in panel (a)), $K = \mathcal{B}_{\rm eff}(q_0)$ (in panel (b)), and $K = 2\mathcal{B}_{\rm eff}(q_0)$ (in panel (c)). The second row shows the corresponding formation probability for temperature conditions $\mathcal{T} = \frac{\mathcal{B}(q_0)}{5}$ (solid line) and $\mathcal{T} = \frac{\mathcal{B}(q_0)}{2}$ (short-dashes).

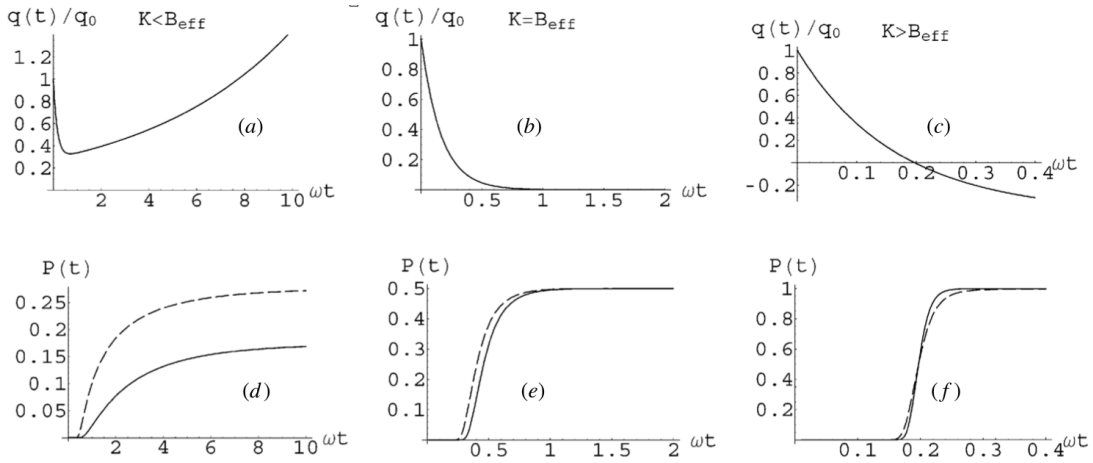

Figure 4.1: Figures (a), (b), and (c) illustrate the average trajectory (Eq. ((4.8))) for the remaining kinetic energies $K < \mathcal{B}_{\rm eff}(q_0)$, $K = \mathcal{B}_{\rm eff}(q_0)$, and $K = 2\mathcal{B}_{\rm eff}(q_0)$, respectively. Figures (d), (e), and (f) show the corresponding fusion probabilities for these energy regimes. Here, the dashed and the solid lines are $\mathcal{T} = \frac{\mathcal{B}_{\rm eff}(q_0)}{2}$ and $\mathcal{T} = \frac{\mathcal{B}_{\rm eff}(q_0)}{5}$, respectively. The graphs are plotted as a function of dimensionless time (ωt), with different scales used for each column. The figure is reproduced from [52].

Panel (a) of Fig. (4.1) shows the evolution of the nucleus towards the fusion saddle point. Here, the surface separation decreases; however, as time progresses, the average trajectory loses momentum and retreats. This tendency implies a quasi-fission process where most of the di-nuclear systems re-separate into projectile and target-like fragments at the exit channel without reaching compound nucleus configurations. Very few systems can fuse thanks to the random force. The corresponding to the formation probability for these conditions peaked at 15% and 10% higher if the temperature is increased from $\mathcal{T} = \frac{\mathcal{B}_{\rm eff}(q_0)}{5}$ to $\mathcal{T} = \frac{\mathcal{B}_{\rm eff}(q_0)}{2}$ as shown in the panel (d), respectively. Conversely, as the remaining kinetic energy (K) is increased to $K = \mathcal{B}_{\rm eff}(q_0)$, the average trajectory evolves to the top of the inner barrier. This means that half of the systems fuse, and the other half re-separate. The formation probability converges to 1/2. When the kinetic energy exceeds the effective barrier (panels (c) and (f)), the average trajectory overpasses the saddle, and the fusion probability is close to one.

The figures show the tendencies of the formation probability as a function of the kinetic energy and temperature. However, we need to parametrise the potential energy surface around the fusion saddle to evaluate the needed model parameters: inner barrier, temperature, and angular frequency. In the present study, we will keep the same potential energy surface prescription given in Ref. [48]. See Chapter 4 for further details on the implementation and how the initial condition (q_0) and coefficient of friction (β) are

determined.

4.2 Analysis of Undamped Langevin System

In the previous Section 4.1, we obtained the solution of the undamped Langevin equation as

$$P_{\mathrm{CN}} = \frac{1}{2}\mathrm{erfc}\left(\sqrt{\frac{\mathcal{B}(s_0)}{\mathcal{T}'}} - \frac{1}{(x+\sqrt{1+x^2})}\sqrt{\frac{K_{\mathrm{rem}}(E_{\mathrm{cm}},\ell)}{\mathcal{T}'}}\right), \tag{4.15}$$

where variable q_0 was replaced with s_0 for consistency. Here $\mathcal{B}(s_0)$ is the initial height of the inner barrier as defined in Eq. (2.112). $K_{\mathrm{rem}}(E_{\mathrm{cm}},\ell)$ is the partial remaining kinetic energy after the capture step given by Eq. (3.25). If we take into account the dispersion of the initial momenta (p_0), the dynamical temperature ($\mathcal{T}'$ (Eq. (4.14))) coincides with the temperature of the Langevin force [52]. The latter is approximated by the geometrical average given in Eq. (2.114).

As mentioned, $x = \frac{\beta}{2\omega}$, and the reduced friction parameter β will be denoted β_{ss} consistent with the previous section. ω is the angular frequency of the parabolic barrier taken as

$$\omega = \sqrt{\frac{2\mathcal{B}(s_0)}{\mu\,(s_0 - s_{\mathrm{sad}})^2}}. \tag{4.16}$$

Here, μ is the reduced mass of the system, and s_{sad} denotes the surface distance variable at the fusion saddle (see, for instance, Fig. 2.25). s_0 represents the initial surface separation of the colliding nuclei after the capture phase or the injection point. We have adopted the same parametrization of the deformation energy surface used in the overdamped evaluation [34, 48], as presented in Chapter 2.

In this context, we assume the same initial surface separation (s_0) and reduced friction parameter (β_{ss}) for all reactions and try to evaluate the dynamics using Eq. (4.15). Thus, the s_0 and β_{ss} will serve as fitting parameters of the model. Only hot fusion reaction data will be analysed using this approach because all these reactions are induced by ^{48}Ca, and all target nuclei exhibit similar deformations. As shown in Subsection 3.1.6, the cold fusion data requires an additional fit parameter dependent on the Coulomb parameter to describe the experiment.

4.2.1 The Model Parameter

This section briefly discusses the model parameters and the implementation of the formation probability within the full Langevin formalism. To begin with, we will use the reaction ^{48}Ca + ^{243}Am for a demonstration. Fig. 2.26 shows the typical $\ell-$independent macroscopic deformation energy surface ($E_{\rm def}$) for ^{48}Ca + ^{243}Am from which the position of the fusion saddle is determined at $s_{\rm sad} = -5.845$ fm. The $s_{\rm sad}$ value correspond to $E^{\rm sad}_{\rm def} = -0.328$ MeV for the fusion saddle. For an arbitrary initial conditions: $s_0 = 6$ fm, one obtains $E^{\rm inj}_{\rm def} = -15.028$ MeV and the inner barrier ($\mathcal{B}(s_0)$) opposing fusion dynamics from the point of contact at $\ell = 0$ is 14.70 MeV. However, this must be corrected by the centrifugal term consistent with Eq. (2.112).

For the given values of the inner barrier $\mathcal{B}(s_0)$ using distances s_0 and the $s_{\rm sad}$, the angular frequency of the parabolic barrier given by Eq. (4.16) is obtained as 7.107×10^{20} s^{-1}. Note that, while $s_{\rm sad}$ and its $E^{\rm sad}_{\rm def}$ is correctly evaluated, the $s_0 = 6$ fm which determined the inner barrier height is arbitrarily chosen here for demonstrative purposes only. The key questions then become: at what precise point (s_0) of the deformation energy surface does the system begin to evolve towards a spherical configuration, and what is the damping factor $\beta_{\rm ss}$? Thus, we have two unknown parameters (s_0 and $\beta_{\rm ss}$) that have to be determined.

4.3 The Optimised Parameters of the Undamped Langevin System

This section reports on the results of the fitted parameters of the undamped Langevin system. The fitting process follows the systematic fitting adopted for the $\ell-$dependent injection point distances (in Section 3.3). The theoretical curve is adjusted to the maximum of the experimental excitation functions for all the hot fusion reactions considered in the fit (see Tab. 3.2). The theoretical maxima are compared on the loss functions defined in the Subsection 3.3.2.1 until convergence or the lowest value is obtained. Note that the parameters are obtained following the same capture model and configurations of the survival probability. The only thing that changes is the compound nucleus formation probability formalism. Therefore, any changes in the results over what is seen in the previous chapters will be due to the compound nucleus formation probability.

Since this is the first time the undamped Langevin formalism (Eq. (4.15)) is evaluated using the potential surface energy map presented in Subsection 2.4.2, it is worth demonstrating how the formation probability compares with already known calculation. To this effect, Fig. 4.2 compares the optimised undamped and overdamped calculation with the injection point distance given by Eq. (3.32). Here, the comparison is made using the angular momentum-dependent injection point distance. The optimised parameters in this case are $s_0 = 7.833$ fm and $\beta_{\rm ss} = 1.104\times10^{21}$ s^{-1}, see Subsection 3.5.2 for more details.

Panel (a) of the figure illustrates how the average compound nucleus formation probability given by Eq. (2.122) for ^{48}Ca + ^{243}Am is compared on both formalisms. Panel (b) illustrates the corresponding evaporation residue cross section for the 2n, 3n, 4n and 5n

channels. The calculation shows good agreement between the overdamped and undamped calculations. However, the differences in the optimised parameter values underscores how each formalism describes the dynamics.

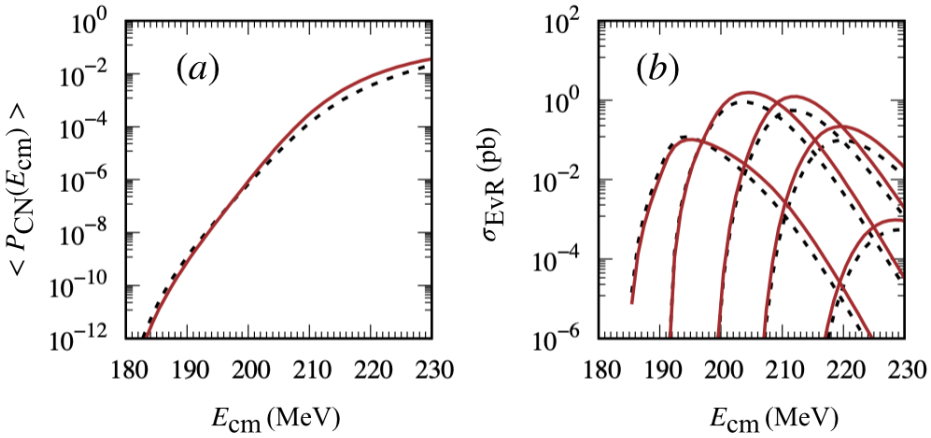

Figure 4.2: Comparison of compound nucleus formation probability at the overdamped (in blacked dashed line) and undamped limit of the Langevin (solid brown line) formalism using ^{48}Ca + ^{243}Am as test case. Here, the overdamped calculations are evaluated using the optimised injection point distance given by Eq. (3.35). (a) The average compound nucleus formation probability using Eq. (2.122). The optimised parameters s_0 = 9.374 fm and β_{ss} =0.117 $\times$ 10^{21} s^{-1} are used to calculate the undamped approach. (b) The corresponding evaporation residue cross sections (Eq. (2.2)) for the 2n, 3n, 4n and 5n channels.

4.3.1 Results

The parameters s_0 and β_{ss} obtained from the fit are 9.374 fm and 0.117 $\times$ 10^{21} s^{-1}, respectively. Note that only hot fusion data are considered for the reasons mentioned earlier. Fig. 4.3 shows how the fitted undamped Langevin parameters describe the experimental data. Here, the $\left(\frac{\sigma_{th}}{\sigma_{exp}}\right)$ ratio is plotted against the targets used in the experiment. The σ_{th} and σ_{exp} are the maxima of the calculated and the experimental excitation functions, respectively. The black, blue and brown coloured markers correspond to the data from DUBNA, GSI (TASCA) and the LBNL, respectively. The 2n, 3n, 4n and 5n data are depicted by the cross, star, open square and solid squares, respectively. The sources of the experimental data used in the fit are presented in Table 3.2. Here, the figure shows the predicted theoretical values are within an order magnitude deviation from the experimental data.

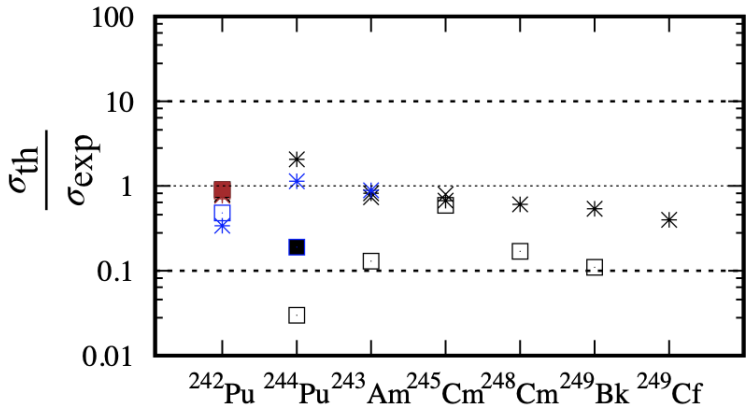

Figure 4.3: Comparison of theoretical and experimental evaporation residue cross sections for hot fusion data given in Table 3.2. $\left(\frac{\sigma_{\rm th}}{\sigma_{\rm exp}}\right)$ is the ratio of the theoretical predictions to the experimental values evaluated in a maximum of a given channel. The 2n, 3n, 4n and 5n reaction channels are depicted by the cross, star, open square and solid squares symbols, respectively. Here, the colours: black, blue, and brown correspond to the laboratories in Dubna, GSI (TASCA), and LBNL, where these cross sections were measured. The theoretical calculations are evaluated using the full Langevin formalism with the optimised parameters $s_0 = 9.374$ fm and $\beta_{\rm ss} = 0.117 \times 10^{21}$ s^{-1}. The respective sources of the experimental data are given in Table 2.3.

Finally, Fig. 4.4 illustrate the complete excitation functions of the reactions used in the fit. The evaporation residue curves regarding the position of the optimum energies are similar to what we have seen in the previous chapter. As evident in Fig. 4.3, the theoretical calculations reasonably reproduced the experimental data within one order of magnitude. As seen in Fig. 3.33 in the higher neutron emission channels (4n and 5n), the kinks are eliminated. The kink, as mentioned before in Fig. 3.33, was because of the restriction of the injection point distance to a finite value ($s_{\rm inj} = -2$ fm) even for energies which would otherwise correspond to smaller $s_{\rm inj}$. This gives rise to a plateau or saturation of the formation probability at this limit, as seen in panel (a) of Fig. 3.8.

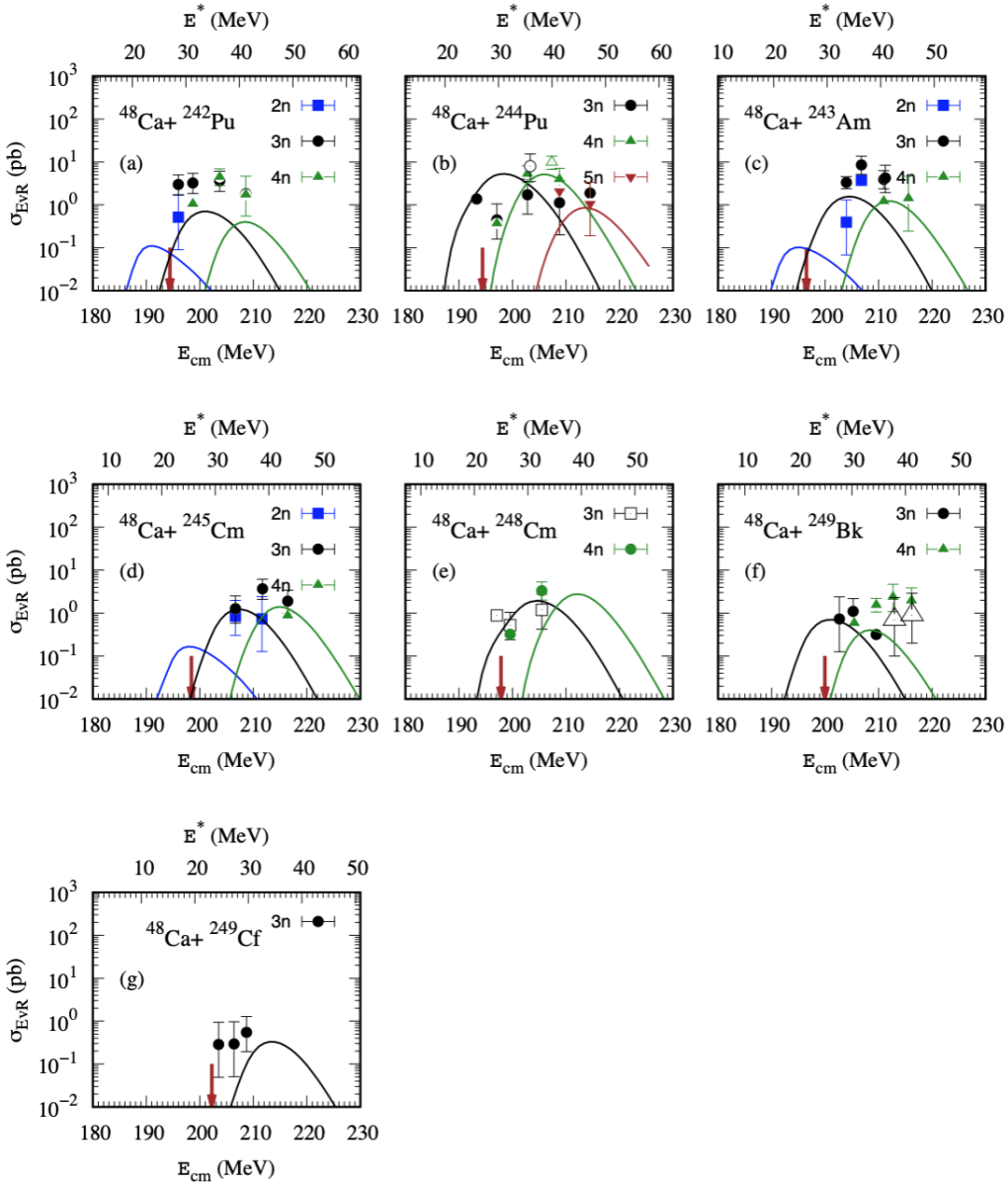

Figure 4.4: The excitation functions for the hot fusion reactions. Here, the solid symbols correspond to the data taken from DUBNA, and the open symbols denote that of the GSI (TASCA). The 2n, 3n, 4n and 5n channels are represented by the blue, black, green, and brown symbols, respectively. The theoretical curves are evaluated using the full Langevin formalism with the optimised parameters $s_0 = 9.374$ fm and $\beta_{ss} = 0.117 \times 10^{21}$ s^{-1}. The sources of the experimental data are indicated in Table 2.3. The position of the brown arrows indicates the mean Coulomb barrier of the reactions.

4.4 Conclusion

In conclusion, this chapter presented the formalism of compound nucleus formation at the undamped limit of Langevin formalism. We optimised the model parameters s_0 and $\beta_{\rm ss}$ of the full Langevin model. As shown in the Subsection 3.1.6, the Coulomb parameter is needed as an extra feature of the model to accurately describe the cold fusion reactions. Therefore, the parameters are optimised for the hot fusion reaction only. The optimised parameters of the fit reproduced the experimental data within one order of magnitude deviation from the experimental data. The values of the friction parameter (β_{ss}) obtained from the fit, re-emphasis the dynamics is not damped as assumed in the overdamped evaluation.

Chapter 5

Wrap-up and Predictions

To this point, we have implemented and investigated the compound nucleus formation probability at the overdamped and undamped limits of the Langevin formalism. During the analysis, we have obtained several sets of optimised model coefficients necessary for calculating the formation probability. In this chapter, we will summarise the predictive powers of each of the approaches discussed so far in this thesis. The objective is to establish the best-optimised method and parameters to implement in the recommended version of the improved Kewpie2 model. To achieve that, we will evaluate the models using the hybrid loss function (symmetric) given by Eq. (3.31):

$$\chi^2_{\mathrm{sym}} = \frac{1}{N-j} \times \sum_i^N \frac{(O_i - E_i)^2}{O_i \times E_i}, \tag{5.1}$$

where O_i are the experimentally measured cross sections (in the excitation functions maxima) and E_i are the cross section values predicted by a given model. N indicates the number of analysed reactions, and j corresponds to the number of parameters optimised, i.e., 2 or 3, depending on the cases. In this chapter, we will compare different approaches and give recommendations based on the above loss function. As demonstrated in Subsection 3.3, such a loss function can deal with situations where deviations between calculations and observations can reach orders of magnitude. Thus, the model that has the lowest score of χ^2_{sym} has the least average deviation from the experimental data.

The tables 5.1 and 5.2 present the model and the respective optimised parameters. The column **Model** corresponds to the model investigated. The linear injection point distance parameterization is the default approach within the FbD model to obtain the formation probability and it is given by Eq. (2.117):

$$s^{\mathcal{L}}_{\mathrm{inj}} = \alpha \times (E_{\mathrm{cm}} - B_0) + \beta_0. \tag{5.2}$$

Here, we are mainly interested in the optimised parameters s_0 and β_{ss} of the new approaches to the injection point distance; therefore, the parameter columns of the linear approach are left empty, and only the χ^2_{sym} value is given for comparison. For more details on the linear parameterization, see Subsection 2.5.1.

The parameterization used in the new approach to the injection point distance (Eq. (3.10)) is given by:

$$s_{\text{inj}}^{\mathcal{N}} = s_0 - \frac{c}{\beta_{\text{ss}}}\sqrt{\frac{2\langle K\rangle_{\text{rem}}}{\mu c^2}}, \tag{5.3}$$

and has two parameters: s_0 and β_{ss}. However, in the quest to improve the quality of the fit, the Coulomb parameter dependence term (Ωz) was added:

$$s_{\text{inj}}^{\mathcal{M}} = s_0 + \Omega z - \frac{c}{\beta_{\text{ss}}}\sqrt{\frac{2\langle K\rangle_{\text{rem}}}{\mu c^2}}. \tag{5.4}$$

Finally, in an attempt to improve the description of the injection point distance, we introduced angular momentum treatment of the remaining kinetic energy at capture and subsequently optimised the parameters:

$$s_{\text{inj}}^{\mathcal{N}}(\ell) = s_0 - \frac{c}{\beta_{\text{ss}}}\sqrt{\frac{2K_{\text{rem}}(E_{\text{cm}}, \ell)}{\mu c^2}}. \tag{5.5}$$

In both Tables, 5.1 and 5.2, the columns without a value imply that the corresponding parameter was not considered in the fit procedure. We will also consider the optimised parameters of the full Langevin formalism on hot fusion data as presented in the Subsection 4.3.

5.1 Wrap-up on Cold Fusion Analysis

Table 5.1 shows the optimised injection point distance parameters obtained in the analysis of 1n only or all, 1n, 2n and 3n, channels of the cold fusion reaction data set (see Table 5.1). The column **CH** corresponds to the channels on which the parameters are optimised. The case of the 1n channel alone indicates the model could not describe the multiple neutron emission channel.

Firstly, the new approach to the injection point distance (Eq. (5.3)) optimised on 1n channel has a smaller $\chi^2_{\text{sym}} = 2.8$ as compared with $\chi^2_{\text{sym}} = 3.8$ of the linear parameterization (Eq. (5.2)). The lower value obtained from the new approach indicates that it better describes the data than the default linear parameterization in the FbD model, as explained in the Subsection 3.1.2. These parameters are obtained using the ordinary linear regression, see Subsection 3.1.2. The reported χ^2_{sym} when the systematic fitting technique is applied to Eq. (5.3) as presented in Subsection 3.4.1 is 2.2.

The modified new approach (Eq. (5.4)), as used to explain the multiple neutron emission channels (1n, 2n and 3n), has $\chi^2_{\text{sym}} = 0.6$, which is a significant improvement over the optimised parameters obtained for the 1n channel alone. This shows the modified new approach to the injection point distance is better suited for describing the cold fusion data in comparison with the original version (Eq. (5.3)). The modified parameterization (Eq. (5.4)) used for the combined cold and hot fusion data sets gives $\chi^2_{\text{sym}} = 1.5$ when

only cold fusion reactions are analyzed. This is a worse result than the one obtained with only the dedicated fit to cold fusion data. On this note, the optimised parameters on the modified injection point distance (Eq. (5.4)) as shown in Table 5.1 on the cold fusion data (1n, 2n and 3n) alone is the best optimised and recommended parameterization for the cold synthesis. The corresponding parameters are highlighted in the bold characters in Table 5.1.

Table 5.1: The table summarizes the optimized fitting parameters of different compound nucleus formation probability formulas for cold fusion reactions. The parameters are obtained by analyzing 1n alone or combined (1n, 2n, and 3n) neutron emission channels. The parameters s_0 (in fm), Ω (in fm) and β_{ss} (in units of s^{-1}), are rated on the χ^2_{sym} metric calculated for a given data set. The lower the metric value, the better the model performance.

Model	s_0 **(fm)**	Ω **(fm)**	$\beta_{ss} \times 10^{-21}$ **(s^{-1})**	χ^2_{sym}	**CH**
Linear Model (Subsection 3.1.2.1)	-	-	-	3.8	1n
New Approach to the Injection Distance (Subsection 3.1.2.1)	12.478	-	0.314	2.8	1n
Modified New Approach to the Injection Distance (Subsection 3.1.6)	15.982	-0.054	1.6	0.6	1n, 2n, 3n
Global Injection Fit for Cold and Hot Synthesis (Subsection 3.1.7)	17.548	-0.051	0.814	1.5	1n, 2n, 3n
Systematic Fit ($\ell-$independent) Subsection 3.4.1	12.680	-	0.321	2.2	1n

Having identified the best-optimised fitting coefficients for the formation probability, we can now compare the results for the formation probability with the calculations performed with other models. To make this comparison, we will adopt the average formation probability given by Eq. (2.122). Fig. 5.1 shows the compound nucleus formation probabilities reported by different authors compared with the current work shown in brown points for $Z_{CN} = 104 - 113$. The current work is added to Fig. 5.1 taken from Ref. [55].

The multiple points corresponding to the same Z_{CN} are for different reactions. In all models presented in Fig. 5.1, the fusion probability calculations are, to some degree, adjusted to the experimental data, as in this work. The differences between the P_{CN} calculations may stem from variation in one of the three stages of the modelling, since, at least one of the three stages in the modelling: capture, formation, survival, is adjusted in order to reproduce the experiment. The question of which model is correct will require in-depth analysis to constrain the models. This can be done by using uncertainty analysis, e.g., applied to reactions that form the same compound nucleus at the same energies but in different projectile-target combinations.

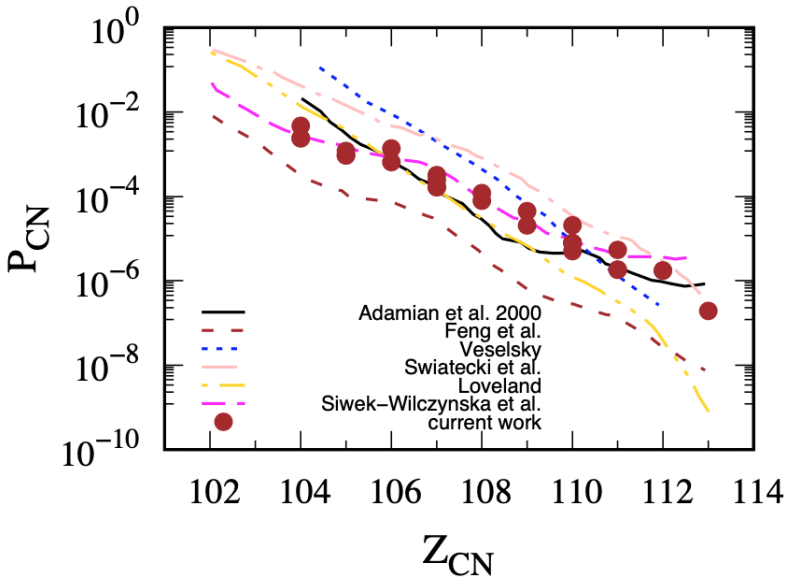

Figure 5.1: The compound nucleus formation probabilities P_{CN} as a function of Z_{CN} obtained using different models are compared with the values obtained in this work (represented by brown dots). The results for $Z_{CN} = 104 - 113$ are here added to the figure extracted from Ref. [55]. The multiple points corresponding to the same Z_{CN} are for different reactions.

5.1.1 Model Testing on Cold Fusion Data

In the previous sections, we have summarised the formation probability calculations and selected the best parameter values for cold fusion reactions. Now, the question is, can we reproduce experimental data that is not considered in the fitting process? Fig. 5.2 illustrates such an example. The experimental data have yet to be published and have been obtained from Dieter Ackermann in private communications.

Here, the dashed black line shows the calculations using the original injection point distance formula given by Eq. (3.14), and the brown curve corresponds to the modified version of the injection point distance approach (Eq. (3.20)). Here, the original version of the injection point distance parametrization agrees better with data than the modified version. However, the modified version only deviates from the experimental points by factor three.

The original Kewpie2 model relied on external evaluations of the formation probability. The presented calculations have good predictive power, and the Kewpie2 model can now be considered a standalone numerical code for simulating production cross sections for super-heavy elements.

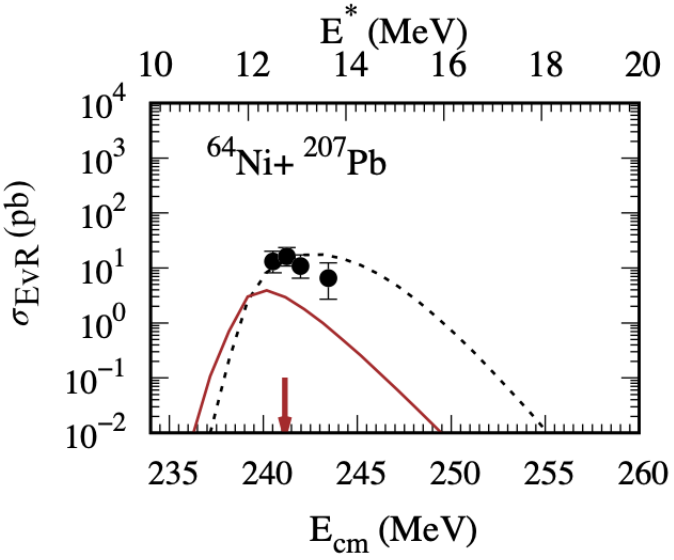

Figure 5.2: Demonstration of the predictive power of the current version of the Kewpie2 model. Points show the unpublished experimental data for the ^{207}Pb(^{64}Ni,1n)^{270}Ds (private communication from Dieter Ackermann). The black dashed line shows predictions of Eq. (3.14) and the brown line those of Eq. (3.21).

5.2 Hot Fusion Residue Excitation Functions

Table 5.2 illustrates the summary of various methods used to describe the formation probability in the hot fusion reactions. Here, we present the parameters for cold and hot fusion reaction data sets. The table highlights which of the formalisms, overdamped or undamped Langevin approach, and which parameterization best describes the experimental data. This analysis is done similarly to the previous chapter using the χ^2_{sym} loss function.

The undamped Langevin formalism has the lowest loss function value, $\chi^2_{\text{sym}} = 2.2$. Since the sole purpose of this comparison is to find which model has the best description of the experimental data, the undamped Langevin formalism presented in the Subsection 4.3 is recommended for describing the formation probability in the hot fusion reactions.

Table 5.2: The table summarizes the optimized fitting parameters of different compound nucleus formation probability formulas for hot fusion reactio data. The parameters s_0 (in fm), Ω (fm) and β_{ss} (s^{-1}), are rated on the χ^2_{sym} metric calculated for the same data set. The lower the metric value, the better the model performance.

Model	s_0 (fm)	Ω (fm)	$\beta_{ss} \times 10^{-21}$ (s^{-1})	Loss
Linear (Subsection 3.1.2.2)	-	-	-	6.5
New Approach to the Injection Distance (Subsection 3.1.2.2)	10.572	-	0.550	6.6
Global Injection Fit for Cold and Hot Synthesis (Subsection 3.1.7)	17.548	-0.051	0.814	7.1
Systematic fitting ℓ-independent New Approach to the Injection Distance (Subsection 3.4.1)	10.096	-	0.6152	3.2
Systematic fitting ℓ-dependent New Approach to the Injection Distance (Subsection 3.5.2)	7.833	-	1.104	4.4
Undamped Langevin System (Subsection 4.3)	9.373	-	0.177	2.2

5.2.1 Predictions on Hot Fusion for Planned and Possible Experiments

As aforementioned, ongoing experimental efforts are dedicated to synthesising elements with atomic numbers greater than $Z_{CN} = 118$. To achieve this, it is important to investigate suitable projectile-target combinations for these experiments. In this section, we present calculations for planned and possible hot fusion reactions with beams heavier than ^{48}Ca that can lead to the synthesis of new isotopes of known elements or to the synthesis of new elements with atomic numbers 119 and 120.

In this case, the undamped Langevin formalism (full Langevin) is considered because it has the lowest χ^2_{sym} value for hot fusion reactions with ^{48}Ca. Table 5.3 presents cross section prediction for possible super-heavy synthesis experiments. The table shows the most probable xn production channel for the listed actinide targets induced with ^{50}Ti, ^{51}V and ^{54}Cr projectiles. The maximum value of the production cross section decreases from ^{50}Ti to ^{54}Cr induced reactions, except for the ^{238}U and ^{237}Np targets. The decreasing production cross section is a consequence of the increasing charge symmetry in the entrance channel, which decreases the probability of the compound nucleus formation.

As shown in Table 5.3, the reaction ^{50}Ti + ^{244}Pu leading to $Z_{CN} = 116$ is the most probable, with a predicted production cross section of 121 fb. This reaction was recently performed at LBNL, where a reported production cross section in the 4n channel is 440^{+580}_{-280} fb, approximately four times higher than the calculated value [36]. In contrast, the predicted production cross sections for $Z = 119$ (^{50}Ti + ^{249}Bk) and $Z = 120$ (^{50}Ti + ^{249}Cf) are 14.6 and 2.2 fb, respectively. These minuscule production cross sections highlight the challenges of synthesising new elements.

Table 5.3: The table shows the most probable *x*n production channels for the listed actinide targets induced with ^{50}Ti, ^{51}V, and ^{54}Cr projectiles. All calculations are based on the undamped Langevin formalism for the formation probability. The predictions from the current version of the Kewpie2 model are compared with those from the FbD calculations (private communication with T. Cap). The empty columns entries in the FbD calculations means that the cross section is below 1 fb.

Targets	^{50}**Ti**		^{51}**V**		^{54}**Cr**	
	This Work ch (fb)	**FbD** (fb)	**This Work** ch (fb)	**FbD** (fb)	**This Work** ch (fb)	**FbD** (fb)
^{238}U	3n 4.4	3-26	3n 0.7	< 9	4n 18.8	19-171
^{237}Np	2n <0.1	-	2n <0.1	-	3n 19.2	41-462
^{242}Pu	4n 75.5	70-640	4n 11.2	13 - 102	4n 7.5	11-94
^{244}Pu	4n 120.9	120-860	5n 18.7	23 - 125	4n 6.2	8-60
^{241}Am	3n 86.5	140-1410	4n 3.0	4 - 43	3n 1.8	11-135
^{243}Am	4n 86.2	110-1140	4n 3.0	3 - 22	3n 2.1	14-135
^{245}Cm	4n 36.1	36-263	4n 0.7	3 - 18	4n 0.7	14-16
^{248}Cm	4n 26.5	36-205	4n 1.6	2 - 22	4n 0.2	< 2
^{249}Bk	4n 14.6	21-252	4n 0.2	<3	4n <0.1	-
^{249}Cf	3n 2.2	2-11	4n 0.7	< 2	4n 0.8	-
^{251}Cf	4n 1.4	4-45	4n 0.1	1.4 - 9.2	4n <0.1	-
^{254}Es	4n <0.1	-	4n <0.1	-	4n <0.1	-

Table 5.3 also compares the Kewpie2 calculations with the FbD calculations (private communication with T. Cap). The FbD data presents lower and upper limits of the calculations resulting from the uncertainty in determining the fusion probability using linear approximation (see Eq. (3.17) and Fig. 2.31). The Kewpie2 model calculations are more pessimistic. Usually, the predicted values are below a lower limit of the FbD calculations.

In conclusion, we highlighted the active experimental and theoretical investigations attempting to synthesise the elements Z_{CN} = 119 and 120. The plausible projectile and target combinations for consideration are ^{51}V + ^{248}Cm [153], ^{54}Cr + ^{243}Am [154], ^{54}Cr + ^{248}Cm [155], and ^{50}Ti + ^{249}Cf [36]. The maximum predicted production cross sections are 1.59 fb, 2.09 fb, 0.18 fb and 2.18 fb, according to Kepwie2 calculations. The corresponding FbD predictions are listed in Table 5.3. The complete 2n, 3n, 4n and 5n excitation functions are shown in Fig. 5.3. For completeness, the calculation for reactions listed in Table 5.3 are shown in Figs. 5.4, 5.5 and 5.6 for the projectiles ^{50}Ti, ^{51}V and ^{54}Cr, respectively. Only predictions with cross sections > 0.1 fb are shown.

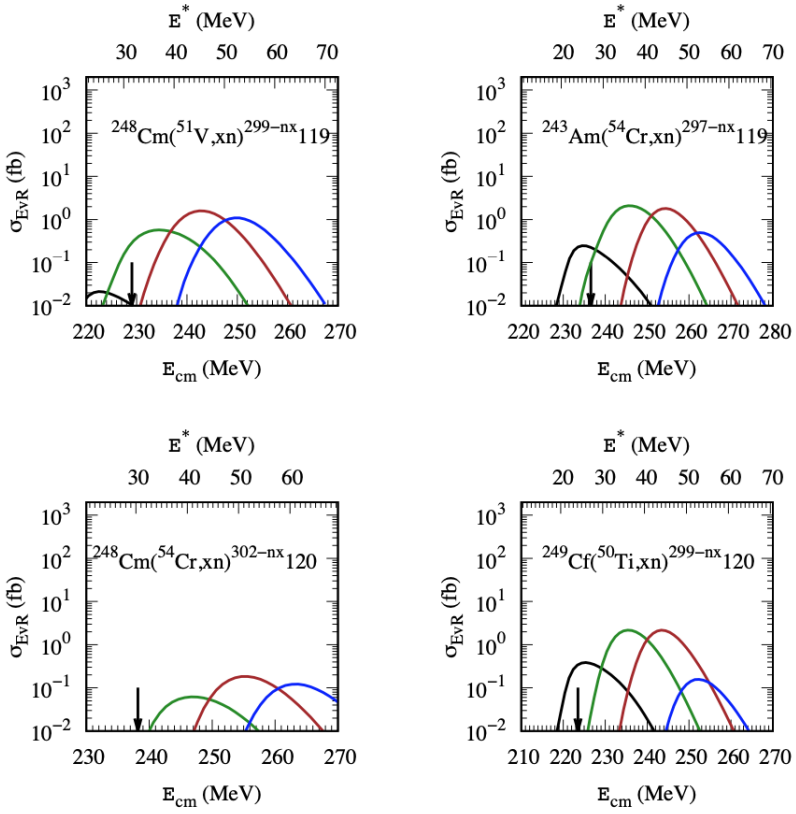

Figure 5.3: Excitation functions for the projectile-target combinations leading to the synthesis of elements with Z_{CN} = 119, and 120 using hot fusion reactions. The curves are ^{51}V +^{248} Cm $\rightarrow^{299}$ 119, ^{54}Cr +^{243} Am $\rightarrow^{297}$ 119, ^{54}Cr +^{248} Cm $\rightarrow^{302}$ 120, and ^{50}Ti +^{249} Cf $\rightarrow^{299}$ 120. The curves for the 2n, 3n, 4n and 5n excitation functions are shown. The position of the black arrows corresponds to the value of the mean Coulomb barrier. The colours black, green, brown and blue denote the 2n, 3n, 4n and 5n channels, respectively. Only reactions with cross sections > 0.1 fb are shown. The theoretical calculations use the undamped Langevin formalism for the formation probability, and the nuclear ground and saddle states properties are taken from the Ref. [69].

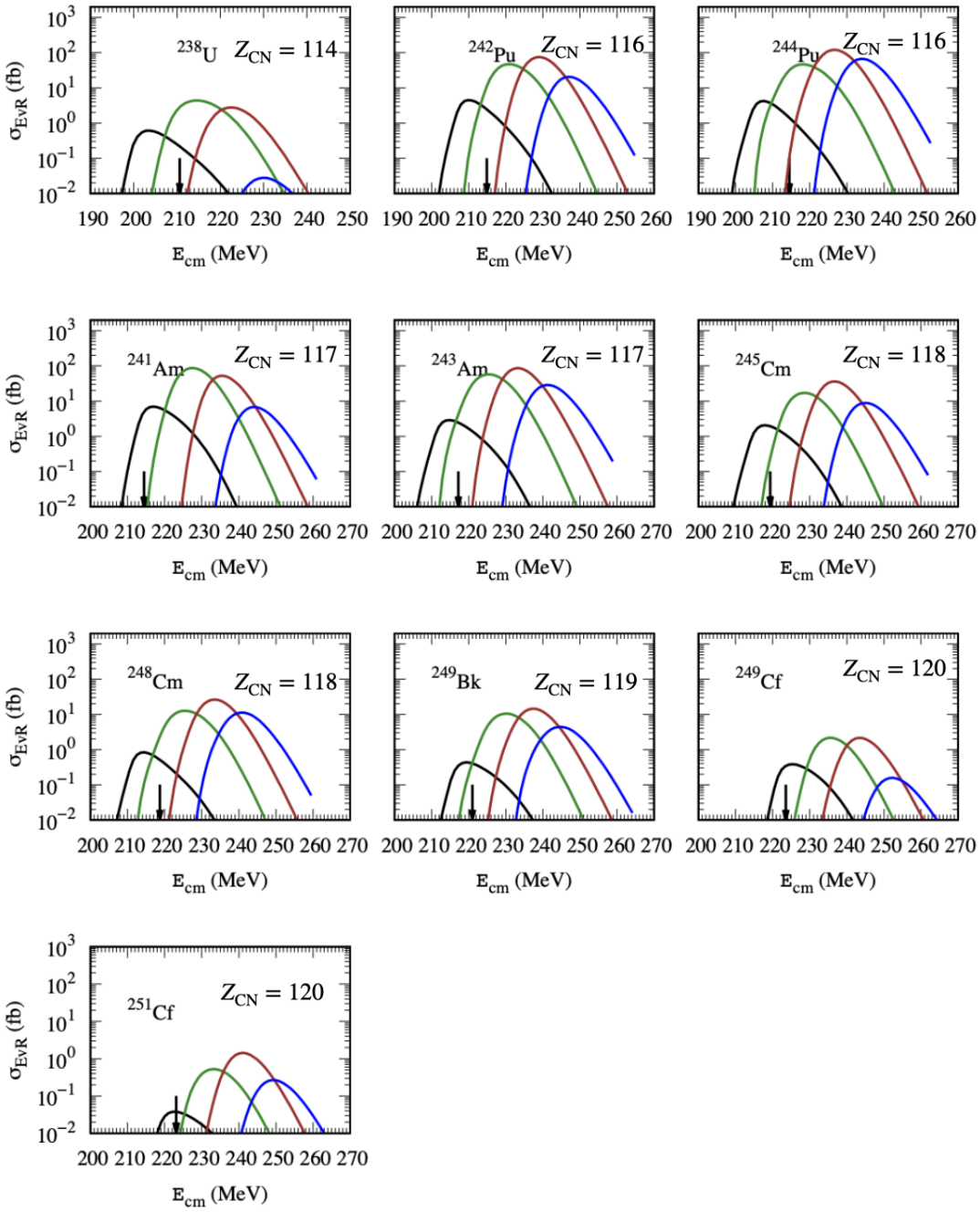

Figure 5.4: The 2n-5n excitation functions for ^{50}Ti induced reactions on the targets indicated in each panel. The position of the black arrows corresponds to the value of the mean Coulomb barrier. The theoretical calculations use the undamped Langevin formalism for the formation probability, and the nuclear ground and saddle states properties are taken from the Ref. [69]. The colours black, green, brown and blue denote the 2n, 3n, 4n and 5n channels, respectively. Only reactions with cross sections > 0.1 fb are shown.

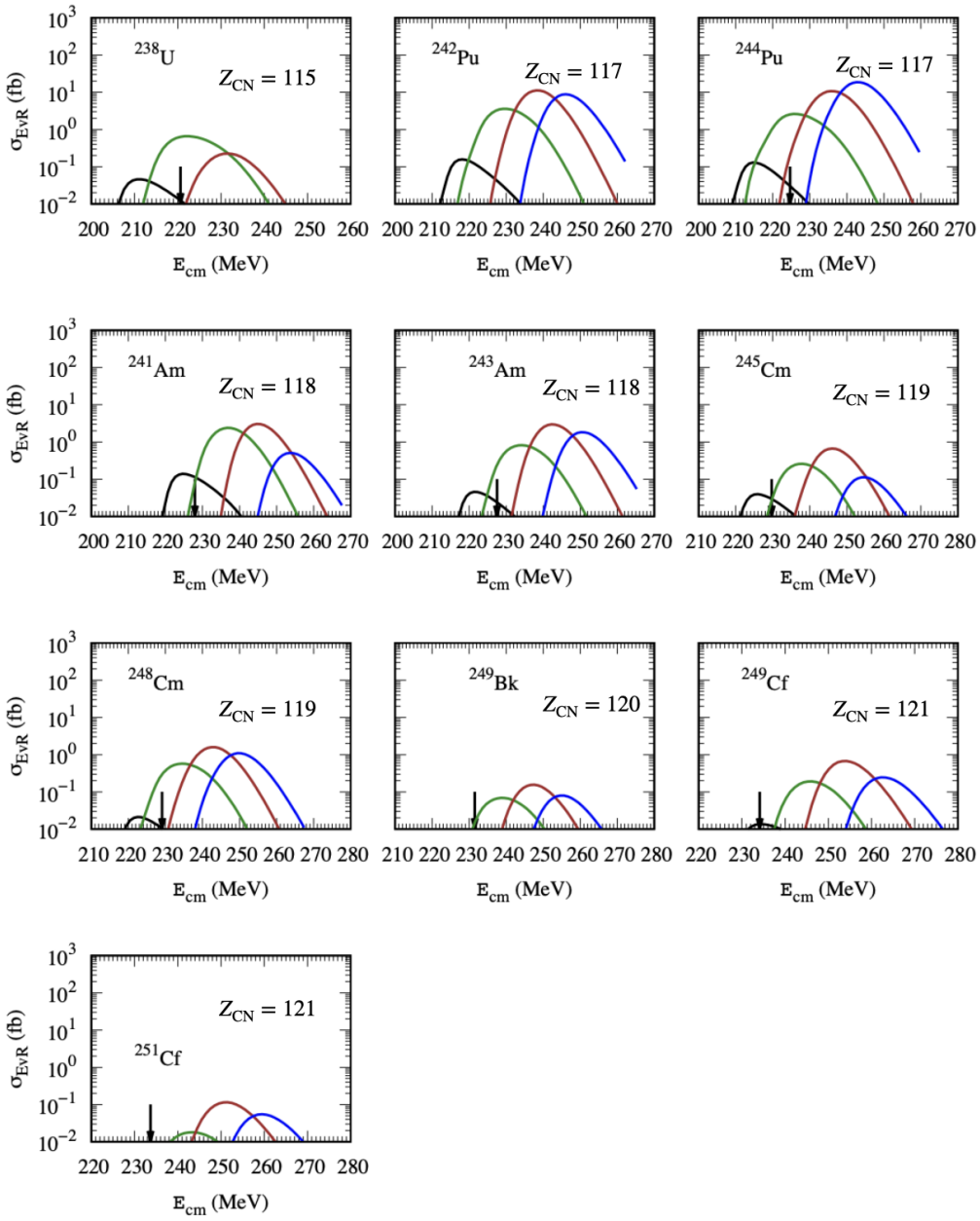

Figure 5.5: The 2n-5n excitation functions for ^{51}V induced reactions on the targets indicated in each panel of the panels. The position of the black arrows corresponds to the value of the mean Coulomb barrier. The theoretical calculations use the undamped Langevin formalism for the formation probability, and the nuclear ground and saddle states properties are taken from the Ref. [69].The colours black, forest-green, brown and blue denotes the 2n, 3n, 4n and 5n channels, respectively. Only reactions with cross sections > 0.1 fb are shown.

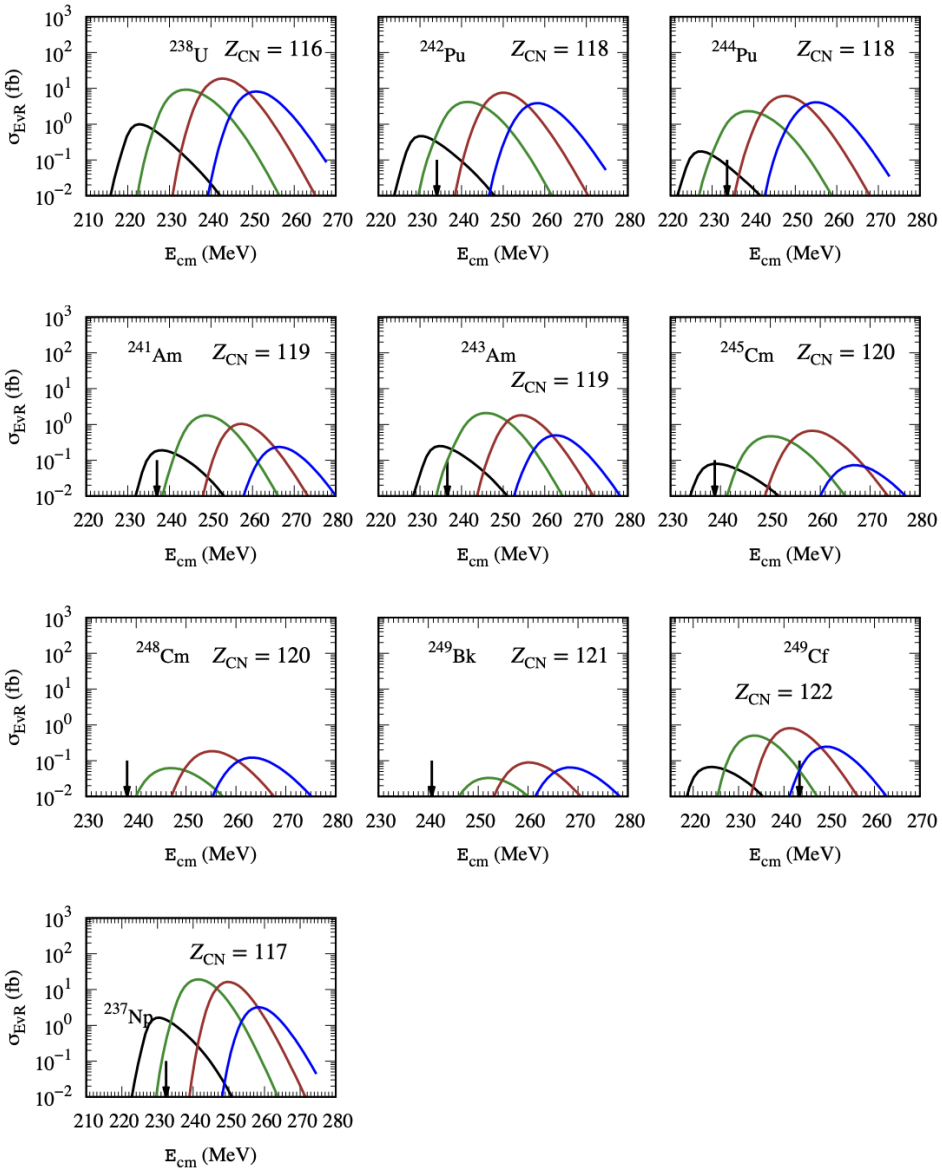

Figure 5.6: The 2n-5n excitation functions for ^{54}Cr induced reactions on the targets indicated in each panel of the panels. The position of the black arrows corresponds to the value of the mean Coulomb barrier. The theoretical calculations use the undamped Langevin formalism for the formation probability, and the nuclear ground and saddle states properties are taken from the Ref. [69]. The colours black, forest-green, brown and blue denotes the 2n, 3n, 4n and 5n channels, respectively. Only reactions with cross sections > 0.1 fb are shown.

5.3 Conclusion

This chapter summarises the results of investigating the compound nucleus formation probability within the Langevin formalism in the Kewpie2 code. The fitting coefficients of the injection point distance, an important parameter of the formation probability at the overdamped limit of Langevin formalism, are constructed based on the loss function metrics. Subsequently, the adoption of the best-optimised parameters is recommended. The current version of the Kewpie2 is bench-marked on excitation function ^{207}Pb(^{64}Ni,1n)^{210}Ds. The theoretically calculated results are within factor three from the experimental data.

Finally, the optimised parameters of the hot fusion injection point distance are compared using the loss function metrics. Here, the model also includes full Langevin formalisms of the compound nucleus formation probability. It turns out that the full Langevin better describes the data than the overdamped approximation with the injection point distance. The model is subsequently used to make predictions for a set of actinide target reactions induced by ^{50}Ti, ^{51}V and ^{54}Cr projectiles. Even though the calculations are pessimistic, they are comparable to the lower limits of the FbD model calculations.

Chapter 6

Constraining the Formation Probability of Superheavy Nuclei

In the previous chapters we have implemented the compound nucleus formation probability in the overdamped and undamped Langevin formalism within the Kewpie2 model. However, an accurate evaluation of the formation probability hinges on the capture and the survival probability because the model parameters are obtained by adjusting the theoretical excitation functions to the maxima of the experimental excitation functions. Therefore, any uncertainty from the capture or survival part will lead to discrepancies between different approaches.

This is evident in Fig. 5.1, where the formation probability differs among models by up to two orders of magnitude. Therefore, to reproduce experimental results, the survival probability is often adjusted to compensate for discrepancies between theoretical predictions and experimental observations. This brings the question: "What are the true values or the bounds of the compound nucleus formation probability?" This chapter aims to identify and isolate uncertainty in the capture and the experimental residue production cross section parts and investigate methods to quantitatively constrain the formation probability step. The success of this study will allow us to improve the reliability of the model predictions.

As we have seen so far, the process of modelling evaporation residue cross section involves three steps: (1) capture, (2) formation, and (3) survival probability. The formalises for the capture cross sections and the survival probability are generally well understood; however, the uncertainty contribution from these steps is far from negligible [53, 73, 156]. For example, the fission barrier is known to impact the survival probability significantly, potentially causing variations of up to two orders of magnitude per 1-2 MeV change in its values [73]. Thus, simply changing the fission barrier could lead to an entirely different set of parameters for the formation probability.

Furthermore, various sub-models, including the level density functions, level density parameter, shell damping parameters of the level density prescriptions, and neutron inverse capture cross sections, can also lead to variation in the formation probability fitted parameter values (s_0 and β_{ss}). Moreover, matching the statistical survival probability modelling to the dynamical limit by incorporating Kramers-Strutinsky and the collective

enhancement will yield different s_0 and β_{ss} parameter values. Lastly, the semi-classical empirical Gaussian barrier distribution (EBD) capture model, as seen in the previous Subsection 2.1.3, may unreliably predict the capture cross section below the Coulomb barrier.

To tackle this question, we will resort to the Bohr hypothesis of compound nucleus formation. Bohr's compound nucleus model proposes a two-step process for nuclear reactions: forming an intermediate compound nucleus followed by its decay. The formation phase consists of two colliding nuclei merging into a compound nucleus in statistical equilibrium. In this state, the CN retains information about the total energy, angular momentum, and other conserved quantities. However, it loses memory of the details of the entrance channel. Therefore, the decay of the compound nucleus through the exit channel is independent of the formation phase [83, 157]. This concept can be applied to different entrance channels, forming a compound nucleus at the same excitation energies, as depicted in Fig. 6.1.

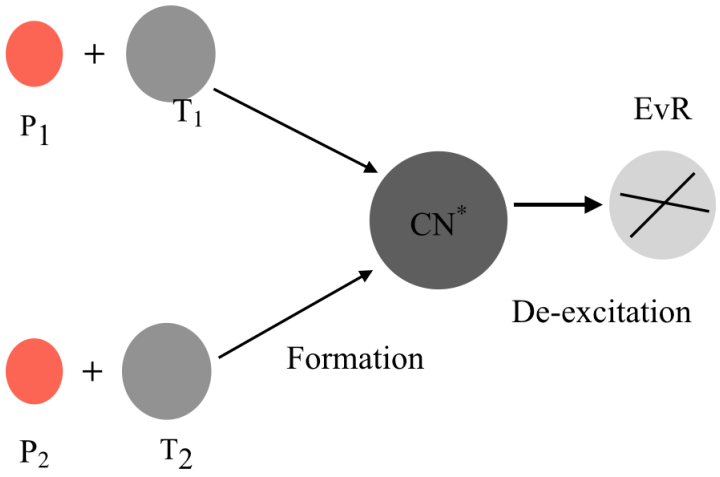

Figure 6.1: A schematic diagram of two different projectile and target combinations $(P_1 + T_1)$ and $(P_2 + T_2)$ leading to the same compound nucleus (CN) formation. The formation (intermediate step) refers to the process of attaining a statistical equilibrium, and the last stage is the exit channel, where the compound nucleus losses energy excess in the de-excitation process avoiding fission by emission of light particles. Fission events are here not considered.

Building on the Bohr independent hypothesis, one can investigate the production cross sections of pairs of reactions leading to the formation of the same compound nucleus:

$$\frac{\sigma^1_{\mathrm{EvR}}}{\sigma^0_{\mathrm{EvR}}} = \frac{\sigma^1_{\mathrm{cap}}}{\sigma^0_{\mathrm{cap}}} \times \frac{{P_{\mathrm{CN}}}^1}{P^0_{\mathrm{CN}}} \times \frac{P^1_{\mathrm{surv}}}{P^0_{\mathrm{surv}}}. \tag{6.1}$$

Here σ_{EvR} stands for the evaporation residue cross sections, and σ_{cap} is a theoretical capture cross section. This is evaluated using the Gaussian empirical barrier distribution model. The P_{CN} and P_{surv} are the average formation and survival probability, respectively. Note, that the formula (6.1) uses an approximate version of Eq. (2.2).

At sufficiently high excitation energies where the number of partial waves contributing to the process in both reactions is equivalent, $P^0_{\mathrm{surv}} \approx P^1_{\mathrm{surv}}$. Then one can reduce Eq. (6.1)

to:

$$\frac{P^1_{\mathrm{CN}}}{P^0_{\mathrm{CN}}} = \frac{\sigma^0_{\mathrm{cap}}}{\sigma^1_{\mathrm{cap}}} \times \frac{\sigma^1_{\mathrm{EvR}}}{\sigma^0_{\mathrm{EvR}}}. \tag{6.2}$$

Here, we are left with the ratio of the compound nucleus formation probability of the respective entrance channel which is equal to the product of the ratios of the capture and EvR cross sections. The capture cross section ratio can be calculated using Eq. (2.34) while the EvR cross sections ratio can be estimated using the experimental data if available. This allows us to estimate the formation probability ratio independently of the survival step.

Now that we have eliminated the survival probability, we can investigate the Eq. (6.2) by propagating the uncertainties in the remaining terms onto $\frac{P^1_{\mathrm{CN}}}{P^0_{\mathrm{CN}}}$. The uncertainty in the capture cross sections is determined following the work in Ref. [73] and the results stated in the Subsection 2.1.2 and details presented in the Appendix A. The EvR cross sections are taken from the experimental data. With this approach, we hope to gain insight into constraining the compound nucleus formation probability, the most uncertain step in the theoretical description of the reactions dynamics. This is referred to as the inverse problem with uncertainty analysis, as shown in Ref. [76].

6.1 Uncertainty in the Formation Probability

An uncertainty analysis involves systematically identifying potential sources of uncertainty, quantifying their magnitudes, and propagating them through the model to understand their impact on the outcome of the model. This process helps us estimate the range of possible outcomes, assess the model's sensitivity to different inputs, and ultimately build confidence in the predictions of the model. However, while uncertainty analysis significantly reduces doubt, it cannot eliminate it due to the inherent limitations of models and incomplete knowledge [76].

We are interested in evaluating the uncertainty in $\left(\frac{P^1_{\mathrm{CN}}}{P^0_{\mathrm{CN}}}\right)$, given by Eq. (6.2). Since we have eliminated the impact of the survival probability based on the assumptions we have previously made ($P^0_{\mathrm{surv}} \approx P^1_{\mathrm{surv}}$), the remaining sources of the uncertainties are due to the capture model and the experimental EvR cross sections. Evaluating this may help us to understand the impact of uncertainty contributions from the capture model and experimental production cross section on the formation probability.

6.1.1 Propagation of Uncertainty

Following the propagation of uncertainty outlined in the B.13, the variation in the $\left(\frac{P^1_{\mathrm{CN}}}{P^0_{\mathrm{CN}}}\right)$ due to the capture model and the experimental uncertainties can be written as:

$$u^2\left(\frac{P^1_{\mathrm{CN}}}{P^0_{\mathrm{CN}}}\right) = \left(\frac{P^1_{\mathrm{CN}}}{P^0_{\mathrm{CN}}}\right)^2 \times \left[\left(\frac{u\left(\sigma^1_{\mathrm{EvR}}\right)}{\sigma^1_{\mathrm{EvR}}}\right)^2 + \left(\frac{u\left(\sigma^0_{\mathrm{EvR}}\right)}{\sigma^0_{\mathrm{EvR}}}\right)^2 + \left(\frac{u\left(\sigma^0_{\mathrm{cap}}\right)}{\sigma^0_{\mathrm{cap}}}\right)^2 + \left(\frac{u\left(\sigma^1_{\mathrm{cap}}\right)}{\sigma^1_{\mathrm{cap}}}\right)^2 - 2\left(\frac{u\left(\sigma^0_{\mathrm{cap}}, \sigma^1_{\mathrm{cap}}\right)}{\sigma^0_{\mathrm{cap}} \times \sigma^1_{\mathrm{cap}}}\right)\right]. \tag{6.3}$$

Here, $\sigma^{0,1}_{\mathrm{EvR}}$ and $u\left(\sigma^{0,1}_{\mathrm{EvR}}\right)$ are the experimental residue production cross sections and the respective uncertainties, whereas, the $\sigma^{0,1}_{\mathrm{cap}}$ and $u\left(\sigma^{0,1}_{\mathrm{cap}}\right)$ are the calculated capture cross sections and their uncertainties. The indices correspond to the different entrance channels that form the same compound nucleus. The $u^2\left(\frac{P^1_{\mathrm{CN}}}{P^0_{\mathrm{CN}}}\right)$ is the variance in the ratio $\left(\frac{P^1_{\mathrm{CN}}}{P^0_{\mathrm{CN}}}\right)^2$ due to the uncertainty of the capture cross section and the experimental EvR cross section. The experimental data (including the uncertainties) are known and will be retrieved from the literature.

The uncertainty analysis of the capture cross section (Eq. (2.34)) according to Ref. [73] as stated in the Section 2.1.2 is recalled here. All the parameters entering Eq. (6.3) are readily available, except for the covariance between the two capture cross sections. This can be obtained following Eq. (B.13) as follows:

$$u\left(\sigma^0_{\mathrm{cap}}, \sigma^1_{\mathrm{cap}}\right) = \sum_{i=1}^{N}\sum_{j=1}^{N} \frac{\partial \sigma^0_{\mathrm{cap}}}{\partial w_i}\frac{\partial \sigma^1_{\mathrm{cap}}}{\partial w_j} u(w_i, w_j), \tag{6.4}$$

where $w_i = [r_0, a, b, c, \sigma_0, C]$. The matrix form expressing Eq. (6.4) for easy evaluation is given as:

$$u\left(\sigma^0_{\mathrm{cap}}, \sigma^1_{\mathrm{cap}}\right) = \left[\frac{\partial \mathrm{Cap}^0}{\partial w_i}\right] \begin{bmatrix} u^2(r_0) & 0 & 0 & 0 & 0 & 0 \\ 0 & u^2(a) & u(a,b) & u(a,c) & 0 & 0 \\ 0 & u(b,a) & u^2(b) & u(b,c) & 0 & 0 \\ 0 & u(c,a) & u(c,b) & u^2(c) & 0 & 0 \\ 0 & 0 & 0 & 0 & u^2(\sigma_0) & u(\sigma_0, C) \\ 0 & 0 & 0 & 0 & u(\sigma_0, C) & u^2(C) \end{bmatrix} \cdot \left[\frac{\partial \mathrm{Cap}^1}{\partial w_j}\right]^{\mathrm{T}} \tag{6.5}$$

In conclusion, we have outlined the formalisms for propagating the uncertainty due to the capture and residue cross sections of the different entrance channels onto the quantity $\left(\frac{P^1_{\mathrm{CN}}}{P^0_{\mathrm{CN}}}\right)$.

6.1.2 Application to ^{258}No

The technique described above is applied to the formation of Nobelium-258 [158] via the following entrance channels:

$$^{258}\text{No} = \begin{cases} 0: & ^{22}\text{Ne} + ^{236}\text{U} \\ 1: & ^{26}\text{Mg} + ^{232}\text{Th} \end{cases}, \tag{6.6}$$

where 0 and 1 correspond to indices identifying reactions. For these reactions, the Coulomb hindrance factors, $Z_P \times Z_T$, are 920 and 1080, respectively. This implies they should not be strongly hindered and the formation probability should be close to 1 in both cases; therefore, $\left(\frac{P^1_{CN}}{P^0_{CN}}\right)$ should be approximately 1. Nevertheless, studying these reactions will give insight into the role of the uncertainty from the capture model and the residue cross section in decreasing the uncertainty in the formation probability.

To begin, Table 6.1 illustrates the experimental measurements with each column corresponding to the reaction (**Reaction**), the excitation energy (E^* in MeV), the EvR cross section (σ^{Exp}_{EvR} in pb), the uncertainty (u(EvR) in pb) and the neutron emission channels (CH). The calculated values of capture cross sections are also shown. As shown in Table 6.1, the excitation energies are high enough to justify the approximation $P^0_{surv} \approx P^1_{surv}$. That is the partial waves contributing to the formation of ^{258}No are exhausted in both reaction channels. This allows us to apply Eq. (6.2) and Eq. (6.1.1). Note that the values of 57 MeV and 60 MeV for the 6n channel are averaged to 58.5 MeV in the theoretical calculations of the capture cross section.

Table 6.1: Two reactions leading to the formation of the same CN*, ^{258}No. The columns describe E^* (in MeV), capture cross sections σ^{th}_{cap} (in mb), evaporation residue cross sections σ^{Exp}_{EvR} (in pb), experimental uncertainties u(EvR) (in pb), and the observed channel (CH). The experimental data are taken from Ref. [158].

Reaction	E^* (MeV)	σ^{th}_{cap} (mb)	$\sigma^{Exp}_{EvR} \pm u$(EvR) (pb)	CH
^{22}Ne +^{236} U	45	155.2 ± 6.02	7 ± 4	4n
	50	300.9 ± 6.26	3 ± 7	5n
	57	487.3 ± 6.16	2 ± 5	6n
^{26}Mg +^{232} Th	45	100.6 ± 5.6	6 ± 2	4n
	50	225.9 ± 6.6	9 ± 5	5n
	60	467.9 ± 6.5	8 ± 3	6n

We begin by investigating the uncertainty propagation of the capture cross section model onto Eq. (6.3). The panels (a) and (b) of Fig. 6.2 illustrate the capture cross section (solid blue lines) for ^{22}Ne + ^{236}U and ^{26}Mg + ^{232}Th, respectively, with the upper and lower limits of the cross sections shown as blue dashed lines ($\sigma^{th}_{cap} \pm u(\sigma^{th}_{cap})$).

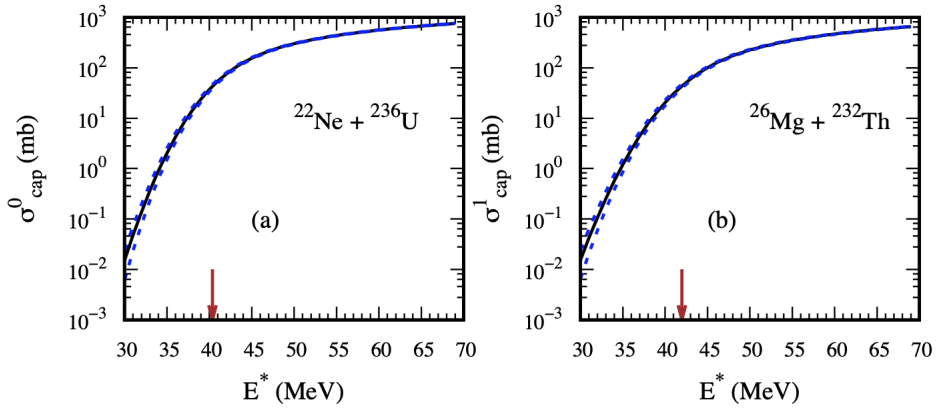

Figure 6.2: Capture cross sections as a function of the excitation energy E^*: (a) for the reaction ^{22}Ne +^{236} U and (b) ^{26}Mg +^{232} Th, leading to the formation of ^{258}No*. The upper and lower dashed lines are the uncertainty intervals evaluated as $\sigma^{\text{th}}_{\text{cap}} \pm u(\sigma^{\text{th}}_{\text{cap}})$. The arrows in each panel represent the excitation energies at the Coulomb barrier energies ($E_{\text{cm}} = B_0$) for each reaction.

Panel (a) of Fig. 6.3 illustrates the relative uncertainty in the capture cross section, for ^{22}Ne + ^{236}U reaction in blue and for ^{26}Mg + ^{232}Th reaction in brown, as a function of the compound nucleus's excitation energy. This excitation energy is related to the energy in the centre of the mass frame via the Q-value of the reaction, as shown in Eq. (2.1): $E_{\text{cm}} = E^* - Q$. The relative uncertainty in both reactions, as depicted in panel (a) of Fig. 6.3, decreases with the increasing energy. As seen previously, the empirical Gaussian barrier distribution model has the lowest uncertainty at high energies.

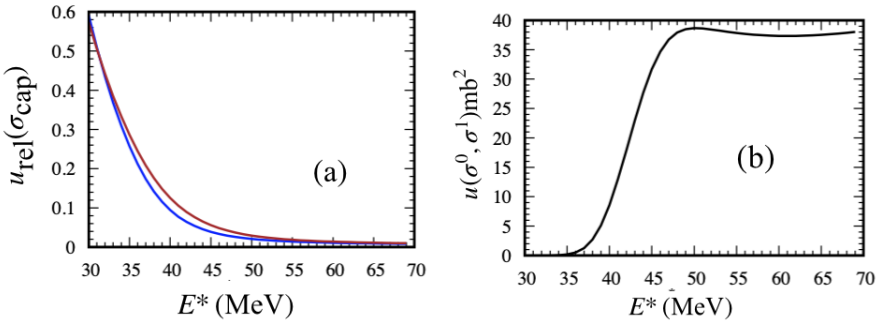

Figure 6.3: Analysis of the capture cross section uncertainties for the reactions ^{22}Ne + ^{236}U and ^{26}Mg + ^{232}Th leading to the formation of ^{258}No. (a) the relative uncertainty of the capture cross sections for the ^{22}Ne + ^{236}U (in red line) and ^{26}Mg + ^{232}Th (in blue line) reactions as a function of the excitation energy E^*. Panel (b) shows the covariance between the capture cross sections evaluated for the two reactions due to the usage of the same capture formula (Eq. 2.34) as a function of energy.

The correlation between the two capture cross sections is shown as a function of energy in panel (b) of Fig. 6.3. Here, the two capture cross sections behave independently at lower energies but exhibit a strong correlation as energy increases between 40 and 50 MeV. The covariance reaches a plateau of around 40 MeV, suggesting that this correlation is strongest at energies between 40 and 50 MeV. Further increases in energy do not significantly change

the covariance.

Having assessed the uncertainty contribution from the capture cross section, we now turn our attention to how it affects the overall uncertainty of $\left(\frac{P^1_{\mathrm{CN}}}{P^0_{\mathrm{CN}}}\right)$ ratio. To answer this, we show the uncertainty contributions from $\left(\frac{\sigma^0_{\mathrm{cap}}}{\sigma^1_{\mathrm{cap}}}\right)$ and $\left(\frac{\sigma^1_{\mathrm{EvR}}}{\sigma^0_{\mathrm{EvR}}}\right)$ terms in Eq. (6.2) independently, and then evaluate the total impact on $\left(\frac{P^1_{\mathrm{CN}}}{P^0_{\mathrm{CN}}}\right)$. The Fig. 6.4 illustrates the relative uncertainties in these quantities, along with the resulting uncertainty in the formation probability ratios.

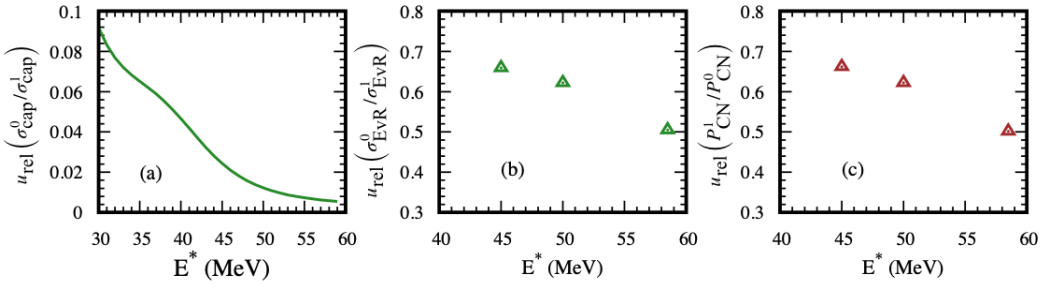

Figure 6.4: (a) Relative uncertainty in the ratio of capture cross sections, $u_{\mathrm{rel}}\left(\frac{\sigma^0_{\mathrm{cap}}}{\sigma^1_{\mathrm{cap}}}\right)$, as a function of the excitation energy. (b) Relative uncertainty in the ratio of evaporation residue cross sections, $u_{\mathrm{rel}}\left(\frac{\sigma^1_{\mathrm{EvR}}}{\sigma^0_{\mathrm{EvR}}}\right)$, as a function of the excitation energy. (c) Relative uncertainty in the ratio of compound nucleus formation probabilities, $u_{\mathrm{rel}}\left(\frac{P^1_{\mathrm{CN}}}{P^0_{\mathrm{CN}}}\right)$, as calculated from the uncertainties in panels (a) and (b).

Fig. 6.4 shows the relative uncertainties of these quantities: $u_{\mathrm{rel}}\left(\frac{\sigma^0_{\mathrm{cap}}}{\sigma^1_{\mathrm{cap}}}\right)$ (in panel (a)), $u_{\mathrm{rel}}\left(\frac{\sigma^1_{\mathrm{EvR}}}{\sigma^0_{\mathrm{EvR}}}\right)$ (in panel (b)), and $u_{\mathrm{rel}}\left(\frac{P^1_{\mathrm{CN}}}{P^0_{\mathrm{CN}}}\right)$ (in panel (c)). Panel (a) demonstrates that the relative uncertainty in the capture cross sections ratios $\left(\frac{\sigma^0_{\mathrm{cap}}}{\sigma^1_{\mathrm{cap}}}\right)$ decreases with increasing energies, reinforcing the observation in panel (a) of Fig. 6.3. The relative uncertainty decreases from about 2.4% at 45 MeV to 1.2% at 50 MeV and 0.4% at 60 MeV. This highlights the increasing accuracy of the capture cross section model at higher energies, as we have previously seen.

We find similar trends in the experimental residue production cross section, which also exhibits a decreasing relative uncertainty with increasing energy. However, the relative uncertainties in this case are larger, with values of 66.2% at 45 MeV, 62.1% at 50 MeV, and 50.2% at 60 MeV. These high values highlight the challenges of low statistics often associated with the synthesis of super-heavy elements.

Finally, panel (c) shows the composed relative uncertainty in $u_{\mathrm{rel}}\left(\frac{P^1_{\mathrm{CN}}}{P^0_{\mathrm{CN}}}\right)$ due to the capture

and the experimental residue cross sections. Here, the uncertainties do not change from what is seen from the evaporation residue (EvR), because the contributions from the capture cross section is small relative to what is seen on EvR. Therefore, we need a reaction with low experimental uncertainties relative to the absolute values for a meaningful comparison. Nevertheless, this analysis suggests that relative uncertainty in $\left(\frac{P^1_{\mathrm{CN}}}{P^0_{\mathrm{CN}}}\right)$ will decrease by optimising the experiment at these energies for higher experimental production cross section and smaller uncertainties compared to the experimental data.

Table 6.2 shows evaluated values of $\frac{P^1_{\mathrm{CN}}}{P^0_{\mathrm{CN}}}$ as a function of the excitation energy. Interestingly, the evaluated values at the two highest energies show that the ratio is close to 0.5, which is lower than 1. This suggest that the more charge symmetric reaction, ^{26}Mg +^{232} Th, may have a lower formation probability than the ^{22}Ne +^{236} U reaction. However, both confidence intervals with a coverage factor of 2 include the value 1, meaning we cannot exclude the general assumption that both reactions are not hindered.

Table 6.2: Ratio of compound nucleus formation probability, $\left(\frac{P^1_{\mathrm{CN}}}{P^0_{\mathrm{CN}}}\right) \pm u\left(\frac{P^1_{\mathrm{CN}}}{P^0_{\mathrm{CN}}}\right)$ of the two different channels leading to ^{258}No at three different excitation energies (E^*). The ratio is calculated for the ^{26}Mg +^{232} Th reaction with respect to the ^{22}Ne +^{236} U reaction. Note that the values of 57 MeV and 60 MeV for the 6n channel in Tab. 6.1 are averaged to 58.5 MeV to make comparisons.

E^* **MeV**	$\left(\frac{P^1_{\mathrm{CN}}}{P^0_{\mathrm{CN}}}\right)$
45.0	1.32 ± 0.88
50.0	0.48 ± 0.30
58.5	0.56 ± 0.28

6.1.3 Formation of ^{259}Db

Here, we consider two reactions that lead to the formation of ^{259}Db [121, 159]:

$$^{259}\mathrm{Db} = \begin{cases} 0: & ^{50}\mathrm{Ti} + ^{209}\mathrm{Bi} \\ 1: & ^{51}\mathrm{V} + ^{208}\mathrm{Pb} \end{cases}, \tag{6.7}$$

where 0 and 1 correspond to indices identifying reactions. Table 6.3 shows the measured EvR cross sections at given excitation energies. Only data for selected values of the excitation energies that can be directly compared are shown. Note that reported values of E^* are usually within ±2 MeV, which allows for comparison of data which are reported not exactly at the same energies.

In the analysis, we will consider only data for the 2n channel because of the significantly smaller uncertainties than those for the 1n channel. For the asymmetric uncertainties, we will use the average value:

$$u(\sigma_{\mathrm{EvR}}) = \frac{|\text{upper limit}|+|\text{lower limit}|}{2}. \tag{6.8}$$

Table 6.3: Two reactions leading to the formation of the same CN*, ^{259}Db*. The columns describe E^* (in MeV), capture cross sections $\sigma_{\rm cap}$ (in mb), evaporation residue cross sections $\sigma_{\rm EvR}^{\rm Exp}$ (in pb) for 1n and 2n channels, respectively, together with the experimental uncertainties u(EvR) (in pb). Last column shows the laboratory where the reaction was measured. The experimental data are taken from Ref. [159] (LBNL) and Ref. [121] (GSI).

Reaction	E^* (MeV)	$\sigma_{\rm cap}$ (mb)	$\sigma_{\rm EvR}^{\rm Exp}$ (pb) (1n)	$\sigma_{\rm EvR}^{\rm Exp}$ (pb) (2n)	LAB
^{50}Ti +^{209} Bi	20.3	4.8 ± 2.9	2600^{+1190}_{-850}	890^{+463}_{-330}	LBNL
	21.8	9.1 ± 4.75	390^{+130}_{-130}	2400^{+300}_{-300}	GSI
	24.6	24.2 ± 9.8	-	2000^{+270}_{-270}	GSI
^{51}V +^{208} Pb	19.5	0.58 ± 0.54	1000^{+460}_{-330}	250^{+170}_{-110}	LBNL
	22.0	2.24 ± 1.73	570^{+550}_{-310}	1660^{+450}_{-370}	LBNL
	24.9	8.07 ± 4.95	-	1400^{+600}_{-430}	LBNL

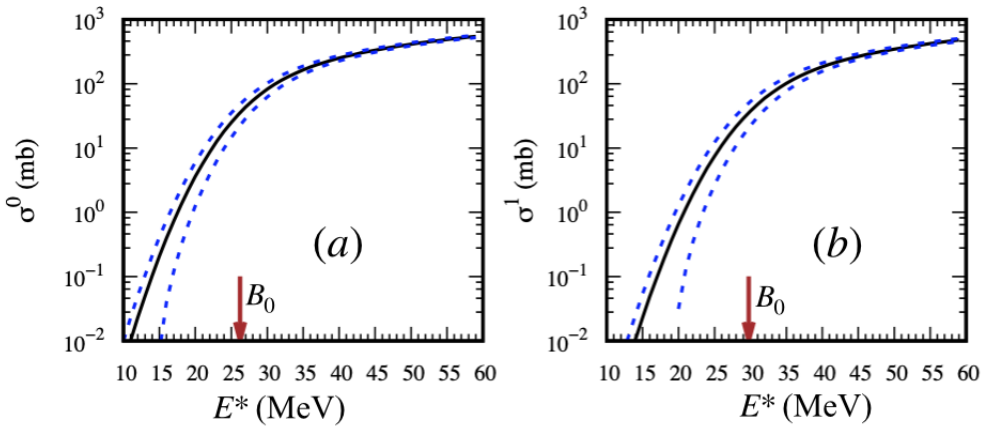

Figure 6.5: Capture cross sections as a function of the excitation energy E^*: (a) for the reaction ^{50}Ti +^{209} Bi and (b) ^{51}V +^{208} Pb, leading to the formation of ^{259}Db. The dashed lines show the uncertainty intervals evaluated as $\sigma_{\rm cap}^{\rm th} \pm u(\sigma_{\rm cap}^{\rm th})$. The arrows in each panel represent the excitation energies at the Coulomb barrier energies ($E_{\rm cm} = B_0$) for each reaction.

Panels (a) and (b) illustrate the capture cross section (solid blue lines) as a function of the excitation energy for the ^{50}Ti +^{209} Bi and ^{51}V +^{208} Pb reactions, respectively. The upper and lower dashed lines correspond to the upper and lower limits of the theoretical calculations: $\sigma_{\rm cap}^{\rm th} \pm u(\sigma)$.

Panel (a) of Fig. 6.5 shows the relative uncertainty in the capture cross section. The solid brown and blue lines correspond to the relative uncertainty for the ^{50}Ti +^{209} Bi and ^{51}V +^{208} Pb reactions, respectively. Panel (b) shows the correlation between the two capture cross sections as a function of E^*. The capture cross section is least correlated at the low energies. However, the trend reverses at the energies above the Coulomb barrier, which also have relatively small uncertainties in the capture cross section. The correlations

between the capture cross sections tend to decrease at much higher energies.

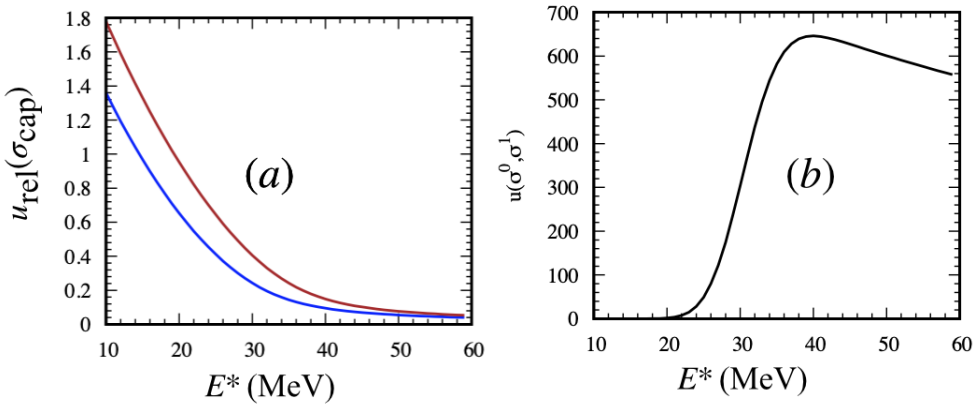

Figure 6.6: Analysis of capture cross section uncertainties for the reactions ^{51}V +^{208} Pb and ^{50}Ti +^{209} Bi leading to the formation of ^{259}Db. (a) the relative uncertainty in the capture cross sections of the reactions, ^{51}V +^{208} Pb (in red line) and ^{50}Ti +^{209} Bi (in blue line) as a function excitation energy E^*. (b) shows the covariance between the capture cross sections evaluated by the two reactions from the same capture model (Eq. 2.34) with increasing energy.

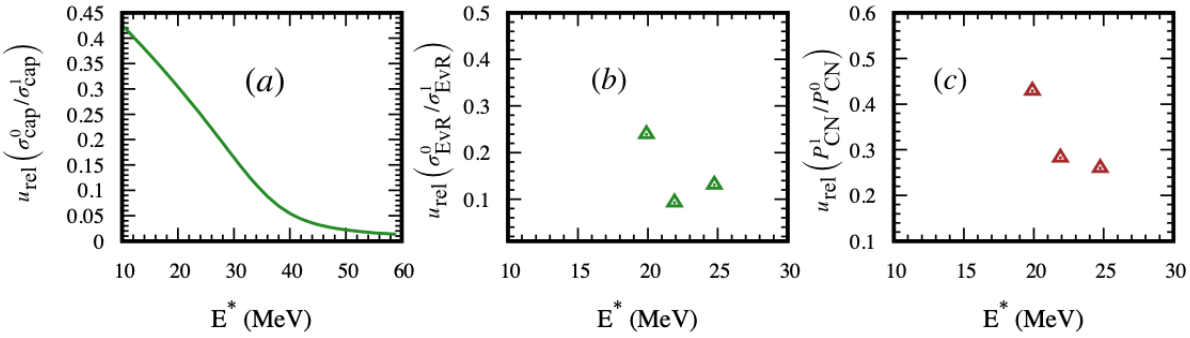

Figure 6.7: (a) Relative uncertainty of the ratio of capture cross sections, $u_{\text{rel}}\left(\frac{\sigma^0_{\text{cap}}}{\sigma^1_{\text{cap}}}\right)$, as a function of the excitation energy. (b) Relative uncertainty of the ratio of evaporation residue cross sections, $u_{\text{rel}}\left(\frac{\sigma^1_{\text{EvR}}}{\sigma^0_{\text{EvR}}}\right)$, as a function of the excitation energy. (c) Relative uncertainty in the ratio of compound nucleus formation probabilities, $u_{\text{rel}}\left(\frac{P^1_{\text{CN}}}{P^0_{\text{CN}}}\right)$, as calculated from the uncertainties in panels (a) and (b).

Finally, Fig. 6.7 illustrate the uncertainty from the capture cross sections $\left(\frac{\sigma^0_{\text{cap}}}{\sigma^1_{\text{cap}}}\right)$, the experimental residue cross sections $\left(\frac{\sigma^1_{\text{EvR}}}{\sigma^0_{\text{EvR}}}\right)$, and their total contribution to the $\left(\frac{P^1_{\text{CN}}}{P^0_{\text{CN}}}\right)$ ratio uncertainty at the respective energies provided in the Table 6.3. These are shown in the panel (a), (b) and (c) of the Fig. 6.7, respectively. The relative uncertainty in the ratios of the two capture cross sections $\left(\frac{\sigma^0_{\text{cap}}}{\sigma^1_{\text{cap}}}\right)$ is illustrated in the panel (a). As expected,

the relative uncertainty decreases with increasing energy, consistent with the previous observations. The relative uncertainty of the ratio of the experimental residue cross sections also decreases with increasing energy, as shown in panel (b). Panel (c) shows the relative uncertainty in the formation probabilities ratio due to the capture and the experimental residue cross sections uncertainties. Similar to the previous observation, the ratios of the formation probability decrease with increasing energy.

Table 6.4: Ratio of compound nucleus formation probability, $\left(\frac{P^1_{\mathrm{CN}}}{P^0_{\mathrm{CN}}}\right) \pm u\left(\frac{P^1_{\mathrm{CN}}}{P^0_{\mathrm{CN}}}\right)$ of the two different channels leading to ^{259}Db at three different excitation energies (E^*). The ratio is calculated for the ^{51}V +^{208} Pb reaction with respect to the ^{50}Ti +^{209} Bi reaction considering data for 2n channels from Tab. 6.3. The excitation energies given are the average values. The column $\left(\frac{P^1_{\mathrm{CN}}}{P^0_{\mathrm{CN}}}\right)_{\mathrm{th}}$ correspond to the theoretically evaluated ratios of the formation probability. This is calculated using Eq. (2.122).

E^* **MeV**	$\left(\frac{P^1_{\mathrm{CN}}}{P^0_{\mathrm{CN}}}\right)_{\mathrm{exp}}$	$\left(\frac{P^1_{\mathrm{CN}}}{P^0_{\mathrm{CN}}}\right)_{\mathrm{th}}$
19.9	2.37 ± 1.00	1.29
21.9	2.86 ± 0.81	1.27
24.75	2.15 ± 0.56	1.28

Table 6.4 shows the formation probability ratio (P_{CN} for ^{51}V+^{208}Pb to P_{CN} for ^{50}Ti+^{209}Bi) for three values of the excitation energy. Those ratios are obtained for 2n channels in Tab 6.3. In this case, the formation probability for a slightly more charge symmetric reaction is at least factor two greater. For all three energies, the obtained values are consistent with each other. The ratio obtained for the 1n channel at around 20 MeV, equal to 3.2, is also supported by the ratio obtained. However, the ratio at around 22 MeV for the 1n channel is higher and closer to 6.

The column $\left(\frac{P^1_{\mathrm{CN}}}{P^0_{\mathrm{CN}}}\right)_{\mathrm{th}}$ is the ratio of the theoretically evaluated formation probability for the reactions (P_{CN} for ^{51}V +^{208} Pb to P_{CN} for ^{50}Ti +^{209} Bi). This is shown as a test of comparison to the model-dependent experimental ratios $\left(\frac{P^1_{\mathrm{CN}}}{P^0_{\mathrm{CN}}}\right)_{\mathrm{exp}}$. The theoretical values are in the experimental confidence interval with a coverage factor of two. Therefore, the uncertainties in the experimental ratios should be reduced to constrain the models.

6.2 Conclusion

This preliminary study shows that uncertainty analysis could give insight into constraining the compound nucleus formation probability. We need experimental data at sufficiently high energies to reduce uncertainty in the empirical Gaussian barrier capture model. At this energy, the partial waves contribution from both entrance channels to the formation of the compound nucleus will be similar and hence justifying the approximation, $P^{0}_{\mathrm{surv}} \approx P^{1}_{\mathrm{surv}}$. Furthermore, reactions with larger residue production cross sections should be selected. This potentially requires investigating a series of projectile and target combinations using the predictive power Kewpie2 model for a new experiment.

Chapter 7

Conclusion and Perspective

This thesis aimed to improve the predictive power of the Kewpie2 code for simulating the production cross section of super-heavy elements formed via fusion-evaporation reactions. The Kewpie2 code is a numerical tool designed to investigate the low-probability events associated with super-heavy nuclei formation in fusion-evaporation reactions [53]. However, while Kewpie2 can independently simulate the capture cross section and survival probability, it was relying on external sources for the compound nucleus formation probability.

7.1 Contribution

To address the limitations of the Kewpie2 model, Chapter 2 focused on updating the compound nucleus survival probability simulation within Kewpie2 and optimizing it to function as a standalone code. This involved thoroughly comparing calculations with an established Fusion-by-Diffusion (FbD) code. To ensure accuracy, the theoretical nuclear ground state and saddle properties used in the simulations were updated to the data from Ref. [69] consistent with the FbD approach.

The thesis also investigates survival probability modelling using the latest data for super-heavy elements. The results of this refinement demonstrate agreement between the Kewpie2 and FbD calculations for the survival probability. Noticeable differences are due to the different formalisms employed for the level density functions, highlighting the importance of these factors in accurately simulating super-heavy element production. The comparison of the survival probability then set the stage for investigating the compound nucleus formation probability.

Building upon the refined survival probability, we investigate the probability of compound nucleus formation using the one-dimensional overdamped limit of the Langevin formalism in Chapter 2. This is simple compared with multidimensional approaches [117], yet a practical tool used to study the dynamics of compound nucleus formation within the FbD model. This approach has been investigated in this study because of its success in predicting the production cross section within the FbD model [68].

The FbD formation probability is a phenomenological model that requires accurately parameterizing and fitting its adjustable parameter called the injection point distance. The injection point distance is an umbrella parameter that accounts for accuracy in reproducing and predicting the production cross sections within the model. The injection point distance is parameterised as a linear function of the difference between the centre of mass energy and the mean Coulomb barrier at the capture phase in the FbD model. The linear injection point distance is adopted and optimised within the Kewpie2 code. The results agreed with what was obtained in the literature. This was a step in making the Kewpie2 a self-contained code simulating the super-heavy production cross section. However, the statistical description of the deduced injection point distances used in the fit using R^2 metrics are 0.71 and 0.83 on cold and hot fusion data, respectively. Here, only 1n emission channels are considered for the cold fusion data. This is because the model inherently could not explain multiple neutron emission channels (2n and 3n) in cold fusion reactions. Considering the sensitivity of the injection point distance modelling in predicting the production cross section, the R^2 values pointed out that there is a room to improve the parameterization.

To solve this, we revisited the formalism of the formation probability within Langevin formalism but from a different perspective as shown in Chapter 3. Here, the dynamics are investigated instead of starting from an effective one-dimensional collective variable used in the overdamped approximation, considering fast and slow variables contributing to the dynamics. Knowing that the slow variables determine the final fate of the dynamics after the convergence of the fast ones. The question then was, what is the impact of eliminating the fast collective variables from the dynamics on the slow ones? Answering this question led to a new approach to parameterising the injection point distance, consistent with the Langevin formalism. This is first reported in the Ref. [81, 82].

The new injection point approach was investigated, and the coefficients were adjusted to the experimental data. It was found that it is better in predicting cross sections for the cold fusion data than the linear approach. For the hot fusion reactions, the linear and the new approaches give the same data description. Here, the R^2 values are 0.86 and 0.82 on the cold and hot fusion data, respectively.

The mass asymmetry and the Coulomb parameters are independently investigated as the model's explanatory features to further improve the predictive power of the new injection point distance. The mass asymmetry feature did not improve the quality of the fit, but the Coulomb parameter significantly increased the model's predictive power. It was found that with the inclusion of the Coulomb parameter dependent term, it is possible to describe the production cross sections of the cold fusion 1n reactions considered in the fit within one order of magnitude deviation from the experimental data. The 2n and 3n channels are equally well described. This is a significant improvement over the linear (FbD) and the new parameterization of the injection point distance. The Coulomb parameter is not considered for the hot fusion reactions since they are only ^{48}Ca induced and the Coulomb parameters are similar for all the projectile-target combinations considered. An attempt is made to combine a single parameterization for cold and hot fusion data by fitting the injection point distance model parameters to these data. The result shows that with the Coulomb parameter included in the fit, we could explain the experimental data within an order of magnitude deviation from the experiment. Description of both cold and hot reactions by one parametrization was never achieved within the FbD model.

Due to the energy-dependent injection distance parameterisation, we introduced angular momentum dependence to accurately describe the dynamics. The inclusion of angular momentum requires re-optimisation of the fitting parameters. The previous fitting technique could not work, and this subsequently led to treating the Kewpie2 as a black box in a systematic fitting technique with a Python Bayesian optimisation library. This is tested by using the typical chi-squared χ^2 and modified chi-squared (χ^2_{mod}) loss functions. The results of a typical χ^2 loss function are biased towards large experimental cross sections, while the smaller ones are heavily penalised (underestimated). To solve this problem, a modified loss function has been adopted. The modified loss function is symmetric and can penalise small and large experimental cross sections equally.

The systematic fitting method is tested with the modified loss function on the angular-momentum independent injection point distance. The test with the previously obtained values yielded similar results for both cold and hot fusion data. The technique is applied to the more complicated injection point distance parametrization with angular momentum dependence. Here, achieving convergence on the cold fusion data was difficult and required further investigation. The hot fusion data, however, converged, and the parameters produced results within an order of magnitude deviation from the experiment.

The optimised parameter (reduced friction coefficient) of the new parameterized injection is equal to 1.104×10^{21} s^{-1}. This raises the question of whether the dynamic is damped, as assumed in the overdamped derivation of the formation formalism. To investigate this further, we adopted a one-dimensional undamped Langevin formalism in Chapter 4. Here, we utilised the same potential energy map from the Fusion-by-Diffusion model. The undamped full Langevin formalism parameters are investigated and adjusted to the hot fusion data set only to ensure that the projectile-target asymmetry is similar in all reactions. The fit uses the systematic fitting technique adopted for the angular momentum-dependent injection point distance parametrization. Here, the hot fusion data is well reproduced within an order of magnitude with respect to the experimental data. Finally, Chapter 5 summarises the results from the analysis, and the best-optimised formation probability models are proposed for Kewpie2 in cold and hot fusion. The updated version of the Kewpie2 is used in predicting the production cross sections of elements with $Z_{\text{CN}} = 119$ and 120.

This thesis has, therefore, fulfilled its objective by improving the predictive power of Kewpie2 for simulating the production cross section of super-heavy nuclides formed via fusion evaporation reactions. The discrepancies between the optimised Kewpie2 and the measured experimental cross section are within an order of magnitude deviation for cold and hot fusion.

7.2 Future prospects

Implementing the formation probability into Kewpie2 code is an important development that extends the model's applicability. The model could be optimised to predict the production cross section involving charge particle emission. The next phase will be thorough analysis on how to constrain the compound nucleus formation probability. Following the

preliminary results from the uncertainty analysis in Section 6, investigating the systematics of hindered and non-hindered ($P_{\mathrm{CN}} = 1$) reactions leading to the same compound nuclei can provide insight into how the formation probability can be constrained.

Furthermore, the macroscopic potential map of the formation phase could be updated consistently with the fission barrier potential map where shell corrections are incorporated [69]. This will ensure an accurate description of the dynamics, as super-heavy elements are largely stabilized by microscopic energies. On this subject, some investigations with a purely diffusive model have been performed [160].

Appendix A

Capture cross section uncertainty

The uncertainty in the capture cross section following B.1.1.1 is simply written as [161, 162]:

$$u^2(\sigma_{\rm cap}) = \left(\frac{\partial\sigma_{\rm cap}}{\partial R_{\rm B}}\right)^2 u^2(R_{\rm B}) + \left(\frac{\partial\sigma_{\rm cap}}{\partial B_0}\right)^2 u^2(B_0) + \left(\frac{\partial\sigma_{\rm cap}}{\partial\sigma_B}\right)^2 u^2(\sigma_B) + 2\left(\frac{\partial\sigma_{\rm cap}}{\partial B_0}\right)\left(\frac{\partial\sigma_{\rm cap}}{\partial\sigma_B}\right) u(B_0,\sigma_B), \tag{A.1}$$

where,

$$\frac{\partial\sigma_{\rm cap}}{\partial R_{\rm B}} = \frac{\sqrt{2\pi}R_{\rm B}\sigma_B}{E_{\rm cm}}\left[X\sqrt{\pi}(1+{\rm erf}(X)) + e^{-X^2}\right], \tag{A.2}$$

$$\frac{\partial\sigma_{\rm cap}}{\partial B_0} = -\frac{\pi R_{\rm B}^2}{2E_{\rm cm}}(1+{\rm erf}(X)), \tag{A.3}$$

and

$$\frac{\partial\sigma_{\rm cap}}{\partial\sigma_B} = \frac{\pi R_{\rm B}^2}{\sqrt{2\pi}E_{\rm cm}}e^{-X^2}. \tag{A.4}$$

The first term corresponds to the uncertainty due to the normalisation factor ($u(R_{\rm B})$), followed by the uncertainty due to the mean Coulomb barrier ($u(B_0)$), $u(\sigma_{\rm B})$ and the last term is the covariance between the B_0 and $\sigma_{\rm B}$, $u(B_0,\sigma_B)$.

Now we need to evaluate uncertainties in the respective submodels. The uncertainty in the evaluation of the capture normalisation factor is given as:

$$u^2(R_{\rm B}) = \left(\frac{\partial R_{\rm B}}{\partial r_0}\right)^2 u^2(r_0), \tag{A.5}$$

with, $\frac{\partial R_{\rm B}}{\partial r_0} = A_1^{\frac{1}{3}} + A_2^{\frac{1}{3}}$, and A_1 and A_2 are the atomic masses of the colliding nuclei. Following this is the uncertainty in the mean Coulomb barrier due to adjusting the parameters a, b, and c to the experiment:

$$\begin{aligned} u^2(B_0) = &\left(\frac{\partial B_0}{\partial a}\right)^2 u^2(a) + \left(\frac{\partial B_0}{\partial b}\right)^2 u^2(b) + \left(\frac{\partial B_0}{\partial c}\right)^2 u^2(c) + 2\left(\frac{\partial B_0}{\partial a}\right)\left(\frac{\partial B_0}{\partial b}\right) u(a,b) \\ &+ 2\left(\frac{\partial B_0}{\partial a}\right)\left(\frac{\partial B_0}{\partial c}\right) u(a,c) + 2\left(\frac{\partial B_0}{\partial b}\right)\left(\frac{\partial B_0}{\partial c}\right) u(b,c), \end{aligned} \tag{A.6}$$

where $\frac{\partial B_0}{\partial a} = z$, $\frac{\partial B_0}{\partial b} = z^2$ and $\frac{\partial B_0}{\partial c} = z^3$.

Finally, the uncertainty in the Coulomb barrier width distribution stemmed from the uncertainty in the mean Coulomb barrier (B_0), the C and the σ_0:

$$u^2(\sigma_B) = \left(\frac{\partial \sigma_B}{\partial B_0}\right)^2 u^2(B_0) + \left(\frac{\partial \sigma_B}{\partial C}\right)^2 u^2(C) + \left(\frac{\partial \sigma_B}{\partial \sigma_0}\right)^2 u^2(\sigma_0) + 2\left(\frac{\partial \sigma_B}{\partial C}\right)\left(\frac{\partial \sigma_B}{\partial \sigma_0}\right) u(C, \sigma_0), \tag{A.7}$$

where $\frac{\partial \sigma_B}{\partial B_0} = C\sqrt{\sigma_1^2 + \sigma_2^2 + \sigma_0^2}$, $\frac{\partial \sigma_B}{\partial C} = B_0\sqrt{\sigma_1^2 + \sigma_2^2 + \sigma_0^2}$, and $\frac{\partial \sigma_B}{\partial \sigma_0} = \frac{B_0 B_0 \sigma_0}{\sqrt{\sigma_1^2+\sigma_2^2+\sigma_0^2}}$.

Appendix B

Fitting procedure

B.1 Ordinary Linear Regression

The parameters of the injection point distance are adjusted to the experiment using linear regression techniques. This section presents a brief overview of its formalism. The regression analysis allows us to establish and investigate relationships between dependent (y) and independent (x_1) variables [163]:

$$y = \beta_0 + \beta_1 x_1 + \epsilon. \tag{B.1}$$

The intercept (β_0) and slope (β_1) are generally called the regression coefficients. The error (ϵ) is the part of the observation that the regression could not explain. Equation (B.1) can be extended to multiple independent variables in what is called multiple regression:

$$y = \beta_0 + \beta_1 x_1 + \beta_2 x_2 + \cdots + \beta_n x_n + \epsilon. \tag{B.2}$$

This is succinctly written as

$$\mathbf{y} = \mathbf{X}\boldsymbol{\beta} + \boldsymbol{\epsilon}, \tag{B.3}$$

where $\mathbf{X}$ is the regressor matrix. $\boldsymbol{\beta}$, $\boldsymbol{\epsilon}$, and $\mathbf{y}$ are the vectors corresponding to the regression coefficients, errors, and the responses, respectively:

$$\mathbf{y} = \begin{bmatrix} y_1 \\ y_2 \\ \vdots \\ y_n \end{bmatrix}, \quad \mathbf{X} = \begin{bmatrix} 1 & x_{11} & x_{12} & \cdots & x_{1k} \\ 1 & x_{21} & x_{22} & \cdots & x_{2k} \\ \vdots & \vdots & \vdots & \ddots & \vdots \\ 1 & x_{n1} & x_{n2} & \cdots & x_{nk} \end{bmatrix}$$

$$\boldsymbol{\beta} = \begin{bmatrix} \beta_0 \\ \beta_1 \\ \vdots \\ \beta_k \end{bmatrix}, \quad \boldsymbol{\epsilon} = \begin{bmatrix} \epsilon_1 \\ \epsilon_2 \\ \vdots \\ \epsilon_n \end{bmatrix}$$

The estimated values $\hat{\boldsymbol{\beta}}$ of the regression coefficients, which are parameters of interest, are obtained by minimizing the sum of squared error:

$$SSE = (\mathbf{y} - \mathbf{X}\boldsymbol{\beta})^T(\mathbf{y} - \mathbf{X}\boldsymbol{\beta}). \tag{B.4}$$

From here, the least squares estimators $\boldsymbol{\beta}$ are readily obtained as:

$$\hat{\boldsymbol{\beta}} = (\mathbf{X}^\top\mathbf{X})^{-1}\mathbf{X}^\top\mathbf{y}. \tag{B.5}$$

The covariance matrix of the least squares estimators $\hat{\boldsymbol{\beta}}$ is given as:

$$\mathrm{Cov}(\hat{\boldsymbol{\beta}}) = \sigma^2(\mathbf{X}^\top\mathbf{X})^{-1} \tag{B.6}$$

where σ^2 denotes the variance of the error terms. The elements on the diagonal of this matrix represent the variances of the individual regression coefficients, and the off-diagonal elements indicate the covariances between different coefficient estimates. This matrix is used to assess the precision and the interdependencies of the estimates. Finally, using he estimators Eq. (B.5), the model predictions are given as:

$$\hat{y} = \mathbf{x}^\top\hat{\boldsymbol{\beta}}. \tag{B.7}$$

B.1.1 Predictions and Uncertainties

Here, the accuracy of the fitted Equation (B.7) is assessed using the mean squared error of the prediction (MSE) and R^2.

• Mean Squared Error The MSE measures the accuracy of the model by evaluating the average of the squared differences between the observed values y_i and the predicted values $\hat{y}$:

$$MSE = \frac{1}{n-p}\sum_{i=1}^{n}(y_i - \hat{y}_i)^2, \tag{B.8}$$

Here, p is the number of explanatory variables. Taking the square root of the MSE, gives the Root Mean Squared Error (RMSE), which provides an estimate of the average magnitude of the errors in the model's predictions, expressed in the same units as the dependent variable.

• R-squared The R-squared (R^2) is a statistical measure that indicates the proportion of the variance in the observations that is predictable from the explanatory variable(s) in a regression model. The R^2 which takes values from 0 to 1 and can be computed as follows,

$$R^2 = \frac{\text{Explained variation}}{\text{Total variation}} = \frac{\sum_{i=1}^{n}(\hat{y}_i - \bar{y})^2}{\sum_{i=1}^{n}(y_i - \bar{y})^2}. \tag{B.9}$$

Here, $\hat{y}_i$ are the model predictions, whereas y_i are the observations and its mean is denoted by $\bar{y}$.

B.1.1.1 Propagation of Uncertainty

The goal is to quantify the uncertainty in the model predicted values of the response variable ($\hat{y}$) that arises from the uncertainty in the estimated model coefficients. This is crucial for establishing the reliability and accuracy of the model's predictions. As an example, consider the simple linear regression model:

$$y = \beta_0 + \beta_1 x_1, \tag{B.10}$$

where β_0 and β_1 are the intercept and slope, respectively. Due to the randomness inherent in any sample of data, the least squares estimates of these parameters (denoted as $\hat{\beta}_0$ and $\hat{\beta}_1$) are uncertain. This uncertainty in the estimated coefficients can propagate, leading to uncertainty in the predicted values of y.

The uncertainty in the predicted values y, is obtained by propagating the uncertainties of the least squares estimators, β_0 and β_1) onto the model's predictions. This is obtained by examining the total differential of the model (B.10):

$$dy = d\beta_0 + x_1 d\beta_1. \tag{B.11}$$

The differential tells us how infinitesimal changes in the coefficients affect the predicted value of y. Finally, by examining the first-order Taylor series expansion of the model $\hat{y}(x_1, \beta_0, \beta_1)$ around the estimated values of the coefficients $\bar{\beta}_0$ and $\bar{\beta}_1$, one obtained,

$$u^2(y) = \left(\frac{\partial y}{\partial \beta_0}\right)^2 u^2(\beta_0) + \left(\frac{\partial y}{\partial \beta_1}\right)^2 u^2(\beta_1) + 2\left(\frac{\partial y}{\partial \beta_0}\right)\left(\frac{\partial y}{\partial \beta_1}\right) u^2(\beta_0, \beta_1). \tag{B.12}$$

Here, the first and seconds terms are the contribution to the total uncertainty due to β_0 and β_1, respectively. The last term is the contribution stemming from possible correlation between the parameters. This concept can be generalized to the multiple linear regression (Eq. (B.2) as

$$u^2(y) = \sum_{i=0}^{N} \left(\frac{\partial y}{\partial \beta_i}\right)^2 u(\beta_i) + 2 \sum_{i=0}^{N-1} \sum_{j=i+1}^{N} \left(\frac{\partial y}{\partial \beta_i}\right)\left(\frac{\partial y}{\partial \beta_j}\right) u(\beta_i, \beta_j), \tag{B.13}$$

where the first term stands for the uncertainty due to each of the least squares estimators and the second are the possible correlations between them. Eq. (B.13) is subsequently applied to evaluating the uncertainty in the s_{inj}^{N}.

B.1.2 Table of Results

B.1.2.1 Cold Fusion

Table B.1: Predictions and the corresponding uncertainties (column $\mathbf{s}_{\mathrm{inj}}^{\mathcal{N}} \pm u(\mathbf{s}_{\mathrm{inj}}^{\mathcal{N}})\mathbf{fm}$), obtained from linear regression using the data in Table 2.2.

No.	Reactions	$\mathbf{s}_{\mathrm{inj}}^{\mathrm{d}}$ **fm**	$\mathbf{s}_{\mathrm{inj}}^{\mathcal{N}} \pm u(\mathbf{s}_{\mathrm{inj}}^{\mathcal{N}})\mathbf{fm}$
1	^{70}Zn +^{208} Pb	0.52	0.50±0.16
2	^{50}Ti +^{209} Bi	4.05	3.50±0.13
3	^{50}Ti +^{208} Pb	4.07	3.42±0.13
4	^{54}Cr +^{209} Bi	3.23	2.49±0.09
5	^{54}Cr +^{208} Pb	3.07	2.50±0.09
6	^{58}Fe +^{208} Pb	2.36	1.89±0.09
7	^{58}Fe +^{209} Bi	2.08	1.79±0.10
8	^{62}Ni +^{208} Pb	1.44	1.98±0.09
9	^{64}Ni +^{207} Pb	0.93	1.40±0.11
10	^{64}Ni +^{208} Pb	1.35	1.08±0.13
11	^{64}Ni +^{209} Pb	0.89	1.09±0.13
12	^{50}Ti +^{208} Pb	3.40	3.42±0.13
13	^{48}Ti +^{208} Pb	4.35	4.58±0.20
14	^{52}Cr +^{208} Pb	3.46	3.75±0.15
15	^{54}Cr +^{209} Bi	2.87	2.49±0.09
16	^{55}Mn +^{208} Pb	2.41	2.85±0.10
17	^{52}Cr +^{209} Bi	3.28	3.61±0.14
18	^{56}Fe +^{208} Pb	2.52	3.17±0.11
19	^{59}Co +^{208} Pb	1.67	2.70±0.10
20	^{64}Ni +^{208} Pb	1.53	1.08±0.13
21	^{65}Cu +^{208} Pb	0.89	1.43±0.11
22	^{51}V +^{208} Pb	3.76	3.75±0.15
23	^{50}Ti +^{209} Bi	3.95	3.50±0.13
24	^{64}Ni +^{208} Pb	1.32	1.08±0.13
25	^{64}Ni +^{209} Pb	0.91	1.09±0.13
26	^{70}Zn +^{208} Pb	0.57	0.50±0.16
27	^{70}Zn +^{209} Pb	0.11	0.38±0.17

B.1.2.2 Hot Fusion

Table B.2: Predictions and the corresponding uncertainties (column $\mathbf{s}_{\mathrm{inj}}^{\mathcal{N}} \pm u(\mathbf{s}_{\mathrm{inj}}^{\mathcal{N}})\mathbf{fm}$), obtained from linear regression using the data in Table 2.3.

No.	^{48}Ca+Reaction	$\mathbf{s}_{\mathrm{inj}}^{\mathrm{d}}$ fm	$\mathbf{s}_{\mathrm{inj}}^{\mathcal{N}} \pm u(\mathbf{s}_{\mathrm{inj}}^{\mathcal{N}})$ fm
1	^{242}Pu,3n	1.90	2.52±0.17
2	^{242}Pu,4n	-1.75	0.34±0.21
3	^{244}Pu,3n	3.90	3.10±0.21
4	^{244}Pu,4n	1.30	1.07±0.17
5	^{244}Pu,5n	-1.05	-1.54±0.37
6	^{243}Am,2n	3.70	3.77±0.26
7	^{243}Am,3n	1.70	2.25±0.16
8	^{243}Am,4n	0.05	0.06±0.23
9	^{245}Cm,2n	3.60	3.55±0.24
10	^{245}Cm,3n	2.00	1.76±0.15
11	^{245}Cm,4n	0.75	-0.45±0.27
12	^{248}Cm,3n	3.30	2.95±0.20
13	^{248}Cm,4n	0.95	0.69±0.19
14	^{249}Bk,4n	3.05	2.78±0.19
15	^{249}Bk,4n	0.90	0.50±0.20
16	^{249}Cf,3n	1.80	1.01±0.17
17	^{242}Pu,2n	3.85	4.16±0.29
18	^{244}Pu,3n	3.25	3.31±0.22
19	^{244}Pu,4n	0.90	1.07±0.17
20	^{249}Bk,3n	3.10	2.78±0.19
21	^{248}Cm,3n	3.40	2.95±0.20
22	^{248}Cm,4n	0.95	0.69±0.19
23	^{242}Pu,3n	2.00	2.52±0.17
24	^{242}Pu,4n	-1.35	0.34±0.21

Bibliography

[1] A. S. Eve and J. Chadwick, "Lord rutherford, 1871-1937," 1936.

[2] H. Becquerel, "Sur les radiations émises par phosphorescence," *Comptes rendus de 1'Academie des Sciences, Paris*, vol. 122, pp. 420–421, 1896.

[3] P. Radvanyi, "The discovery of radioactivity," *Europhysics News*, vol. 27, no. 2, pp. 57–59, 1996.

[4] J. Chadwick, "Possible existence of a neutron," *Nature*, vol. 129, no. 3252, pp. 312–312, 1932.

[5] M. G. Mayer and J. H. D. Jensen, "Eugene p. wigner," *Physics: 1963-1970*, vol. 4, p. 1, 1964.

[6] M. G. Mayer, "The shell model," *Science*, vol. 145, no. 3636, pp. 999–1006, 1964.

[7] R. López-Ruiz and J. Sanudo, "Evidence of magic numbers in nuclei by statistical indicators," *Open Systems & Information Dynamics*, vol. 17, no. 03, pp. 279–286, 2010.

[8] G. Fea, "Tabelle riassuntive e bibliografia delle trasmutazioni artificiali," *Il Nuovo Cimento (1924-1942)*, vol. 12, no. 6, pp. 368–406, 1935.

[9] Y. T. Oganessian and K. P. Rykaczewski, "A beachhead on the island of stability," *Physics Today*, vol. 68, no. 8, pp. 32–38, 2015.

[10] J. Lilley, *Nuclear physics: principles and applications*. John Wiley & Sons, 2013.

[11] A. C. Hayes, "Applications of nuclear physics," *Reports on Progress in Physics*, vol. 80, no. 2, p. 026301, 2017.

[12] G. T. Seaborg, "The transuranium elements," *Science*, vol. 104, no. 2704, pp. 379–386, 1946.

[13] D. Hoffman, F. Lawrence, J. Mewherter, and F. Rourke, "Detection of plutonium-244 in nature," *Nature*, vol. 234, no. 5325, pp. 132–134, 1971.

[14] C. A. Levine and G. T. Seaborg, "The occurrence of plutonium in nature," *Journal of the American Chemical Society*, vol. 73, no. 7, pp. 3278–3283, 1951.

[15] P. K. Kuroda, "Origin of the elements: pre-fermi reactor and plutonium-244 in nature," *Accounts of Chemical Research*, vol. 12, no. 2, pp. 73–78, 1979.

[16] K. H. Lieser, *Nuclear and radiochemistry: fundamentals and applications*. John Wiley & Sons, 2008.

[17] R. Vandenbosch, *Nuclear fission*. Elsevier, 2012.

[18] N. Bohr and J. A. Wheeler, "The mechanism of nuclear fission," *Physical Review*, vol. 56, no. 5, p. 426, 1939.

[19] F. D. Mackie and G. Baym, "Compressible liquid drop nuclear model and mass formula," *Nuclear Physics A*, vol. 285, no. 2, pp. 332–348, 1977.

[20] A. Di Nitto, J. Khuyagbaatar, D. Ackermann, L.-L. Andersson, E. Badura, M. Block, H. Brand, I. Conrad, D. Cox, C. E. Düllmann, *et al.*, "Study of non-fusion products in the ti50+ cf249 reaction," *Physics Letters B*, vol. 784, pp. 199–205, 2018.

[21] A. Sobiczewski, F. Gareev, and B. Kalinkin, "Closed shells for z> 82 and n> 126 in a diffuse potential well," *Physics Letters*, vol. 22, no. 4, pp. 500–502, 1966.

[22] Y. Oganessian, "Synthesis and decay properties of superheavy elements," *Pure and applied chemistry*, vol. 78, no. 5, pp. 889–904, 2006.

[23] S. Heinz and H. Devaraja, "Nucleosynthesis in multinucleon transfer reactions," *The European Physical Journal A*, vol. 58, no. 6, p. 114, 2022.

[24] V. Zagrebaev and W. Greiner, "Synthesis of superheavy nuclei: A search for new production reactions," *Physical Review C*, vol. 78, no. 3, p. 034610, 2008.

[25] J. J. Cowan, F.-K. Thielemann, and J. W. Truran, "The r-process and nucleochronology," *Physics Reports*, vol. 208, no. 4-5, pp. 267–394, 1991.

[26] J.-J. Li, N. Tang, Y.-H. Zhang, M.-H. Zhang, C. Wang, X.-R. Zhang, L. Zhu, and F.-S. Zhang, "Progress on production cross-sections of unknown nuclei in fusion evaporation reactions and multinucleon transfer reactions," *International Journal of Modern Physics E*, vol. 32, no. 01, p. 2330002, 2023.

[27] V. Zagrebaev, S. Zemlyanoy, E. Kozulin, Y. Kudryavtsev, V. Fedosseev, R. Bark, and H. Othman, "Production and study of heavy neutron rich nuclei formed in multi-nucleon transfer reactions," *Hyperfine Interactions*, vol. 216, pp. 109–113, 2013.

[28] D. Ackermann, T. Ahn, D. Bazin, S. B. Novo, G. Berg, M. Brahim, C. Campbell, R. Casten, K. Chipps, S. Chouhan, *et al.*, "A recoil separator for rea12," *Hall*, 2021.

[29] H. Devaraja, A. Yeremin, S. Heinz, and A. Popeko, "The study of multi-nucleon transfer reactions for synthesis of new heavy and superheavy nuclei," *Physics of Particles and Nuclei Letters*, vol. 19, no. 6, pp. 693–716, 2022.

[30] S. Hofmann, "Synthesis and properties of superheavy elements," *Journal of Nuclear and Radiochemical Sciences*, vol. 4, no. 1, pp. R1–R13, 2003.

[31] S. Hofmann, S. N. Dmitriev, C. Fahlander, J. M. Gates, J. B. Roberto, and H. Sakai, "On the discovery of new elements (iupac/iupap provisional report) provisional report of the 2017 joint working group of iupac and iupap," *Pure and Applied Chemistry*, vol. 90, no. 11, pp. 1773–1832, 2018.

[32] S. Hofmann, S. N. Dmitriev, C. Fahlander, J. M. Gates, J. B. Roberto, and H. Sakai, "On the discovery of new elements (iupac/iupap report) report of the 2017 joint working group of iupac and iupap," *Pure and Applied Chemistry*, vol. 92, no. 9, pp. 1387–1446, 2020.

[33] Y. T. Oganessian and V. Utyonkov, "Super-heavy element research," *Reports on Progress in Physics*, vol. 78, no. 3, p. 036301, 2015.

[34] T. Cap, K. Siwek-Wilczyńska, and J. Wilczyński, "Nucleus-nucleus cold fusion reactions analyzed with the l-dependent "fusion by diffusion" model," *Physical Review C*, vol. 83, no. 5, p. 054602, 2011.

[35] K. Morita, K. Morimoto, D. Kaji, H. Haba, K. Ozeki, Y. Kudou, T. Sumita, Y. Wakabayashi, A. Yoneda, K. Tanaka, *et al.*, "New result in the production and decay of an isotope, 278113, of the 113th element," *journal of the physical society of japan*, vol. 81, no. 10, p. 103201, 2012.

[36] J. Gates, R. Orford, D. Rudolph, C. Appleton, B. Barrios, J. Benitez, M. Bordeau, W. Botha, C. Campbell, J. Chadderton, *et al.*, "Towards the discovery of new elements: Production of livermorium (z= 116) with 50ti," *arXiv preprint arXiv:2407.16079*, 2024.

[37] S. Hofmann, D. Ackermann, S. Antalic, V. Comas, S. Heinz, J. Heredia, F. Heßberger, J. Khuyagbaatar, B. Kindler, I. Kojouharov, *et al.*, "Probing shell effects at z= 120 and n= 184," *GSI scientific report*, vol. 10, p. 131, 2008.

[38] Y. T. Oganessian, V. Utyonkov, Y. V. Lobanov, F. S. Abdullin, A. Polyakov, R. Sagaidak, I. Shirokovsky, Y. S. Tsyganov, A. Voinov, A. Mezentsev, *et al.*, "Attempt to produce element 120 in the pu 244+ fe 58 reaction," *Physical Review C—Nuclear Physics*, vol. 79, no. 2, p. 024603, 2009.

[39] J. Khuyagbaatar, A. Yakushev, C. E. Düllmann, D. Ackermann, L.-L. Andersson, M. Asai, M. Block, R. Boll, H. Brand, D. Cox, *et al.*, "Search for elements 119 and 120," *Physical Review C*, vol. 102, no. 6, p. 064602, 2020.

[40] S. Hofmann, F. Heßberger, D. Ackermann, G. Münzenberg, S. Antalic, P. Cagarda, B. Kindler, J. Kojouharova, M. Leino, B. Lommel, *et al.*, "New results on elements 111 and 112," *The European Physical Journal A-Hadrons and Nuclei*, vol. 14, pp. 147–157, 2002.

[41] Y. T. Oganessian, V. Utyonkov, M. Shumeiko, F. S. Abdullin, G. Adamian, S. Dmitriev, D. Ibadullayev, M. Itkis, N. Kovrizhnykh, D. Kuznetsov, *et al.*, "Synthesis and decay properties of isotopes of element 110: Ds 273 and ds 275," *Physical Review C*, vol. 109, no. 5, p. 054307, 2024.

[42] Y. T. Oganessian, V. Utyonkov, M. Shumeiko, F. S. Abdullin, S. Dmitriev, D. Ibadullayev, M. Itkis, N. Kovrizhnykh, D. Kuznetsov, O. Petrushkin, *et al.*, "New isotope ds 276 and its decay products hs 272 and sg 268 from the th 232+ ca 48 reaction," *Physical Review C*, vol. 108, no. 2, p. 024611, 2023.

[43] A. Nasirov, A. Yusupov, and B. Kayumov, "Small cross section of the synthesis of darmstadtium in the ca 48+ th 232 reaction," *Physical Review C*, vol. 110, no. 1, p. 014618, 2024.

[44] C. Theisen, P. Greenlees, T.-L. Khoo, P. Chowdhury, and T. Ishii, "In-beam spectroscopy of heavy elements," *Nuclear Physics A*, vol. 944, pp. 333–375, 2015.

[45] D. Ackermann and C. Theisen, "Nuclear structure features of very heavy and superheavy nuclei—tracing quantum mechanics towards the 'island of stability'," *Physica Scripta*, vol. 92, no. 8, p. 083002, 2017.

[46] A. Lopez-Martens, K. Hauschild, and G. Collaboration, "Spectroscopy of super heavy elements with gabriela," *The European Physical Journal A*, vol. 58, no. 7, p. 134, 2022.

[47] F. Déchery, H. Savajols, M. Authier, A. Drouart, J. Nolen, D. Ackermann, A. Amthor, B. Bastin, A. Berryhill, D. Boutin, *et al.*, "The super separator spectrometer s3 and the associated detection systems: Sirius & leb-reglis3," *Nuclear Instruments and Methods in Physics Research Section B: Beam Interactions with Materials and Atoms*, vol. 376, pp. 125–130, 2016.

[48] W. Świątecki, K. Siwek-Wilczyńska, and J. Wilczyński, "Fusion by diffusion. ii. synthesis of transfermium elements in cold fusion reactions," *Physical Review C*, vol. 71, no. 1, p. 014602, 2005.

[49] V. Zagrebaev and W. Greiner, "Cross sections for the production of superheavy nuclei," *Nuclear Physics A*, vol. 944, pp. 257–307, 2015.

[50] W. Loveland, "Synthesis of transactinide nuclei using radioactive beams," *Physical Review C*, vol. 76, no. 1, p. 014612, 2007.

[51] G. Adamian, N. Antonenko, and W. Scheid, "Isotopic dependence of fusion cross sections in reactions with heavy nuclei," *Nuclear Physics A*, vol. 678, no. 1-2, pp. 24–38, 2000.

[52] D. Boilley, Y. Abe, and J.-D. Bao, "Inverse kramers formula and fusion dynamics of heavy ions," *The European Physical Journal A-Hadrons and Nuclei*, vol. 18, no. 4, pp. 627–631, 2003.

[53] H. Lü, A. Marchix, Y. Abe, and D. Boilley, "Kewpie2: A cascade code for the study of dynamical decay of excited nuclei," *Computer Physics Communications*, vol. 200, pp. 381–399, 2016.

[54] B. Cauchois, *Uncertainly analysis : towards more accurate predictions for the synthesis of superheavy nuclei*. PhD thesis, Grand Accélérateur National d'Ions Lourds, France, 2018.

[55] R. Naik, W. Loveland, P. Sprunger, A. Vinodkumar, D. Peterson, C. Jiang, S. Zhu, X. Tang, E. Moore, and P. Chowdhury, "Measurement of the fusion probability p cn for the reaction of ti 50 with pb 208," *Physical Review C*, vol. 76, no. 5, p. 054604, 2007.

[56] A. J. Cole, *Statistical models for nuclear decay: from evaporation to vaporization*. CRC Press, 2000.

[57] J. Khuyagbaatar, D. Hinde, I. Carter, M. Dasgupta, C. E. Düllmann, M. Evers, D. Luong, R. du Rietz, A. Wakhle, E. Williams, *et al.*, "Experimental study of the quasifission, fusion-fission, and de-excitation of cf compound nuclei," *Physical Review C*, vol. 91, no. 5, p. 054608, 2015.

[58] N. Antonenko, E. Cherepanov, A. Nasirov, V. Permjakov, and V. Volkov, "Competition between complete fusion and quasi-fission in reactions between massive nuclei. the fusion barrier," *Physics Letters B*, vol. 319, no. 4, pp. 425–430, 1993.

[59] G. Adamian, N. Antonenko, W. Scheid, and V. Volkov, "Treatment of competition between complete fusion and quasifission in collisions of heavy nuclei," *Nuclear Physics A*, vol. 627, no. 2, pp. 361–378, 1997.

[60] E. Cherepanov, G. Adamian, N. Antonenko, and V. Volkov, "Fusion of massive nuclei and synthesis of superheavy elements in the framework of the dns concept," in *AIP Conference Proceedings*, vol. 425, pp. 41–50, American Institute of Physics, 1998.

[61] Y. Abe, D. Boilley, B. G. Giraud, and T. Wada, "Diffusion over a saddle with a langevin equation," *Physical Review E*, vol. 61, no. 2, p. 1125, 2000.

[62] V. Zagrebaev, Y. Aritomo, M. Itkis, Y. T. Oganessian, and M. Ohta, "Synthesis of superheavy nuclei: How accurately can we describe it and calculate the cross sections?," *Physical Review C*, vol. 65, no. 1, p. 014607, 2001.

[63] C. Shen, G. Kosenko, and Y. Abe, "Two-step model of fusion for the synthesis of superheavy elements," *Physical Review C*, vol. 66, no. 6, p. 061602, 2002.

[64] W. Swiatecki, K. Siwek-Wilczynska, and J. Wilczynski, "Fusion by diffusion," *Acta Physica Polonica B*, vol. 34, no. 4, p. 2049, 2003.

[65] Y. Aritomo, "Dynamical study on the synthesis of super-heavy elements," *Progress of Time-Dependent Nuclear Reaction Theory*, vol. 2, pp. 255–282, 2019.

[66] H. A. Kramers, "Brownian motion in a field of force and the diffusion model of chemical reactions," *Physica*, vol. 7, no. 4, pp. 284–304, 1940.

[67] W. Swiatecki, "The dynamics of nuclear coalescence or reseparation," *Physica Scripta*, vol. 24, no. 1B, p. 113, 1981.

[68] T. Cap, M. Kowal, and K. Siwek-Wilczyńska, "The fusion-by-diffusion model as a tool to calculate cross sections for the production of superheavy nuclei," *The European Physical Journal A*, vol. 58, no. 11, pp. 1–18, 2022.

[69] P. Jachimowicz, M. Kowal, and J. Skalski, "Properties of heaviest nuclei with $98 \leq z \leq 126$ and $134 \leq n \leq 192$," *Atomic Data and Nuclear Data Tables*, vol. 138, p. 101393, 2021.

[70] P. Möller, A. Sierk, T. Ichikawa, and H. Sagawa, "Nuclear ground-state masses and deformations: Frdm (2012)," *Atomic Data and Nuclear Data Tables*, vol. 109-110, pp. 1–204, 2016.

[71] S. Goriely, N. Chamel, and J. Pearson, "Further explorations of skyrme-hartree-fock-bogoliubov mass formulas. xvi. inclusion of self-energy effects in pairing," *Physical Review C*, vol. 93, p. 034337, 2016.

[72] S. Goriely, N. Chamel, and J. Pearson, "Latest results of skyrme-hartree-fock-bogoliubov mass formulas," in *Journal of Physics: Conference Series*, vol. 665, p. 012038, IOP Publishing, 2016.

[73] B. Cauchois, *Uncertainly analysis : towards more accurate predictions for the synthesis of superheavy nuclei*. Theses, Normandie Université, June 2018.

[74] B. Bouriquet, Y. Abe, and D. Boilley, "Kewpie: A dynamical cascade code for decaying exited compound nuclei," *Computer physics communications*, vol. 159, no. 1, pp. 1–18, 2004.

[75] A. Marchix, "Study of the influence of the shell correction energy on nuclear reactions leading to the region of superheavy nuclei," tech. rep., CM-P00066289, 2007.

[76] H. Lü, *Synthesis of Super-Heavy Elements: Role of Uncertainty Analysis in Theoretical Modeling*. PhD thesis, Université de Caen Normandie, 2015.

[77] P. Fröbrich and R. Lipperheide, "Theory of nuclear reactions," *(No Title)*, 1996.

[78] C. Simenel, P. McGlynn, A. Umar, and K. Godbey, "Comparison of fission and quasi-fission modes," *Physics Letters B*, vol. 822, p. 136648, 2021.

[79] D. Hinde, M. Dasgupta, and E. Simpson, "Experimental studies of the competition between fusion and quasifission in the formation of heavy and superheavy nuclei," *Progress in Particle and Nuclear Physics*, vol. 118, p. 103856, 2021.

[80] J. R. Nix and A. J. Sierk, "Calculation of compound-nucleus cross sections for symmetric very-heavy-ion reactions," *Physical Review C*, vol. 15, no. 6, p. 2072, 1977.

[81] D. Boilley, Y. Abe, B. Cauchois, and C. Shen, "Elimination of fast variables and initial slip: a new mechanism for fusion hindrance in heavy-ion collisions," *Journal of Physics G: Nuclear and Particle Physics*, vol. 46, no. 11, p. 115102, 2019.

[82] D. Boilley, Y. Abe, B. Cauchois, and C. Shen, "Erratum: Elimination of fast variables and initial slip: a new mechanism for fusion hindrance in heavy-ion collisions (2019 j. phys. g: Nucl. part. phys. 46 115102)," *Journal of Physics G: Nuclear and Particle Physics*, vol. 46, p. 129601, nov 2019.

[83] N. Bohr, "Neutron capture and nuclear constitution," *Nature*, vol. 137, no. 3461, pp. 344–348, 1936.

[84] W. Reisdorf and M. Schädel, "How well do we understand the synthesis of heavy elements by heavy-ion induced fusion?," *Zeitschrift für Physik A Hadrons and Nuclei*, vol. 343, pp. 47–57, 1992.

[85] K. Hagino, "Hot fusion reactions with deformed nuclei for synthesis of superheavy nuclei: An extension of the fusion-by-diffusion model," *Physical Review C*, vol. 98, no. 1, p. 014607, 2018.

[86] K. Siwek-Wilczyńska and J. Wilczyński, "Empirical nucleus-nucleus potential deduced from fusion excitation functions," *Physical Review C*, vol. 69, no. 2, p. 024611, 2004.

[87] W. Greiner, J. A. Maruhn, *et al.*, *Nuclear models*. Springer, 1996.

[88] D. Hinde, M. Dasgupta, J. Leigh, J. Lestone, J. Mein, C. Morton, J. Newton, and H. Timmers, "Fusion-fission versus quasifission: Effect of nuclear orientation," *Physical review letters*, vol. 74, no. 8, p. 1295, 1995.

[89] V. E. Viola Jr and T. Sikkeland, "Total cross sections for fission of u 238 induced by he 4 and heavy ions," *Physical Review*, vol. 128, no. 2, p. 767, 1962.

[90] C. Morton, D. Hinde, J. Leigh, J. Lestone, M. Dasgupta, J. Mein, J. Newton, and H. Timmers, "Resolution of the anomalous fission fragment anisotropies for the o 16+ 208 pb reaction," *Physical Review C*, vol. 52, no. 1, p. 243, 1995.

[91] A. Pacheco, J. F. Niello, D. DiGregorio, M. Di Tada, J. Testoni, Y. Chan, E. Chávez, S. Gazes, E. Plagnol, and R. Stokstad, "Capture reactions in the ca 4 0, 4 8+ 197 au and ca 4 0, 4 8+ 208 pb systems," *Physical Review C*, vol. 45, no. 6, p. 2861, 1992.

[92] H. Timmers, D. Ackermann, S. Beghini, L. Corradi, J. He, G. Montagnoli, F. Scarlassara, A. Stefanini, and N. Rowley, "A case study of collectivity, transfer and fusion enhancement," *Nuclear Physics A*, vol. 633, no. 3, pp. 421–445, 1998.

[93] R. Bock, Y. Chu, M. Dakowski, A. Gobbi, E. Grosse, A. Olmi, H. Sann, D. Schwalm, U. Lynen, W. Müller, *et al.*, "Dynamics of the fusion process," *Nuclear Physics A*, vol. 388, no. 2, pp. 334–380, 1982.

[94] H. G. Clerc, J. G. Keller, C. C. Sahm, K. H. Schmidt, H. Schulte, and D. Vermeulen, "Fusion-fission and neutron-evaporation-residue cross-sections in 40 Ar- and 50 Ti-induced fusion reactions," *Nucl. Phys. A*, vol. 419, pp. 571–588, 1984.

[95] H. Sann, R. Bock, Y. Chu, A. Gobbi, A. Olmi, U. Lynen, W. Müller, S. Bjørnholm, and H. Esbensen, "Deformability as a critical factor in initiating fusion between very heavy ions," *Physical Review Letters*, vol. 47, no. 18, p. 1248, 1981.

[96] S. Hassani and P. Grangé, "Neutron multiplicities in fission viewed as a diffusion process," *Physics Letters B*, vol. 137, no. 5-6, pp. 281–286, 1984.

[97] K. Siwek-Wilczyńska, T. Cap, M. Kowal, A. Sobiczewski, and J. Wilczyński, "Predictions of the fusion-by-diffusion model for the synthesis cross sections of z= 114–120 elements based on macroscopic-microscopic fission barriers," *Physical Review C*, vol. 86, no. 1, p. 014611, 2012.

[98] W. Hauser and H. Feshbach, "The inelastic scattering of neutrons," *Physical review*, vol. 87, no. 2, p. 366, 1952.

[99] V. Weisskopf, "Statistics and nuclear reactions," *Physical Review*, vol. 52, no. 4, p. 295, 1937.

[100] V. F. Weisskopf and D. H. Ewing, "Radiative capture of neutrons," *Physical Review*, vol. 57, p. 472, 1940.

[101] A. Gavron, "Statistical model calculations in heavy ion reactions," *Physical Review C*, vol. 21, no. 1, p. 230, 1980.

[102] I. Dostrovsky, Z. Fraenkel, and G. Friedlander, "Monte carlo calculations of nuclear evaporation processes. iii. applications to low-energy reactions," *Physical Review*, vol. 116, no. 3, p. 683, 1959.

[103] V. Strutinsky, "The fission width of excited nuclei," *Physics Letters B*, vol. 47, no. 2, pp. 121–123, 1973.

[104] M. Grossjean and H. Feldmeier, "Level density of a fermi gas with pairing interactions," *Nuclear Physics A*, vol. 444, no. 1, pp. 113–132, 1985.

[105] J. Huizenga and L. Moretto, "Nuclear level densities," *Annual Review of Nuclear Science*, vol. 22, no. 1, pp. 427–464, 1972.

[106] W. Reisdorf, "Analysis of fissionability data at high excitation energies: I. the level density problem," *Zeitschrift für Physik A Atoms and Nuclei*, vol. 300, no. 2-3, pp. 227–238, 1981.

[107] A. V. Ignatyuk, G. N. Smirenkin, and A. S. Tishin, "Phenomenological description of energy dependence of the level density parameter," *Yad. Fiz., v. 21, no. 3, pp. 485-490*, 3 1975.

[108] A. Rahmatinejad, A. Bezbakh, T. Shneidman, G. Adamian, N. Antonenko, P. Jachimowicz, and M. Kowal, "Level-density parameters in superheavy nuclei," *Physical Review C*, vol. 103, no. 3, p. 034309, 2021.

[109] P. Möller, J. Nix, W. Myers, and W. Swiatecki, "Nuclear ground-state masses and deformations," *arXiv preprint nucl-th9308022*, 1993.

[110] P. Fröbrich and I. Gontchar, "Langevin description of fusion, deep-inelastic collisions and heavy-ion-induced fission," *Physics reports*, vol. 292, no. 3-4, pp. 131–237, 1998.

[111] A. Junghans, M. De Jong, H.-G. Clerc, A. Ignatyuk, G. Kudyaev, and K.-H. Schmidt, "Projectile-fragment yields as a probe for the collective enhancement in the nuclear level density," *Nuclear Physics A*, vol. 629, no. 3-4, pp. 635–655, 1998.

[112] K. Nishio, H. Ikezoe, M. Asai, K. Tsukada, S. Mitsuoka, K. Tsuruta, K. Satou, C. Lin, and T. Ohsawa, "Evidence of complete fusion in the subbarrier 16 o+ 238 u reaction," *Physics of Atomic Nuclei*, vol. 69, pp. 1399–1404, 2006.

[113] K. Eskola, P. Eskola, M. Nurmia, and A. Ghiorso, "Studies of lawrencium isotopes with mass numbers 255 through 260," *Physical Review C*, vol. 4, no. 2, p. 632, 1971.

[114] J. Nitschke, M. Fowler, A. Ghiorso, R. Leber, M. Leino, M. Nurmia, L. Somerville, K. Williams, E. Hulet, J. Landrum, *et al.*, "Search for an 80 ms spontaneous fission activity in bombardments of 249bk with 15n," *Nuclear Physics A*, vol. 352, no. 1, pp. 138–146, 1981.

[115] A. Ghiorso, J. Nitschke, J. Alonso, C. Alonso, M. Nurmia, G. Seaborg, E. Hulet, and R. Lougheed, "Element 106," *Physical Review Letters*, vol. 33, no. 25, p. 1490, 1974.

[116] Y. Abe, S. Ayik, P.-G. Reinhard, and E. Suraud, "On stochastic approaches of nuclear dynamics," *Physics reports*, vol. 275, no. 2-3, pp. 49–196, 1996.

[117] V. Zagrebaev and W. Greiner, "Unified consideration of deep inelastic, quasi-fission and fusion–fission phenomena," *Journal of Physics G: Nuclear and Particle Physics*, vol. 31, no. 7, p. 825, 2005.

[118] T. Cap, M. Kowal, and K. Siwek-Wilczyńska, "Diffusion as a possible mechanism controlling the production of superheavy nuclei in cold fusion reactions," *Physical Review C*, vol. 105, no. 5, p. L051601, 2022.

[119] J. Blocki and W. Swiatecki, "Nuclear-deformation energies according to a liquid-drop model with a sharp surface," tech. rep., Lawrence Berkeley National Lab.(LBNL), Berkeley, CA (United States), 1982.

[120] S. Hofmann, F. Heßberger, D. Ackermann, S. Antalic, P. Cagarda, B. Kindler, P. Kuusiniemi, M. Leino, B. Lommel, O. Malyshev, R. Mann, G. Mu¨nzenberg, A. Popeko, S. S´aro, B. Streicher, and A. Yeremin, "Properties of heavy nuclei measured at the gsi ship," *Nuclear Physics A*, vol. 734, pp. 93–100, 2004.

[121] F. Heßberger, S. Hofmann, D. Ackermann, V. Ninov, M. Leino, G. Münzenberg, S. Saro, A. Lavrentev, A. Popeko, A. Yeremin, *et al.*, "Decay properties of neutron-deficient isotopes 256, 257 db, 255 rf, 252, 253 lr," *The European Physical Journal A-Hadrons and Nuclei*, vol. 12, pp. 57–67, 2001.

[122] S. Nelson, C. Folden III, K. Gregorich, I. Dragojević, C. E. Düllmann, R. Eichler, M. Garcia, J. Gates, R. Sudowe, and H. Nitsche, "Comparison of complementary reactions for the production of bh 261, 262," *Physical Review C—Nuclear Physics*, vol. 78, no. 2, p. 024606, 2008.

[123] S. Hofmann, F. Heßberger, D. Ackermann, S. Antalic, P. Cagarda, S. Ćwiok, B. Kindler, J. Kojouharova, B. Lommel, R. Mann, *et al.*, "The new isotope 270 110 and its decay products 266 hs and 262 sg," *The European Physical Journal A-Hadrons and Nuclei*, vol. 10, pp. 5–10, 2001.

[124] S. Hofmann, V. Ninov, F. Heßberger, P. Armbruster, H. Folger, G. Münzenberg, H. Schött, A. Popeko, A. Yeremin, A. Andreyev, *et al.*, "The new element 111," *Zeitschrift für Physik A Hadrons and Nuclei*, vol. 350, pp. 281–282, 1995.

[125] I. Dragojević, K. Gregorich, C. E. Düllmann, M. Garcia, J. Gates, S. Nelson, L. Stavsetra, R. Sudowe, and H. Nitsche, "Influence of projectile neutron number in the 208 pb (48 ti, n) 255 rf and 208 pb (50 ti, n) 257 rf reactions," *Physical Review C—Nuclear Physics*, vol. 78, no. 2, p. 024605, 2008.

[126] C. Folden III, I. Dragojevic, M. Garcia, J. Gates, S. Nelson, D. Hoffman, H. Nitsche, C. E. Duellmann, R. Sudowe, K. Gregorich, *et al.*, "Measurement of the {sup 208} pb ({sup 52} cr, n){sup 259} sg excitation function," *Physical Review. C, Nuclear Physics*, vol. 79, no. 2, 2009.

[127] C. Folden III, S. Nelson, C. E. Düllmann, J. Schwantes, R. Sudowe, P. Zielinski, K. Gregorich, H. Nitsche, and D. Hoffman, "Excitation function for the production of bh 262 (z= 107) in the odd-z-projectile reaction pb 208 (mn 55, n)," *Physical Review C—Nuclear Physics*, vol. 73, no. 1, p. 014611, 2006.

[128] S. Nelson, I. Dragojevic, M. Garcia, J. Gates, H. Nitsche, K. Gregorich, and R. Sudowe, "Lightest isotope of bh produced via the {sup 209} bi ({sup 52} cr, n){sup 260} bh reaction," *Physical Review Letters*, vol. 100, no. 2, 2008.

[129] I. Dragojević, K. Gregorich, C. E. Düllmann, J. Dvorak, P. Ellison, J. Gates, S. Nelson, L. Stavsetra, and H. Nitsche, "New isotope hs 263," *Physical Review C—Nuclear Physics*, vol. 79, no. 1, p. 011602, 2009.

[130] S. Nelson, K. Gregorich, I. Dragojević, J. Dvořák, P. Ellison, M. Garcia, J. Gates, L. Stavsetra, M. Ali, and H. Nitsche, "Comparison of complementary reactions in the production of mt," *Physical Review C—Nuclear Physics*, vol. 79, no. 2, p. 027605, 2009.

[131] T. Ginter, K. Gregorich, W. Loveland, D. Lee, U. Kirbach, R. Sudowe, C. Folden III, J. Patin, N. Seward, P. Wilk, *et al.*, "Confirmation of production of element 110 by the 208 pb (64 ni, n) reaction," *Physical Review C*, vol. 67, no. 6, p. 064609, 2003.

[132] C. Folden III, C. E. Duellmann, G. Pang, J. Schwantes, P. Zielinski, H. Nitsche, D. Hoffman, K. Gregorich, H. Mahmud, and R. Sudowe, "Development of an odd-z-projectile reaction for heavy element synthesis: Pb {sup 208}(ni {sup 64}, n) d {sup 271} s and pb {sup 208}(cu {sup 65}, n) 111 {sup 272}," *Physical Review Letters*, vol. 93, 2004.

[133] J. M. Gates, S. L. Nelson, K. E. Gregorich, I. Dragojević, C. E. Düllmann, P. A. Ellison, C. M. Folden III, M. A. Garcia, L. Stavsetra, R. Sudowe, *et al.*, "Comparison of reactions for the production of db 258, 257: 208 pb (51 v, xn) and 209 bi (50 ti, xn)," *Physical Review C—Nuclear Physics*, vol. 78, no. 3, p. 034604, 2008.

[134] K. Morita, K. Morimoto, D. Kaji, H. Haba, E. Ideguchi, R. Kanungo, K. Katori, H. Koura, H. Kudo, T. Ohnishi, *et al.*, "Production and decay of the isotope 271 ds (z= 110)," *The European Physical Journal A-Hadrons and Nuclei*, vol. 21, pp. 257–263, 2004.

[135] K. Morita, K. Morimoto, D. Kaji, H. Haba, E. Ideguchi, J. C. Peter, R. Kanungo, K. Katori, H. Koura, H. Kudo, *et al.*, "Production and decay properties of 272111 and its daughter nuclei," *journal of the physical society of japan*, vol. 73, no. 7, pp. 1738–1744, 2004.

[136] K. Morita, K. Morimoto, D. Kaji, T. Akiyama, S.-i. Goto, H. Haba, E. Ideguchi, K. Katori, H. Koura, H. Kudo, *et al.*, "Experiment on synthesis of an isotope 277112 by 208pb+ 70zn reaction," *Journal of the Physical Society of Japan*, vol. 76, no. 4, p. 043201, 2007.

[137] K. Morita, K. Morimoto, D. Kaji, T. Akiyama, S.-i. Goto, H. Haba, E. Ideguchi, R. Kanungo, K. Katori, H. Koura, *et al.*, "Experiment on the synthesis of element 113 in the reaction 209bi (70zn, n) 278113," *Journal of the physical Society of Japan*, vol. 73, no. 10, pp. 2593–2596, 2004.

[138] Y. T. Oganessian, V. Utyonkov, Y. V. Lobanov, F. S. Abdullin, A. Polyakov, I. Shirokovsky, Y. S. Tsyganov, G. Gulbekian, S. Bogomolov, B. Gikal, *et al.*, "Measurements of cross sections and decay properties of the isotopes of elements 112, 114, and 116 produced in the fusion reactions u 233, 238, pu 242, and cm 248+ ca 48," *Physical Review C—Nuclear Physics*, vol. 70, no. 6, p. 064609, 2004.

[139] Y. T. Oganessian, V. Utyonkov, Y. V. Lobanov, F. S. Abdullin, A. Polyakov, I. Shirokovsky, Y. S. Tsyganov, G. Gulbekian, S. Bogomolov, B. Gikal, *et al.*, "Measurements of cross sections for the fusion-evaporation reactions pu 244 (ca 48, xn) 292- x 114 and cm 245 (ca 48, xn) 293- x 116," *Physical Review C—Nuclear Physics*, vol. 69, no. 5, p. 054607, 2004.

[140] Y. T. Oganessian, F. S. Abdullin, S. Dmitriev, J. Gostic, J. Hamilton, R. Henderson, M. Itkis, K. Moody, A. Polyakov, A. Ramayya, *et al.*, "New insights into the am 243+ ca 48 reaction products previously observed in the experiments on elements 113, 115, and 117," *Physical Review Letters*, vol. 108, no. 2, p. 022502, 2012.

[141] Y. T. Oganessian and V. Utyonkov, "Super-heavy element research," *Reports on Progress in Physics*, vol. 78, no. 3, p. 036301, 2015.

[142] Y. T. Oganessian, V. Utyonkov, Y. V. Lobanov, F. S. Abdullin, A. Polyakov, I. Shirokovsky, Y. S. Tsyganov, G. Gulbekian, S. Bogomolov, B. Gikal, *et al.*, "Measurements of cross sections and decay properties of the isotopes of elements 112, 114, and 116 produced in the fusion reactions u 233, 238, pu 242, and cm 248+ ca 48," *Physical Review C—Nuclear Physics*, vol. 70, no. 6, p. 064609, 2004.

[143] Y. T. Oganessian and V. Utyonkov, "Super-heavy element research," *Reports on Progress in Physics*, vol. 78, no. 3, p. 036301, 2015.

[144] Y. T. Oganessian and V. Utyonkov, "Super-heavy element research," *Reports on Progress in Physics*, vol. 78, no. 3, p. 036301, 2015.

[145] J. Gates, C. E. Düllmann, M. Schädel, A. Yakushev, A. Türler, K. Eberhardt, J. Kratz, D. Ackermann, L.-L. Andersson, M. Block, *et al.*, "First superheavy element experiments at the gsi recoil separator tasca: The production and decay of element 114 in the pu 244 (ca 48, 3-4 n) reaction," *Physical Review C—Nuclear Physics*, vol. 83, no. 5, p. 054618, 2011.

[146] C. E. Düllmann, M. Schädel, A. Yakushev, A. Türler, K. Eberhardt, J. Kratz, D. Ackermann, L.-L. Andersson, M. Block, W. Brüchle, *et al.*, "Production and decay of element 114: High cross sections and the new nucleus hs 277," *Physical Review Letters*, vol. 104, no. 25, p. 252701, 2010.

[147] C. E. Düllmann, D. Ackermann, A. Yakushev, and J. Khuyagbaatar, "48ca+ 249bk fusion reaction leading to element z= 117: Long-lived α-decaying 270db and discovery of 266lr," *Physical Review Letters*, vol. 112, no. 17, 2014.

[148] L. Stavsetra, K. Gregorich, J. Dvorak, P. Ellison, I. Dragojević, M. Garcia, and H. Nitsche, "Independent verification of element 114 production in the ca 48+ pu 242 reaction," *Physical review letters*, vol. 103, no. 13, p. 132502, 2009.

[149] J. Blocki, F. Brut, T. Srokowski, and W. Swiatecki, "The order to chaos transition in axially symmetric nuclear shapes," *Nuclear Physics A*, vol. 545, no. 1-2, pp. 511–521, 1992.

[150] P. I. Frazier, "A tutorial on bayesian optimization," 2018.

[151] P. Liu, *Bayesian Optimization: Theory and Practice Using Python*. Springer, 2023.

[152] D. J. Lizotte, "Practical bayesian optimization," *a*, 2008.

[153] M. Tanaka, P. Brionnet, M. Du, J. Ezold, K. Felker, B. J. Gall, S. Go, R. K. Grzywacz, H. Haba, K. Hagino, *et al.*, "Probing optimal reaction energy for synthesis of element 119 from 51v+ 248cm reaction with quasielastic barrier distribution measurement," *journal of the physical society of japan*, vol. 91, no. 8, p. 084201, 2022.

[154] L. Sun, Z. Zhang, Z. Gan, S. Xu, M. Zhang, J. Wang, M. Huang, L. Ma, H. Yang, H. Zhou, *et al.*, "Systematics of production cross sections in cr 54-induced fusion evaporation reactions," *Physical Review C*, vol. 110, no. 1, p. 014319, 2024.

[155] S. Hofmann, S. Heinz, R. Mann, J. Maurer, G. Münzenberg, S. Antalic, W. Barth, H. Burkhard, L. Dahl, K. Eberhardt, *et al.*, "Review of even element super-heavy nuclei and search for element 120," *The European Physical Journal A*, vol. 52, pp. 1–34, 2016.

[156] H. Lü, D. Boilley, Y. Abe, and C. Shen, "Synthesis of superheavy elements: Uncertainty analysis to improve the predictive power of reaction models," *Physical Review C*, vol. 94, no. 3, p. 034616, 2016.

[157] M. Fluss, J. Miller, J. d'Auria, N. Dudey, B. Foreman Jr, L. Kowalski, and R. Reedy, "Investigation of the bohr-independence hypothesis for nuclear reactions in the continuum: α+ co 59, p+ ni 62 and α+ fe 56, p+ cl 59," *Physical Review*, vol. 187, no. 4, p. 1449, 1969.

[158] A. Yeremin, D. Bogdanov, V. Chepigin, V. Gorshkov, A. Kabachenko, O. Malyshev, A. Popeko, R. Sagaidak, G. Ter-Akopian, and A. Lavrentjev, "The electrostatic separator vassilissa performance and experimental results," *Nuclear Instruments and Methods in Physics Research Section B: Beam Interactions with Materials and Atoms*, vol. 126, no. 1, pp. 329–333, 1997. International Conference on Electromagnetic Isotope Separators and Techniques Related to Their Applications.

[159] J. M. Gates, S. L. Nelson, K. E. Gregorich, I. Dragojević, C. E. Düllmann, P. A. Ellison, C. M. Folden III, M. A. Garcia, L. Stavsetra, R. Sudowe, *et al.*, "Comparison of reactions for the production of db 258, 257: 208 pb (51 v, xn) and 209 bi (50 ti, xn)," *Physical Review C*, vol. 78, no. 3, p. 034604, 2008.

[160] T. Cap, A. Augustyn, M. Kowal, and K. Siwek-Wilczyńska, "Dipole-driven multidimensional fusion: An insightful approach to the formation of superheavy nuclei," *Physical Review C*, vol. 109, no. 6, p. L061603, 2024.

[161] I. BIPM, I. IFCC, I. ISO, and O. IUPAP, "Evaluation of measurement data—guide to the expression of uncertainty in measurement, jcgm 100: 2008 gum 1995 with minor corrections," *Joint Committee for Guides in Metrology*, vol. 98, 2008.

[162] L. Kirkup and R. B. Frenkel, *An introduction to uncertainty in measurement: using the GUM (guide to the expression of uncertainty in measurement)*. Cambridge University Press, 2006.

[163] D. C. Montgomery, E. A. Peck, and G. G. Vining, *Introduction to linear regression analysis*. John Wiley & Sons, 2021.